Polarisation Coherence Imaging of Electric and Magnetic Fields in Plasmas

Alex Thorman

A thesis submitted for the degree of
Doctor of Philosophy of
The Australian National University

April, 2018

Declaration

This thesis is an account of research undertaken between May 2013 and April 2018 at The Research School of Physics and Engineering, College of Physical and Mathematical Sciences, The Australian National University, Canberra, Australia.

Except where acknowledged in the customary manner, the material presented in this thesis is, to the best of my knowledge, original, my own work and has not been submitted in whole or part for a degree in any university.

Alex Thorman
April, 2018

Acknowledgements

I am most thankful to John Howard my primary supervisor for the inspiration, opportunities, stimulating challenges and endless ideas he has presented to me during this research. I am also grateful to Clive Michael for the many invaluable discussions and insights along the way. Boyd Blackwell's expertise and the many dedicated hours he spent working on H-1 are much appreciated. Many of the experiments would not have been possible without the technical expertise and solutions developed by Michael Blacksell and Mark Gwynneth. I would like to thank many people in the research school, in particular Cormac Corr, Gerrard Borg, Romana Lester, Cameron Samuell and Shaun Haskey.

I wish to praise my partner Catherine, my family and friends for their unwavering support, encouragement and belief over the course of my studies and I will be forever appreciative.

Steve Allen and Brian Victor were integral to the success of the DIII-D IMSE experiments along with contributions from others in the wider Lawrence Livermore National Laboratory and DIII-D teams. I am grateful to Robert and Helen Crompton for the Crompton Award funding which made it possible for me to travel to San Diego to undertake these experiments. The work on DIII-D was supported in part by the U.S. Department of Energy, Office of Science, Office of Fusion Energy Sciences, using the DIII-D National Fusion Facility, a DOE Office of Science user facility, under Award No(s). DE-FC02-04ER54698 and DE-AC52-07NA27344.

I would also like to thank the Australian Government Research Training Program and AINSE Ltd (Post Graduate Research Award) for providing financial assistance to enable the work in this thesis.

Abstract

Polarisation coherence imaging is a powerful spectroscopic diagnostic for high spatial resolution measurements of strong electric and/or magnetic fields inside high temperature fusion plasmas. The motional Stark effect (MSE) is the principal application for the technique, involving measurement of the Balmer-α polarised emission from high velocity neutral beam atoms subjected to a strong $\mathbf{v} \times \mathbf{B}$ electric field. The research in this thesis examines all aspects of polarisation coherence imaging including: the atomic physics of the Stark-Zeeman split light emission; the optical physics and measurement principles involved in the technique; and experimental measurements on the DIII-D tokamak and H-1 heliac.

The polarisation properties of single electron atoms in crossed electric and magnetic fields are revealed to be more complex than previously recognised due to the remaining degeneracy in the Stark-Zeeman energy levels and the absence of a well-defined magnetic quantum number. A linear perturbation theory analysis finds distinct polarisation structures for the σ emission that apply when the fine-structure of the atom and microscopic electric fields are considered. Only the $\sigma_{\pm 1}$ polarisation orientation is sensitive to upper-state populations, which are known to be non-statistical for MSE beam-into-gas calibrations, however with appropriate viewing geometries and neutral beam injection directions the effect can be made negligible. Similarly beam-into-gas calibrations of the $\sigma_{\pm 1} : \pi_{\pm 3}$ line intensity ratio are found to be sensitive to upper-state populations and are therefore potentially invalid. Equations for the linear and circular polarisation of each Balmer-α transition are formulated, correct to second order in the Zeeman:Stark splitting ratio, for straightforward interpretation of the Stokes parameters. Calculations reveal the net circular polarisation fraction for the $\pi_{\pm 3}$ and $\pi_{\pm 4}$ emission is $\sim 20\%$ for typical beam energies.

Various imaging polarimeter designs exist and their different advantages and calibration challenges are examined. Some imaging MSE strategies encode the Stark-Zeeman circular polarisation at the same spatial frequency as the linear polarisation, however fortunately it is established that the interferometric delay can be tuned to mitigate the circular polarisation signal without severely reducing the linear polarisation signal. A newly developed non-axial ray model is capable of predicting and characterising additional spatial carriers generated by a sequence of displacer waveplates.

An imaging MSE diagnostic was benchmarked against existing conventional MSE polarimeters on DIII-D and delivered new capabilities for measuring the magnetic pitch angle from 2 neutral beams and on the high field side of DIII-D. The imaging measurements from each neutral beam were self-consistent and good agreement was demonstrated with conventional MSE measurements for shots with magnetic field and plasma current in the standard direction, however the agreement is lost for shots with either reversed field or current direction. An analysis of the magnetic axis position independently measured with the conventional MSE, imaging MSE, electron cyclotron emission and magnetics is presented to elucidate differences between the MSE measurements. The ferroelectric liquid crystal waveplate used in the imaging polarimeter was discovered to have spatially non-

uniform retardance, hence it is imperative for the illumination of the calibration source to replicate the ray paths of the neutral beam emission through the optical system. A systematic distortion is apparent in the images above and below the midplane, possibly due to remaining uncertainties from the Faraday rotation calibration or the illumination source dependence.

Phase resolved imaging on the H-1 heliac revealed a 7MHz temporal oscillation in the light intensity that has the structure of a propagating wave. Using multiple viewing geometries and a magnetic field strength scan it was revealed that the wave characteristics are consistent with electron density perturbations produced by an electromagnetic ion cyclotron wave propagating near the last closed flux surface. The parallel velocity of the observed RF wave is comparable to the electron thermal speed suggesting that Landau damping of the wave energy to electrons drives the edge electron heating on H-1.

Contents

List of Figures

List of Tables

List of Symbols

Chapter 1

a_0	Bohr Radius
α	Horizontal angle between the neutral beam and toroidal direction
$\mathbf{B}$	Magnetic field
e	Elementary charge
$\mathbf{E}$	Electric field
$\mathbf{E}_L$	Motional electric field ($\mathbf{v} \times \mathbf{B}$)
$\mathbf{E}_r$	Plasma radial electric field
h	Planck Constant
$\mathbf{i}$	View direction (from emission towards observation point)
$\mathbf{j}$	Plasma current density
λ	Wavelength (light)
n	Principal quantum number
ν	Frequency (light)
ψ	Angle between $\mathbf{E}$ and $\mathbf{i}$
ψ_p	Poloidal magnetic flux (Eq. 1.5)
q	Safety factor (Eq. 1.6)
Q	Charge
(R, ϕ, Z)	Cylindrical coordinates
(ρ, ϕ, θ)	Toroidal coordinates
θ_E	Angle of motional electric field in plane perpendicular to $\mathbf{v}$ (Eq. 1.14)
θ_{pitch}	Magnetic field pitch angle (Eq. 1.15)
θ_π	Polarisation orientation of the Stark π emissions
θ_σ	Polarisation orientation of the Stark σ emission
$\mathbf{v}$	Neutral beam velocity

Chapter 2

A	Spontaneous emission rate coefficient
α	Fine structure constant (dimensionless, n.b. difference to Ch. 1)
$b_{n,ij}$	Mixing coefficient for perturbed quantum state
δ	Scaled difference between the population of upper-state pairs (Eq. 2.53)
δ_{ij}	Kronecker delta function
$\delta()$	Dirac delta function
$\mathbf{E}_0$	Holtsmark field strength
E_{state}	Energy of a particular quantum state

ϵ	Characteristic Stark splitting (Eq. 2.1, energy)
g_l	Electron orbital g-factor
g_s	Electron spin g-factor
γ	Characteristic Zeeman splitting (Eq. 2.2, energy)
H	Hamiltonian (Eq. 2.6)
$\mathbf{H}$	Polarimeter horizontal axis (Eq. 2.16)
$\hbar$	Reduced Planck constant
I_0	Intensity of light
j	Total angular momentum quantum number
$k = n_1 - n_2$	Parabolic quantum numbers
l	Orbital angular momentum (azimuthal) quantum number
$\mathbf{L}$	Orbital angular momentum operator
m or m_l	Orbital angular momentum projection ('magnetic') quantum number
m_e	Electron mass
m_s	Spin projection quantum number
m_j	Total angular momentum projection quantum number
n_e	Electron density
N_{state}	Population of a quantum state
ω	Angular frequency (light)
p	Polarisation fraction
p_l	Linear polarisation fraction
p_c	Circular polarisation fraction
φ	Angle $\mathbf{i}$ projects in the xy plane (Fig. 2.1)
q_0	n=2 level characteristic Stark-Zeeman splitting (Eq. 2.3, energy)
q_1	n=3 level characteristic Stark-Zeeman splitting (Eq. 2.4, energy)
$\mathbf{r} = (x, y, z)$	Position vector in the rest frame of the atom
$\mathbf{r}_{ij}$	Dipole vector for a particular atomic transition
ρ	Angle between $\mathbf{B}$ and $\mathbf{v}$ (n.b. difference to Ch. 1)
ρ^{state1}_{state2}	Off diagonal elements of the proton impact excitation density matrix
$\mathbf{s} = (s_0, s_1, s_2, s_3)$	Stokes vector
$\bar{\mathbf{s}}$	Dimensionless Stokes vector (Eq. 2.20)
$\mathbf{S}$	Spin angular momentum operator
$\sigma^{\pm}$	Circular σ transitions with sign indicating handedness
σ^B	Linear σ transitions polarised in the $\mathbf{B}$ direction
σ^v	Linear σ transitions polarised in the $\mathbf{E} \times \mathbf{B}$ direction
σ_{state}	Proton impact excitation cross section from ground state to a particular state
τ	Elevation of $\mathbf{B}$ to xy plane (Fig. 2.1)
θ	Linear polarisation orientation (n.b. difference to Ch. 1)
$\mathbf{V}$	Polarimeter vertical axis (Eq. 2.17)
ξ	Polarisation ellipticity angle (Fig. 2.2)
ξ_c	Ellipticity angle of dipole vector in xy plane (Fig. 2.9)
ξ_r	Ellipticity angle of dipole vector in yz plane (Fig. 2.9)

Chapter 3

$A(,)$	Spatial carrier wave amplitude of a particular carrier
α	Ray incidence angle on waveplate (Fig. 3.3, n.b. difference to Ch. 1 and 2)
α_l	Interferogram phase offset for the linear polarisation spectrum (Eq. 3.47)
α_c	Interferogram phase offset for the circular polarisation spectrum
β	Ray azimuthal angle on waveplate (Fig. 3.3)
δ_c	Offset of α_c from the ideal $\pm 90°$ (Eq. 3.52)
$\hat{\mathbf{e}}$	Orientation of extraordinary ray polarisation
η	Offset of FLC delay from 180°
f	Focal length of camera lens
$f(\omega)$	Interference filter transmission profile
$F(\theta, \xi, \Delta\alpha)$	Deviation from ideal switched IMSE system phase response
g and h	Phase correction functions needed for non-ideal switched IMSE system
k_x and k_y	Spatial carrier wavenumber in the camera image
$\mathbf{k}$	Ray propagation vector through the optical system (Eq. 3.15)
κ	Birefringent delay dispersion gradient (Eq. 3.13)
L	Thickness of birefringent crystal
$m_\pm$	Circular polarisation interferogram phase sign flip factor (Eq. 3.52)
n_e and n_o	Refractive index for extraordinary and ordinary ray (n.b. difference to Ch. 2)
Δn	Birefringence
$\bar{n}$	Averaged refractive index
$\hat{\mathbf{o}}$	Orientation of ordinary ray polarisation
ω_0	Angular frequency at the centre of the multiplet
ω_T	Periodicity of the birefringent sinusoidal filter (Eq. 3.14, angular frequency)
$\mathbf{p}(\omega)$	Polarimeter Stokes weighting function (Eq. 3.9)
$\hat{\mathbf{p}}$	Orientation of the p polarised ray (parallel to surface)
Δp	Phase difference between alternate images in the switched IMSE system
P	Polariser Mueller matrix (Eq. 3.7)
ϕ	Phase delay between extraordinary and ordinary rays (radians, function of frequency and position/angle)
ϕ_0	Phase delay at the central frequency of the emission
$R(angle)$	Mueller rotation matrix (Eq. 3.6)
ρ	Angle the waveplate optic axis projects onto its surface (Fig. 3.3, n.b. difference to Ch. 1 and 2)
ρ_a	Rotation angle of extraordinary ray relative to horizontal (Eq. 3.40)
$\hat{\mathbf{s}}$	Orientation of the s polarised ray (perpendicular to surface)
S	Intensity measured by the polarimeter
$\mathbf{T}$	Polariser transmission axis
Θ	Cut angle of uniaxial birefringent crystal optic axis to surface (Fig. 3.3)
υ	Angular frequency offset from the centre of the multiplet
w_{term}	Polarised Stokes component carrier wave weightings (Eq. 3.67 and 3.68)
$W(delay)$	Waveplate Mueller matrix (Eq. 3.5)
(x, y)	Position on imaging sensor (n.b. difference to Ch. 2)
$\mathbf{X}$	Uniaxial crystal optic axis (Eq. 3.18)
ξ_I	Interferometric ellipticity (Eq. 3.54)
ζ_l	Linear polarisation interferogram contrast (Eq. 3.46)
ζ_c	Circular polarisation interferogram contrast

Chapter 4

B_t	Toroidal magnetic field strength
I_p	Plasma current
$R_{location}$	Radial coordinate of the neutral beam-sightline intersection for a particular location on the beam
θ_l	Inferred polarisation angle from a linear polarisation calibration

Chapter 5

d	Plasma sheath thickness (Eq. 5.1)
E_n	Amplitude of n^{th} harmonic component of the sheath RF electric field
I_n	Emission intensity of n^{th} harmonic component of a RF wave
ι	Rotational transform of the magnetic field
J_e	Sheath saturation current (Eq. 5.2)
$\mathbf{k}$	Plasma wave vector
k_ρ	Wave vector component in the radial direction (dimensionless)
κ_H	Ratio of currents in helical:toroidal field coils
κ_V	Ratio of currents in vertical:toroidal field coils
m	Poloidal/perpendicular mode number
n	Toroidal/parallel mode number
n_e	Electron density (n.b. difference to Ch. 3)
ω	RF antenna angular frequency $\equiv$ driven plasma wave angular frequency
ω_{ci}	Ion cyclotron frequency for ion i (Eq. 5.4)
ϕ_B	Toroidal Boozer angle
ρ	Radial coordinate (n.b. difference to earlier chapters)
T	Antenna RF period
T_{gate}	Intensifier gate (time) width
τ	Lifetime of excited atomic state (n.b. difference to Ch. 2)
θ	Propagation angle of plasma wave relative to $\mathbf{B}$ (n.b. difference to earlier chapters)
θ_B	Poloidal Boozer angle
θ_1	Phase of first harmonic component of sheath RF electric field
v_p	Wave phase velocity
$v_\parallel$	Wave phase velocity in the direction of $\mathbf{B}$
V	Antenna voltage
V_A	Alfven velocity (Eq. 5.5)
Z_i	Net charge of atom (after multiplication by e)

Chapter 1

Introduction

The research conducted for this thesis is intended to advance the development of fusion power as an energy source. This chapter outlines the motivation for fusion power research and the role of experimental spectroscopic measurements in developing our understanding of the physical processes in magnetic confinement fusion devices.

Spectroscopy of Stark and/or Zeeman split emission lines is one of the few options available for measuring the electric and magnetic fields ($\mathbf{E}$ and $\mathbf{B}$) that confine a 10^8K fusion plasma. In particular motional Stark effect (MSE) polarimetry is the most widely used technique for constraining the magnetic field distribution, involving measurement of the neutral beam Balmer-α polarisation angle to find the orientation of $\mathbf{E} = \mathbf{v} \times \mathbf{B}$ (beam velocity $\mathbf{v}$). Since the first measurements almost 30 years ago[1], MSE has become a routine diagnostic on most magnetic confinement devices, however the spatial resolution of the conventional measurement technique is limited to 10s of individual channels. More recently a polarisation coherence imaging technique has been developed for high resolution imaging MSE (IMSE) measurements[2].

The research in this thesis covers all aspects of polarisation coherence imaging, including the fundamental atomic physics, measurement principles and applied experiments. The atomic physics research will be of interest to a reader looking to understand the fundamental processes involved in the Stark-Zeeman split Balmer-α emission. Significant breakthroughs are made in the understanding of the emission when the upper-states of the transition are not equally populated and the work dispels previous findings that MSE beam-into-gas calibration is invalid for the σ polarisation. High level equations for calculating the circular polarisation of the Balmer-α emission independently of the underlying atomic physics are presented. The equations are convenient for experimentalists seeking to take advantage of the additional information carried by the circular polarisation or to understand coupling between linear and circular polarisation at a non-ideal mirror.

The underpinning principles and components used for polarisation coherence imaging are described in detail for the benefit of readers that are new to the technique. Particular attention is given to new insights derived from the Stark-Zeeman circular polarisation results as well as a newly formulated non-axial ray model that is needed to predict all of the spatial carriers produced by a sequence of displacer waveplates.

The functionality and performance of the polarisation coherence imaging technique is highlighted by IMSE experiments conducted on the DIII-D tokamak. These measurements delivered first time benchmarking of IMSE against well-established conventional MSE polarimeters and enhanced the capabilities of the DIII-D system with the ability to measure from the high field side from a second neutral beam. The experiments also highlight the main design considerations and challenges encountered when implementing an IMSE diagnostic. Experiments intended to demonstrate further capabilities of the po-

larisation coherence imaging technique with a measurement of the dynamic Stark effect in the H-1 heliac sheath were abandoned due to insufficient localisation of the light intensity. However a by-product of the H-1 7MHz phase resolved imaging was the realisation of the diagnostic capability to directly image radiofrequency (RF) heating waves, detected from density and subsequent light intensity perturbations in the plasma. An electromagnetic ion cyclotron wave detected in the H-1 plasma is thought to be responsible for the previously unexplained edge electron heating and the imaging technique may prove useful for RF wave measurements on other fusion devices.

1.1 Energy Production and Consumption

Electricity usage, and more generally energy usage, are synonymous with advanced societies in the world. Many technologies we use on a daily basis rely on energy that has been produced for operating electrical devices, heating, transportation and industrial processes. Currently the dominant sources of baseload electricity that society relies on in day to day life are carbon, hydro and nuclear fission based. Annual global energy production has increased, from 255EJ in 1973 to 573EJ in 2014, and is expected to further increase to at least 628EJ by 2040[3]. Furthermore many technological advances achieved by mankind are linked to the development of new energy sources. For example the furthest man made object from earth, the Voyager-1 space probe, relies on high-energy density radioisotope thermoelectric generators. It is therefore important to pursue new energy sources, to sustainably meet our current needs but also to increase our opportunities for making new discoveries and technological advances.

There are a number of limitations and well known negative side-effects of sourcing energy from carbon based fuels. In 1973 15Gt of carbon dioxide was emitted from energy generation and this has since risen to 32Gt in 2014[3]. These emission have contributed to an increase in the carbon dioxide concentration in the atmosphere from 290 to 390 parts per million between 1850 and 2014[4]. This has coincided with globally averaged combined land and ocean surface temperatures rising by 0.85 ± 0.2°C between 1880 and 2012 and global mean sea levels rising by 0.19 ± 0.02m between 1901 and 2010[4]. Concerns around atmospheric carbon dioxide concentrations, the resulting effects on the climate and further flow on impacts have hastened the need to produce energy from non-carbon based sources such as renewables (solar, wind, hydro, geothermal etc), nuclear fission and nuclear fusion. To limit the long-term concentration of carbon dioxide below 450 parts per million it is projected that the carbon dioxide emissions from energy production will need to drop to 19Gt in 2040[3], an almost 50% reduction in the emissions intensity compared to 2014.

Nuclear fusion is the least developed of these non-carbon based technologies but a 2050 realisation of fusion power to the grid is targeted[5], although projections may be pushed back further[6]. In the long term fusion is considered to be the 'ultimate' power source as it can produce both clean and continuous baseload power without any drawbacks such as energy resource scarcity, risk of nuclear proliferation and long-lived radioactive wastes. However in the short to medium term carbon emission reduction targets are expected to be achieved predominately by renewable energy sources.

1.2 Fusion Power

The most feasible nuclear reaction for terrestrial fusion power generation is that between deuterium and tritium (hydrogen isotopes) ions to form an energetic helium ion and a neutron, depicted in Fig. 1.1 and given in the equation,

$$ {}^{2}_{1}\mathrm{D} + {}^{3}_{1}\mathrm{T} = {}^{4}_{2}\mathrm{He}(3.5\mathrm{MeV}) + {}^{1}_{0}\mathrm{n}(14.1\mathrm{MeV}) \tag{1.1} $$

where the superscript values indicate the total number of nucleons and the subscript values the number of protons. The energy released in the reaction results from the mass deficit between the deuterium and tritium reactants and the helium and neutron products. The energy released is described by Einstein's famous equation $E = mc^2$ where E is the energy, m is the mass deficit and c is the speed of light. The reaction has a high energy density of $300\mathrm{TJ\,kg^{-1}}$. This is four times greater than the nuclear fission energy density of $80\mathrm{TJ\,kg^{-1}}$ and over 10 million times greater than carbon based reactions which typically have an energy density of $\sim 20\mathrm{MJ\,kg^{-1}}$. Furthermore deuterium is readily available from sea water and therefore averts resource scarcity inequalities. Tritium is unstable with a half-life of 12 years, however it can be produced from nuclear reactions with lithium which is relatively abundant for the quantities of tritium required. The reaction does not directly produce any long lived radioactive waste, however fusion reactor materials will become activated after interacting with the high energy neutrons. Research is ongoing to select and develop reactor materials that have low activation.

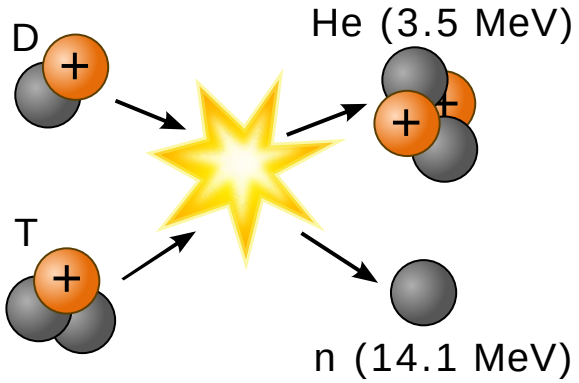

Figure 1.1: Reaction diagram for the fusion of deuterium and tritium. Protons are depicted in orange and neutrons in grey.

For the positively charged deuterium and tritium ions to get close enough to fuse, their Coulomb repulsion must be overcome, requiring incredibly high energies and temperatures. The required temperature for the controlled fusion reaction is approximately $T = 10^8\mathrm{K}$ ($\equiv 100$ million°C) which compares to $T = 10^7\mathrm{K}$ in the centre of the sun. Electrons ionise from the deuterium and tritium atoms as the fuel is heated. This results in a plasma of electrons and ions that interact strongly with electric and magnetic fields, dwarfing the interaction of gravity. The energy gained by the helium ion in the reaction will provide further heat to the plasma while the neutrons escape the reaction vessel to heat water in surrounding 'blankets'. Steam produced from the heated water is used to drive a turbine to produce electricity in the same process that is used in conventional power stations. Fusion reactors cannot 'meltdown' from a chain-reaction as the temperatures required for the reaction are immediately lost if the plasma expands.

The most promising and widely researched technique for confining the hot plasma is with strong $1-10$T magnetic fields, known as magnetic confinement fusion. The charged electrons and ions are confined in the directions perpendicular to the magnetic field and will orbit the field with a gyroradius of

$$r_g = \frac{mv_\perp}{|Q|B} \tag{1.2}$$

where m is the mass of the particle, $v_\perp$ is the velocity of the particle perpendicular to the field, Q is the charge and B is the magnetic field strength. Evidently a smaller gyroradius is achieved with light particles and strong magnetic fields. The gyroradius increases at higher temperatures as $v_\perp \propto \sqrt{T}$.

Inertial confinement fusion is an alternative stream of fusion research that utilises high energy laser or particle beams to compress and heat small capsules of deuterium and tritium. However, the efficiency and ability to produce large quantities of power with this technique is problematic.

While it is possible to achieve unconfined fusion explosions for creating energy it is not feasible to safely and repeatedly capture useful energy from such explosions.

1.3 Magnetic Confinement Fusion

As outlined in the previous section the positively charged ions and negatively charged electrons of the plasma are confined in the directions perpendicular to a strong magnetic field. However the plasma remains unconfined in the direction parallel to the magnetic field and therefore prone to significant energy losses where the magnetic field intersects a material surface. To achieve a high confinement efficiency the magnetic field must inevitably be curved into a circle such that it closes in on itself, forming a donut shaped 'magnetic bottle' to prevent any end losses. For this reason cylindrical (radial distance R, azimuthal angle ϕ, height Z) and toroidal (radial coordinate ρ, toroidal/azimuthal angle ϕ, poloidal angle θ [but subscripted p]) geometry coordinates are used frequently in this field of research. An example of a magnetic confinement device, known as a tokamak, is shown in the left of Fig. 1.2. The primary toroidal magnetic field is established with several current carrying coils (shown in blue) that circle about the torus in the poloidal direction. The vacuum magnetic field from these coils can be calculated from Ampere's law to be

$$B_\phi = \frac{\mu_0 NI}{2\pi R} \tag{1.3}$$

where μ_0 is the vacuum permeability, N is the number of toroidal field coils (TFCs), I is the current carried in each coil and R is the distance from the central axis of the torus. However this toroidal magnetic field alone is insufficient to confine the plasma, due to particle drifts that are produced by the toroidal field gradient $B_\phi \propto 1/R$ and the curvature of the magnetic field. A secondary magnetic field in the poloidal direction can be introduced to give the magnetic field an overall helical structure that destabilises and overcomes the effect of the gradient and curvature drifts.

There are two different strategies for establishing this poloidal magnetic field. The tokamak device is the most widely researched strategy where a toroidal current is induced in the plasma by ramping the current in a central solenoid, as illustrated in the left of Fig. 1.2. This plasma current generates a poloidal component for the magnetic field that is shown in the right of Fig. 1.2. The current driven in the plasma gives rise to Ohmic heating

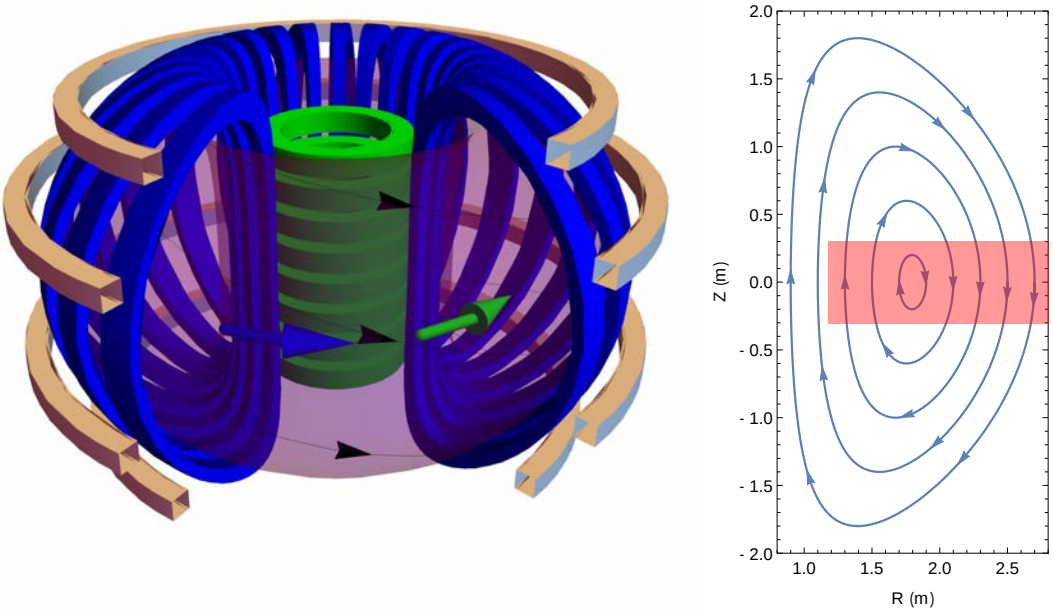

Figure 1.2: (Left) Diagram of a tokamak showing the major magnetic field coils and the plasma. The blue toroidal field coils carry a constant current producing a strong magnetic field in the direction of the blue arrow. Currents are ramped (dI/dt) in the green solenoid to induce a current in the plasma shown with the green arrow. This plasma current produces the poloidal magnetic field. The cream vertical/poloidal magnetic field coils are used for additional shaping of the plasma. Overall the magnetic field in the device is helical shown with the black lines and arrows. (Right) Poloidal cross section of the plasma showing magnetic flux surfaces and the direction of the magnetic field. The dominant toroidal magnetic field component directed into the page is not shown. $\sim 3 \times 10^6 \mathrm{m\,s^{-1}}$ hydrogen or deuterium neutral beams are often injected into the region highlighted in red to provide additional plasma heating and non-inductive current drive.

from collisions between particles in the plasma. As the plasma is heated the resistivity and effectiveness of the Ohmic heating decrease and therefore additional heating sources such as high energy deuterium beam injection or electromagnetic wave heating are required. The current ramp in the central solenoid has a limited range and must be supplemented with non-inductive current drive mechanisms for long pulse operation, an obvious requirement for a power station.

The JET tokamak holds the record for the largest fusion power output with 16MW produced from the fusion reaction which required 24MW of applied heating power. Heat losses in current magnetic confinement devices are larger than the fusion power produced due to instabilities and collisional transport that limit the confinement of the plasma. Empirical scaling laws based on the parameters and performance of current tokamaks predict that the ITER tokamak, currently under construction in France, will produce 500MW of fusion power from a heating power of 50MW (a power gain factor of 10). Further details of the operating principles of tokamaks can be found elsewhere, for example Ref. [7] is an exposition on tokamaks.

An alternative magnetic confinement strategy is to establish the poloidal magnetic field

with external field coils using devices known as stellarators. The toroidal symmetry of the tokamak must be sacrificed to achieve a poloidal field using external coils, increasing the complexity of the system. The stellarator has a number of advantages over the tokamak as it does not require a plasma current and is therefore free of current driven instabilities and can operate in a steady state mode. However stellarators are less researched than tokamaks, owing to the greater early success of tokamaks and the added complexity of stellarators.

1.3.1 Plasma Equilibrium

For the plasma to be in equilibrium the outward plasma pressure must be balanced by the magnetic field. This force balance can be summarised by the equation

$$\nabla p = \mathbf{j} \times \mathbf{B} \tag{1.4}$$

where $\mathbf{j}$ is the current density in the plasma and ∇p the pressure gradient. Taking the dot product of each side with $\mathbf{B}$ gives that $\mathbf{B}.\nabla p = 0$, implying that the magnetic field must lie in a toroidal surface of constant pressure. Maxwell's law $\nabla \cdot \mathbf{B} = 0$ further implies that the magnetic flux through a fixed boundary is independent of the shape of the enclosing surface. It follows that the surfaces of constant pressure also have constant magnetic flux. It is therefore convenient to define a poloidal flux function by

$$\psi_p(R, Z) = \int_S \mathbf{B} \cdot d\mathbf{a} \tag{1.5}$$

where S is a circle of radius R at height Z. An example of the shape of the flux surfaces is seen in the right of Fig. 1.2. Ions and electrons are confined to the magnetic field (ignoring drifts and collisions) and therefore the flux surfaces effectively confine the hot plasma in the centre of the device from the cooler plasma near the walls.

The rate at which the magnetic field curves around the flux surface (helicity) is strongly linked to the stability of a flux surface. This rate is called the safety factor or q-profile and can be calculated from the integral

$$\begin{aligned} q =& \frac{1}{2\pi} \oint \frac{B_\phi}{R B_p} ds \\ =& \frac{1}{2\pi} \oint \frac{1}{R \tan \theta_{pitch}} ds \end{aligned} \tag{1.6}$$

where the path ds is taken around a flux surface in a poloidal plane, $B_p = \sqrt{B_R^2 + B_Z^2}$ is the poloidal magnetic field strength and $\theta_{pitch} = \arctan(B_p/B_\phi)$ is the 'pitch' of the magnetic field. Surfaces with a low order rational safety factor (such as 1, 2 or 1/2) are susceptible to instabilities as the magnetic field closes in on itself after a short distance such that any instability can grow quickly.

The confinement and stability of the plasma is intrinsically linked to the magnetic field inside the plasma. Valuable measurements of the magnetic field inside the device can be obtained from magnetic pickup coils external to the plasma. For example a Rogowski coil measures the total toroidal current flowing in the plasma while the local toroidal and poloidal magnetic field can be measured from individual pickup coils. The toroidal loop voltage can simply be measured with a toroidal loop of wire, allowing the local poloidal magnetic flux to then be calculated from the time integral of the loop voltage (Faraday's

Law). The combination of the local poloidal field and poloidal flux measurements can be extrapolated over the plasma current free region to estimate the last closed flux surface of the plasma. However accurate extrapolation further into the plasma is not possible as the toroidal current density profile j_ϕ in the plasma is not fully constrained by these external measurements. Diagnostics capable of measuring the magnetic field inside the plasma are therefore essential, particularly to understand instabilities in the plasma relating to the q-profile and to study advanced tokamak scenarios where non-inductive currents are deliberately driven at precise locations in the plasma to improve confinement.

1.4 Spectroscopy of the Balmer-α Emission

The Balmer-α 656nm ($n = 3 \rightarrow 2$) hydrogen (or deuterium) transition is often the brightest emission line in the visible optical spectrum, making it ideal as a non-perturbative diagnosis tool. In the hot core of a fusion device the plasma is completely ionised, hence atomic emission from this region is precluded. However high energy neutral hydrogen or deuterium beams injected into the plasma, typically for heating purposes, provide a source of atomic electrons that make so called active spectroscopy possible in the core of the plasma. A further benefit of active spectroscopy is that the emission region is well localised due to the relatively narrow width of the beam. Neutral beam atoms can be excited from collisions with the plasma and go on to emit light as they are de-excited. Alternatively the beam atoms can donate/charge-exchange an electron to a plasma ion to form an excited atom that will also emit light.

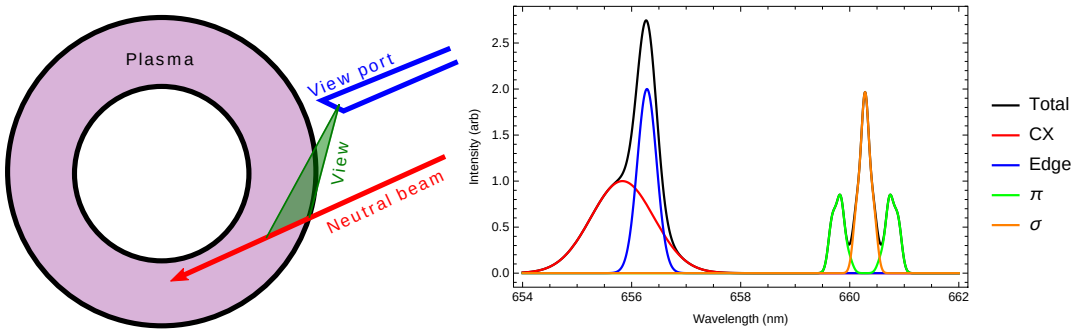

Figure 1.3: (Left) Geometry of the neutral beam and imaging MSE view for the KSTAR tokamak. (Right) Mock D_α spectrum for a viewing chord intersecting the neutral beam. The 'cold' plasma edge emission, hot core charge-exchange (CX) emission and redshifted Stark split neutral beam emission components are shown. Emission lines from impurities in the plasma and possible half and third energy components resulting from the acceleration of heavier D_2^+ and D_3^+ beam ions are not shown.

A simplified example of the D_α spectrum for a sightline intersecting a neutral beam is shown in Fig. 1.3. Each of the components has a different Doppler broadening width due to the different velocity spread (temperature) of their source atoms and a different Doppler shift due to the different average velocity parallel to the sightline. Hence spectrally resolved measurements have the capacity to measure the temperature and average velocity of the emitting species. For example in Fig. 1.3, the charge-exchange (CX) emission component from the core of the plasma is slightly blueshifted due to the plasma rotation velocity and has greater thermal Doppler broadening compared to the unshifted 656.3nm emission from the cooler edge region of the plasma. Furthermore emission lines can become

split and polarised in the presence of an electric and/or magnetic field in the plasma. This is the case for the neutral beam atoms which are subjected to a strong motional electric field leading to the redshifted ≈ 660nm primarily Stark split emission seen in Fig 1.3. σ and π polarised components can be resolved when the Stark and/or Zeeman splitting of the emission is sufficiently large relative to the Doppler broadening. In this case polarimetric measurements of the Stokes vector can deliver up to three additional quantities pertaining to the orientation of the electric and/or magnetic fields compared to more straightforward intensity measurements. Further properties of this component of the emission are considered in more detail in the next section.

1.4.1 Motional Stark Effect Spectroscopy

The motional Stark effect (MSE) is the most widely used diagnostic technique on tokamaks and stellarators for measuring the orientation of the magnetic field inside the plasma. MSE diagnostics observe the Stark split Doppler shifted component of the Balmer-alpha emission[8] shown in Fig. 1.3. The technique was first used to measure the magnetic field 'pitch angle' on the PBX-M tokamak in 1989[1] and is now widely used on magnetic confinement devices that have neutral beams.

The neutral beam atoms of velocity $\mathbf{v}$ cross the magnetic field $\mathbf{B}$ and therefore experience a motional electric field

$$\mathbf{E_L} = \mathbf{v} \times \mathbf{B} = \mathbf{v} \times \mathbf{B}_{\perp \mathbf{v}} \tag{1.7}$$

in their rest frame. The motional electric field causes the light emission to be split into discrete lines via the Stark effect. The atomic physics of the Stark effect is considered in detail later in Chapter 2 but here the key properties of the emission are outlined. For typical neutral beam energies ($\sim$ 100keV) the linear Stark effect is the largest energy splitting mechanism and gives rise to resolvable π and σ components, shown in Fig. 1.3, that are linearly polarised parallel and perpendicular to the electric field respectively[9]. The central σ cluster is composed of three separate lines and the two π wings also consist of 3 separate lines. Each of the 9 lines is split/separated from its nearest neighbours by

$$\Delta\nu = \frac{3ea_0|\mathbf{E}|}{2h} \tag{1.8}$$

$$\text{or } \Delta\lambda \approx \frac{3ea_0|\mathbf{E}|\lambda_0^2}{2hc} \tag{1.9}$$

where ν is the frequency of the light, e is the electron charge, a_0 is the Bohr radius, h is the Planck constant and λ_0 is the unshifted Balmer-α wavelength. For a 100keV deuterium beam injected at 60° to a 3T magnetic field the motional electric field is 8MV m^{-1} producing a splitting of $\Delta\lambda = 0.22$nm. Each of these 9 bright lines are Doppler broadened resulting from the velocity spread of the neutral beam and range of angles collected by the viewing optics. Hence it is only possible to resolve the π and σ components and make a measurement when $\mathbf{v} \times \mathbf{B}$ is large. The intensity of the π and σ components scale with the angle ψ between the view direction and $\mathbf{E}$. The relationship is given by

$$I_\sigma \propto 1 + \cos^2\psi \tag{1.10}$$

$$I_\pi \propto \sin^2\psi. \tag{1.11}$$

Given this background information it is possible to separate MSE diagnostic measure-

ments into three different categories. Firstly the electric field orientation (Eq. 1.7) can be ascertained from the linear polarisation orientation of the π and/or the σ emission. Secondly the electric field orientation is also encoded in the intensity ratio of the π to σ emission components (Eq. 1.11). Thirdly the magnitude of the electric field can be measured from the spectral line splitting (Eq. 1.8). MSE polarimetry is the most widely used technique as it is capable of achieving high accuracy and temporal resolution. MSE line ratio measurements are less common as they require significant splitting to resolve individual lines and the measurement can depend on the upper-state populations of the transition. A key advantage of the MSE line splitting technique is that it is insensitive to polarisation and is therefore being considered for the ITER MSE system where mirrors in the optical relay chain are expected to have degraded polarisation preservation properties that evolve over time. A drawback is that spectrally resolved measurements have a limited etendue (light throughput) and only a second order dependence on B_Z/B_ϕ.

1.4.2 Relationship Between the MSE Polarisation Angle and the Magnetic Field

From Eq. 1.7 it is not immediately obvious what information the polarisation orientation conveys about the magnetic field due to the beam velocity and viewing geometry effects that complicate the link between the two quantities. Here the link between the polarisation orientation and magnetic field is outlined along with some of the complicating factors for the measurement. The neutral beam velocity can be expressed in cylindrical (R, ϕ, Z) coordinates as

$$\mathbf{v} = v(-\sin\alpha, \cos\alpha, 0) \tag{1.12}$$

where $\alpha(R, Z)$ is the angle between the velocity and the toroidal direction. The motional electric field is then given by

$$\begin{aligned} \mathbf{E}_L &= v(B_Z\cos\alpha, B_Z\sin\alpha, -\sin\alpha B_\phi - \cos\alpha B_R) \\ \hat{\mathbf{E}}_L &= \sin\theta_E(\cos\alpha, \sin\alpha, 0) - \cos\theta_E(0,0,1) \qquad (1.13) \\ \text{where} \quad \tan\theta_E &= \frac{B_Z}{\sin\alpha B_\phi + \cos\alpha B_R}. \qquad (1.14) \end{aligned}$$

The θ_E term has been deliberately factored out of the equation to highlight that the orientation of the motional electric field can be parameterised by a single angle when the neutral beam direction is known precisely. This is to be expected because the orientation of the motional electric field must lie in the plane perpendicular to $\mathbf{v}$. On the tokamak midplane ($Z = 0$) it is generally a good approximation that $B_R = 0$ in which case the pitch of the magnetic field is related to θ_E through the equation

$$\tan\theta_{pitch} = \frac{B_p}{B_\phi} \approx \sin\alpha\tan\theta_E. \tag{1.15}$$

With some simple assumptions about the shape of the flux surfaces[1, 10] it is possible to determine the safety factor in Eq. 1.6 and the toroidal current density j_ϕ from a measurement of θ_E.

The MSE technique does not directly measure θ_E and the viewing geometry used for the polarimeter must be considered to relate the polarisation orientation θ_σ (or $\theta_\pi = \theta_\sigma + 90°$) to θ_E. The polarisation orientation is dependent on the projection of the electric field

in the plane perpendicular to the view direction. With the viewing direction defined in cylindrical coordinates by the unit vector $\hat{\mathbf{i}} = (i_R,\, i_\phi,\, i_Z)$ the linear polarisation orientation θ_σ of the σ component is related to θ_E via

$$\tan\theta_E = \frac{(i_R^2 + i_\phi^2)\tan\theta_\sigma}{(i_\phi - i_R i_Z \tan\theta_\sigma)\cos\alpha - (i_R + i_Z i_\phi \tan\theta_\sigma)\sin\alpha}. \tag{1.16}$$

Hence the polarimetric measurement can be used to give θ_E and some assumptions can then be used to obtain θ_{pitch}, q and j_ϕ. However more commonly an equilibrium solver is used to fit a solution to the polarisation orientation measurements, especially when external magnetic measurements are also available. It should be noted that $\theta_E = \theta_\sigma = 0$ when the magnetic field is purely in the toroidal direction, which is the case at the magnetic axis.

Electric fields in the rest frame of the device can complicate the MSE measurement. Generally there is a radial electric field in the plasma that can be up to $\sim 100\mathrm{kV\,m^{-1}}$. The radial electric field can be expressed in cylindrical coordinates by $\mathbf{E}_r = (E_R,\, 0,\, E_Z) \propto \nabla\psi_p$. The loop voltage driving the current in the plasma contributes an E_ϕ component that is usually $\sim 1\mathrm{V\,m^{-1}}$ and can be neglected. The true electric field in the rest frame of the beam atoms is therefore

$$\mathbf{E} = \mathbf{E}_L + \mathbf{E}_r. \tag{1.17}$$

In this situation $\mathbf{E}$ is not precisely perpendicular to the beam velocity, hence the electric field orientation is dependent on two angular coordinates but only a single angle is obtained from the measurement of θ_σ. So-called 'A coefficients'[11, 12] are typically used to represent the now underdetermined measurement of $\mathbf{E}_L$ and $\mathbf{E}_r$ or effectively θ_E and $|\mathbf{E}_r|/|\mathbf{E}_L|$. The details of the calculations can be found in the references but a noteworthy observation is that the polarisation orientation is insensitive to any radial electric field component parallel to $\hat{\mathbf{i}}$. For example if $\hat{\mathbf{i}} = (-1,\, 0,\, 0)$ then the measurement is insensitive to the magnitude of E_R.

The finite width of the neutral beam can also complicate the interpretation of MSE as the measurement is line-integrated over the ≈ 10cm width and spread of velocities of the neutral beam. It has been shown that there can be differences in the linear polarisation orientation between an ideal thin neutral beam and the actual neutral beam[13]. Additionally the spatial resolution of the measurement is limited when the line integration region intersects across a large range of flux surfaces. For this reason MSE-P measurements are typically made viewing tangentially to the flux surface to limit the range of flux surfaces sampled and therefore maximising the spatial resolution.

1.4.3 MSE Polarimetry Measurement Techniques

The original[1] and most widely used technique for measuring the MSE linear polarisation utilises two photoelastic modulators (PEMs)[14, 15] and a polariser to modulate the light signal at 10s of kHz. Narrowband filters are used to isolate either a σ or a π component of the multiplet before being measured with a photodetector. The temporally modulated signal can either be analysed with lock-in amplifiers or digitised before it is demodulated. The technique is used on most major tokamaks around the world such as DIII-D[16], JET[17] and KSTAR[18], however, the measurement is notoriously challenging. For example partially polarised reflections in the device can corrupt the measurement, as found on Tore Supra[19] where MSE was abandoned. Furthermore the polarisation preservation

of the transmission is crucial and the Stark-Zeeman circular polarisation presents challenges when there is a non-ideal mirror in the system, as realised for some DIII-D MSE channels[20].

The MSE emission is net unpolarised when integrating over the full multiplet (in the case that the upper $n = 3$ states of the emission are equally populated) as the σ and π components are orthogonally polarised. Therefore the narrowband filter is essential for the PEM measurement technique to isolate either a σ or π dominated region with high polarisation fraction. However the Doppler shift of the MSE spectrum is dependent on the angle between the neutral beam and the sightline which varies across the view of the beam, evident earlier in Fig. 1.3. Hence each radial viewing position typically requires a separate filter and detector to isolate the corresponding portion of the spectra. For this reason conventional PEM systems are limited to 10s of channels viewing the midplane of the neutral beam.

Other MSE polarisation measurement techniques include imaging MSE[2] (considered in the next section), spectro-polarimetry[21], complete spectro-polarimetry[22] and laser induced florescence[23]. These alternative MSE techniques are not discussed here in detail, however broader overviews can be found in Refs. [24] and [25].

1.4.4 Imaging Motional Stark Effect

The more recently developed imaging MSE (IMSE) technique[2] has many similarities with the 'coherence imaging' technique developed for measuring plasma temperatures and flow velocities[26]. The IMSE polarisation coherence imaging technique involves coupling the polarisation and spectral information together to achieve the spectral discrimination without any need for narrowband filters. Significant spectral symmetry exists between the central σ MSE cluster and the orthogonally polarised π wings on either side. IMSE takes advantage of this symmetry to achieve the required spectral discrimination by effectively applying a sinusoidal spectral filter over the multiplet. The orthogonally polarised σ and π components are constructively interfered by delaying the π wings by $\approx \pm 180°$ relative to the σ component to produce a large net signal. Additionally the birefringent optics used in the measurement establish spatial carrier fringes in the image to encode the information and achieve strong signal for the full range of Doppler shifts across the field of view. By capturing all components of the emission IMSE has the advantages of greater light throughput, effective averaging over variations in the polarisation angle across the spectrum and insensitivity to broadband polarised backgrounds. The components and measurement principles used for the technique are covered in detail in Chapter 3. An example of a spatially encoded IMSE image and a forward model of the polarisation angle profile are given in Fig. 1.4.

Imaging the neutral beam captures significantly more information than the 10s of channels typically measured on the midplane of the device with conventional MSE and the enhanced radial resolution of IMSE has made it possible to resolve edge pedestal structures on the KSTAR tokamak[27]. Furthermore IMSE has the added advantage that the polarisation angle is also captured in the vertical direction in the images, opening up the possibility of measuring the toroidal current profile directly from the images. From Eq. 1.14 it is evident that MSE is particularly sensitive to B_Z, given that B_R is small near the midplane where the beam is injected and B_ϕ is approximately known (vacuum solution in Eq. 1.3). Maxwell's equations can be applied to express the toroidal current

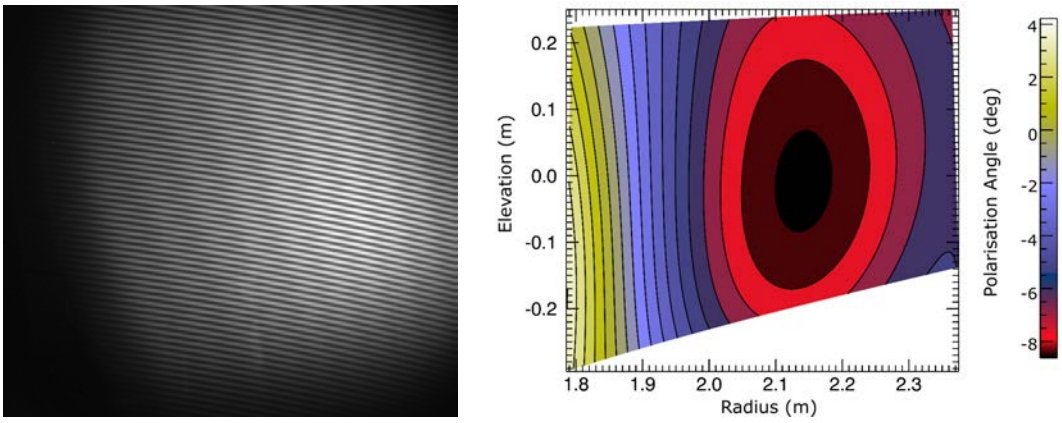

Figure 1.4: (Left) Example of an IMSE measurement (in camera coordinates) on the KSTAR tokamak showing the spatial carrier fringes that encode the polarisation information. The neutral beam velocity is rightward in the image and the plasma edge is evident where the light intensity begins. (Right) Forward modelled MSE polarisation angle expected from the KSTAR view.

density in terms of B_Z, given by

$$\mu_0 j_\phi(R,Z) = \underbrace{-\frac{\partial B_Z(R,Z)}{\partial R}}_{\text{Midplane MSE}} + \underbrace{\frac{R_0}{R}\frac{\partial B_R(R_0,Z)}{\partial Z}}_{\text{Boundary Condition}} \underbrace{-\frac{1}{R}\int_{R_0}^{R} R\frac{\partial^2 B_Z(R,Z)}{\partial Z^2}dR}_{\text{Vertical Information}}. \tag{1.18}$$

The first term is captured by both conventional MSE midplane measurements (Z=0) and IMSE (all Z). Meanwhile the boundary condition term can be calculated at the last closed flux surface position (R_0, Z) using external magnetics and/or the shape of the boundary evident in the IMSE images. The most challenging term to measure is the vertical information term and only imaging measurements have the capability to take vertical $\partial/\partial Z$ gradients. However, the integral of a second derivative is prone to noise and it remains to be seen if sufficiently accurate IMSE images can be obtained to directly apply Eq. 1.18 to the data. Regardless, the additional information captured by IMSE has already delivered new opportunities for understanding plasma structures and dynamics.

1.4.5 MSE Beam-Into-Gas Calibration

A common technique for calibrating MSE diagnostics observes the neutral beam injected into the tokamak filled with neutral gas, known as beam-into-gas (BIG) calibration. In the absence of any plasma currents the magnetic field is known accurately from the currents in the external coils. Hence BIG is a valuable in-situ method to calibrate the diagnostic as it incorporates all optical effects such as viewing geometry, the finite neutral beam width and divergence, Faraday rotation and non-ideal mirrors. BIG is of increased value to IMSE calibration as the technique also replicates the Doppler shift and illumination profile of the plasma measurements. However the validity of BIG calibration is contentious, it is considered favourably on some devices while on others it is not trusted for a couple of different reasons outlined here.

Since the earliest MSE measurements it has been observed that the $\pi : \sigma$ intensity ratio deviates from theoretical predictions assuming equally populated upper-levels of the Balmer-alpha transition[8, 21]. Plasma densities in modern fusion devices are not

sufficiently large for the upper-states to achieve equal populations obeying Boltzmann statistics. As a result collisional-radiative models are required for accurate interpretation of MSE line ratios and MSE spectral measurements when the spectral broadening is significant. A recent collisional-radiative atomic model was found to agree with experimental results from the JET tokamak that indicate the upper-state populations are non-statistical[28, 29].

The BIG gas densities are lower than the operating plasma densities, resulting in upper-state ($n = 3$) populations that are further from a statistical distribution and $\pi : \sigma$ intensity ratios that are noticeably different from the plasma measurements. Nevertheless, at first glance one expects the polarisation properties of the MSE emission to be independent of the density and upper-state populations. However detailed collisional-radiative modelling has predicted that the σ linear polarisation will significantly deviate from the ideal orientation for BIG shots[30]. For this reason BIG is not used for MSE calibration on DIII-D. This finding has a theoretical basis established in the earlier work[31] which calculated the polarisation structure of the combined Stark-Zeeman effect based on tabulated quantum states[32].

The reported success of BIG calibration on fusion devices is varied and a brief summary is presented here. BIG π polarisations observed on NSTX are remarkably accurate, within 0.03° of prediction[33]. On Alcator C-Mod there is a significant, up to 20°, discrepancy between the expected π polarisation angle and the BIG measurements. This is thought to be due to unwanted emission in the filter passband from fast 'secondary neutrals', produced by ionisation and subsequent renuetralisation of beam atoms. The effect is amplified for neutral beams injected with a large radial component and with higher gas pressures[34]. Smaller deviations (0.4°) measuring the σ polarisation on TFTR are also suggested to originate from secondary neutrals[35, 33]. Measurements on MAST have reported a gas density dependence for the BIG calibration accuracy which is again thought to be related to secondary neutrals[36]. BIG calibrations are used on KSTAR to provide corrections of up to 1° for π emission as the offset is not observed to be related to secondary neutrals[37].

1.5 Magnetic Confinement Fusion Devices

In this section the magnetic confinement fusion devices relevant to the work in this thesis are introduced.

1.5.1 H-1 Heliac

H-1 heliac is a helical axis stellarator that was constructed in Canberra at the Australian National University in 1992[38] and is in the process of being transferred to China as of 2018. The major features of H-1 are shown in Fig. 1.5 and its key operating parameters are included in Table 1.1. The magnetic field is established with a circular poloidal field coil that loops through the 36 TFCs. The TFCs are off-centred from the poloidal field coil such that the plasma rotates three times around the poloidal field coil per toroidal rotation. Additional shaping for the plasma is achieved with four vertical field coils and a helical field coil that is twisted around the poloidal field coil. The pressure and plasma currents in H-1 are relatively small, hence the q-profile is well-known without the need for internal measurements of the poloidal field. H-1 is heated with two radiofrequency (RF) saddle loop antennas[39] (since upgraded in 2010) which are seen in the right of Fig 1.5. The frequency of the waves launched from the antenna is tuned to match the cyclotron

frequency of the hydrogen ions (protons) about the magnetic field, in what is known as ion cyclotron resonance heating. Experimental measurements of RF heating waves observed on the H-1 heliac are presented in Chapter 5.

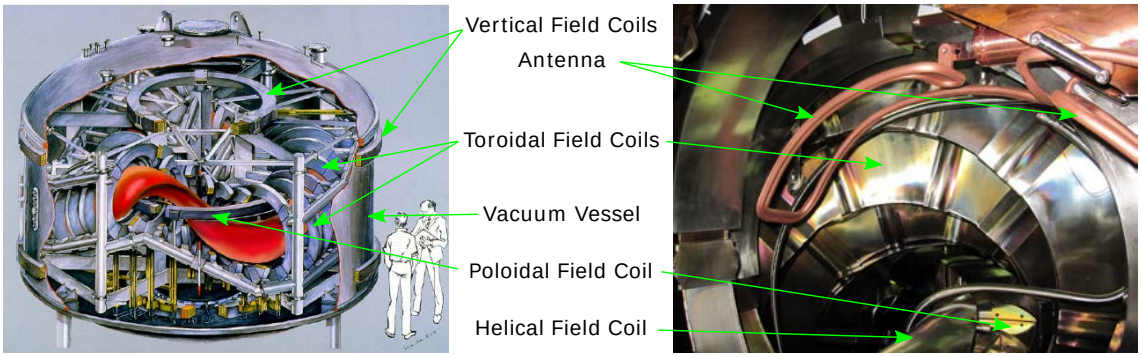

Figure 1.5: (Left) Diagram of the H-1 heliac. The plasma (red) rotates helically around the poloidal field coil and through the 36 TFCs. The poloidal cross section of the plasma makes a bean-like shape. The magnetic field coils are inside the vacuum vessel, apart from the two large vertical field coils. (Right) Photo taken inside H-1 during a vent showing the copper antenna straps and magnetic field coils.

	H-1	DIII-D	KSTAR	ITER
Major Radius (m)	1	1.67	1.8	6.2
Minor Radius (m)	0.2	0.67	0.5	2
Plasma Volume (m^3)	0.9	20	14	840
Magnetic Field (T)	<1	2.2	3.5	5.3
Plasma Current (MA)	NA	2	2	15
Temperature (keV)	~ 0.01	~ 10	~ 10	~ 10
Shot Duration (second)	0.1	10	72	400
Heating Power (MW)	0.4	30	28	50

Table 1.1: Key operating parameters for the H-1 heliac, DIII-D tokamak, KSTAR tokamak and for comparison the ITER tokamak.

1.5.2 DIII-D Tokamak

DIII-D is a tokamak located in San Diego, USA which has been operational since the 1980s. Later in Chapter 4 results are presented from an imaging motional Stark effect diagnostic that was constructed and operated on DIII-D to measure the magnetic field pitch angle. DIII-D is considered an 'advanced tokamak' as it can achieve plasma conditions comparable to those expected on ITER. Some of its key features are 8 heating neutral beams, highly flexible plasma shaping owing to the multitude of poloidal field coils and a comprehensive suite of diagnostics for the plasma. A diagram of the tokamak is shown in Fig. 1.6 and its key operating parameters are also given in Table 1.1.

1.5.3 KSTAR Tokamak

The Korean Superconducting Tokamak Advanced Research (KSTAR), located in Daejeon, South Korea has been operational since 2008. KSTAR is similar in size to DIII-D and its

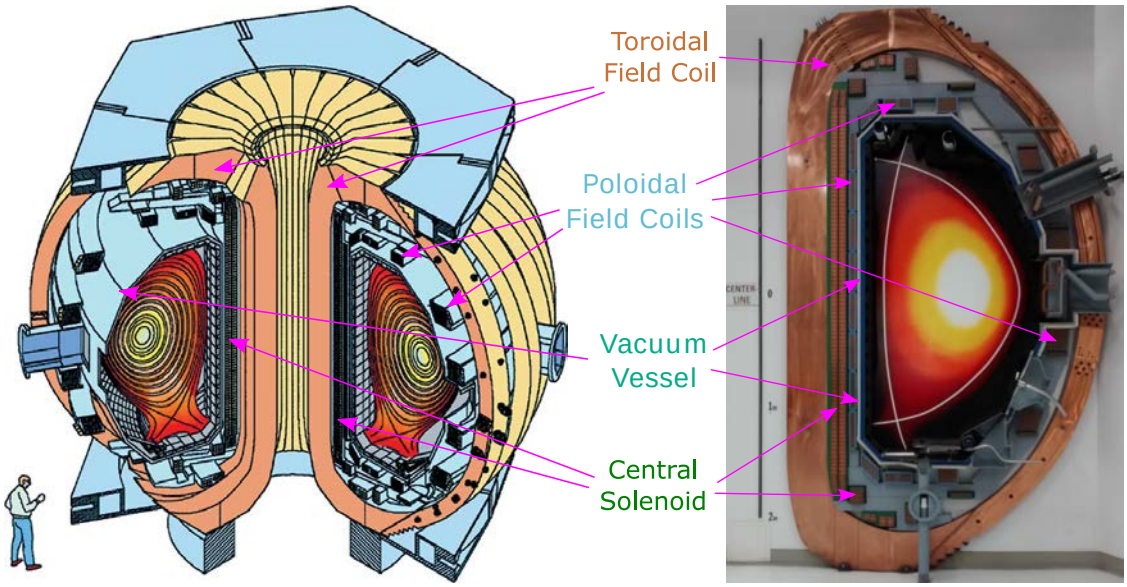

Figure 1.6: (Left) Diagram of the DIII-D tokamak with the plasma and flux surfaces shown in red-yellow. The D shaped TFCs are in yellow/orange. (Right) Model cross section of the DIII-D tokamak showing the major features of the device.

key operating parameters are also given in Table 1.1. KSTAR features fully superconducting magnets, making it particularly relevant to ITER and allowing for high toroidal field long pulse operation, with shots of up to 300s targeted. A number of imaging MSE experimental campaigns have been conducted on KSTAR as part of this research[40, 27, 41]. These experiments are not considered in detail in this thesis, however a number of examples are given relating to the 'tangential' viewing geometry used for these experiments.

1.6 Thesis Context

Here an outline of the breakthroughs and achievements in each thesis chapter is presented. Each chapter builds on work from the previous chapters but given the range of fields covered (atomic/quantum physics in Chapter 2, optical physics in Chapter 3, optical and plasma physics in Chapters 4 and 5) effort has been made to produce simplified general results in Chapter 2 that are applicable to the later chapters. Key insights and conclusions are emphasised with italicised text in the thesis.

In Chapter 2 it is revealed that existing atomic models of the MSE Balmer-α emission are flawed or incomplete and none are capable of predicting both upper-state populations and circular polarisation effects. In particular previous findings relating to the σ_0 polarisation orientation and $\sigma_{\pm1} : \pi_{\pm3}$ intensity ratio are invalidated. Significant progress is made in realising a model capable of predicting upper-state populations and circular polarisation effects. A detailed linear perturbation theory model of the Balmer-α emission is gradually built up by considering the influence of each additional interaction. The relatively straightforward Mathematica code used for the calculations is also presented for the benefit of expanding or replicating the calculations (Sec. 2.3). Initially only the dominant Stark interaction is considered in Sec. 2.4 where the well-known parabolic states and $\sigma^{\pm}$ transitions are characterised. A solid understanding of the pure Stark effect is crucial for recognising the disparities that arise when further interactions are considered. Next the

Zeeman effect is additionally included in Sec. 2.5 and it is revealed that there is a degree of freedom in the Stark-Zeeman solution that has not previously been realised. Two new distinct Stark-Zeeman solutions are presented, only one of which reduces to the pure Stark results in the absence of the Zeeman effect. The observable differences between the two solutions that emerge when relevant pairs of upper-states are unequally populated are formulated. Furthermore it is shown that mechanisms exist for the relevant pairs of upper-state to become unequally populated (Sec. 2.5.4). To ascertain the physically relevant Stark-Zeeman solution further weaker interactions must be considered. It is shown pure Stark solution is favoured when microscopic electric fields are large (Sec. 2.5.6) but that the alternate Stark-Zeeman solution is favoured when only the fine-structure is considered (Sec. 2.5.5).

Significant attention is given to describing the elliptical nature of the Stark-Zeeman transitions, an effect that is often overlooked. The effect of the elliptical transitions on the linear polarisation orientation and circular polarisation is elucidated using a simplified geometrical explanation (Sec. 2.6). Generalised equations for the Stark-Zeeman circular polarisation are presented for the first time along with a number of associated applications and detrimental effects of the circular component.

Chapter 3 describes the crucial measurement principles and optical components involved in the polarisation coherence imaging diagnostic for the benefit of a reader less familiar with the technique (Sections 3.1 and 3.3). Each of the different polarimeter designs are outlined along with the relative advantages and challenges of each encoding strategy (Sections 3.4 and 3.5). Particular attention is given to deriving and understanding two of the more subtle effects that can complicate IMSE measurements in some circumstances. Firstly the effects of the newly formulated Stark-Zeeman circular polarisation fraction are considered (Sec. 3.3.2) and the potential for coupling to the linear polarisation spatial carriers in each polarimeter design is examined. In cases where the polarimeter is sensitive to the circular polarisation it is shown that the interferometric delay can be tuned to reduce or eliminate this sensitivity. Secondly a model is developed to understand and predict weak non-axial ray produced spatial carrier fringes that have been observed in polarimeters with multiple spatial carriers (Sec. 3.2). This model for the non-axial ray effect is implemented to ascertain the polarisation information contained in the weaker carriers and to explore strategies for eliminating them to increase the bandwidth for the primary carriers.

A two month IMSE campaign undertaken on the DIII-D tokamak is detailed in Chapter 4. The radial view used for the polarimeter gave rise to significant line integration effects which are necessary to consider when interpreting the measurements (Sec. 4.1). A large range of factors worthy of consideration for the IMSE calibration are described (Sec. 4.2). Particular attention is given to effects specific to the chosen IMSE polarimeter design, such as the influence of the Stark-Zeeman circular polarisation and the spatial non-uniformity of the ferroelectric liquid crystal waveplate. The IMSE measurements are shown to be consistent with the conventional polarimeter on the midplane for standard DIII-D shots (Sec. 4.3.1). Furthermore the IMSE system is capable of measuring from two different beams and the measurements from each beam are also consistent (Sec. 4.3.5). However a comparison of the imaging data with an EFIT equilibrium forward model reveals some discrepancies above and below the midplane and possible shortcomings in the calibration are considered (Sec. 4.3.2). For shots with either reversed toroidal magnetic field or plasma current there are also inconsistencies between the conventional and IMSE measurements (Sec. 4.3.3). This inconsistency is considered in more detail by comparing the magnetic

axis inferred from a larger range of diagnostics (Sec 4.3.4). Finally beam voltage and instrumental effects relating to the IMSE Doppler shift sensitivity are also considered (Sec. 4.3.6).

A second polarisation coherence imaging based experiment was designed to measure the 7MHz RF electric field in the sheath of the H-1 plasma in the vicinity of the antenna (Sec 5.1). Unfortunately it appears the signal from the region directly underneath the antenna was insufficiently localised for the electric field to be detected. However in the process of capturing phase resolved images a light intensity perturbation was detected in the plasma (Sec. 5.2.4). The perturbation has the characteristics of a propagating wave and this is the first time the technique has been used to image RF heating waves. To better understand the wave properties four different viewing geometries were used, resulting in the identification of two waves with different characteristics. A magnetic field scan revealed that the wave directly underneath the antenna has the characteristics of an ion cyclotron wave (Sec. 5.2.6) and that the parallel phase velocity of the wave is comparable to the electron thermal speed. An ion cyclotron wave is therefore suspected to be the cause of edge electron heating on H-1 (Sec. 5.2.8).

Chapter 2

Balmer-α Polarisation in the Presence of Electric and Magnetic Fields

The atomic modelling presented in this chapter was initially developed for polarimetric measurement of the dynamic Stark effect in the relatively 'low' temperature sheath near the RF antenna on the H-1 heliac. The Stark effect, Zeeman effect and fine-structure interaction were anticipated to have comparable magnitude for the measurement giving rise to more complicated linear and circular polarisations. A model of the emission is therefore essential for interpretation of the H-1 measurements. Analytic results are not accessible when the fine structure is considered and neither the Stark or Zeeman effect dominate, hence the numerical modelling results for the H-1 spectra are presented later in Chapter 5.

While developing the model a range of discrepancies were identified in the existing literature on the motional Stark effect (MSE) emission. In Chapter 1 beam-into-gas (BIG) was introduced as a desirable technique for calibrating an MSE polarimeter, however the validity of the technique remains contentious due to subtle effects that arise when the upper-states of the Balmer-α are unequally populated. For example an MSE line ratio measurement technique proposed by Pablant et al (eg Ref. [42]) is based on the assertion that σ_1 and π_3 derive from the same upper-state such that the $\sigma_1 : \pi_3$ emission rates are independent of state populations. In direct contradiction, atomic modelling by Iwamae et al (Ref. [43]) found that the σ_1 emission can derive from an upper-state free of any π_3 emission. As another example, atomic modelling in Refs. [30] and [31] found that the linear polarisation orientation of the σ_0 emission is strongly dependent on upper-state populations, however in this chapter it is shown that this is not the case. The subtleties that have contributed to these discrepancies in the literature are outlined in Section 2.5. It is shown however that the $\sigma_{\pm 1}$ polarisation orientation may be sensitive to upper-state populations however there a several mitigating factors that imply BIG is a reliable polarimetric calibration technique. To best elucidate these discrepancies and highlight their resolution the Stark-Zeeman modelling presented in this chapter is deliberately kept as general as possible and specific examples are only considered where necessary.

The net circular polarisation from the Stark-Zeeman effect, outlined in Section 2.6, is arguably a greater concern for MSE calibration than upper-state population effects. This is particularly relevant for a π measuring polarimeter in the presence of an imperfect mirror, as realised on DIII-D[20]. A generalised characterisation of the circular polarisation is presented along with straightforward formulas for approximating the circularity of each

Balmer-α transition that can be applied without any knowledge of the underlying atomic physics.

This chapter has foundations in Refs. [44] and [31] and elaborates on the article already published for this research in Ref. [45]. The background theory needed to replicate the calculations is presented in Sections 2.1-2.3 and the well-known pure Stark effect results are revisited in Section 2.4. Key results of the combined Stark-Zeeman effect are presented in Section 2.5 which focuses on non-statistical upper-state population effects and Section 2.6 which focuses on the elliptical nature of the transitions.

2.1 Background

Parameters, ϵ and γ, commonly used for the Stark and Zeeman energy splitting respectively are

$$\epsilon = 3ea_0|\mathbf{E}|, \tag{2.1}$$

$$\gamma = \frac{e\hbar}{2m_e}|\mathbf{B}|, \tag{2.2}$$

while for the combined Stark-Zeeman effect the energy splitting for the $n = 2$ and $n = 3$ levels is conveniently given by[32]

$$q_0 = \sqrt{\epsilon^2 + \gamma^2}, \tag{2.3}$$

$$q_1 = \sqrt{9\epsilon^2 + 4\gamma^2}, \tag{2.4}$$

where e is the elementary charge, a_0 is the Bohr radius, $\hbar$ is the reduced Planck constant and m_e is the mass of the electron. When $\mathbf{E} = \mathbf{E_L} = \mathbf{v} \times \mathbf{B}$ the 'ratio' of the Stark and Zeeman effects is

$$\frac{\epsilon}{\gamma} = \frac{6m_e a_0|\mathbf{v}|\sin\rho}{\hbar} = \frac{6}{\alpha}\frac{|v|}{c}\sin\rho, \tag{2.5}$$

where ρ is the angle between $\mathbf{v}$ and $\mathbf{B}$, and α is the fine structure constant. Essentially the ϵ: γ ratio only depends on the neutral beam velocity and injection angle relative to the magnetic field. $\epsilon/\gamma = 6.6$ when an 80keV neutral deuterium beam injected at 60° to the magnetic field. This beam energy and injection angle are used in this chapter for numerical examples along with $|\mathbf{B}| = 2$T. Often this ratio is underestimated, with an example miscalculation in Ref. [46], creating the impression that the Zeeman effect can always be neglected. However, it has long been known that the Zeeman effect produces a measurable circular polarisation fraction for the MSE emission[16].

The fine structure interactions scales as $E_1\alpha^2/n^2$ where $E_1 = 13.6$eV is the ground state energy of the hydrogen atom and n is the principal quantum number. For the $n = 3$ level this energy corresponds to the Zeeman effect (scales as $n\gamma$) for a magnetic field of ~ 0.1T or the Stark effect (scales as $n^2\epsilon$) for an electric field of $\sim 30\text{kV m}^{-1}$. For the measurements on H-1 the magnetic field is 0.5T and the expected dynamic electric field is roughly 500kV m^{-1}. Meanwhile for MSE measurements the magnetic fields are generally > 2T and motional electric fields are $> 5000\text{kV m}^{-1}$.

2.2 Perturbation Theory

The deuterium wave functions in the presence of electric and magnetic fields are calculated using first order perturbation theory. While an emphasis is placed on MSE measurements, the calculations presented here are general and treat the magnetic and electric fields independently. The procedure used here is similar to that detailed in Refs. [44] and [31], however for comparison with the pure Stark effect it is convenient to orientate the coordinate system with the electric field along the z-axis, as shown in Fig. 2.1.

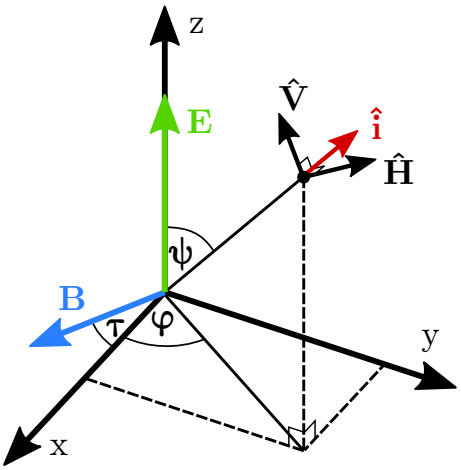

Figure 2.1: Coordinate system used throughout this chapter. The electric field **E** lies in the z-axis and the magnetic field **B** lies in the xy plane with an inclination angle τ to the x-axis. In the case of motional and/or radial electric fields $\tau = 0$ and in the case of a purely motional electric field the beam velocity must also lie in the xy plane. The emission is viewed from direction **i** with polar angle ψ and azimuthal angle φ. Without loss of generality the horizontal axis of the polarimeter is defined to be orthogonal to the electric field such that $\mathbf{H} = \mathbf{E} \times \hat{\mathbf{i}}$. The vertical axis of the detector is then $\hat{\mathbf{V}} = \hat{\mathbf{i}} \times \hat{\mathbf{H}}$.

The Hamiltonian for the system is:

$$H = H_0 + H_{FS} + H_E + H_B, \tag{2.6}$$

$$\begin{aligned} H_E &= e\mathbf{E} \cdot \mathbf{r} \\ &= \frac{\epsilon z}{3a_0} = \frac{\epsilon r \cos\psi}{3a_0} \end{aligned} \tag{2.7}$$

$$\begin{aligned} H_B &= \frac{e}{2m_e}(g_l \mathbf{L} + g_s \mathbf{S}) \cdot \mathbf{B} \\ &= \frac{\gamma}{\hbar}\big(\cos\tau(g_l L_x + g_s S_x) + \sin\tau(g_l L_z + g_s S_z)\big), \end{aligned} \tag{2.8}$$

where H_0 is the Coulomb interaction Hamiltonian for the atom, H_{FS} is the fine structure Hamiltonian, H_E is the Stark effect Hamiltonian and H_B is the Zeeman effect Hamiltonian. **E** and **B** are the electric and magnetic fields respectively, **r**, **L** and **S** are the position, orbital angular momentum and spin angular momentum operators, $g_l = 1$ is the orbital g-factor and $g_s \approx 2$ is the spin g-factor. Tabulated values for $(H_0 + H_{fs})$ that include spin-orbit coupling, relativistic effects and the Lamb shift are used instead of a functional form as shown later with Eq. 2.10.

First order perturbation theory is valid when the external fields are much weaker than the Coulomb interaction within the atom, i.e. $|\mathbf{E}| \ll \frac{e}{4\pi\epsilon_0 a_0^2}$, and that quantum states of

different principal quantum number do not mix, valid when $n^2\epsilon \ll E_1/n^2$. The well-known solution for the unperturbed Hamiltonian is

$$\begin{aligned}|\Phi_{n,\alpha}\rangle =& |n,l,m_l,m_s\rangle \\ =& R_{nl}(r)Y_l^{m_l}(\psi,\varphi)\begin{pmatrix}\frac{1}{2}+m_s\\ \frac{1}{2}-m_s\end{pmatrix},\end{aligned} \tag{2.9}$$

where n is the principal quantum number, l the orbital angular momentum quantum number, m_l the z-projection of the orbital angular momentum, m_s the z-projection of the electron spin, $R_{nl}(r)$ are the non-relativistic radial 'eigenfunctions' and $Y_l^{m_l}(\psi,\varphi)$ are the spherical harmonic functions with spherical coordinates (r,ψ,φ). Greek letter subscripts are used to represent allowable combinations of l, m_l and m_s and it should be noted Condon-Shortley phase convention is used for the spherical harmonics unlike in Refs.[44] and [9].

The first step is to evaluate the matrices $H_{n,\alpha\beta} = \langle\Phi_{n,\alpha}\,|\,H\,|\,\Phi_{n,\beta}\rangle$ for the n=2 (8×8 matrix) and n=3 (18×18 matrix) levels. The contributions of the Stark and Zeeman effect Hamiltonian elements to $H_{n,\alpha\beta}$ are straightforward to integrate with the Wolfram Mathematica computer program. The fine structure is diagonal in the $|n,l,j,m_j\rangle$ basis (i.e. $|n,l,j,m_j\rangle$ are eigenstates of H_0+H_{FS}) and the energies E_{nl_j} measured to high precision[47]. j is the total angular momentum and $m_j = m_l + m_s$ is the z-projection of the total angular momentum. Utilising eigenfunction property $(H_0+H_{fs})\,|n,l,j,m_j\rangle = E_{nl_j}\,|n,l,j,m_j\rangle$ and the orthogonality relationship $\sum_{l,j,m_j}|n,l,j,m_j\rangle\langle n,l,j,m_j| = 1$ it is possible to show that

$$\begin{aligned}&\langle n,l,m_l,m_s|\,H_0+H_{fs}\,\big|n,l',m_l',m_s'\big\rangle \\ &= \delta_{ll'}\delta_{(m_l+m_s)(m_l'+m_s')}\sum_j C^{l,s,j}_{m_l,m_s,m_l+m_s}C^{l,s,j}_{m_l',m_s',m_l+m_s}E_{nl_j},\end{aligned} \tag{2.10}$$

where $C^{l,s,j}_{m_l,m_s,m_j} = \langle n,l,m_l,m_s\,|\,n,l,j,m_j\rangle$ are the Clebsch-Gordon coefficients. In Eq. 2.10 the possible summation values are limited to $j = l\pm 1/2$ with the requirement that $j\geq m_j = m_l+m_s$. The $H_{2,\alpha\beta}$ matrix is presented in Table 2.1. The $H_{3,\alpha\beta}$ matrix is not shown as it is 18×18 but it is straightforward to calculate with the code in the following section.

$\lvert n,l,m_l,m_s\rangle$	$\langle 2,0,0,\frac{1}{2}\rvert$	$\langle 2,0,0,-\frac{1}{2}\rvert$	$\langle 2,1,0,\frac{1}{2}\rvert$	$\langle 2,1,0,-\frac{1}{2}\rvert$	$\langle 2,1,1,\frac{1}{2}\rvert$	$\langle 2,1,1,-\frac{1}{2}\rvert$	$\langle 2,1,-1,\frac{1}{2}\rvert$	$\langle 2,1,-1,-\frac{1}{2}\rvert$
$\lvert 2,0,0,\frac{1}{2}\rangle$	$E_{2s_{1/2}}$ $+\frac{q_s}{2}\gamma\sin\tau$	$\frac{q_s}{2}\gamma\cos\tau$	$-\epsilon$	0	0	0	0	0
$\lvert 2,0,0,-\frac{1}{2}\rangle$	$\frac{q_s}{2}\gamma\cos\tau$	$E_{2s_{1/2}}$ $-\frac{q_s}{2}\gamma\sin\tau$	0	$-\epsilon$	0	0	0	0
$\lvert 2,1,0,\frac{1}{2}\rangle$	$-\epsilon$	0	$\frac{1}{3}\left(E_{2p_{1/2}}+2E_{2p_{3/2}}\right)$ $+\frac{q_s}{2}\gamma\sin\tau$	$\frac{q_s}{2}\gamma\cos\tau$	$\frac{q_l}{\sqrt{2}}\gamma\cos\tau$	$\frac{\sqrt{2}}{3}\left(E_{2p_{3/2}}-E_{2p_{1/2}}\right)$	$\frac{q_l}{\sqrt{2}}\gamma\cos\tau$	0
$\lvert 2,1,0,-\frac{1}{2}\rangle$	0	$-\epsilon$	$\frac{q_s}{2}\gamma\cos\tau$	$\frac{1}{3}\left(E_{2p_{1/2}}+2E_{2p_{3/2}}\right)$ $-\frac{q_s}{2}\gamma\sin\tau$	0	$\frac{q_l}{\sqrt{2}}\gamma\cos\tau$	$\frac{\sqrt{2}}{3}\left(E_{2p_{3/2}}-E_{2p_{1/2}}\right)$	$\frac{q_l}{\sqrt{2}}\gamma\cos\tau$
$\lvert 2,1,1,\frac{1}{2}\rangle$	0	0	$\frac{q_l}{\sqrt{2}}\gamma\cos\tau$	0	$E_{2p_{3/2}}$ $+\left(g_l+\frac{q_s}{2}\right)\gamma\sin\tau$	$\frac{q_s}{2}\gamma\cos\tau$	0	0
$\lvert 2,1,1,-\frac{1}{2}\rangle$	0	0	$\frac{\sqrt{2}}{3}\left(E_{2p_{3/2}}-E_{2p_{1/2}}\right)$	$\frac{q_l}{\sqrt{2}}\gamma\cos\tau$	$\frac{q_s}{2}\gamma\cos\tau$	$\frac{1}{3}\left(2E_{2p_{1/2}}+E_{2p_{3/2}}\right)$ $+\left(g_l-\frac{q_s}{2}\right)\gamma\sin\tau$	0	0
$\lvert 2,1,-1,\frac{1}{2}\rangle$	0	0	$\frac{q_l}{\sqrt{2}}\gamma\cos\tau$	$\frac{\sqrt{2}}{3}\left(E_{2p_{3/2}}-E_{2p_{1/2}}\right)$	0	0	$\frac{1}{3}\left(2E_{2p_{1/2}}+E_{2p_{3/2}}\right)$ $-\left(g_l-\frac{q_s}{2}\right)\gamma\sin\tau$	$\frac{q_s}{2}\gamma\cos\tau$
$\lvert 2,1,-1,-\frac{1}{2}\rangle$	0	0	0	$\frac{q_l}{\sqrt{2}}\gamma\cos\tau$	0	0	$\frac{q_s}{2}\gamma\cos\tau$	$E_{2p_{3/2}}$ $-\left(g_l+\frac{q_s}{2}\right)\gamma\sin\tau$

Table 2.1: $H_{n,\alpha\beta}$ matrix for the n=2 states with electric and magnetic fields as defined in Fig. 2.1 and the fine structure. The table is equivalent to that in Ref. [44], only with a change in coordinate system and the use of Condon-Shortley phase convention.

The i^{th} eigenvector, $b_{n,i\eta}$, of the $H_{n,\alpha\beta}$ matrix describes the mixing coefficients for the

perturbed wave functions $|\Psi_{n,i}\rangle$ such that

$$|\Psi_{n,i}\rangle = \sum_{\eta} b_{n,i\eta} \, |\Phi_{n,\eta}\rangle \tag{2.11}$$

and the energy of perturbed state is the corresponding eigenvalue $E_{n,i}$. By design the perturbed wavefunctions satisfy

$$\langle \Psi_{n,i}| \, H \, |\Psi_{n,j}\rangle = \delta_{ij} E_{n,i}, \tag{2.12}$$

The dipole vector describing the polarisation of a transition between the n=3 and n=2 levels can be calculated using

$$\begin{aligned} \mathbf{r}_{ij} &= \langle \Psi_{2,i} \, | \, \mathbf{r} \, | \, \Psi_{3,j} \rangle \\ &= \sum_{\alpha\beta} b^*_{2,i\alpha} b_{3,j\beta} \, \langle \Phi_{2,\alpha} \, | \, \mathbf{r} \, | \, \Phi_{3,\beta} \rangle \, . \end{aligned} \tag{2.13}$$

Integration of the $\langle \Phi_{2,\alpha} \, | \, \mathbf{r} \, | \, \Phi_{3,\beta} \rangle$ terms is also straightforward in Mathematica. In general the real part of $(\mathbf{r}_{ij} e^{-\iota\omega_{ij} t})$ traces out an ellipse in time with angular frequency $\omega_{ij} = (E_{3,j} - E_{2,i})/\hbar$. The spontaneous emission rate coefficient for the transition is given by

$$A_{ij} = \frac{e^2 \omega_{ij}^3}{3\pi\epsilon_0 \hbar c^3} \, |\mathbf{r}_{ij}|^2 \, . \tag{2.14}$$

The observed polarisation of the emission is dependent on the viewing direction and is obtained by taking the projection of the dipole vector. The view direction has polar angle $0 \leq \psi \leq \pi$ and azimuthal angle $0 \leq \varphi < 2\pi$ such that it is

$$\hat{\mathbf{i}} = (\sin\psi \cos\varphi, \, \sin\psi \sin\varphi, \, \cos\psi). \tag{2.15}$$

The polarimeter axes are also defined in Fig. 2.1 such that:

$$\hat{\mathbf{H}} = (-\sin\varphi, \, \cos\varphi, \, 0), \tag{2.16}$$

$$\hat{\mathbf{V}} = (-\cos\psi\cos\varphi, \, -\cos\psi\sin\varphi, \, \sin\psi). \tag{2.17}$$

A rotation matrix can be used to generalise the orientation of the polarimeter axes but for simplicity this definition is fixed to the orientation of **E**.

The components of the dipole vector projection and dimensionless Stokes vector for each transition are then:

$$(r_H)_{ij} = \mathbf{r}_{ij}.\hat{\mathbf{H}}, \tag{2.18}$$

$$(r_V)_{ij} = \mathbf{r}_{ij}.\hat{\mathbf{V}}, \tag{2.19}$$

$$\begin{aligned} \bar{\mathbf{s}} &= (\bar{s}_0, \, \bar{s}_1, \, \bar{s}_2, \, \bar{s}_3) \\ &= \frac{1}{|r|^2} \left(|r_H|^2 + |r_V|^2, \, |r_H|^2 - |r_V|^2, \, 2\,\mathrm{Re}[r_H r_V^*], \, 2\,\mathrm{Im}[r_H r_V^*] \right) , \end{aligned} \tag{2.20}$$

where the ij subscript is implied for each term in Eq. 2.20. The Stokes vector describes the polarisation ellipse traced out in time by the electric field of the light wave at the

detector which can be expressed in geometric terms as

$$\begin{aligned}\mathbf{s} &= I_0(1,\, p\cos 2\xi\cos 2\theta,\, p\cos 2\xi\sin 2\theta,\, p\sin 2\xi), \\ &= I_0(1,\, p_l\cos 2\theta,\, p_l\sin 2\theta,\, p_c)\end{aligned} \tag{2.21}$$

where $0 \leq p \leq 1$ is the degree of polarisation, θ is the orientation of the polarisation ellipse's major-axis and ξ is it's ellipticity angle, as defined in Fig. 2.2. Alternatively the linear polarisation fraction is defined as $p_l = p\cos 2\xi = \sqrt{s_1^2 + s_2^2}/s_0$ $(0 \leq p_l \leq 1)$and the circular polarisation fraction as $p_c = \sin 2\xi = s_3/s_0$ $(-1 \leq p_c \leq 1)$. The Stokes vector

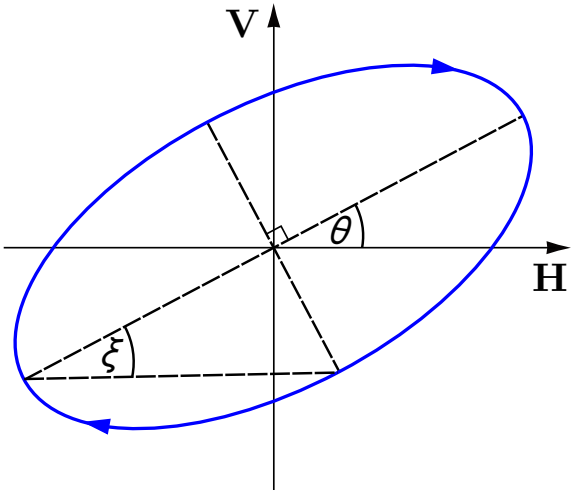

Figure 2.2: Polarisation ellipse observed from point of view of the detector. The elliptical polarisation is right handed such that $\xi > 0$ $(s_3 > 0)$. The convention used defines the polarisation from the point of view of the detector looking towards the emission source.

(power per unit solid angle per angular frequency) for the emission is then

$$\mathbf{s}(\omega) = \frac{3}{8\pi}\sum_j N_{3,j}\sum_i \hbar\omega_{ij}A_{ij}\bar{\mathbf{s}}_{ij}\delta\left(\omega - \omega_{ij}(1 + \hat{\mathbf{i}}\cdot\mathbf{v}/c)\right), \tag{2.22}$$

where $N_{3,j}$ is the number of beam atoms in the $|\Psi_{3,j}\rangle$ state and ω is the angular frequency of the light. In Eq. 2.22 there are $8\times 18 = 144$ different possible transitions (when electron spin is included) which are summed incoherently to give the Stokes vectors. Invariably the equation must be integrated over the collection volume, velocities distribution and the range of angles. An example Stokes vector resolved spectrum for the D_α MSE emission is illustrated later in Fig. 2.13.

2.3 Mathematica Code

The Mathematica code that implements and interprets the linear perturbation calculations described in the previous section is included as a supplementary file to the thesis. The Mathematica notebook is included for those looking to replicate the results and can be examined in parallel with the reading of this chapter but it is not essential. The calculations are for the $n = 3 \rightarrow 2$ transition but the code can easily be adapted for other values of n and therefore different transitions.

2.4 Stark Effect

Linear Stark effect theory provides a close approximation for the transitions rates, splitting and linear polarisation of the measured MSE spectrum. The well-known results are revisit and reformulate here as a useful comparison point for calculations later that include additional interactions. In this case the Hamiltonian is $H = H_0 + H_E$ and for simplicity the electron spin can be ignored as states with opposite spin do not mix and transitions between states of opposite spin are forbidden.

The parabolic states $|n, k, m_l\rangle$ are the natural solution for the Stark effect and are expressed in terms of $|n, l, m_l\rangle$ states in Tables 2.2 (n=2) and 2.3 (n=3). The probability densities for the parabolic states are plotted later in Fig. 2.4. The energy splitting of the parabolic states is related to the quantum number $k = n_1 - n_2$, where $n_1 \geq 0$ and $n_2 \geq 0$ are the parabolic quantum numbers, under the restriction that $n_1 + n_2 + 1 = n - |m_l|$. The energy of a parabolic state is given by

$$E_{n,k} = \frac{E_1}{n^2} + \frac{nk}{2}\epsilon. \tag{2.23}$$

A description of the transitions is presented in this paragraph before a mathematical treatment is given in the following paragraph. Transitions with $\Delta m_l = 0$, known as π, have dipole vectors that oscillate along the axis of the external electric field. Therefore π transition are linearly polarised but have zero intensity when viewing along the axis of the field. Transitions with $\Delta m_l = \pm 1$, known as $\sigma^{\pm}$, have dipole vectors that circle around the axis of the external electric field with handedness dependent on the sign of Δm_l. Projecting a circular dipole vector along the viewing axis $\mathbf{i}$ gives an elliptical polarisation where the major axis is perpendicular to projection of the electric field, as illustrated in the left of Fig. 2.3. Therefore linear polarisation orientation (θ in Eq. 2.21) of the σ emission is always perpendicular to the π emission, independent of the viewing angle or upper-state populations. With an equal intensity of left and right handed transitions the net circular polarisation fraction ($p \sin 2\xi$) is zero, resulting in a linear polarisation intensity ($p \cos 2\xi$) dependent on the viewing angle.

$\|n,l,m_l\rangle$ \ $\|n,k,m_l\rangle$	$\|2,1,0\rangle$	$\|2,-1,0\rangle$	$\|2,0,1\rangle$	$\|2,0,-1\rangle$
$\|2,0,0\rangle$	$\frac{1}{\sqrt{2}}$	$\frac{1}{\sqrt{2}}$	0	0
$\|2,1,0\rangle$	$\frac{-1}{\sqrt{2}}$	$\frac{1}{\sqrt{2}}$	0	0
$\|2,1,1\rangle$	0	0	1	0
$\|2,1,-1\rangle$	0	0	0	1

Table 2.2: $n = 2$ mixing coefficients $b_{2,kl}$ linking from the $|n, l, m_l\rangle$ states to the $|n, k, m_l\rangle$ states via $|2, k, m_l\rangle = \sum_l b_{2,kl} |2, l, m_l\rangle$.

A quantitative summary of the rate coefficient, transition type and energy for the $n = 3 \to 2$ transitions are presented in Table 2.4. With the coordinate system as defined

$\lvert n,l,m_l\rangle \backslash \lvert n,k,m_l\rangle$	$\lvert 3,2,0\rangle$	$\lvert 3,-2,0\rangle$	$\lvert 3,0,0\rangle$	$\lvert 3,0,2\rangle$	$\lvert 3,0,-2\rangle$	$\lvert 3,1,1\rangle$	$\lvert 3,1,-1\rangle$	$\lvert 3,-1,1\rangle$	$\lvert 3,-1,-1\rangle$
$\lvert 3,0,0\rangle$	$\frac{1}{\sqrt{3}}$	$\frac{1}{\sqrt{3}}$	$\frac{1}{\sqrt{3}}$	0	0	0	0	0	0
$\lvert 3,1,0\rangle$	$\frac{-1}{\sqrt{2}}$	$\frac{1}{\sqrt{2}}$	0	0	0	0	0	0	0
$\lvert 3,2,0\rangle$	$\frac{1}{\sqrt{6}}$	$\frac{1}{\sqrt{6}}$	$-\sqrt{\frac{2}{3}}$	0	0	0	0	0	0
$\lvert 3,2,2\rangle$	0	0	0	1	0	0	0	0	0
$\lvert 3,2,-2\rangle$	0	0	0	0	1	0	0	0	0
$\lvert 3,1,1\rangle$	0	0	0	0	0	$\frac{1}{\sqrt{2}}$	0	$\frac{1}{\sqrt{2}}$	0
$\lvert 3,2,1\rangle$	0	0	0	0	0	$\frac{-1}{\sqrt{2}}$	0	$\frac{1}{\sqrt{2}}$	0
$\lvert 3,1,-1\rangle$	0	0	0	0	0	0	$\frac{1}{\sqrt{2}}$	0	$\frac{1}{\sqrt{2}}$
$\lvert 3,2,-1\rangle$	0	0	0	0	0	0	$\frac{-1}{\sqrt{2}}$	0	$\frac{1}{\sqrt{2}}$

Table 2.3: $n = 3$ mixing coefficients $b_{3,kl}$ linking from the $|n, l, m_l\rangle$ states to the $|n, k, m_l\rangle$ states via $|3, k, m_l\rangle = \sum_l b_{3,kl} |3, l, m_l\rangle$.

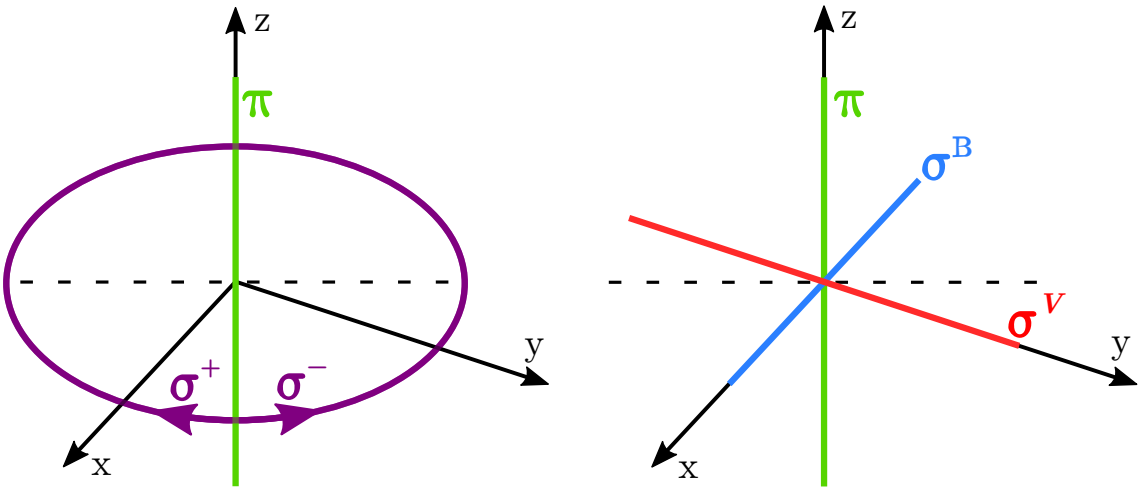

Figure 2.3: (Left) Polarisation structure of the pure Stark effect transitions with a general viewing direction. The π emission is a projection of a dipole oscillation along the electric field axis. The $\sigma^{\pm}$ emission is produced from a circular dipole orbiting in the xy-plane which projects as an ellipse. The major axis of the ellipse, depicted with the dashed line, is perpendicular to the projection of the z-axis. (Right) Polarisation structure of the $|n, k, m_l\rangle_L$ states in the limit $\gamma/\epsilon \to 0$. The partial linear polarisation is only orthogonal to the π emission, depicted by the dashed line, when the σ^B and σ^v transitions have equal emission rates (or with a $\psi = \pi/2$ view). Otherwise the linear polarisation orientation will be weighted towards the σ with greater emission rate.

in Fig. 2.1, the dipole vector and dimensionless Stokes vector for each transition are:

$$\hat{\mathbf{r}}_{\pi} = (0,\ 0,\ 1), \tag{2.24}$$

$$\bar{\mathbf{s}}_{\pi} = (\sin^2\psi,\ -\sin^2\psi,\ 0,\ 0), \tag{2.25}$$

$$\hat{\mathbf{r}}_{\sigma^{\pm}} = (\pm 1,\ -i,\ 0)/\sqrt{2}, \tag{2.26}$$

$$\bar{\mathbf{s}}_{\sigma^{\pm}} = \frac{1}{2}(1 + \cos^2\psi,\ \sin^2\psi,\ 0,\ \pm 2\cos\psi). \tag{2.27}$$

Evidently from the Stokes vectors the π component is linearly polarised along $\mathbf{V}$ (the projection of $\mathbf{E}$) and the $\sigma^{\pm}$ linear polarisation fractions are parallel to $\mathbf{H}$ (perpendicular to the projection of $\mathbf{E}$), as expected. *The net polarisation orientation of a combined σ emission is independent of the $\sigma^+ : \sigma^-$ intensity ratio* ($\theta = 0°$ as $\sum s_2 = 0$ and $\sum s_1 > 0$)

and is therefore referred to as a 'robust' polarisation structure. The only consequence of an unequal intensity ratio would be the presence of a net circular polarisation fraction.

$\|n,k,m_l\rangle$	$\|2,1,0\rangle$	$\|2,-1,0\rangle$	$\|2,0,1\rangle$	$\|2,0,-1\rangle$
$\|3,2,0\rangle$	$(1681)\pi_4$	$(1)\pi_8$	$(18)\sigma_6^+$	$(18)\sigma_6^-$
$\|3,-2,0\rangle$	$(1)\pi_{-8}$	$(1681)\pi_{-4}$	$(18)\sigma_{-6}^+$	$(18)\sigma_{-6}^-$
$\|3,0,0\rangle$	$(729)\pi_{-2}$	$(729)\pi_2$	$(882)\sigma_0^+$	$(882)\sigma_0^-$
$\|3,0,2\rangle$	-	-	$(4608)\sigma_0^-$	-
$\|3,0,-2\rangle$	-	-	-	$(4608)\sigma_0^+$
$\|3,1,1\rangle$	$(1936)\sigma_1^-$	$(16)\sigma_5^-$	$(1152)\pi_3$	-
$\|3,1,-1\rangle$	$(1936)\sigma_1^+$	$(16)\sigma_5^+$	-	$(1152)\pi_3$
$\|3,-1,1\rangle$	$(16)\sigma_{-5}^-$	$(1936)\sigma_{-1}^-$	$(1152)\pi_{-3}$	-
$\|3,-1,-1\rangle$	$(16)\sigma_{-5}^+$	$(1936)\sigma_{-1}^+$	-	$(1152)\pi_{-3}$

Table 2.4: Transitions between n=3 and n=2 states for the pure Stark effect. The format is $(Rate)Type_{\text{Energy}}$ where the distinction between handedness of the σ transition is made with + and - superscripts. The magnitude of the dipole vector is related to the intensity in the parenthesis via the relationship $|r_{ij}|^2 = 2^{14}3^6a_0^2(Rate)/5^{14}$. The energy offset is in multiples of $\epsilon/2$ and positive energies indicate transitions of higher frequency and therefore lower wavelength (note this convention is not universal in the literature). The transition probabilities agree with those presented in Table 20b of Ref. [9].

When σ^+ and σ^- transitions have equal rate coefficients and upper-state populations it is valid to treat them as a combined emission, with dimensionless Stokes vector given by

$$\bar{\mathbf{s}}_\sigma = \bar{\mathbf{s}}_{\sigma^+} + \bar{\mathbf{s}}_{\sigma^-} = (1 + \cos^2\psi,\, \sin^2\psi,\, 0,\, 0). \tag{2.28}$$

This condition is automatically satisfied for the weak σ_6 and σ_{-6} emissions as they have equal $\sigma^\pm$ transition rate and derive from the same upper-state, as seen in Table 2.4. The condition only holds for σ_0 if $N_{|3,0,2\rangle} = N_{|3,0,-2\rangle}$, for σ_1 if $N_{|3,1,1\rangle} = N_{|3,1,-1\rangle}$ and for σ_{-1} if $N_{|3,-1,1\rangle} = N_{|3,-1,-1\rangle}$. Therefore a complete understanding of the observed polarisation requires knowledge of the relative populations of these upper-state pairs.

2.4.1 Ground State Proton Impact Excitation Cross Sections

In the case of MSE the strongest excitation mechanism for the neutral beam atoms is collisions with fully stripped plasma ions, with most excitations coming from the ground state. In our coordinate system the neutral beam atoms must have a velocity in the xy-plane when the electric field is purely motional. The excitation cross section for the perturbed states can be expressed in terms of $|n,l,m_l\rangle$ states with quantisation axis in the direction of the neutral beam atoms[29]. The cross section for proton impact excitation

from the ground state to the n=2 and n=3 levels are given in Refs. [48] and [29] to be:

$$\sigma_{|2,\pm1,0\rangle} = \frac{1}{2}\sigma_{2s_0} + \frac{1}{2}\sigma_{2p_1}, \tag{2.29}$$

$$\sigma_{|2,0,\pm1\rangle} = \frac{1}{2}\sigma_{2p_0} + \frac{1}{2}\sigma_{2p_1}, \tag{2.30}$$

$$\sigma_{|3,\pm2,0\rangle} = \frac{1}{3}\sigma_{3s_0} + \frac{1}{24}\sigma_{3d_0} + \frac{1}{2}\sigma_{3p_1} + \frac{1}{8}\sigma_{3d_2} - \frac{\sqrt{2}}{6}\,\mathrm{Re}\left(\rho^{3d_0}_{3s_0}\right), \tag{2.31}$$

$$\sigma_{|3,0,0\rangle} = \frac{1}{3}\sigma_{3s_0} + \frac{1}{6}\sigma_{3d_0} + \frac{1}{2}\sigma_{3d_2} + \frac{\sqrt{2}}{3}\,\mathrm{Re}\left(\rho^{3d_0}_{3s_0}\right), \tag{2.32}$$

$$\sigma_{|3,0,\pm2\rangle} = \frac{3}{8}\sigma_{3d_0} + \frac{1}{2}\sigma_{3d_1} + \frac{1}{8}\sigma_{3d_2}, \tag{2.33}$$

$$\sigma_{|3,\pm1,\pm1\rangle} = \frac{1}{4}\left(\sigma_{3p_0} + \sigma_{3p_1} + \sigma_{3d_1} + \sigma_{3d_2}\right), \tag{2.34}$$

where σ_{nl_m} are diagonal elements of the density matrix and $\rho^{nl_m}_{n'l'_{m'}}$ are the off-diagonal elements. That is, *pairs of upper-states individually producing σ^+ and σ^- for a given energy* (Table 2.4) *are expected to have the same upper-state populations.* More generally this should be expected for all excitation mechanisms because the relevant pairs have identical probability densities as seen in Fig. 2.4 and only differ in the sign of their orbital angular momentum m_l.

2.5 Stark-Zeeman Effect

We now consider the impacts of including the Zeeman effect from the magnetic field in the calculations. The Stark-Zeeman Hamiltonian is $H = H_0 + H_E + H_B$. Again spin is ignored as the Zeeman effect only applies a fixed offset to the energy levels for opposite spin states (Paschen-Back regime). The magnetic field is orthogonal to the motional electric field and removes the rotational invariance about the electric field by introducing a second preferred direction for the atom. The projection of the orbital angular momentum operator, $\mathbf{L}_z$, does not commute with both the Stark and Zeeman Hamiltonians (unless $\tau = 0$ or π) implying the quantum number m_l is no longer valid. Consequently the notion of π and σ emission can only be accurate when either the Stark or Zeeman effect dominates over the other. Some of the implications of this second preferred direction have been explored by Yuh in Ref. [31]. Yuh's conclusion was that the σ emission is not produced by circular $\sigma^\pm$ dipole vectors about the $\mathbf{E}$ axis, but instead is a combination of linear oscillations along the $\mathbf{B}$ and $\mathbf{E}\times\mathbf{B}$ axes. However this analysis overlooks the remaining degeneracy in the Stark-Zeeman energy levels that leaves a degree of freedom in the orthogonalisation of the degenerate states, hence the polarisation structure is underdetermined.

2.5.1 Importance of Degeneracy

The tabulated Stark-Zeeman states[32] used by Yuh do not all converge to the parabolic states of the pure Stark effect in the limit $\gamma/\epsilon \to 0$. The remaining degeneracy in the energy levels, displayed in Fig. 2.5, is the underlying cause of the non-convergence. The eigenvectors (mixing coefficients) with degenerate eigenvalues form a subspace that can be freely orthogonalised. As an example consider a superposition of parabolic states given by

$$|n,k,M\rangle = \cos\eta\,|n,k,m_l\rangle + \sin\eta\,|n,k,-m_l\rangle \tag{2.35}$$

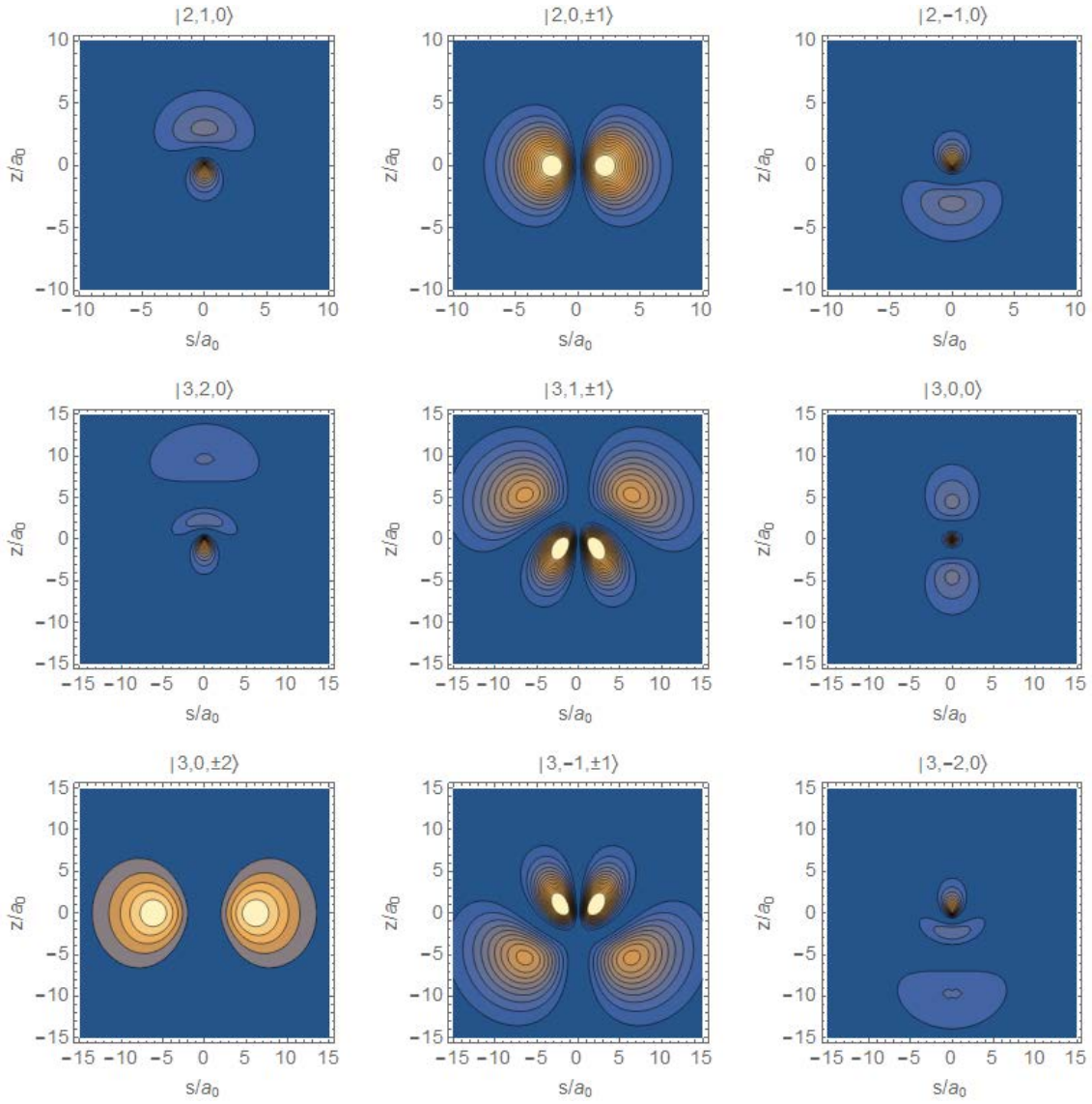

Figure 2.4: 2D cross sections of the probability distributions for the parabolic states of the pure Stark effect. The distributions are symmetric about the z-axis of the electric field.

where η is a free variable. $|n, k, M\rangle$ is still a valid solution of Eq. 2.12 for the Stark effect perturbed Hamiltonian $H_0 + H_E$. However when there is only an electric field the states must be rotationally invariant about the field, effectively ruling out such a superposition of parabolic states. Essentially m_l was a valid quantum number that distinguished between the degenerate states. Now in the case of the Stark-Zeeman effect there is no symmetry about the fields and the choice of orthogonalisation for eigenvectors with degenerate eigenvalues is undetermined. As a result the projection of the degenerate state's angular momentum is also underdetermined and is given by

$$\langle n, k, M| \, L_z \, |n, k, M\rangle = m_l \cos 2\eta \tag{2.36}$$

Therefore the value of $\Delta \langle L_z \rangle$ (analogous to Δm_l) for a transition, depends on the free choices of η for each pairing of degenerate states. *Consequently the resulting polarisation structure is also underdetermined.*

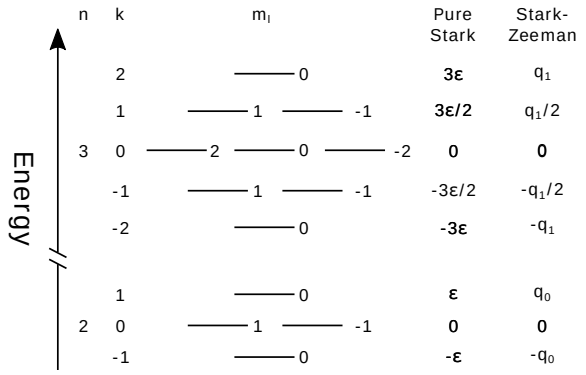

Figure 2.5: Energy and degeneracy of the n=2 and n=3 levels of the pure Stark states and Stark-Zeeman states. In the Stark-Zeeman case the degeneracy only exists when the electric and magnetic fields are orthogonal. k remains a valid quantum number for the Stark-Zeeman effect while m_l does not.

This underdetermined structure resulting from the degeneracy only produces observable differences when the upper-state populations, $N_{3,j}$ in Eq. 2.22, of the degenerate states are unequal. When upper-state are known to be non-statistically populated it is necessary to remove the degree of freedom by including further interactions that remove all degeneracy in the system. Sections 2.5.2 and 2.5.3 outline two different orthogonalisation of degenerate Stark-Zeeman states. The physical relevance of these states is then outlined afterwards in Sections 2.5.5 and 2.5.6. For tractability only zeroth order effects in γ/ϵ are considered in the rest of Section 2.5. Higher order γ/ϵ effects are then considered later in Sec. 2.6 in which case equally populated upper-states are assumed for simplicity.

2.5.2 Circular Stark-Zeeman States

The Stark-Zeeman states that converge to the parabolic states when the magnetic field vanishes can be determined by considering the more general situation when **B** is not orthogonal to **E**, that is when $\tau \neq 0$. In this case the energy levels are all non-degenerate and are given by:

$$E_{|2,\pm1,0\rangle} = \pm\frac{1}{\sqrt{2}}\sqrt{q_0^2 + \sqrt{q_0^4 - 4\gamma^2\epsilon^2\sin^2\tau}}, \tag{2.37}$$

$$E_{|2,0,\pm1\rangle} = \pm\frac{1}{\sqrt{2}}\sqrt{q_0^2 - \sqrt{q_0^4 - 4\gamma^2\epsilon^2\sin^2\tau}}, \tag{2.38}$$

$$E_{|3,\pm2,0\rangle} = \pm\frac{1}{\sqrt{2}}\sqrt{q_1^2 + \sqrt{q_1^4 - 144\gamma^2\epsilon^2\sin^2\tau}}, \tag{2.39}$$

$$E_{|3,0,0\rangle} = 0 \tag{2.40}$$

$$E_{|3,0,\pm2\rangle} = \pm\frac{1}{\sqrt{2}}\sqrt{q_1^2 - \sqrt{q_1^4 - 144\gamma^2\epsilon^2\sin^2\tau}}, \tag{2.41}$$

$$E_{|3,1,\pm1\rangle} = \frac{1}{2}\sqrt{q_1^2 \pm 12\gamma\epsilon\sin\tau}, \tag{2.42}$$

$$E_{|3,-1,\pm1\rangle} = -\frac{1}{2}\sqrt{q_1^2 \mp 12\gamma\epsilon\sin\tau}. \tag{2.43}$$

The energies in Fig. 2.5 are returned by substituting $\tau = 0$ into the equations. The Stark-Zeeman states that are continuous with the parabolic states as $\gamma/\epsilon \to 0$ are obtained by taking the corresponding eigenvectors for the above eigenvalues in the limit that $\tau \to 0$. These states are labelled $|n, k, m_l\rangle_C$ (where 'C' indicates 'circular') and the mixing coefficients for these Stark-Zeeman states in the special case where $\mathbf{E} \perp \mathbf{B}$ are presented in Tables 2.5 (n=2) and 2.6 (n=3). The m_l quantum number therefore remains dependable when $\gamma \ll \epsilon$ for the $|n, k, m_l\rangle_C$ states, hence the transition have the same 'robust' emission structure as Table 2.4. That is, individual π and σ linear polarisations are orthogonal independent of viewing angle. Differences between the ground state proton impact excitation cross sections for the pure Stark states and 'circular' Stark-Zeeman states can be neglected when $\gamma \ll \epsilon$, as reasoned in Ref. [29].

$\|n,l,m_l\rangle \setminus \|n,k,m_l\rangle_C$	$\|2,1,0\rangle_C$	$\|2,-1,0\rangle_C$	$\|2,0,1\rangle_C$	$\|2,0,-1\rangle_C$
$\|2,0,0\rangle$	$\frac{\epsilon}{\sqrt{2}q_0}$	$\frac{\epsilon}{\sqrt{2}q_0}$	$\frac{\gamma}{\sqrt{2}q_0}$	$\frac{\gamma}{\sqrt{2}q_0}$
$\|2,1,0\rangle$	$\frac{-1}{\sqrt{2}}$	$\frac{1}{\sqrt{2}}$	0	0
$\|2,1,1\rangle$	$\frac{-\gamma}{2q_0}$	$\frac{-\gamma}{2q_0}$	$\frac{\epsilon/q_0+1}{2}$	$\frac{\epsilon/q_0-1}{2}$
$\|2,1,-1\rangle$	$\frac{-\gamma}{2q_0}$	$\frac{-\gamma}{2q_0}$	$\frac{\epsilon/q_0-1}{2}$	$\frac{\epsilon/q_0+1}{2}$

Table 2.5: $n = 2$ mixing coefficients $b_{2,(km_l)\alpha}$ linking from the $|n, l, m_l\rangle \equiv |\Phi_{n,\alpha}\rangle$ states to the 'circular' Stark-Zeeman states such that $|2, k, m_l\rangle_C = \sum_\alpha b_{2,(km_l)\alpha} |\Phi_{2,\alpha}\rangle$. The $|n, k, m_l\rangle_C$ states reduce to the parabolic states, presented in Table 2.2, as $\gamma/\epsilon \to 0$.

$\|n,l,m_l\rangle \setminus \|n,k,m_l\rangle_C$	$\|3,2,0\rangle_C$	$\|3,-2,0\rangle_C$	$\|3,0,0\rangle_C$	$\|3,0,2\rangle_C$	$\|3,0,-2\rangle_C$	$\|3,1,1\rangle_C$	$\|3,1,-1\rangle_C$	$\|3,-1,1\rangle_C$	$\|3,-1,-1\rangle_C$
$\|3,0,0\rangle$	$3\sqrt{3}\epsilon^2$	$3\sqrt{3}\epsilon^2$	$\frac{9\epsilon^2-4\gamma^2}{\sqrt{3}}$	$\frac{4\gamma^2}{\sqrt{3}}$	$\frac{4\gamma^2}{\sqrt{3}}$	$2\sqrt{6}\gamma\epsilon$	$2\sqrt{6}\gamma\epsilon$	$2\sqrt{6}\gamma\epsilon$	$2\sqrt{6}\gamma\epsilon$
$\|3,1,0\rangle$	$\frac{-3\epsilon q_1}{\sqrt{2}}$	$\frac{3\epsilon q_1}{\sqrt{2}}$	0	0	0	$-\gamma q_1$	$-\gamma q_1$	γq_1	γq_1
$\|3,2,0\rangle$	$\frac{\sqrt{3}(3\epsilon^2+2\gamma^2)}{\sqrt{2}}$	$\frac{\sqrt{3}(3\epsilon^2+2\gamma^2)}{\sqrt{2}}$	$\frac{-\sqrt{2}(9\epsilon^2+2\gamma^2)}{\sqrt{3}}$	$-\sqrt{\frac{2}{3}}\gamma^2$	$-\sqrt{\frac{2}{3}}\gamma^2$	$-\sqrt{3}\gamma\epsilon$	$-\sqrt{3}\gamma\epsilon$	$-\sqrt{3}\gamma\epsilon$	$-\sqrt{3}\gamma\epsilon$
$\|3,2,2\rangle$	γ^2	γ^2	$2\gamma^2$	$\frac{9\epsilon^2+3\epsilon q_1+2\gamma^2}{2}$	$\frac{9\epsilon^2-3\epsilon q_1+2\gamma^2}{2}$	$\frac{-\gamma(q_1+3\epsilon)}{\sqrt{2}}$	$\frac{\gamma(q_1-3\epsilon)}{\sqrt{2}}$	$\frac{-\gamma(q_1+3\epsilon)}{\sqrt{2}}$	$\frac{\gamma(q_1-3\epsilon)}{\sqrt{2}}$
$\|3,2,-2\rangle$	γ^2	γ^2	$2\gamma^2$	$\frac{9\epsilon^2-3\epsilon q_1+2\gamma^2}{2}$	$\frac{9\epsilon^2+3\epsilon q_1+2\gamma^2}{2}$	$\frac{\gamma(q_1-3\epsilon)}{\sqrt{2}}$	$\frac{-\gamma(q_1+3\epsilon)}{\sqrt{2}}$	$\frac{\gamma(q_1-3\epsilon)}{\sqrt{2}}$	$\frac{-\gamma(q_1+3\epsilon)}{\sqrt{2}}$
$\|3,1,1\rangle$	$-3\gamma\epsilon$	$-3\gamma\epsilon$	$-6\gamma\epsilon$	$\gamma(3\epsilon+q_1)$	$\gamma(3\epsilon-q_1)$	$\frac{9\epsilon^2+3\epsilon q_1-4\gamma^2}{2\sqrt{2}}$	$\frac{9\epsilon^2-3\epsilon q_1-4\gamma^2}{2\sqrt{2}}$	$\frac{9\epsilon^2+3\epsilon q_1-4\gamma^2}{2\sqrt{2}}$	$\frac{9\epsilon^2-3\epsilon q_1-4\gamma^2}{2\sqrt{2}}$
$\|3,2,1\rangle$	γq_1	$-\gamma q_1$	0	0	0	$\frac{-q_1(q_1+3\epsilon)}{2\sqrt{2}}$	$\frac{q_1(q_1-3\epsilon)}{2\sqrt{2}}$	$\frac{q_1(q_1+3\epsilon)}{2\sqrt{2}}$	$\frac{-q_1(q_1-3\epsilon)}{2\sqrt{2}}$
$\|3,1,-1\rangle$	$-3\gamma\epsilon$	$-3\gamma\epsilon$	$-6\gamma\epsilon$	$\gamma(3\epsilon-q_1)$	$\gamma(3\epsilon+q_1)$	$\frac{9\epsilon^2-3\epsilon q_1-4\gamma^2}{2\sqrt{2}}$	$\frac{9\epsilon^2+3\epsilon q_1-4\gamma^2}{2\sqrt{2}}$	$\frac{9\epsilon^2-3\epsilon q_1-4\gamma^2}{2\sqrt{2}}$	$\frac{9\epsilon^2+3\epsilon q_1-4\gamma^2}{2\sqrt{2}}$
$\|3,2,-1\rangle$	γq_1	$-\gamma q_1$	0	0	0	$\frac{q_1(q_1-3\epsilon)}{2\sqrt{2}}$	$\frac{-q_1(q_1+3\epsilon)}{2\sqrt{2}}$	$\frac{-q_1(q_1-3\epsilon)}{2\sqrt{2}}$	$\frac{q_1(q_1+3\epsilon)}{2\sqrt{2}}$

Table 2.6: $n = 3$ mixing coefficients $b_{3,(km_l)\alpha}$ that produce the 'circular' Stark Zeeman states via $|3, k, m_l\rangle_C = \sum_\alpha b_{3,(km_l)\alpha} |\Phi_{3,\alpha}\rangle$. The coefficients must be normalised by q_1^2.

2.5.3 Linear Stark-Zeeman States

In the previous section it was shown that the remaining Stark-Zeeman degeneracy is broken when $\tau \neq 0$. Other weaker interactions that also break the remaining degeneracy need to be considered to determine the correct quantum states and polarisation of the transitions. In this section an alternative orthogonalisation of the degenerate states is considered, denoted $|n, k, m_l\rangle_L$ (where 'L' denotes 'linear'), which are more natural when the fine structure of the atom is considered in Sec. 2.5.5.

$|3, 0, 0\rangle_C$ and the non-degenerate states are the same for the 'C' and 'L' Stark-Zeeman

solutions. The remaining $|n,k,m_l\rangle_L$ states are formed using the relationships:

$$\left|2,0,\pm\tilde{1}\right\rangle_L = \frac{1}{\sqrt{2}}\left(|2,0,1\rangle_C \mp |2,0,-1\rangle_C\right), \tag{2.44}$$

$$\left|3,0,\pm\tilde{2}\right\rangle_L = \frac{1}{\sqrt{2}}\left(|3,0,2\rangle_C \pm |3,0,-2\rangle_C\right), \tag{2.45}$$

$$\left|3,1,\pm\tilde{1}\right\rangle_L = \frac{1}{\sqrt{2}}\left(|3,1,1\rangle_C \mp |3,1,-1\rangle_C\right), \tag{2.46}$$

$$\left|3,-1,\pm\tilde{1}\right\rangle_L = \frac{1}{\sqrt{2}}\left(|3,-1,1\rangle_C \mp |3,-1,-1\rangle_C\right). \tag{2.47}$$

The tilde notation is used as the quantum number m_l is no longer valid for these $|n,k,m_l\rangle_L$ states, even in the limit $\gamma/\epsilon \to 0$, but the value is kept for identification purposes. For all of these states $\langle L_z\rangle = 0$ when $\gamma \ll \epsilon$, hence the σ transitions are drastically different from the $\Delta m = \pm 1$ pure Stark $\sigma^{\pm}$ transitions. This difference between the $|n,k,m_l\rangle_C$ and $|n,k,m_l\rangle_L$ polarisation structures is illustrated in Fig. 2.3. The σ dipole vectors now oscillate linearly along the $\mathbf{B}$ and $\mathbf{E}\times\mathbf{B}$ directions and are referred to as σ^B and σ^v respectively. This polarisation structure is illustrated in the right of Fig. 2.3) where the differences between the pure Stark σ polarisation structure are evident.

$\|n,l,m_l\rangle \setminus \|n,k,m_l\rangle_L$	$\|2,1,0\rangle_L$	$\|2,-1,0\rangle_L$	$\left\|2,0,\tilde{1}\right\rangle_L$	$\left\|2,0,-\tilde{1}\right\rangle_L$
$\|2,0,0\rangle$	$\frac{\epsilon}{\sqrt{2}q_0}$	$\frac{\epsilon}{\sqrt{2}q_0}$	0	$\frac{\gamma}{q_0}$
$\|2,1,0\rangle$	$\frac{-1}{\sqrt{2}}$	$\frac{1}{\sqrt{2}}$	0	0
$\|2,1,1\rangle$	$\frac{-\gamma}{2q_0}$	$\frac{-\gamma}{2q_0}$	$\frac{1}{\sqrt{2}}$	$\frac{\epsilon}{\sqrt{2}q_0}$
$\|2,1,-1\rangle$	$\frac{-\gamma}{2q_0}$	$\frac{-\gamma}{2q_0}$	$\frac{-1}{\sqrt{2}}$	$\frac{\epsilon}{\sqrt{2}q_0}$

Table 2.7: 'Linear' Stark-Zeeman n=2 states that differ from the 'circular' Stark-Zeeman states in Table. 2.5. The tilde notation is used to indicate where the m_l quantum number is incorrect in the limit $\gamma/\epsilon \to 0$. This table is equivalent to Table III in Ref. [32] after rotating for the different choice of coordinate systems. For example $\left|2,0,\tilde{1}\right\rangle_L \equiv |n=2,l=1,m_{l_x}=0\rangle$ where the x subscript indicates the orbital angular momentum projection is now in the x direction as opposed to the usual z direction.

A quantitative summary of the rate coefficient, transition type and energy of each $|n,k,m_l\rangle_L$ transition is given in Table. 2.8. The dipole vector and dimensionless Stokes vectors for the σ^v and σ^B transitions are ($\gamma \ll \epsilon$):

$$\hat{\mathbf{r}}_{\sigma^{\mathbf{B}}} = (1,\ 0,\ 0), \tag{2.48}$$

$$\bar{\mathbf{s}}_{\sigma^B} = (\sin^2\varphi + \cos^2\psi\cos^2\varphi,\ \sin^2\varphi - \cos^2\psi\cos^2\varphi,\ \cos\psi\sin 2\varphi,\ 0), \tag{2.49}$$

$$\hat{\mathbf{r}}_{\sigma^{\mathbf{v}}} = (0,\ 1,\ 0) \tag{2.50}$$

$$\bar{\mathbf{s}}_{\sigma^v} = (\cos^2\varphi + \cos^2\psi\sin^2\varphi,\ \cos^2\varphi - \cos^2\psi\sin^2\varphi,\ -\cos\psi\sin 2\varphi,\ 0). \tag{2.51}$$

These Stokes vectors now contain a nonzero s_2 component. Therefore the individual σ^B and σ^v polarisation orientations are dependent on the viewing direction and no longer perpendicular to $\mathbf{E}$. This σ^B and σ^v polarisation structure is different to the pure Stark effect in Sec. 2.4 where an unequal rate of $\sigma^{\pm}$ emissions produces a net s_3 component instead without affecting the polarisation orientation. *Only when σ^B and σ^v have the same emission rate will the linear polarisation be perpendicular to* $\mathbf{E}$, in which case their

Stokes vectors sum to the same result as that in Eq. 2.28. This phenomenon also has a dependence on viewing angle such that there is no contaminating s_2 component when viewing at $\psi = \pi/2$ (perpendicular to $\mathbf{E}$) or $\varphi = n\pi/2$.

$\lvert n,k,m_l\rangle_L$	$\lvert 2,1,0\rangle_L$	$\lvert 2,-1,0\rangle_L$	$\lvert 2,0,\tilde{1}\rangle_L$	$\lvert 2,0,-\tilde{1}\rangle_L$
$\lvert 3,2,0\rangle_L$	$(1681)\pi_4$	$(1)\pi_8$	$(18)\sigma_6^B$	$(18)\sigma_6^v$
$\lvert 3,-2,0\rangle_L$	$(1)\pi_{-8}$	$(1681)\pi_{-4}$	$(18)\sigma_{-6}^B$	$(18)\sigma_{-6}^v$
$\lvert 3,0,0\rangle_L$	$(729)\pi_{-2}$	$(729)\pi_2$	$(882)\sigma_0^B$	$(882)\sigma_0^v$
$\lvert 3,0,\tilde{2}\rangle_L$	$(0)\sigma_{-2}^v$	$(0)\sigma_2^v$	$(2304)\sigma_0^B$	$(2304)\sigma_0^v$
$\lvert 3,0,-\tilde{2}\rangle_L$	$(0)\sigma_{-2}^B$	$(0)\sigma_2^B$	$(2304)\sigma_0^v$	$(2304)\sigma_0^B$
$\lvert 3,1,\tilde{1}\rangle_L$	$(\mathbf{1936})\sigma_{\mathbf{1}}^{\mathbf{B}}$	$(16)\sigma_5^B$	$(1152)\pi_3$	$(0)\sigma_3^B$
$\lvert 3,1,-\tilde{1}\rangle_L$	$(\mathbf{1936})\sigma_{\mathbf{1}}^{\mathbf{v}}$	$(16)\sigma_5^v$	$(0)\sigma_3^B$	$(1152)\pi_3$
$\lvert 3,-1,\tilde{1}\rangle_L$	$(16)\sigma_{-5}^B$	$(\mathbf{1936})\sigma_{\mathbf{-1}}^{\mathbf{B}}$	$(1152)\pi_{-3}$	$(0)\sigma_{-3}^B$
$\lvert 3,-1,-\tilde{1}\rangle_L$	$(16)\sigma_{-5}^v$	$(\mathbf{1936})\sigma_{\mathbf{-1}}^{\mathbf{v}}$	$(0)\sigma_{-3}^B$	$(1152)\pi_{-3}$

Table 2.8: Transitions between n=3 and n=2 states for the combined Stark-Zeeman effect with the $\lvert n,k,m_l\rangle_L$ states in the limit $\gamma/\epsilon \to 0$. The notation is similar to that in Table 2.4. Bold font is used to indicate the strong transitions where σ^v and σ^B pairs derive from different upper-states resulting in an upper-state population dependent polarisation orientation.

After transforming coordinate systems only the $\lvert 3,0,m_l\rangle_L$ states differ from those in Tables I and II of Ref. [32] which have been arbitrarily orthogonalised without consideration of further interactions. The table of transition from the states in Ref. [32] are calculated and shown in Table 2.9. The finding in Ref. [31] that the σ_0^v and σ_0^B emissions have unequal rates from the same upper-state is thought to be invalid, as seen by comparing with the physically relevant $\lvert n,k,m_l\rangle_L$ states formulated here in Table 2.8. Additionally the suggestion in Ref. [31] that the σ^v polarisation structure approaches the pure Stark σ structure as $\gamma/\epsilon \to 0$ is incorrect.

$\lvert n,k,m_l\rangle$	Tbl.III 2^{nd}	Tbl.III 3^{rd}	Tbl.III 4^{th}	Tbl.III 1^{st}
Tbl.I 1^{st}	$(1681)\pi_4$	$(1)\pi_8$	$(18)\sigma_6^B$	$(18)\sigma_6^v$
Tbl.I 2^{nd}	$(1)\pi_{-8}$	$(1681)\pi_{-4}$	$(18)\sigma_{-6}^B$	$(18)\sigma_{-6}^v$
Tbl.I 5^{th}	$(486)\pi_{-2}$	$(486)\pi_2$	$(\mathbf{12})\sigma_{\mathbf{0}}^{\mathbf{B}}$	$(\mathbf{2700})\sigma_{\mathbf{0}}^{\mathbf{v}}$
Tbl.I 6^{th}	$(243)\pi_{-2}$	$(243)\pi_2$	$(\mathbf{3174})\sigma_{\mathbf{0}}^{\mathbf{B}}$	$(\mathbf{486})\sigma_{\mathbf{0}}^{\mathbf{v}}$
Tbl.II 1^{st}	-	-	$(2304)\sigma_0^v$	$(2304)\sigma_0^B$
Tbl.II 2^{nd}	$(1936)\sigma_1^B$	$(16)\sigma_5^B$	$(1152)\pi_3$	-
Tbl.I 3^{rd}	$(1936)\sigma_1^v$	$(16)\sigma_5^v$	-	$(1152)\pi_3$
Tbl.II 3^{rd}	$(16)\sigma_{-5}^B$	$(1936)\sigma_{-1}^B$	$(1152)\pi_{-3}$	-
Tbl.I 4^{th}	$(16)\sigma_{-5}^v$	$(1936)\sigma_{-1}^v$	-	$(1152)\pi_{-3}$

Table 2.9: Transitions between the Stark-Zeeman states given in Ref. [32]. The ordering of states is similar to that in Tables 2.4 and 2.8. The difference is only observable if the upper-states are unequally populated.

The net linear polarisation orientation of a particular σ line can be calculated using Eqs. 2.49 and 2.51. If the σ^B emission has transition rate A_B deriving from an upper-state with population N_B and the σ^v emission has transition rate A_v deriving from an upper-state with population N_v then the net polarisation orientation is given by (calculated from

Eqs. 2.49 and 2.51 using an atan2 function):

$$\theta_\sigma = \arctan\left(\frac{y}{\sqrt{x^2+y^2}+x}\right) \tag{2.52}$$

$$\begin{aligned} \text{where} \quad y &= 2\delta\cos\psi\sin 2\varphi, \\ x &= \sin^2\psi - \delta\cos 2\varphi(1+\cos^2\psi) \end{aligned}$$

$$\text{and} \quad \delta = \frac{N_B A_B - N_v A_v}{N_B A_B + N_v A_v}. \tag{2.53}$$

Now if a pairing of σ^B and σ^v emissions have the same transition rate and derive from the same upper-state or upper-states with equal populations, then $N_B A_B = N_v A_v$ implying $\theta_\sigma = 0$ (i.e. perpendicular to $\mathbf{E}_L$ as expected). From Table 2.8 it is seen that the σ^B and σ^v pairs for the σ_6, σ_{-6} and σ_0 lines derive from the same upper-states and have equal transition rates from those particular upper-states. Hence their polarisation orientation is independent of the upper-state populations. On the other hand, as highlighted in Table 2.8, the σ_1^B and σ_1^v pair derive from different upper-levels, namely $\left|3,1,\tilde{1}\right\rangle_L$ and $\left|3,1,-\tilde{1}\right\rangle_L$. Therefore $\delta \neq 0$ when $N_{\left|3,1,\tilde{1}\right\rangle_L} \neq N_{\left|3,1,-\tilde{1}\right\rangle_L}$, implying the σ_1 polarisation orientation is not guaranteed to be perpendicular to $\mathbf{E}_L$. Similarly the σ_{-1} polarisation orientation is dependent on the relative population of $N_{\left|3,-1,\tilde{1}\right\rangle_L}$ and $N_{\left|3,-1,-\tilde{1}\right\rangle_L}$. Example calculations for the $\sigma_{\pm 1}$ polarisation orientation for a beam-into-gas calibration are presented in the next section.

2.5.4 Relative Upper-State Populations

In the limit that $\gamma = 0$ the probability densities for the Stark-Zeeman states can be expressed in spherical coordinates (r, ψ, φ) as,

$$\left|\,|n,k,m_l\rangle_C\,\right|^2 = f_{n,k,|m_l|}(r,\psi), \tag{2.54}$$

$$\left|\,|n,k,\tilde{m}_l\rangle_L\,\right|^2 = \begin{cases} 2\cos^2(m_l\varphi) f_{n,k,|m_l|}(r,\psi) & |m_l| > 0 \\ 2\sin^2(m_l\varphi) f_{n,k,|m_l|}(r,\psi) & |m_l| < 0. \end{cases} \tag{2.55}$$

The probability densities for the 'circular' states are independent of φ and are therefore symmetric about the electric field axis. On the other hand the probability densities for the degenerate pairs of 'linear' states have a significant dependence on φ. This asymmetry can be seen in Fig. 2.6 for the $|3,1,\pm\tilde{1}\rangle_L$ pair which compares to the axially symmetric case earlier in Fig. 2.4.

For these degenerate states the ground state proton impact excitation cross sections

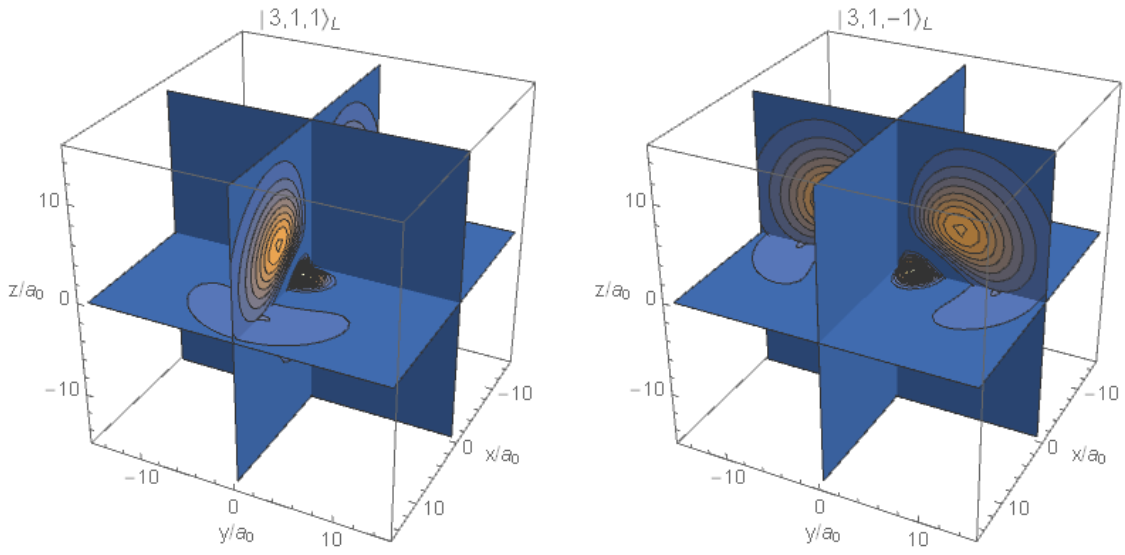

Figure 2.6: 3D probability distributions of the $|3,1,\pm\tilde{1}\rangle_L$ states visualised with the 2D cross sections.

when $\gamma/\epsilon \to 0$ are now:

$$\sigma_{|2,0,\tilde{1}\rangle_L} = \cos^2\rho\ \sigma_{2p_0} + \sin^2\ \rho\sigma_{2p_1}, \tag{2.56}$$

$$\sigma_{|2,0,-\tilde{1}\rangle_L} = \sin^2\rho\ \sigma_{2p_0} + \cos^2\rho\ \sigma_{2p_1}, \tag{2.57}$$

$$\sigma_{|3,0,\tilde{2}\rangle_L} = \frac{1}{4}\sin^2 2\rho\,(3\sigma_{3d_0} + \sigma_{3d_2}) + \cos^2 2\rho\ \sigma_{3d_1}, \tag{2.58}$$

$$\sigma_{|3,0,-\tilde{2}\rangle_L} = \frac{1}{4}\cos^2 2\rho\,(3\sigma_{3d_0} + \sigma_{3d_2}) + \sin^2 2\rho\ \sigma_{3d_1}, \tag{2.59}$$

$$\sigma_{|3,\pm1,\tilde{1}\rangle_L} = \frac{1}{2}\cos^2\rho\,(\sigma_{3p_0} + \sigma_{3d_1}) + \frac{1}{2}\sin^2\rho\ \ (\sigma_{3p_1} + \sigma_{3d_2}), \tag{2.60}$$

$$\sigma_{|3,\pm1,-\tilde{1}\rangle_L} = \frac{1}{2}\sin^2\rho\,(\sigma_{3p_0} + \sigma_{3d_1}) + \frac{1}{2}\cos^2\rho\ \ (\sigma_{3p_1} + \sigma_{3d_2}), \tag{2.61}$$

where ρ is the angle between the beam velocity and magnetic field. *In general the cross sections for the degenerate pairs are not equal*, unlike those in Sec. 2.4.1. Hence it can be expected that these states can have different populations, particularly when gas or plasma densities are low. However there is a dependence on the injection angle of the neutral beam relative to **B** that must be considered. In particular if $\rho = 45°$ the cross section for the $|3,1,\pm\tilde{1}\rangle_L$ pair are equal, indicating equal populations and in turn a σ_1 emission that is orthogonal to π as desired. On the other hand, for a radially injected beam ($\rho = 90°$), the differences in the cross sections are the most pronounced, potentially producing unequal populations and a σ_1 polarisation non-orthogonal to the π. A similar argument is true for the $|3,-1,\pm\tilde{1}\rangle_L$ pair and the σ_{-1} emission.

An example of the deviation in the $\sigma_{\pm1}$ polarisation orientation from orthogonality with **E** for the KSTAR imaging MSE view (Fig. 1.3) is shown in Fig. 2.7. The cross sections in Eqs. 2.60 and 2.61 for a 40keV/u neutral beam can be estimated from plots in Ref. [29] to be $\sigma_{3p_0} = 0.058\pi a_0^2$, $\sigma_{3p_1} = 0.038\pi a_0^2$, $\sigma_{3d_1} = 0.010\pi a_0^2$ and $\sigma_{3d_2} = 0.002\pi a_0^2$. To estimate the population factor δ and the θ_σ deviation in the low density limit it is naively assumed that this is the only excitation pathway. The actual value of δ is expected to be closer to

zero when further excitation pathways are considered and as statistical populations are approached, more so for beam-into-plasma shots. The deviation is less than 0.2° near the midplane and only approaches 1° in the lower left edge of the image where $\varphi \approx 25°$, $\psi \approx 105°$ and $\varphi \approx -8°$. It should be noted the port is 28.5cm above the midplane and that a midplane view would give greater reduction by more closely matching $\psi = \pi/2$ in the centre of the image. The deviation would be further reduced by 60% when including the upper-state population independent σ_0 signal in the measurement or by 80% for an imaging MSE measurement that effectively averages over the full spectrum. *Hence the BIG deviation, even in this worst case scenario, is expected on the midplane to remain under* 0.1°*, the accuracy often targeted for polarimetric MSE measurements and under* 0.2° *in the extremity of the image.*

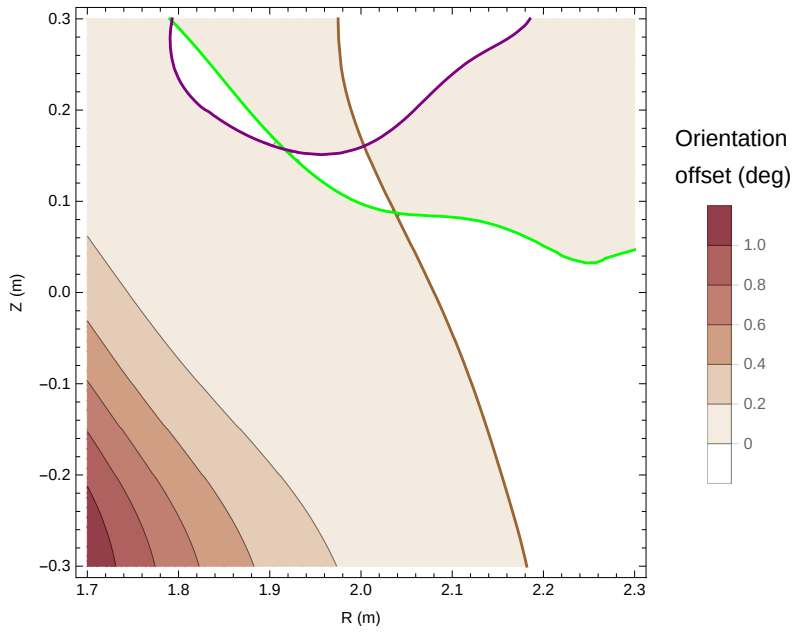

Figure 2.7: Example $\sigma_{\pm 1}$ polarisation orientation deviation from being orthogonal to **E** using for the KSTAR IMSE view. There are three contours where this upper-state population dependence vanishes; $\rho = 45°$ in brown, $\psi = \pi/2$ in green and $\varphi = 0$ in purple.

The results are similar for other MSE systems having sightlines tangent to the flux surfaces. An example was given in Ref. [45] for the primary DIII-D MSE system channel at $R = 1.78$m[49]. It should be noted that the precise values of ψ and φ depend on the equilibrium magnetic field but this channel is near the magnetic axis such that the magnetic field will usually have a dominant component in the negative toroidal direction. In this case $\psi = 93.0°$ as the port is slightly below the midplane, $\varphi = -174.2°$ and the 40keV/u beam is injected at angle $\rho = 49.6°$. Again assuming ground state proton impact is the only excitation pathway, an estimate for the population factor of $\delta = -0.041$ is obtained in the low density limit. From Eq. 2.52 this corresponds to a deviation of only $\theta_{\sigma_{\pm 1}} = 0.024°$.

$\sigma_{\pm 1} : \pi_{\pm 3}$ Intensity Ratio

The ground state cross sections for the degenerate $|n, k, m_l\rangle_L$ pairs sum to the same value as the pure Stark effect cross sections pairs, suggesting there will be little difference between the spectra. However the different angular intensity distributions of the σ^B and

σ^v emissions, evident in Eq. 2.49 and 2.51, must be considered. It can be shown that the intensity of an emission line composed of σ^B and σ^v polarised components is

$$I_\sigma \propto 1 + \cos^2\psi - \delta\cos 2\varphi \sin^2\psi. \tag{2.62}$$

As an example when viewing in the direction of the magnetic field the σ^B emission has zero intensity while σ^v is bright. Thus the detector would only see a bright π_3 emission from the $|3,1,\tilde{1}\rangle_L$ state but would see both π_3 and σ_1 from the $|3,1,-\tilde{1}\rangle_L$ state, implying a $\pi_3 : \sigma_1$ intensity ratio dependent on the relative populations of $|3,1,\pm\tilde{1}\rangle_L$. This effect has the potential to alter the s_0 spectrum for beam-into-gas calibrations even when $\gamma \ll \epsilon$. A similar effect would also occur for the $\pi_{-3} : \sigma_{-1}$ intensity ratio from the $|3,-1,\pm\tilde{1}\rangle_L$ states. This result differs to that in Ref. [42] where it is suggested that the $\sigma_{\pm1} : \pi_{\pm3}$ intensity ratio is independent of upper-state populations. The results here imply that *the polarisation orientation BIG calibration is more reliable than an intensity ratio measurement* when operating near $\psi = \pi/2$ due to upper-state population effects.

2.5.5 Inclusion of the Fine Structure

So far the physical relevance of the $|n,k,m_l\rangle_C$ and $|n,k,m_l\rangle_L$ states has been hinted at without going into detail. The physical relevance is only revealed when further weaker interactions that break the degeneracy and determine the system are considered. In the next two sections the competing influence of the fine-structure and microscopic electric fields is described. The $|n,k,m_l\rangle_L$ states do not approach the pure Stark effect states as the Zeeman effect vanishes. In reality this discontinuity will not exist as other weaker interactions contribute to break the degeneracy. Here the largest fixed interaction, the fine structure of the atom, is considered. Opposite spin states can now mix when the fine structure is considered, therefore the electron spin must also be included and the full Hamiltonian outlined in Sec. 2.2 is used.

Including the fine structure leads to unwieldy solutions but similarities exist with the analytic Stark-Zeeman solutions. For standard magnetic field strengths and neutral beam velocities encountered in fusion devices, the fine structure breaks the remaining degeneracy to produce *Stark-Zeeman-fine structure states that are similar to the* $|n,k,m_l\rangle_L$ *states* and reduce to them when the Stark and Zeeman effect dominate the fine structure (i.e. when $n^2\epsilon$ and $n\gamma \gg E_1\alpha^2/n^2$ where α is the fine structure constant). The transitions for the Stark-Zeeman-fine structure Hamiltonian are given in Table 2.10. After partitioning the table 2×2 the result is very similar to that of the $|n,k,m_l\rangle_L$ transitions presented in Table 2.8.

$\lvert 3,k,m_l,m_s\rangle$	$\lvert 2,k,m_l,m_s\rangle$ $\delta E(\mu\text{eV})$	$\lvert 2,1,0,+\rangle$ 886.3	$\lvert 2,1,0,-\rangle$ 650.0	$\lvert 2,-1,0,+\rangle$ -659	$\lvert 2,-1,0,-\rangle$ -886.2	$\lvert 2,0,\tilde{1},+\rangle$ 127.1	$\lvert 2,0,\tilde{1},-\rangle$ -106.2	$\lvert 2,0,-\tilde{1},+\rangle$ 126.6	$\lvert 2,0,-\tilde{1},-\rangle$ -106.9
$\lvert 3,2,0,+\rangle$	2415.7	$(1690)\pi_4$	-	$(1)\pi_8$	-	$(18)\sigma_6^B$	-	$(16)\sigma_6^v$	-
$\lvert 3,2,0,-\rangle$	2182.8	-	$(1692)\pi_4$	-	-	$(1)\pi_{6^-}$	$(18)\sigma_6^B$	-	$(17)\sigma_6^v$
$\lvert 3,-2,0,+\rangle$	-2176.0	$(2)\pi_{-8}$	-	$(1679)\pi_{-4}$	-	$(17)\sigma_{-6}^B$	$(1)\pi_{-6^+}$	$(16)\sigma_{-6}^v$	-
$\lvert 3,-2,0,-\rangle$	-2406.7	-	$(2)\pi_{-8}$	-	$(1682)\pi_{-4}$	-	$(17)\sigma_{-6}^B$	-	$(17)\sigma_{-6}^v$
$\lvert 3,0,0,+\rangle$	123.4	$(733)\pi_{-2}$	-	$(719)\pi_2$	-	$(865)\sigma_0^B$	$(4)\sigma_{0^+}^v$	$(893)\sigma_0^v$	$(4)\sigma_{0^+}^B$
$\lvert 3,0,0,-\rangle$	-108.4	-	$(733)\pi_{-2}$	-	$(718)\pi_2$	$(4)\sigma_{0^-}^v$	$(863)\sigma_0^B$	$(4)\sigma_{0^-}^B$	$(892)\sigma_0^v$
$\lvert 3,0,\tilde{2},+\rangle$	128.2	$(9)\sigma_{-2}^v$	$(1)\sigma_{-2^+}^B$	$(8)\sigma_2^v$	-	$(2307)\sigma_0^B$	$(7)\sigma_{0^+}^v$	$(2237)\sigma_0^v$	$(7)\sigma_{0^+}^B$
$\lvert 3,0,\tilde{2},-\rangle$	-103.6	-	$(3)\sigma_{-2}^v$	$(1)\sigma_{2^-}^B$	$(2)\sigma_2^v$	$(7)\sigma_{0^-}^v$	$(2309)\sigma_0^B$	$(7)\sigma_{0^-}^B$	$(2248)\sigma_0^v$
$\lvert 3,0,-\tilde{2},+\rangle$	128.2	$(9)\sigma_{-2}^B$	$(1)\sigma_{-2^+}^v$	$(8)\sigma_2^B$	-	$(2272)\sigma_0^v$	$(7)\sigma_{0^+}^B$	$(2273)\sigma_0^B$	$(7)\sigma_{0^+}^v$
$\lvert 3,0,-\tilde{2},-\rangle$	-103.6	-	$(3)\sigma_{-2}^B$	$(1)\sigma_{2^-}^v$	$(2)\sigma_2^B$	$(7)\sigma_{0^-}^B$	$(2272)\sigma_0^v$	$(7)\sigma_{0^-}^v$	$(2285)\sigma_0^B$
$\lvert 3,1,\tilde{1},+\rangle$	1272.5	$(1941)\sigma_1^B$	-	$(14)\sigma_5^B$	-	$(1152)\pi_3$	-	$(2)\sigma_3^B$	$(3)\pi_{3^+}$
$\lvert 3,1,\tilde{1},-\rangle$	1040.4	-	$(1942)\sigma_1^B$	$(1)\pi_{5^-}$	$(13)\sigma_5^B$	$(1)\sigma_{3^-}^B$	$(1152)\pi_3$	$(3)\pi_{3^-}$	-
$\lvert 3,1,-\tilde{1},+\rangle$	1272.0	$(1929)\sigma_1^v$	-	$(13)\sigma_5^v$	-	$(1)\sigma_3^B$	$(3)\pi_{3^+}$	$(1140)\pi_3$	-
$\lvert 3,1,-\tilde{1},-\rangle$	1040.7	-	$(1927)\sigma_1^v$	-	$(13)\sigma_5^v$	$(3)\pi_{3^-}$	$(1)\sigma_3^B$	-	$(1146)\pi_3$
$\lvert 3,-1,\tilde{1},+\rangle$	-1023.0	$(18)\sigma_{-5}^B$	$(1)\pi_{-5^+}$	$(1934)\sigma_{-1}^B$	-	$(1145)\pi_{-3}$	$(1)\sigma_{-3^+}^B$	$(1)\sigma_{-3}^B$	$(3)\pi_{-3^+}$
$\lvert 3,-1,\tilde{1},-\rangle$	-1254.7	-	$(18)\sigma_{-5}^B$	-	$(1936)\sigma_{-1}^B$	-	$(1144)\pi_{-3}$	$(3)\pi_{-3^-}$	-
$\lvert 3,-1,-\tilde{1},+\rangle$	-1022.8	$(17)\sigma_{-5}^v$	-	$(1922)\sigma_{-1}^v$	-	$(1)\sigma_{-3}^B$	$(3)\pi_{-3^+}$	$(1134)\pi_{-3}$	-
$\lvert 3,-1,-\tilde{1},-\rangle$	-1255.2	-	$(18)\sigma_{-5}^v$	-	$(1920)\sigma_{-1}^v$	$(3)\pi_{-3^-}$	$(1)\sigma_{-3}^B$	-	$(1139)\pi_{-3}$

Table 2.10: Transition structure of the Stark-Zeeman effect when including the fine structure for an 80keV deuterium beam injected at 60° to a 2T magnetic field. The ordering of the states is similar to Tables 2.4 and 2.8 but now with pairs of opposite spin states, m_s, denoted with + and - signs. The populations $N_{3,j}$ are split between two states, hence the sum of the transition probabilities has now roughly doubled relative to that in Table 2.8. Weak transitions between opposite spin states, now possible due to the fine structure interaction, have energies offset by $\approx g_s\gamma$ from the standard value that is indicated with a plus or minus after the energy value. Intensities have been rounded to the nearest integer. The ellipticity angle of each transition is not captured in this table.

Now that the fine structure has been considered it is appropriate to comment on other similar models. The fine-structure and non-zero γ/ϵ effects included in Table 2.10 lead to some minor differences with the Stark-Zeeman results shown earlier. For example the σ_0^B and σ_0^v emission from individual upper-levels have slightly different transition probabilities. As a result the linear polarisation angle of the σ_0 emission can only marginally deviate from the pure Stark effect case. The summed transition probability of σ_0^B is 0.8% greater than σ_0^v with the greatest deviation from an individual state being 3%. For typical MSE viewing geometries with $\psi \approx \pi/2$ this effect is negligible ($\ll 0.1\circ$) and can be calculated from Eq. 2.52. This contradicts the data presented in Figure 13 of Ref. [30] that indicates that the σ_0 polarisation can deviate by several degrees. A recent 'bug' fix made in 2015 to the 'Flexible Atomic Code'[50] has been tested and it was found that the more straightforward result in Figure 1 of Ref. [30] changes before and after the fix was made. This 'bug' has possibly contributed to the predicted σ_0 deviation that disagrees with the result that is presented here. The diamagnetic Zeeman effect included in Ref. [30] has been tested in calculations here and found to have a negligible effect on the results, in agreement with the assessment in Ref. [44].

In Ref. [51] the Stark-Zeeman-fine structure states are derived and are therefore expected to be similar to $|n,k,m\rangle_L$. However the state populations are determined assuming the states are similar to the parabolic states. It is evident from the differences between Eqs. 2.29-2.34 and 2.56-2.61 that this will force equal emission rates of $\sigma_{\pm1}^B : \sigma_{\pm1}^v$ when this is not necessarily the case.

Table 2.10 indicates that the $\sigma_{\pm1} : \pi_{\pm_3}$ emission rate is approximately independent of upper-state populations as pairs of $\sigma_{\pm1}$ and $\pi_{\pm_3}$ emission derive from the same upper-states with transition probability in ratio. This contradicts Table 1 in Ref. [43] that suggests there are n=3 levels emitting only $\pi_{\pm3}$ without any $\sigma_{\pm1}$. The cause of this disagreement is unknown but the method used here is thought to be effectively the same as that used in Ref. [43]. Possibly that model has not taken into account the angular intensity distribution effects by only considering a viewing direction along the y-axis ($\mathbf{E}\times\mathbf{B}$ axis), in which case the $\sigma_{\pm1}^v$ has zero intensity from the $|3,\pm1,-1\rangle_L$ states leaving only a bright $\pi_{\pm3}$ emission. Regardless, the $\sigma_{\pm1}^B$ and $\sigma_{\pm1}^v$ emissions have a viewing angle dependence that could introduce an intensity dependence on upper-state populations, as reasoned in Sec. 2.5.4 and Eq. 2.62. This effect has likely been miscalculated in Ref. [30] due to the previously discussed 'bug'.

2.5.6 Microscopic Electric Fields

Fluctuating microscopic electric fields within the plasma that have a component parallel to the magnetic field will superpose with the motional electric field such that $\tau \neq 0$. This will instead *break the degeneracy in favour of the 'circular' Stark-Zeeman states*, as discussed in Sec. 2.5.2, instead of the 'linear' Stark-Zeeman states favoured by the fine structure. Here the crossover point between these two degeneracy splitting mechanisms is discussed. The Holtsmark field strength $|\mathbf{E_0}| = 2.6en_e^{2/3}/(4\pi\epsilon_0)$ provides a characteristic strength for microscopic field distribution in a plasma of electron density n_e[52]. Requiring the component of the microscopic field to be parallel to the magnetic field results in an average reduction of 1/2. Thus $|\mathbf{E_0}|/2 = 40\text{kV m}^{-1}$ for a $n_e = 10^{20}\text{m}^{-3}$ plasma which compares with the example motional electric field of 4.8MV m^{-1} produced by injecting an 80keV deuterium beam at 60° to a 2T field.

The $|3,\pm1,\pm1\rangle_L$ Stark-Zeeman states are of critical importance for the σ polarisation

orientation as they produce individual $\sigma^B_{\pm1}$ or $\sigma^v_{\pm1}$ emissions. From Table 2.10 we see the fine-structure splits the Stark-Zeeman degenerate $\left|3,1,\pm\tilde{1},+\right\rangle$ levels by 0.5μeV. A parallel microscopic electric field becomes the dominant degeneracy splitting mechanism for strengths above 10kV m^{-1} as seen in the left of Fig. 2.8. The similarity of the states to the $|n,k,\tilde{m}\rangle_L$ and $|n,k,m\rangle_C$ bases is best visualised from $\langle L_z\rangle/\hbar$ plotted in the right of Fig. 2.8. Over the range of $1-50\text{kV m}^{-1}$ the states transform from being similar to the $|3,1,\pm1\rangle_L$ states to being similar to the $|3,1,\pm1\rangle_C$ states. Therefore with increasing microscopic field the polarisation structure transforms from the upper-state population dependent σ^B_1 and σ^v_1 emission to the 'robust' σ^+_1 and σ^-_1 emission. For intermediate values of $\langle L_z\rangle$ the $\sigma_{\pm1}$ transitions will be elliptical with major-axes aligned along $\mathbf{B}$ and $\mathbf{v}\times\mathbf{B}$.

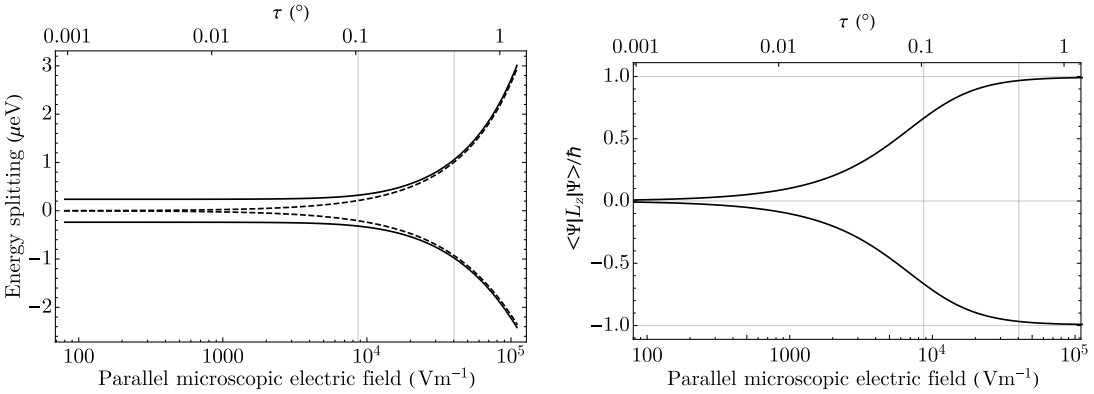

Figure 2.8: (Left) Degeneracy splitting when including an electric field component parallel to the magnetic field ($\tau\neq0$). The dashed lines are the energy of the Stark-Zeeman $|3,1,\pm1\rangle$ levels given in Eq. 2.42. The solid lines are the energy splitting of the Stark-Zeeman-fine-structure $|3,1,\pm\tilde{1},+\rangle$ states. The left and right vertical gridlines indicate 50% of the Holtsmark field strength for plasma densities of 10^{19}m^{-3} and 10^{20}m^{-3} respectively (see text). (Right) Expectation value of angular momentum in the direction of the total electric field for the $|3,1,\pm\tilde{1},+\rangle$ states.

The $\left|3,0,\pm\tilde{2}\right\rangle$ Stark-Zeeman-fine structure states have almost identical energies with 128.2μeV for the spin aligned pair and −103.7μeV for the anti-aligned pair. Therefore a weaker parallel electric field is required to overcome the degeneracy splitting of the fine structure. These states transform from the $\left|3,0,\pm\tilde{2}\right\rangle_L$ structure to the $|3,0,\pm2\rangle_C$ structure over the range $0.1-10\text{V m}^{-1}$. The fine-structure splits the $\left|2,0,\pm\tilde{1}\right\rangle$ levels by about 0.4μeV requiring a parallel microscopic electric field of $1-100\text{kV m}^{-1}$ to transform to the $|2,0,\pm1\rangle_C$ similar states.

Although microscopic electric fields will change the orientation of each emission slightly, the net effect is expected to average to the macroscopic field. Radial electric fields in the plasma are orthogonal to $\mathbf{B}$ and therefore may change the polarisation orientation without affecting the underlying polarisation structure.

2.5.7 Conclusion

Microscopic electric fields are not expected for beam-into-gas shots, hence $|n,k,m_l\rangle_L$ similar states are expected. Hence, as discussed earlier, there is the possibility for the $\sigma_{\pm1}$ polarisation orientation to be non-orthogonal to $\mathbf{E}$ or for the $\sigma_{\pm1}:\pi_{\pm3}$ ratio to change from that expected with equally populated upper-states. However the $\sigma_{\pm1}$ polarisation

orientation is unlikely to deviate significantly because of geometric viewing factors and the beam injection angle dependence.

For high density plasma shots there will be significant microscopic electric fields, hence most of the states will be similar to the parabolic-like $|n,k,m_l\rangle_C$ *states* where many of the results from pure Stark theory remain valid. There will be some remaining $|n,k,m_l\rangle_L$ and intermediate states for atoms where the microscopic electric field is weak or perpendicular to **B**. Calculations of the microscopic electric field distribution are required to ascertain the precise distribution of each type of state.

2.6 Stark-Zeeman Effect with Equal Upper-State Populations

Until this point in the chapter the influence of the relative magnitude of the Zeeman effect has been ignored ($\gamma \ll \epsilon$) and only upper-state population effects resulting from the symmetry breaking of the magnetic field have been considered. The Stark-Zeeman effect also introduces a measurable net circularity for the emission which has both potential deleterious and useful effects that are not well understood. Here a generalised representation of the circular polarisation is presented that allows for straightforward and accurate approximations that are independent of the choice of Stark-Zeeman states when upper-states are equally populated. Results when considering both unequal upper-state populations, fine-structure and the relative magnitude of γ/ϵ are unwieldy. Hence they are not considered in favour of presenting generalised analytic results for the Stark-Zeeman effect in the absence of fine structure.

2.6.1 Stokes Parameters to Second Order in γ/ϵ

Table 2.11 presents coefficients relevant to the Stark-Zeeman transitions that apply in the following approximations of the Stokes vectors. Correct to first order in γ/ϵ the light intensity and linear polarisation intensity of the Stark-Zeeman emission lines is the same as that of the pure Stark effect. This well-known Stark effect result is

$$s_0 = \begin{cases} (Rate)(1+\cos^2\psi) & \text{for } \sigma \\ (Rate)\sin^2\psi & \text{for } \pi \end{cases} \tag{2.63}$$

$$p_l = \sqrt{s_1^2 + s_2^2} = (Rate)\sin^2\psi \tag{2.64}$$

The $(Rate)$ terms are given in Table 2.11 for each of the 15 transition energies. Angles (ψ,φ) were defined in Fig 2.1.

The elliptical transitions created by the Zeeman effect introduce a net circular polarisation and linear polarisation orientation defect. Correct to second order in γ/ϵ the linear polarisation orientation and circular polarisation is,

$$\theta = \frac{1}{2}\arctan\frac{s_2}{s_1} = (Defect)\frac{\sin 2\varphi\cos\psi}{\sin^2\psi} + \begin{cases} 0 & \text{for } \sigma \\ \pi/2 & \text{for } \pi \end{cases} \tag{2.65}$$

$$\begin{aligned} s_3 &= 2(Rate)(Circularity)\sin\psi\cos\varphi \\ &= 2(Rate)(Circularity)(\hat{\mathbf{B}}\cdot\hat{\mathbf{i}}) \end{aligned} \tag{2.66}$$

where $(Defect)$ and $(Circularity)$ are given in Table 2.11. The intensities of the different

Transition	Energy Shift	Rate	Angle Defect	Circularity
σ_0	0	5490	$\frac{197\gamma^2}{1098\epsilon^2}$	0
$\sigma_{\pm1}$	$\pm\left(\frac{q_1}{2}-q_0\right)$	1936	$\frac{5\gamma^2}{33\epsilon^2}$	$\mp\frac{\gamma}{3\epsilon}$
$\pi_{\pm2}$	$\pm q_0$	729	$\frac{289\gamma^2}{13122\epsilon^2}$	$\mp\frac{17\gamma}{81\epsilon}$
$\pi_{\pm3}$	$\pm\frac{q_1}{2}$	2304	$\frac{\gamma^2}{8\epsilon^2}$	$\mp\frac{\gamma}{2\epsilon}$
$\pi_{\pm4}$	$\pm(q_1-q_0)$	1681	$\frac{9409\gamma^2}{30258\epsilon^2}$	$\mp\frac{97\gamma}{123\epsilon}$
$\sigma_{\pm5}$	$\pm\left(\frac{q_1}{2}+q_0\right)$	16	$\frac{\gamma^2}{\epsilon^2}$	$\pm\frac{5\gamma}{3\epsilon}$
$\sigma_{\pm6}$	$\pm q_1$	18	$\frac{25\gamma^2}{18\epsilon^2}$	$\pm\frac{4\gamma}{3\epsilon}$
$\pi_{\pm8}$	$\pm(q_1+q_0)$	1	$\frac{\gamma^2}{18\epsilon^2}$	$\pm\frac{\gamma}{3\epsilon}$

Table 2.11: Stark-Zeeman factors for each transition required in Eqs. 2.63-2.66. The energy shifts are exact. The transition rates are correct to first order in γ/ϵ while the angle defect and circularity are both correct to second order.

transitions can be scaled without affecting these generalised results when the relevant pairings of upper-states that produce each emission line have equal populations. For the pure Stark effect the circularity and angle defect are both zero. Second order changes in the intensity and linear polarisation fraction compensate for the introduced circular polarisation such that $s_0^2 \geq s_1^2 + s_2^2 + s_3^2$ is maintained for each transition. As an example the Stokes vector for each emission line when viewing anti-parallel to the magnetic field are listed in Table 2.12 for $\epsilon/\gamma = 6.6$. The s_3 spectrum has odd symmetry about σ_0 while s_0 and s_1 have even symmetry. The following sections describe the causes and implications of the circular polarisation and the angle defect.

Transition	σ_0	$\sigma_{\pm1}$	$\pi_{\pm2}$	$\pi_{\pm3}$	$\pi_{\pm4}$	$\sigma_{\pm5}$	$\sigma_{\pm6}$	$\pi_{\pm8}$
$s_0(\mathrm{nW\,sr^{-1}})$	14.452	5.141	1.948	6.152	4.555	0.043	0.046	0.003
$s_1(\mathrm{nW\,sr^{-1}})$	14.452	5.115	-1.917	-6.073	-4.427	0.037	0.042	-0.003
$s_3(\mathrm{nW\,sr^{-1}})$	0	$\mp$0.514	$\mp$0.126	$\mp$0.931	$\mp$1.070	$\pm$0.020	$\pm$0.018	$\pm$0.000

Table 2.12: Table of the Stokes spectra for an 80keV deuterium beam velocity injected at 60° to the magnetic field. Upper-states are equally populated with $N_{3,j} = 1$ such that the result is independent of the choice of Stark-Zeeman states. The view direction is parallel to the magnetic field such that $(\psi, \varphi) = (\pi/2, 0)$. The polarimeter axes are aligned such that $s_2 = 0$.

2.6.2 Non-Zero Circular Polarisation Fraction

The Zeeman effect introduces a net circularity to the emission which can be understood by considering the $|n, k, m_l\rangle_C$ states in the limit that $\epsilon/\gamma \to 0$. The pure Zeeman effect transitions in this case are listed in Table 2.13.

Comparing Tables 2.4 and 2.13 we see the Stark π_4 transition (z-axis oscillation) corresponds with a σ^- Zeeman transition (yz-plane circular oscillation). In the intermediate Stark-Zeeman case the dipole vector then has a large real z component and a small imaginary y component, overall resulting in an elliptical dipole vector in the plane perpendicular to magnetic field. Meanwhile the Stark π_{-4} transition corresponds with a σ^+ Zeeman transition resulting in an elliptical dipole vector of opposite handedness. Similarly the π_2 and π_3 Stark transitions correspond with σ^- Zeeman transitions while π_{-2} and π_{-3} Stark

$\lvert n,k,m_l\rangle_C$	$\lvert 2,1,\tilde{0}\rangle_C$	$\lvert 2,-1,\tilde{0}\rangle_C$	$\lvert 2,0,\tilde{1}\rangle_C$	$\lvert 2,0,-\tilde{1}\rangle_C$
$\lvert 3,2,\tilde{0}\rangle_C$	$(4608)\sigma_1^-$	-	-	-
$\lvert 3,-2,\tilde{0}\rangle_C$	-	$(4608)\sigma_{-1}^+$	-	-
$\lvert 3,0,\tilde{0}\rangle_C$	$(882)\sigma_{-1}^+$	$(882)\sigma_1^-$	$(729)\pi_0$	$(729)\pi_0$
$\lvert 3,0,\tilde{2}\rangle_C$	$(18)\sigma_{-1}^+$	$(18)\sigma_1^-$	$(1681)\pi_0$	$(1)\pi_0$
$\lvert 3,0,-\tilde{2}\rangle_C$	$(18)\sigma_{-1}^+$	$(18)\sigma_1^-$	$(1)\pi_0$	$(1681)\pi_0$
$\lvert 3,1,\tilde{1}\rangle_C$	$(1152)\pi_0$	-	$(1936)\sigma_1^-$	$(16)\sigma_1^-$
$\lvert 3,1,-\tilde{1}\rangle_C$	$(1152)\pi_0$	-	$(16)\sigma_1^-$	$(1936)\sigma_1^-$
$\lvert 3,-1,\tilde{1}\rangle_C$	-	$(1152)\pi_0$	$(1936)\sigma_{-1}^+$	$(16)\sigma_{-1}^+$
$\lvert 3,-1,-\tilde{1}\rangle_C$	-	$(1152)\pi_0$	$(16)\sigma_{-1}^+$	$(1936)\sigma_{-1}^+$

Table 2.13: Transitions between n=3 and n=2 states for the pure Zeeman effect with the $\lvert n,k,m_l\rangle_C$ states. The π dipole vector is oriented along the magnetic field (x-axis) and $\sigma^{\pm}$ dipole vectors circle the magnetic field in the yz-plane. The energy splitting is in units of γ.

transitions correspond with σ^+ Zeeman transitions. These elliptical Stark-Zeeman dipole vectors are illustrated in the left of Fig. 2.9.

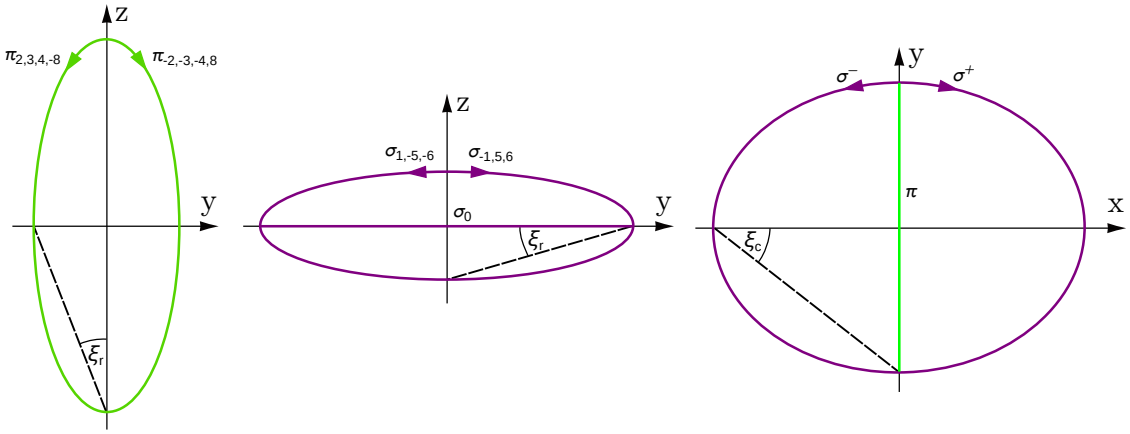

Figure 2.9: Plot of the Stark-Zeeman π (Left) and σ (Middle) dipole vectors in the plane perpendicular to **B**. The $\pi_{\pm 2}$, $\pi_{\pm 4}$ dipole vectors lie purely in the yz plane while the $\pi_{\pm 3}$ has a very small component in the x direction (third order). Note that ξ_r is related to ξ in Fig. 2.2, but is generally different due to projection effects. (Right) Dipole vectors in the plane perpendicular to **E**. For the σ transitions ξ_c is less than 45° when $\gamma/\epsilon > 0$.

The σ_0 and $\sigma_{\pm 1}$ Stark transitions (xy-plane circular oscillation) correspond to π Zeeman transitions (x-axis oscillation). In the $\gamma \ll \epsilon$ regime this leads to the Stark σ transitions that are slightly elliptised (stretched) in the direction of the magnetic field, shown in the right of Fig. 2.9. Additionally in this intermediate regime the $\sigma_{\pm 1}$ dipole vectors acquire a small component in the direction of the electric field as in the middle plot of Fig. 2.9. Both σ_1 transitions acquire the same handedness about **B**, opposite to that of both σ_{-1}. The interpretation for the σ emission is different for the $\lvert n,k,m_l\rangle_C$ and $\lvert n,k,m_l\rangle_L$ states, but the net circularity is the same for the two cases when upper-states are equally populated. The ellipticity angles of the dipole vectors, as defined in Fig. 2.9, are given in Table 2.14. The concept of separate Stark and Zeeman effect linear and circular emissions introduced in Ref. [51] is non-physical as *the Stark and Zeeman effects are coupled and*

gives rise to elliptical dipole transitions.

	$\sigma_{0\ \lvert 3,0,0\rangle_C}$	$\sigma_{0\ \lvert 3,0,\pm 2\rangle_C}$	$\sigma_{\pm 1}$	$\pi_{\pm 2}$	$\pi_{\pm 3}$	$\pi_{\pm 4}$	$\sigma_{\pm 5}$	$\sigma_{\pm 6}$	$\pi_{\pm 8}$
ξ_r	0	0	$\pm\frac{\gamma}{3\epsilon}$	$\pm\frac{17\gamma}{81\epsilon}$	$\pm\frac{\gamma}{2\epsilon}$	$\pm\frac{97\gamma}{123\epsilon}$	$\mp\frac{5\gamma}{3\epsilon}$	$\mp\frac{4\gamma}{3\epsilon}$	$\mp\frac{\gamma}{3\epsilon}$
ξ_c	$\frac{\pi}{4}-\frac{31\gamma^2}{252\epsilon^2}$	$\frac{\pi}{4}-\frac{\gamma^2}{12\epsilon^2}$	$\frac{\pi}{4}-\frac{5\gamma^2}{66\epsilon^2}$	$\frac{\pi}{2}$	$\frac{\pi}{2}-\frac{5\gamma^2}{108\epsilon^2}$	$\frac{\pi}{2}$	$\frac{\pi}{4}-\frac{\gamma^2}{2\epsilon^2}$	$\frac{\pi}{4}-\frac{25\gamma^2}{36\epsilon^2}$	$\frac{\pi}{2}$

Table 2.14: Angles for the elliptical dipole vectors for each transition, as defined in Fig. 2.9. The angles are correct to second order in γ/ϵ

The dipole vector and dimensionless Stokes vector for an elliptical Stark-Zeeman π transition in the yz plane are,

$$\hat{\mathbf{r}}_\pi = (0,\ -i\sin\xi_r,\ \cos\xi_r), \tag{2.67}$$

$$\begin{aligned}\bar{\mathbf{s}}_\pi =& \big(\sin^2\psi\cos^2\xi_r + (\cos^2\varphi+\cos^2\psi\sin^2\varphi)\sin^2\xi_r,\ -\sin^2\psi\cos^2\xi_r \\ &+ (\cos^2\varphi-\cos^2\psi\sin^2\varphi)\sin^2\xi_r,\ -\cos\psi\sin 2\varphi\sin^2\xi_r,\ -\sin\psi\cos\varphi\sin 2\xi_r\big).\end{aligned} \tag{2.68}$$

Expressed relative to the orientation of the magnetic field, the $\bar{s}_3$ component is

$$\left(\bar{\mathbf{s}}_3\right)_\pi = -\hat{\mathbf{B}}\cdot\hat{\mathbf{i}}\sin 2\xi_r. \tag{2.69}$$

Either Eq. 2.66 can be used with the second order circularity approximations in Table 2.11 or the geometric interpretation in Eq. 2.69 can be used with the angles ξ_r in Table 2.14 to get the same result for the π transitions.

The angle ξ_c is also needed for the second order approximation of the σ Stokes vector, leading to a more complicated geometrical interpretation. The dipole vector for the σ transitions is

$$\mathbf{r}_{\sigma^\pm} = (\pm\cos\xi_c\cos\xi_r,\ -i\sin\xi_c\cos\xi_r,\ \sin\xi_c\sin\xi_r) \tag{2.70}$$

and the resulting Stokes vector is unwieldy. Nevertheless the key results are summarised in Eqs. 2.63-2.66 and Table 2.11.

Possible Applications of the Circular Polarisation

An example of the s_3/s_0 circular polarisation fraction expected for the summed π_{2-4} emission is presented in Fig. 2.10 for the KSTAR IMSE viewing geometry and an 80keV deuterium beam. It is evident that the circular polarisation fraction for standard MSE conditions is significant. The majority of the circular polarisation is from the $\sigma_{\pm 1}$, $\pi_{\pm 3}$ and $\pi_{\pm 4}$ lines. A number of potentially useful applications of the circular polarisation are outlined here.

Assuming that the neutral beam velocity is known precisely then the motional electric field is restricted to lie in a 2D plane perpendicular to $\mathbf{v}$, since $\mathbf{E} = \mathbf{v}\times\mathbf{B} = \mathbf{v}\times\mathbf{B}_{\perp\mathbf{v}}$. Therefore measurements relating to the motional electric field are only sensitive to $\mathbf{B}_{\perp\mathbf{v}}$. The orientation of $\mathbf{B}_{\perp\mathbf{v}}$ is typically determined from the polarisation orientation of the MSE emission or alternatively from the intensity ratio of some π and σ transitions (assuming equally populated upper-state populations). The magnitude of $\mathbf{B}_{\perp\mathbf{v}}$ can also be determined spectroscopically from a measurement of the line-splitting. However when assuming the Zeeman effect is negligible there is no information available about $\mathbf{B}_{\parallel\mathbf{v}}$. That said, for a horizontally injected beam at the midplane it is typically valid to assume $B_r = 0$ in which case B_z and B_ϕ are already know from $\mathbf{B}_{\perp\mathbf{v}}$ and $\mathbf{B}_{\parallel\mathbf{v}}$ is redundant. However

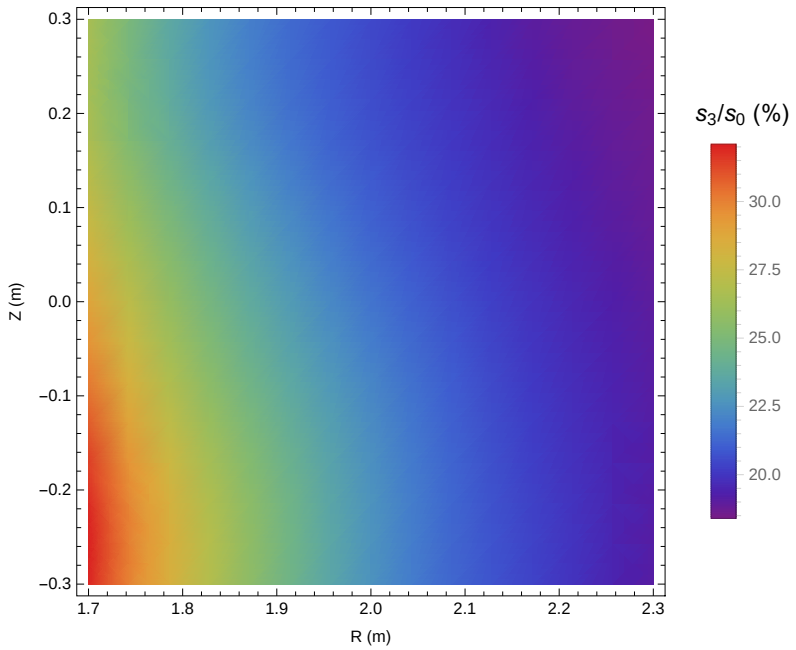

Figure 2.10: Relative fraction of circular to linear polarisation from the π_{2-4} transitions for an 80keV deuterium beam assuming equally populated states.

for an inclined beam injection or measurement away from the midplane $\mathbf{B}_{\|\mathbf{v}}$ may be of interest.

If an individual π line can be isolated then its circular polarisation can be used to complete the measurement of the magnetic field orientation. From Eq. 2.66 the circular polarisation is proportional to

$$\begin{aligned}\hat{\mathbf{B}} \cdot \hat{\mathbf{i}} =& \hat{\mathbf{B}} \cdot \hat{\mathbf{i}}_{\perp\mathbf{v}} + \hat{\mathbf{B}} \cdot \hat{\mathbf{i}}_{\|\mathbf{v}} \\ =& \hat{\mathbf{B}}_{\perp\mathbf{v}} \cdot \hat{\mathbf{i}}_{\perp\mathbf{v}} + \hat{\mathbf{B}}_{\|\mathbf{v}} \cdot \hat{\mathbf{i}}_{\|\mathbf{v}}\end{aligned} \tag{2.71}$$

The remaining unknown $\hat{\mathbf{B}}_{\|\mathbf{v}}$ *is therefore available from the circular polarisation measurement.* Eq. 2.66 is weakly dependent on $\sin\rho$ (ρ is the angle between $\mathbf{v}$ and $\mathbf{B}$) via the γ/ϵ term so the calculation can be iterated to overcome this dependence. The circular polarisation can be normalised to the known linear polarisation fraction to remove any dependence on upper-state populations and unpolarised light. In case that π lines are not individually resolvable an accurate measurement becomes more challenging as it requires knowledge of the relative throughputs and upper-state populations of each of the π components, as each has a different ellipticity, as given in table 2.11. It is likely that the effect of the fine-structure on the circular polarisation may also need to be considered for such a measurement.

A precise measurement of $\mathbf{B}_{\|\mathbf{v}}$ from a single channel from Eq. 2.71 requires the radial electric field E_r to be negligible. In the case where E_r is not negligible assumptions could instead be made that $B_r = 0$ near the midplane. The circular polarisation fraction measurement could then be used to separate out the motional and radial electric field contributions. In either case ($B_r \neq 0$ or $E_r \neq 0$) the circular polarisation carries additional information that is useful as a further constraint, or at the very least can be used as a crosscheck for the polarisation preservation properties of the mirrors in the optical labyrinth.

The circular polarisation fraction also has applications for a polarimetric measurement of the central σ emission. *The s_3 spectrum has odd symmetry about σ_0*, as seen in table 2.12, *which could be used to verify how well the narrowband filter has been tuned.* Conventional MSE polarimeters encode s_3 at different carrier frequencies to the s_1 and s_2, making it possible to use the digitised MSE signal to compare the net linear and circular polarisation lying in the filter passband. An example of such a measurement is shown in Fig. 2.11 for a shot with variable beam voltage that causes the MSE multiplet to 'move' under the filter passband. As expected, the beam voltage that gives the maximum linear polarisation roughly coincides with the zero crossing of the circular polarisation. Notably the narrowband filters for the 1.78m and 1.93m channels appear to be insufficiently blueshifted given they have circular polarisation intensities crossing zero near 77keV and linear polarisation intensities peaking near 79keV. The basic analysis here does not include asymmetries in the filter passband, temporal changes in the emission intensity and temporal changes in the Stark splitting. These effects may lead to the small differences between the beam energies of the circular polarisation zero crossings and linear polarisation maxima. The filter for the 1.63m channel appears to be too blueshifted given the linear polarisation crosses zero much earlier than the other channels and the circular polarisation fraction appears as if it would cross zero at a beam energy of $\approx$ 85keV. Notably there appears to be a temporally varying contamination in the circular polarisation fraction for the 1.63m channel, possibly due to a Zeeman split impurity line in the filter passband.

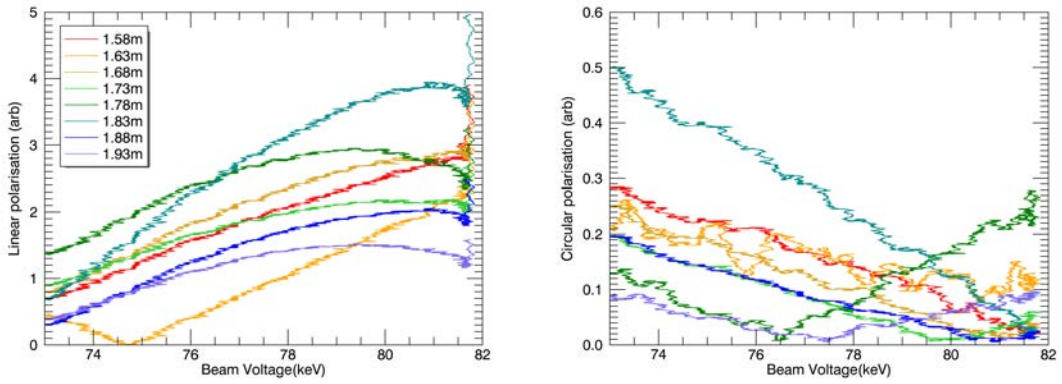

Figure 2.11: Linear (left) and circular (right) polarisation intensity measured from 8 of the tangential conventional MSE channels for shot 166400 from $0.3 - 0.9$s. The beam voltage is initially 82keV and decreases to 73keV in this period. The polarisation intensities have been scaled with the appropriate Bessel functions but the total intensity of the light is not available from the signals so it is not possible to give 'normalised' polarisation fractions. The system is expected to deliver the greatest linear polarisation at 81keV. More details on this shot are given in Section 4.3.6.

In Fig. 2.11 the relative magnitudes of the circular and linear polarisation appear to be consistent with the Stark-Zeeman calculation. For example the 1.83m channel has a maximum linear polarisation of 4 arbitrary units while the circular polarisation is 0.5 arbitrary units near the crossover of the π and σ emissions and it seems plausible that the circular polarisation maximum would peak would peak at approximately 1 arbitrary unit when centred over the π emission, in agreement with the $\sim 25\%$ circular polarisation fraction example in Fig. 2.10.

Detrimental Effects of the Circular Polarisation Fraction

The circular polarisation fraction can also have some detrimental effects on MSE measurements. The circular s_3 Stokes component of the emission can couple to the linear s_1 and s_2 Stokes components at an imperfect mirror[20] or port window with stress induced birefringence. Mirrors are commonly used on MSE diagnostics to reflect light towards the polarimeter and it only requires a small difference in the s and p reflectivity or dephase for the circular polarisation to alter the linear polarisation orientation. It should be noted that with a standard dual PEM polarimeter the s_3 component is modulated at different frequencies to the linear components, independently of any misalignments and only in the presence of a mirror can the measurement be corrupted. Of particular interest to polarisation coherence imaging is that for some polarimeter designs the linear and circular polarisation are carried at the same spatial carrier frequency. Minimising, calibrating for and decoupling the effects of the circular polarisation requires knowledge of the s_3 spectrum.

The coupling of circular to linear polarisation is of particular relevance to any ITER MSE polarimeter where the mirrors will be significantly degraded by plasma exposure such that the s and p reflectivity ratio and dephasing are expected to be far from ideal. While the heating neutral beams on ITER have energies of 1000keV the γ/ϵ ratio only decreases by a factor of 3.5 relative to the example here of 80keV. The π_3 emission will be 5% circularly polarised, assuming a $\rho = 45°$ injection angle to the magnetic field and a $\varphi = 0°$ view parallel to the field. The calibration procedure therefore needs to account for this circular polarisation fraction to avoid similar effects to those observed on DIII-D[20].

2.6.3 Linear Polarisation Orientation of Elliptical Transitions - 'Angle Defect'

The linear polarisation orientation of the Stark-Zeeman emission is slightly different to the pure Stark effect due to the elliptical nature of the dipole vectors. The 'angle defect' is usually negligible compared to the desired 0.1° accuracy of the measurement and has been partially covered in Ref. [53]. Here a simple geometric description of the effect is presented.

A three dimensional elliptical dipole vector projects onto the polarimeter as a two dimensional ellipse. However, the major axis of the projected ellipse is in general different to the direct projection of the 3D elliptical dipole vector's major axis. In other words taking the major axis before or after projecting the dipole vector produces a different result. From Eq. 2.68 it follows that the linear polarisation angle of an elliptical π transition is

$$\theta_\pi = \frac{\pi}{2} + \frac{\sin 2\varphi \cos\psi}{2\sin^2\psi}\xi_r^2 + O(\xi_r^4), \tag{2.72}$$

consistent with Eq. 2.65. This geometric effect does not occur when viewing along one of the $\psi = \pi/2$ or $\varphi = n\pi/2$ planes but increases when looking at an angle to all three of these planes. An example of the average angle defect for the KSTAR viewing geometry is illustrated in Fig. 2.12 where the defect remains under 0.01° across most of the view. In the lower left corner the effect reaches 0.1°, an effect pronounced by the 28.5° elevation of the view above the midplane. Similar results are expected for tangential views on other devices as the sightlines are significantly aligned with the magnetic field $(\psi, \varphi) = (\pi/2, 0)$ such that *the effect is usually negligible.*

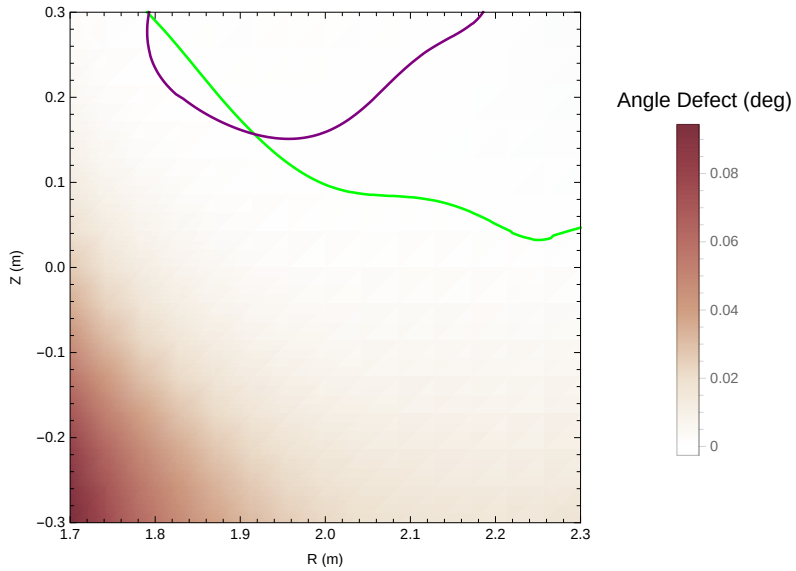

Figure 2.12: Linear polarisation angle defect for KSTAR IMSE view (weighted average across the 15 different lines) with an 80keV beam. The defect vanishes at the contours where $\psi = \pi/2$ (green) and $\varphi = 0$ (purple).

2.6.4 Approximation of the MSE Spectrum

As outlined in Sec. 2.5.4, the polarisation orientation of the σ transitions is expected to have a negligible dependence on upper-state populations. Likewise the angle defect resulting from the elliptical transition is negligible when using tangential MSE viewing geometries.

The Stark-Zeeman effect introduces a circular polarisation fraction to the emission that is unique for each individual line, as outlined in Sec. 2.6.2. Hence for the Stark-Zeeman effect the Stokes resolved spectra can be generalised to,

$$\boldsymbol{s}(\omega) = I(\omega)(1,\, p_{l,MSE}(\omega)\cos 2\theta_\sigma,\, p_{l,MSE}(\omega)\sin 2\theta_\sigma,\, p_{c,MSE}(\omega)) \tag{2.73}$$

where θ_σ is the angle of the polarimeter axis relative to the σ emission, $\sqrt{p_{l,MSE}^2 + p_{c,MSE}^2} \leq 1$, $-1 < p_{l,MSE}(\omega) < 0$ for a π dominated region of the spectrum and $0 < p_{l,MSE}(\omega) < 1$ for a σ dominated region. An example spectra is shown in Fig. 2.13 with some artificial Doppler broadening and $\theta_\sigma = 0$. This representation of the Stokes resolved spectra is used in the formulation of imaging MSE polarimeters in the following chapter. Eq. 2.73 doesn't precisely incorporate line of sight integration effects but is a good approximation for viewing geometries tangential to the flux surfaces. With equal upper-state populations both $p_{l,MSE}$ and $p_{c,MSE}$ are expected to integrate across the multiplet to zero, however this is not necessarily the case, for example on MAST BIG experiments the π emission dominates the σ emission[36].

2.7 Conclusion

The predicted polarisation structure of the Balmer-α emission was found to depend on what interactions were included in the model. This is summarised below,

- With the pure Stark effect the axial symmetry about the electric field results in

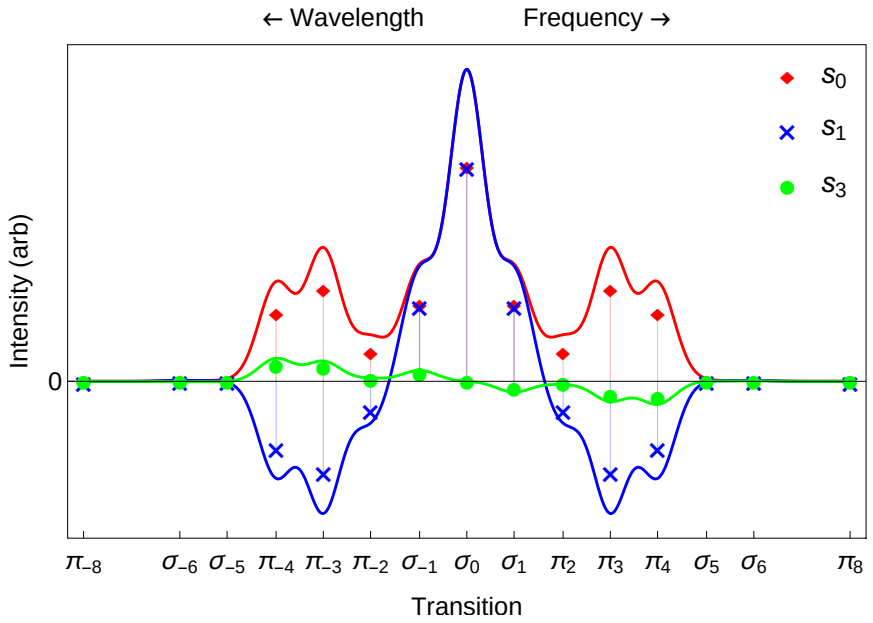

Figure 2.13: Plot of the Stokes spectra for an 80keV deuterium beam velocity injected at 60° to the magnetic field ($\gamma/\epsilon = 0.15$). The view looks along the magnetic field such that $(\psi, \varphi) = (\pi/2, 0)$ and $\text{sign}(\mathbf{i}\cdot\mathbf{B}) > 0$ and the polarimeter axes are aligned such that $s_2 = 0$.

a $\sigma^{\pm}$ polarisation structure. In this case the σ polarisation orientation is always perpendicular to π, independent of upper-state populations. The model in Refs. [28, 29] is an example of this.

- When the (crossed) magnetic field is also included, the axial symmetry is lost and there is no preferred way to diagonalise the degenerate states. Therefore infinite different solutions exist, including the newly formulated $|n,k,m\rangle_C$ and $|n,k,m\rangle_L$ states as well as the Isler states of Ref. [32]. The $|n,k,m\rangle_C$ and $|n,k,m\rangle_L$ states have $\sigma^{\pm}$ and $\sigma^{v,B}$ polarisation structures respectively. The $\sigma_{\pm 1}$ polarisation orientation from the $|n,k,m\rangle_L$ states has a weak dependence on upper-state populations but the σ_0 polarisation orientation remains perpendicular to π.

- When the fine-structure is also considered the perturbed states are similar to the $|n,k,m\rangle_L$ states. There are observable differences between these states and the pure Stark parabolic states. The states derived for calculations in Refs. [44, 43, 51] are expected to be $|n,k,m\rangle_L$ similar states.

- The magnetic field and electric field will not be precisely perpendicular in the plasma, owing to microscopic electric fields. If the microscopic field is sufficiently large the states become similar to $|n,k,m\rangle_C$ and the pure Stark parabolic states.

- When the quadratic Stark effect is considered, the $\pm m$ pairs of states remain degenerate (in the absence of the Zeeman effect) or are very weakly split relative to the fine structure (when the Zeeman effect is also considered for standard beam energies), hence the quadratic Stark effect is not expected to have a significant effect on the polarisation structure. Similarly the diamagnetic Zeeman effect does not have a noticeable effect on the polarisation structure.

Evidently when the microscopic electric fields are considered the standard pure Stark effect is a good approximation for calculating the upper-state populations, more so for high density plasmas. Hence the modelling with parabolic states in Refs. [28, 29] is expected to be reliable, however the reason given that "The Zeeman effect, in turn, alters only the polarization[sic] properties of the emitted radiation without affecting state populations." is discredited by the findings in Sec. 2.5.4. It has been shown that the Zeeman effect can have an effect on both the polarisation ($\sigma^{\pm}$ vs $\sigma^{v,B}$) and the state populations (Sec. 2.5.4). The steps involved in the calculation of the polarisation spectrum is summarised in the Fig. 2.14 flow diagram. The diagram is intended to highlight that the quantum states are foundational to both the polarisation of the emission and the populations of the states.

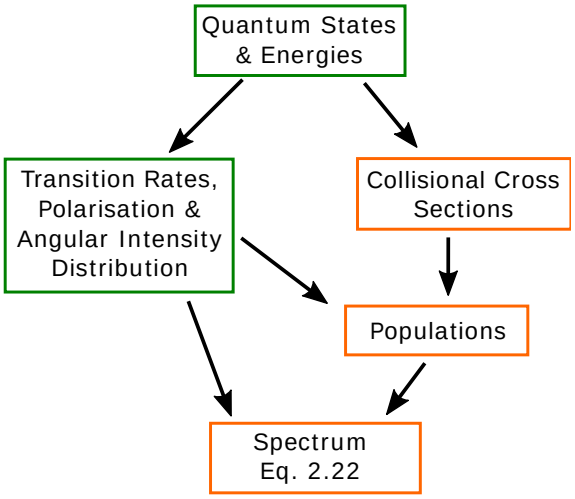

Figure 2.14: Steps involved in calculating the Stokes resolved polarisation spectra. Green boxes indicate aspects that have been considered in detail here while orange boxes indicate aspects that have been considered but not in completeness.

The degeneracy in the Stark-Zeeman energy levels when $\mathbf{E} \perp \mathbf{B}$ is the underlying factor that has given rise to a large range of different predictions for the MSE emission. The degeneracy leads to an underdetermined polarisation structure for the Balmer-alpha emission that has not previously been realised. Atomic models are therefore sensitive to the weaker interactions that break the degeneracy. As a result, *small errors in the implementation of the weaker interactions can have significant effects on the predictions of a model* and it is thought such errors exist in Refs. [30] and possibly [43].

The linear polarisation orientation of the σ_0 and π emissions are predicted to be an accurate indicator of the electric field orientation in both plasma shots and BIG, independent of the density and upper-state populations. There is a possibility for the $\sigma_{\pm 1}$ linear polarisation orientation to deviate from prediction based on the pure Stark effect. However the difference is expected to be small owing to: high electron densities contributing a microscopic electric field that breaks the degeneracy in favour of the more 'robust' $|n, k, m_l\rangle_C$ states (for plasma shots only); beam injection angles close to $\rho = 45°$ creating more equally populated upper-state pairs; the greater intensity and throughput of σ_0 relative to $\sigma_{\pm 1}$; and using viewing directions with a significant component perpendicular to the electric field and parallel/antiparallel to the magnetic field. Therefore the source of the BIG contaminations observed on DIII-D[30] remains unclear.

There is no reported evidence that measured σ linear polarisation orientations deviate

with a viewing angle dependence given in Eq. 2.52 or that the deviation increases at lower gas densities. Discrepancies in BIG data are often attributed to emission from secondary neutrals[34] which predicts greater errors at higher gas densities. Therefore the polarisation structure effects presented here and secondary neutral effects should be distinguishable but an experimental measurement would require non-standard viewing directions and a more radially injected beam.

The circular polarisation fraction of the MSE emission is significant and the approximations presented provide a good starting point for calculations without the need to delve into the underlying quantum mechanics and atomic physics. Useful applications for the circular polarisation exist, it can be used as an additional constraint for a π MSE measurement or to determine how well a σ isolating narrowband filter has been centred. The possibility for the circular polarisation to couple to the linear polarisation at a non-ideal mirror is often overlooked but can have a significant deleterious effect on the measurement.

Chapter 3

Polarisation Coherence Imaging Diagnostics

Polarimetry of Stark and/or Zeeman split atomic emission lines is a powerful non-perturbative technique for measuring the orientation of the electric and/or magnetic field in a plasma. Integrated over a Stark-Zeeman split multiplet there is no net polarisation (when upper-states are equally populated), hence some spectral discrimination is required to achieve a net polarisation fraction. Narrowband filters are commonly used to isolate a portion of the multiplet emission with large polarisation fraction for polarisation analysis. However when the Doppler shift varies across the field of view, as with the MSE measurement, a single narrowband cannot isolate the same portion of the spectra for the entire view. The polarisation coherence imaging techniques described in this chapter combines the polarisation and spectral information into a single measurement to achieve a high polarisation fraction from the entire multiplet. A focus here is given to the MSE emission but the results could be generalised to other Stark-Zeeman split multiplet lines.

Since imaging motional Stark effect (IMSE) was first proposed[2] a number of technical advances and deeper insights have followed such as replacing delay-Savart plate combinations with single displacer waveplates and more consideration has gradually been given to circular polarisation. This chapter describes the principles of IMSE and the various encoding strategies that have been presented in numerous publications[2, 54, 55, 40, 56, 57]. An emphasis is placed on clarifying the impacts of the Stark-Zeeman net circular polarisation on the imaging polarimeter and developing a generalised framework for treating non-axial rays in a polarimeter.

3.1 Polarimetry Principles for IMSE

The four Stokes parameters that describes the polarisation state of light are outlined in Chapter 2 in Fig. 2.2 and Eqs. 2.20 and 2.21. As a recap the Stokes vector can be expressed

$$\begin{aligned}\mathbf{s}(\omega) =&(s_0,\, s_1,\, s_2,\, s_3)\\ =&I_0\big(1,\, p\cos 2\xi\cos 2\theta,\, p\cos 2\xi\sin 2\theta,\, p\sin 2\xi\big)\end{aligned} \tag{3.1}$$

where ω is the light angular frequency and it is understood from here on that I_0, p, θ and ξ are functions of ω. For the MSE emission, summarised in Section 2.6.4 (or more

precisely in Eqs. 2.63-2.66 and Table 2.11), the Stokes vector can be approximated with

$$\mathbf{s}(\omega) = I(\omega)(1,\, p_{l,MSE}(\omega)\cos 2\theta_\sigma,\, p_{l,MSE}(\omega)\sin 2\theta_\sigma,\, p_{c,MSE}(\omega)) \tag{3.2}$$

where θ_σ is constant. Optical detectors can only measure the total intensity of the light s_0, therefore the polarisation must first be manipulated before it can be measured. Polarisers are essential to a polarimeter as they alter the intensity of the light by transmitting only a particular orientation of linear polarisation. Linearly polarised light ($p = 1$ and $\xi = 0$) with orientation θ incident on a horizontal transmission polariser will have an output intensity obeying Malus's law which is

$$S_0 = \frac{1}{2}(s_0 + s_1) = I_0 \cos^2\theta. \tag{3.3}$$

Upper-case S is used for the intensity transmitted by a polarimeter, while lower case $\mathbf{s}$ is used for the initial Stokes vector incident on the polarimeter.

3.1.1 Birefringent Optics

Anisotropic birefringent materials can be used to rotate the linear polarisation and convert between linear and circular polarisation. For a homogeneous material the refractive index can be defined for three principal axes of electric field oscillation. Materials such as glass are isotropic and the refractive index is the same for all principal axes and on the other hand most crystal structures are anisotropic. Uniaxial birefringent materials have one principal axis, known as the optic axis, with refractive index n_e and the two remaining axes have refractive index n_o. The birefringence of such a uniaxial material is defined to be $\Delta n = n_e - n_0$. Polarised light propagating in the material can be decomposed into two polarisations, one orthogonal to the optic axis known as the ordinary ray and one with a component along the optic axis known as the extraordinary ray. The phase delay of the extraordinary ray relative to the ordinary ray on exiting the material is then

$$\phi = \frac{2\pi L \Delta n(\lambda)}{\lambda} = \frac{\omega L \Delta n(\omega)}{c} \tag{3.4}$$

where L is the thickness of the material and λ is the wavelength of the light. It is often more convenient to express the delay in terms of the angular frequency ω of the light. A crystal waveplate with delay of $\phi = \pm\pi/2$ radians is known as a quarter-wave plate. If the input ordinary and extraordinary ray are in phase then at the output they will be in quadrature, resulting in elliptical or circular polarisation, depending on their relative input intensities. For a phase delay of $\pm\pi$ radians the crystal is known as a half-wave plate and effectively mirrors linear polarisation about its extraordinary axis and switches the handedness of the circular polarisation.

3.1.2 The Mueller Matrix Formalism

Mueller matrix formalism is commonly used for calculating the effects of waveplates and polarisers on the Stokes vector. Mueller matrices are more general than Jones matrices as they can handle partially polarised light ($p < 1$). The Mueller matrix for a waveplate

with horizontal extraordinary axis is

$$W(\phi) = \begin{pmatrix} 1 & 0 & 0 & 0 \\ 0 & 1 & 0 & 0 \\ 0 & 0 & \cos\phi & -\sin\phi \\ 0 & 0 & \sin\phi & \cos\phi \end{pmatrix}. \tag{3.5}$$

The handedness of the circular polarisation is defined from the point of view of the detector such that right hand circularly polarised light has positive s_3 component. The coordinate system can be rotated counter-clockwise

$$R(\rho) = \begin{pmatrix} 1 & 0 & 0 & 0 \\ 0 & \cos\rho & \sin\rho & 0 \\ 0 & -\sin\rho & \cos\rho & 0 \\ 0 & 0 & 0 & 1 \end{pmatrix} \tag{3.6}$$

such that a waveplate with extraordinary axis at angle ρ (counterclockwise looking from detector) can be generalised to $W(\phi, \rho) = R(-\rho) \cdot W(\phi) \cdot R(\rho)$.

The Mueller matrix for a polariser with horizontal transmission is

$$P = \frac{1}{2} \begin{pmatrix} 1 & 1 & 0 & 0 \\ 1 & 1 & 0 & 0 \\ 0 & 0 & 0 & 0 \\ 0 & 0 & 0 & 0 \end{pmatrix}. \tag{3.7}$$

A polariser with transmission axis at angle ρ is therefore represented with $P(\rho) = R(-\rho) \cdot P \cdot R(\rho)$.

A general polarimeter capable of measuring all components of the Stokes parameters is pictured in Fig. 3.1. The signal transmitted by this polarimeter is

$$\begin{aligned} S_0(\omega) =& \Big(\big[P \cdot R(-\pi/4) \cdot W(\phi_2) \cdot R(\pi/4) \cdot W(\phi_1) \cdot R(\pi/4) \big] \cdot \mathbf{s}(\omega) \Big)_0 \\ =& \frac{1}{2} \mathbf{p}(\omega) \cdot \mathbf{s}(\omega) \end{aligned} \tag{3.8}$$

$$\text{where} \quad \mathbf{p}(\omega) = (1, -\sin\phi_1 \sin\phi_2, \cos\phi_2, \cos\phi_1 \sin\phi_2). \tag{3.9}$$

The ω dependence of the Stokes vector (Eq. 2.22) and delays of the waveplates (Fig. 3.2 and Eq. 3.4) can have a dependence on the frequency of the light.

There are several different encoding strategies that could be employed for such a polarimeter to measure all components of the Stokes vector. Variable retarders (waveplate with adjustable delay) could be used to isolate components of the Stokes vector with different combinations of ϕ_1 and ϕ_2 if the temporal variation in the signal strength is slow. For example with $\phi_1 = \pm\pi/2$ and $\phi_2 = \pi/2$ the system would measure s_0 and s_1, with $\phi_2 = 0, \pi$ the system would measure s_0 and s_2 and with $\phi_1 = 0$ and $\phi_2 = \pm\pi/2$ the system would measure s_0 and s_3. Alternatively if the spatial variation of the polarisation is small, four individual polarimeters could be used to measure nearby spatial locations[22] or micro-polariser arrays could be employed.

The established choice for conventional MSE systems is temporal amplitude modulation at frequencies f_n of tens of kHz such that $\phi_n = \cos(2\pi f_n t)$ using photoelastic modulators, as described in Ref. [1]. Although conventionally the analysing polariser is

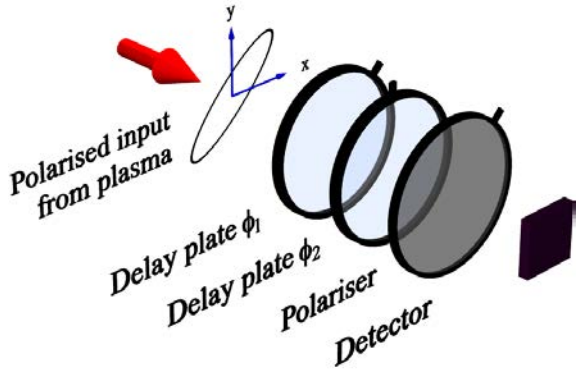

Figure 3.1: A generalised polarimeter with two waveplates of delay ϕ_1 and ϕ_2 at 45° and 90° respectively. The analysing polariser is at 45°. The quoted angles and notches in the diagram describe the orientation of the extraordinary axes of the waveplates and the transmission axis of the polariser.

rotated by 22.5° due to the traditional use of lock-in amplifiers. With high speed digitisers it is possible to access all carrier frequencies such that the polarimeter geometry in Fig. 3.1 produces a stronger signal.

3.1.3 Dispersion

In equation 3.9 $\phi_2(\omega)$ can be designed to simultaneously act as an interferometric filter across σ and π components of an emission multiplet with the appropriate choice of birefringent crystal. Alpha Barium Borate (αBBO) is a commonly used uniaxial material and is referred to as negative uniaxial because $\Delta n < 0$ or $n_e < n_o$. The phase delay as a function of wavelength is plotted in the left of Fig. 3.2 for an αBBO crystal. The refractive indices are determined using the empirically derived Sellmeier equation for βBBO given by[58]

$$n_o^2 = 2.7359 + \frac{0.018780\mu m^2}{\lambda^2 - 0.018220\mu m^2} - 0.01354\mu m^{-2}\lambda^2, \tag{3.10}$$

$$n_e^2 = 2.3753 + \frac{0.012240\mu m^2}{\lambda^2 - 0.016670\mu m^2} - 0.01516\mu m^{-2}\lambda^2. \tag{3.11}$$

The cosine of the delay is plotted in the right of Fig. 3.2. For a thin waveplate with delay less than a single wave (2π radians), such as an ideal quarter or half-wave plate, the delay is approximately constant over a wavelength range of a few nanometres. Thin waveplates are therefore ideal for manipulating the Stokes vector of light over a range of wavelengths/frequencies. Meanwhile thicker birefringent crystals with many waves of delay have significant dispersion, as in Fig. 3.2. Thicker crystals are therefore useful in polarisation interferometers as will become more evident later in Section 3.3 where $\cos\phi(\omega)$ and $\sin\phi(\omega)$ act as spectral filters. The local periodicity ω_T of such a filter is related to

the linear approximation of the frequency dispersion given by

$$\left.\frac{\partial\phi}{\partial\omega}\right|_{\omega=\omega_0} \approx \left(1+\frac{\omega}{\Delta n}\frac{\partial\Delta n}{\partial\omega}\right)\left.\frac{\phi}{\omega}\right|_{\omega=\omega_0} = \kappa\frac{\phi_0}{\omega_0} \tag{3.12}$$

$$\text{where}\quad \kappa = \left(1+\frac{\omega}{\Delta n}\frac{\partial\Delta n}{\partial\omega}\right)\Bigg|_{\omega=\omega_0}. \tag{3.13}$$

At angular frequency ω_0 the local periodicity of the filter is then

$$\omega_T = \frac{2\pi}{\kappa\phi_0}\omega_0. \tag{3.14}$$

At 660nm, the approximate wavelength of red-shifted MSE emission the αBBO refractive indices are $n_e = 1.549$ and $n_o = 1.666$ while $\kappa = 1.07$.

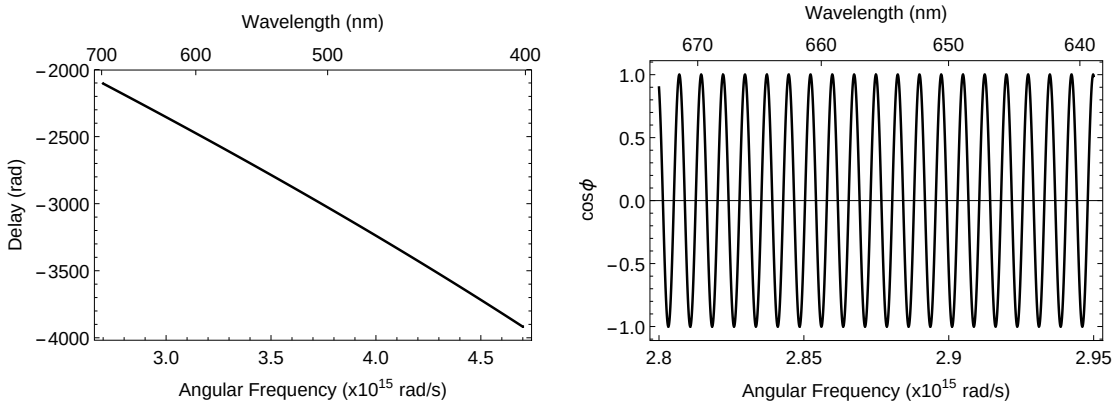

Figure 3.2: (Left) Phase delay for a 2mm αBBO crystal. The delay is approximately linear as a function of frequency. (Right) The cosine of the phase delay in the region of the Balmer-alpha emission. The 1.7nm period is on the order of magnitude of the Stark splitting between the π and σ components of the MSE emission.

3.1.4 Phase Delay Angular Dependence and Displacer Waveplates

A powerful encoding strategy for the polarimeter is to modulate a spatial heterodyne carrier wave that is imaged onto a camera sensor. Until this point we have only considered the case where the waveplate optic axis is parallel to the surface of the plate and light is normally incident on the plate. However the delay can have a significant dependence on the incident angle of the ray when the optic axis is not parallel to the surface of the plate. This angular dependence is exploited to achieve a carrier wave for the IMSE system to spatially encode the polarisation information.

In air the propagation vector $\mathbf{k}$ of a ray can be parameterised by spherical polar angles (α, β), illustrated in Fig. 3.3, such that

$$\hat{\mathbf{k}} = (-\sin\alpha\cos\beta,\ -\sin\alpha\sin\beta,\ \cos\alpha) \tag{3.15}$$

where $\alpha = 0$ defines the optical axis of the system (distinct from the waveplate optic axis). The lens arrangement used will define a mapping between the view direction $\hat{\mathbf{i}}$ relative to the fields (Fig. 2.1) and the propagation vector $\hat{\mathbf{k}}$. For a pinhole or ideal thin lens of focal

length f the light will focus on the image sensor at positions

$$x = -f\tan\alpha\cos\beta = -f\alpha\cos\beta + O(\alpha^3), \tag{3.16}$$
$$y = -f\tan\alpha\sin\beta = -f\alpha\sin\beta + O(\alpha^3). \tag{3.17}$$

For many of the experiments in this thesis a $f = 85$mm focal length lens was used with a PCO.edge 5.5 sCMOS camera which has a 16.64mm × 14.04mm sensor composed of 2560 × 2160 6.5µm pixels. For the extreme case of the corner pixels this corresponds to $\alpha = 0.128\text{rad} = 7.3°$. Although usually the diagonal pixels are typically beyond the region of interest such that the central-top pixel provides a more representative maximum angle which is $\alpha = 0.083\text{rad} = 4.7°$. This value of α is used in some examples later in this chapter.

For a uniaxial material the optic axis can be parameterised by angles (Θ, ρ), illustrated in Fig. 3.3, such that it is given by

$$\hat{\mathbf{X}} = (\cos\Theta\cos\rho,\ \cos\Theta\sin\rho,\ \sin\Theta). \tag{3.18}$$

The ordinary and extraordinary rays will have different phase velocities and refract at different angles through the uniaxial material. The relative phase shift between the extraordinary and ordinary ray on exiting the crystal is the primary interest and has been calculated to be[59]

$$\begin{aligned}\phi =& \frac{\omega L}{c}\left(\frac{n_o\sqrt{n_e^2(n_e^2\sin^2\Theta + n_o^2\cos^2\Theta) - (n_e^2 - (n_e^2 - n_o^2)\cos^2\Theta\sin^2(\beta-\rho))n^2\sin^2\alpha}}{n_e^2\sin^2\Theta + n_o^2\cos^2\Theta}\right.\\ &\left. - \sqrt{n_o^2 - n^2\sin^2\alpha} - \frac{n(n_o^2 - n_e^2)\sin\Theta\cos\Theta\cos(\beta-\rho)\sin\alpha}{n_e^2\sin^2\Theta + n_o^2\cos^2\Theta}\right).\end{aligned} \tag{3.19}$$

where n is the refractive index of the external medium which is typically air with $n \approx 1$. β and ρ are related to δ, used in Ref. [59], by $\delta = \beta - \rho$. This generalisation of δ has been made to facilitate calculations with multiple waveplates having different orientations, ρ, of their optic axes. In the case where $\alpha = 0$ and $\Theta = 0$ Eq. 3.19 simplifies to the more familiar Eq. 3.4.

For a regular waveplate the optic axis is parallel to the xy-plane such that $\Theta = 0$. The delay for a waveplate with vertical optic axis ($\rho = 90°$) reduces to

$$\begin{aligned}\phi =& \frac{\omega L\Delta n}{c}\left(1 + \frac{\left(n_o\cos^2\beta - n_e\sin^2\beta\right)\alpha^2}{2n_e n_o^2}\right) + O(\alpha^4)\\ =& \frac{\omega L\Delta n}{c}\left(1 + \frac{n_o x^2 - n_e y^2}{2n_e n_o^2 f^2}\right) + O(\alpha^4).\end{aligned} \tag{3.20}$$

We see that the phase delay has a fixed offset given by Eq. 3.4 as well as an angular or spatial hyperbolic phase with eccentricity of $\sqrt{1 + n_o/n_e}$. The hyperbolic pattern can be used to locate the orientation of the optic axis.

Waveplates with $0° < \Theta < 90°$ are used in IMSE polarimeters and are known as displacers. To find an analytic approximation of Eq. 3.19 it is worthwhile letting $\bar{n} = (n_e + n_o)/2$ such that $n_e = \bar{n} + \Delta n/2$ and $n_o = \bar{n} - \Delta n/2$. Usually $\Delta n/\bar{n} \sim 0.1$ so that second order terms in $\Delta n/\bar{n}$ can be dropped as a simplifying approximation. In this case,

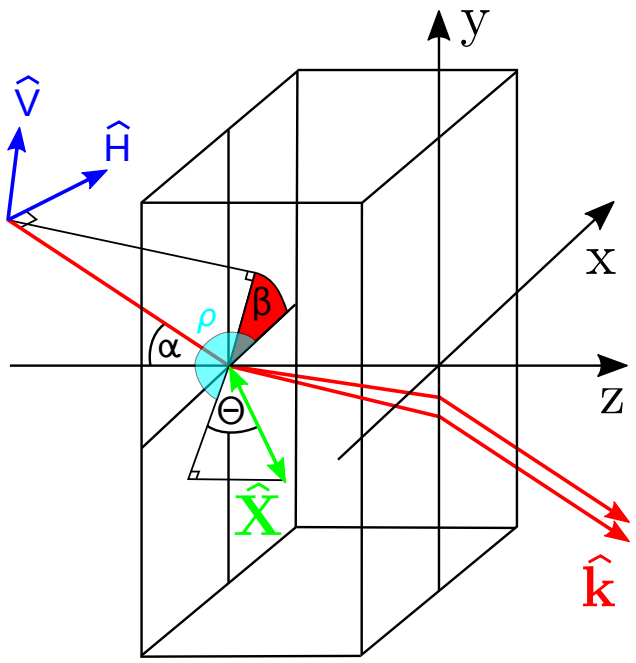

Figure 3.3: Illustration of the ray and optic axis angles. The incident ray propagates at angle $0 \leq \alpha < \pi/2$ to the crystal normal and projects to the angle $0 \leq \beta < 2\pi$ in the xy-plane. The optic axis of the crystal is at $0 \leq \Theta < \pi/2$ to its surface and projects to the angle $0 \leq \rho < 2\pi$ in the xy-plane. The horizontal polarisation reference $\hat{\mathbf{H}}$ is defined later in Eq. 3.30.

with $\rho = 90°$, Eq. 3.19 simplifies to

$$\phi = \frac{\omega L \Delta n}{c}\left(\cos^2\Theta + \frac{\sin 2\Theta \sin\beta}{\bar{n}}\alpha + \frac{\sin^2\Theta + \frac{1}{2}\cos 2\beta \cos^2\Theta}{\bar{n}^2}\alpha^2 + O(\alpha^3)\right) + O(\Delta n^2). \tag{3.21}$$

The zeroth order term in α is the delay for an axial (normal incidence) ray and is,

$$\phi_{offset}(\omega) = \frac{\omega L}{c}\left(\frac{n_o n_e}{\sqrt{n_e^2 \sin^2\Theta + n_o^2 \cos^2\Theta}} - n_o\right) \tag{3.22}$$

$$= \frac{\omega L \Delta n \cos^2\Theta}{c} + O(\Delta n^2). \tag{3.23}$$

Including the higher order Δn terms for the delay offset results in a $\approx 5\%$ difference when considering αBBO crystal with $\Theta = 45°$. Importantly when $\Theta \neq 0$ Eq. 3.21 also has a first order term in α that produces a linear ramp in the delay. It can be expressed in terms of the (x, y) position in the focal plane as

$$\phi_{shear}(\omega, y) = -\frac{\omega L \Delta n \sin 2\Theta}{\bar{n} c f} y = k_y y$$

$$\text{where} \quad k_y = -\frac{\omega L \Delta n \sin 2\Theta}{\bar{n} c f}. \tag{3.24}$$

Evidently the maximum ramp gradient occurs at $\Theta = 45°$ (including the third order Δn terms offsets this result slightly). When taking the sine or cosine of ϕ_{shear} in Eq. 3.5

the carrier k_y will be the dominant spatial feature in the interferometric image when an appropriate choice is made for f, L and Θ. Understanding the effects of the displacer can be challenging as the delay has a linear dependence on both ω and y.

In Eq. 3.21 the quadratic term in α is

$$\phi_{hyperbolic}(\omega, x, y) = \frac{\omega L \Delta n}{4\bar{n}^2 c f^2} \left((3 - \cos 2\Theta) x^2 - (3\cos 2\Theta - 1) y^2 \right) \tag{3.25}$$

and produces a hyperbolic imprint when $\Theta < \operatorname{arccot}\sqrt{2} \approx 35^\circ$ or an elliptical imprint when $\Theta > \approx 35^\circ$. The net result is a curvature of the linear ramp that makes it straightforward to determine the orientation of the optic axis.

The linear and quadratic phase delay approximations for an αBBO displacer cut at $\Theta = 45^\circ$ are plotted in Fig. 3.4. The zeroth order delay in this case is -606.78rad but the approximation in Eq. 3.23 only gives -574.68rad. The exact delay from Eq. 3.19 is plotted in the left of Fig. 3.5 while the right plot shows the difference relative to the approximations in Eqs. 3.22, 3.24 and 3.25. It is evident that including terms up to second order in α reproduces the dominant features of the displacer phase delay.

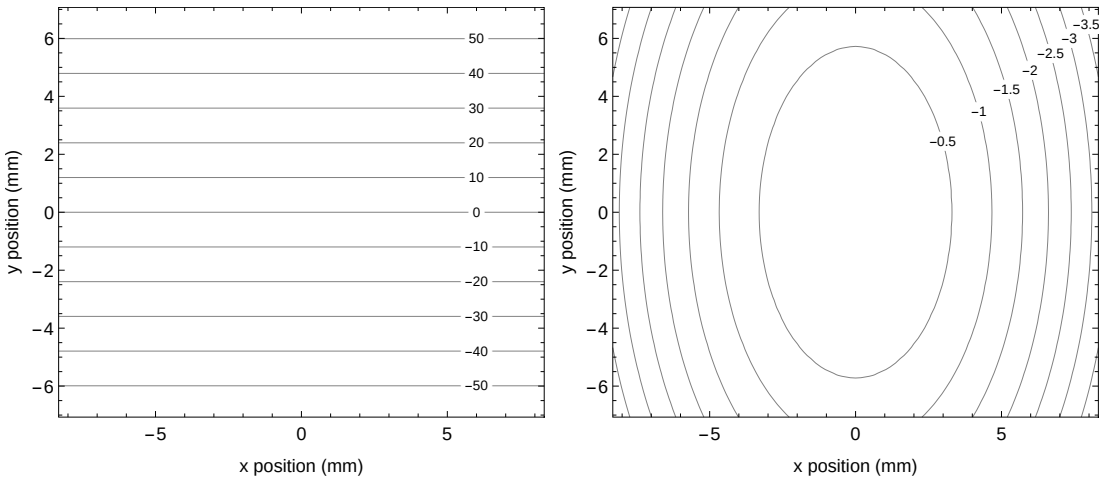

Figure 3.4: (Left) The linear delay shear in radians given by Eq. 3.24 for an αBBO displacer focused onto a PCO.edge camera ($L = 1$mm, $f = 85$mm, $\Theta = 45^\circ$, $\rho = 90^\circ$ and $\lambda = 660$nm). (Right) The quadratic dependence given in Eq. 3.25, which is elliptical for $\Theta = 45^\circ$.

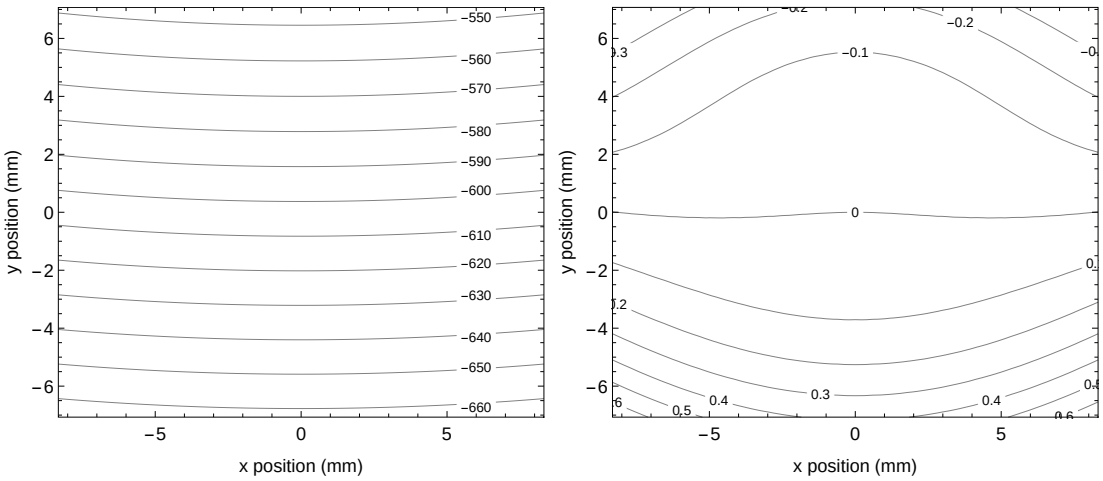

Figure 3.5: (Left) The delay in radians using the exact formula in Eq. 3.4. (Right) Difference between the exact delay (shown on left) and the approximate delay in Eqs. 3.22-3.25.

It should be noted that the definition of κ in Eq. 3.13 becomes more complicated when $\Theta > 0$ and $\alpha > 0$ however the differences with the $\Theta = \alpha = 0$ case are small. This is evident in Fig. 3.6 where κ value remains within 0.4% of the $\kappa = 1.0669$ @660nm value from Eq. 3.13. For lithium niobate, an alternative birefringent material, with $\kappa = 1.2662$ the variation across the image is within 0.8%.

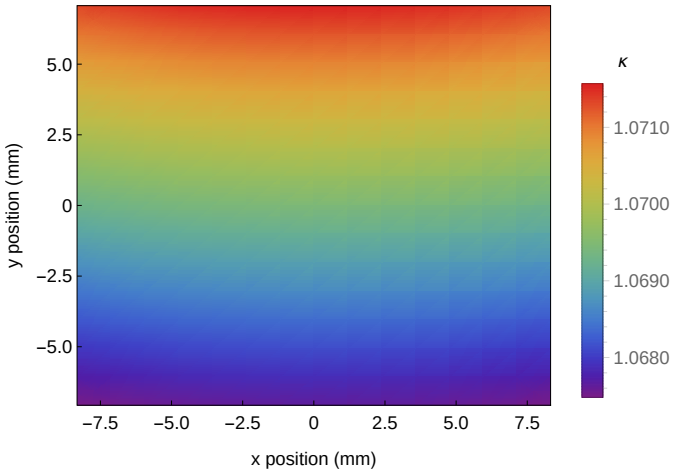

Figure 3.6: κ dispersion factor for a $\Theta = \pi/4$ αBBO displacer focused onto the PCO edge with an 85mm lens.

Savart Plate

To achieve carrier fringes without any zeroth order delay ϕ_{offset} it is possible to combine two displacers of equal thickness and cut angle Θ. When the two displacers are at $\Delta\rho = 90°$ to each other the ordinary (extraordinary) ray in the first displacer becomes the extraordinary (ordinary) ray in the second displacer and vice versa. The effect is that the zeroth order delays cancel, while the linear shear terms partially combine to produce

$\sqrt{2}$ times the shear of a single displacer. The optimal cut angle for maximising the phase shear is $\Theta = 45°$ when $\Delta n/n$ is small. An example of a Savart plate and the associated delay pattern is illustrated in Fig. 3.7. The Mueller matrix for the Savart plate is

$$W_S(\phi) = \begin{pmatrix} 1 & 0 & 0 & 0 \\ 0 & \cos(\phi_{S_1} - \phi_{S_2}) & 0 & \sin(\phi_{S_1} - \phi_{S_2}) \\ 0 & 0 & 1 & 0 \\ 0 & -\sin(\phi_{S_1} - \phi_{S_2}) & 0 & \cos(\phi_{S_1} - \phi_{S_2}) \end{pmatrix}. \tag{3.26}$$

where ϕ_{S_1} is the delay of the first displacer and ϕ_{S_2} the delay of the second.

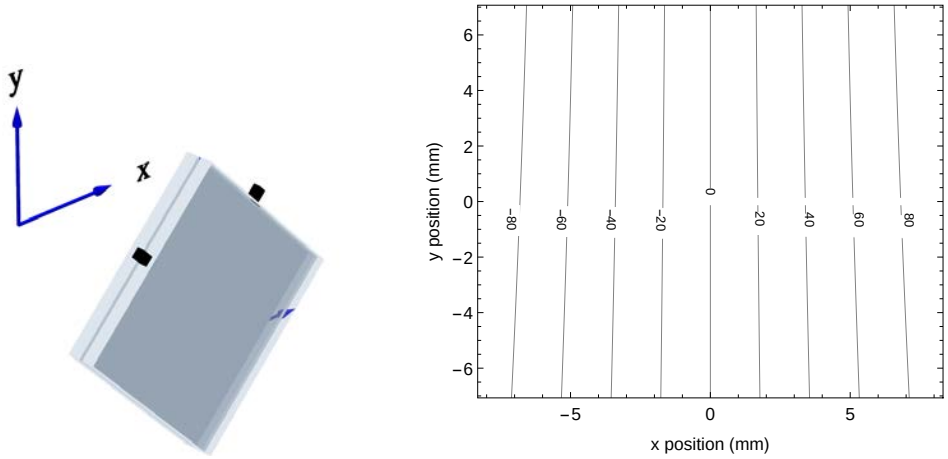

Figure 3.7: (Left) Schematic of a Savart plate composed of two 1mm αBBO displacers, both cut at $\Theta = 45°$. Square waveplates are used here for displacers, with the notches indicating the orientation of ρ. In this instance the initial displacer is at $\rho = 45°$ and the second is at $\rho = 135°$. (Right) Delay produced by the Savart plate in the focal plane of an 85mm lens. The second order term in α contributes to produce the 'fanning' pattern.

A Savart plate can be 'field-of-view-widened' to eliminate the hyperbolic term that results in spatial curvature of the delay shear. This is achieved by inserting a half-wave plate between the two displacers as illustrated in Fig. 3.8. Now the extraordinary (ordinary) ray in the first displacer is rotated 90° such that it is an ordinary (extraordinary) ray in the second displacer which has necessarily been rotated a further 90°. The phase shear in this case is double that of a single displacer, unlike the $\sqrt{2}$ increase for the simple Savart plate. An example of a field-widened Savart plate and the associated delay are also illustrated in Fig. 3.8.

3.2 Effects of Non-Axial Rays

It is essential to consider in detail the behaviour of non-axial rays in an imaging interferometer. In this section a subtle effect relating to the rotation of non-axial extraordinary and ordinary rays (i.e. rays with $\alpha > 0$) is formulated and described.

3.2.1 Generalised Malus's Law

Light passing through a polariser at angle ρ followed by a horizontal polariser will have an output intensity that obeys the well-known Malus's law given in Eq. 3.3. In particular when the initial polariser is vertically transmitting ($\rho = 90°$) the transmitted intensity after

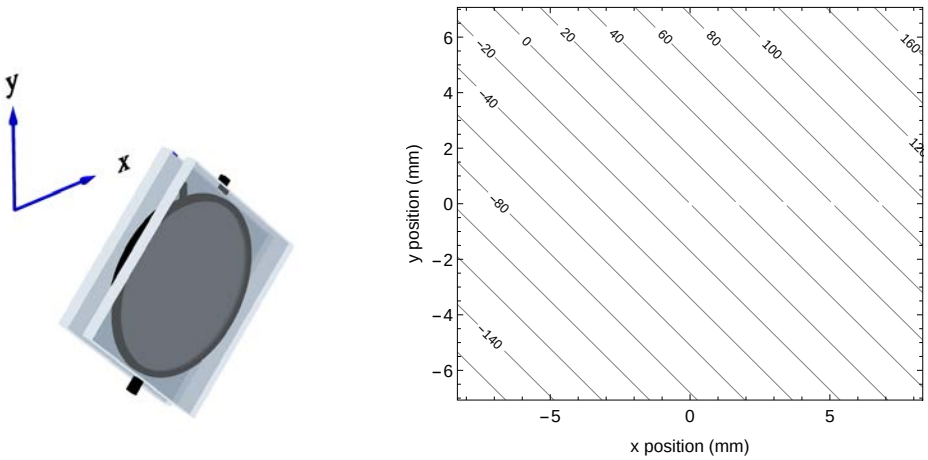

Figure 3.8: (Left) Schematic of a field widened (FW) Savart plate with two 1mm αBBO displacers and a $\rho = 90°$ vertically oriented half-wave plate between the displacers. (Right) Delay produced by the FW Savart plate in the focal plane of an 85mm lens. There is no second order component resulting in an almost uniform shear with $\sqrt{2}$ times the gradient of the standard Savart plate.

the second polariser will be zero. For a real world polariser there is a limiting extinction ratio that depends on the polariser's capacity to completely polarise the light. However there is also a more subtle effect that non-axial rays will not be perfectly extinguished by crossed polarisers, even with idealised polarisers. Here we consider an ideal wire-grid polariser which transmits light orthogonally polarised to the thinly spaced wires. The vertical transmission polariser has horizontal wires such that the transmitted ray is polarised in the direction

$$\hat{\mathbf{T}}_\mathbf{i} \propto \hat{\mathbf{k}} \times (1,\, 0,\, 0) = (0,\, \cos\alpha,\, \sin\alpha \sin\beta), \tag{3.27}$$

where the proportional sign is used to indicate that the right hand side of the equation is not necessarily normalised. Now for the final polariser the transmitted ray is polarised in the direction

$$\hat{\mathbf{T}}_\mathbf{f} \propto \hat{\mathbf{k}} \times (0,\, 1,\, 0) = (\cos\alpha,\, 0,\, \sin\alpha \cos\beta). \tag{3.28}$$

It is evident that $\hat{\mathbf{T}}_\mathbf{i} \cdot \hat{\mathbf{T}}_\mathbf{f} \neq 0$ when $\alpha \neq 0$ and $\beta \neq n\pi/2$, indicating that there remains some transmission for non-axial rays. The angle difference from orthogonality between $\hat{\mathbf{T}}_\mathbf{i}$ and $\hat{\mathbf{T}}_\mathbf{f}$ is

$$\begin{aligned} \Delta =& \arcsin\left(\hat{\mathbf{T}}_\mathbf{i} \cdot \hat{\mathbf{T}}_\mathbf{f}\right) \\ =& \frac{1}{2}\alpha^2 \sin 2\beta + O\left(\alpha^4\right) \end{aligned} \tag{3.29}$$

The transmitted intensity for ideal crossed wire-grid polarisers is $I = I_0 \sin^2\Delta$ which has lowest order term α^4. For the representative incident angle $\alpha = 4.7°$ the resulting transmission is 0.001% when $\sin 2\beta = 1$. This is less than the inverse extinction ratio of the wire-grid polarisers and is therefore not a readily observable effect. This effect is easy to visualise by viewing gridded graph paper from various angles. The lines on the paper only appear to be precisely perpendicular when looking normally at the paper ($\alpha = 0$) or when looking along the horizontal or vertical lines $\beta = n\pi/2$. Only when looking at

a steep angle does the non-orthogonality become significant. This polariser example only serves as an illustration, the effect is more severe when a displacer waveplate is considered.

3.2.2 For a Waveplate with an Arbitrary Optic Axis

We now consider non-axial rays in a birefringent plate with an optic axis that is not parallel to its surface, that is when $\Theta > 0$. Firstly the polarisation orientation must be referenced relative to some axes, which is chosen to be the axis horizontal to $\hat{\mathbf{k}}$ given by

$$\hat{\mathbf{H}} \propto (0,\, 1,\, 0) \times \hat{\mathbf{k}} = (\cos\alpha,\, 0,\, \sin\alpha\cos\beta). \tag{3.30}$$

The new propagation vector of the refracted ordinary ray in the crystal $\hat{\mathbf{k}}_o$ can be calculated using Snell's Law, given by $n_{air}\sin\alpha = n_o \sin\alpha_o$. Taking that $n_{air} = 1$ we have that

$$\begin{aligned}\hat{\mathbf{k}}_o &= (-\sin\alpha_o\cos\beta,\, -\sin\alpha_o\sin\beta, \cos\alpha_o) \\ &= \left(-\frac{\sin\alpha\cos\beta}{n_o},\, -\frac{\sin\alpha\sin\beta}{n_o},\, \sqrt{1-\frac{\sin^2\alpha}{n_o^2}}\right)\end{aligned} \tag{3.31}$$

and the ordinary ray polarisation within the crystal is therefore given by

$$\hat{\mathbf{o}} \propto \hat{\mathbf{k}}_o \times \hat{\mathbf{X}}. \tag{3.32}$$

In the general case this and the following calculations are unwieldy expressions involving the angles α, β, Θ and ρ along with the refractive index n_o. For this reason only a final Taylor series approximation is given explicitly at the end of the calculation.

To find the polarisation components in the air that correspond to the extraordinary and ordinary ray in the crystal we must follow how the polarisation transforms as it refracts at the air-crystal interface. The $\hat{\mathbf{s}}$ polarisation component (unrelated to Stokes vector) perpendicular to the surface normal is common for both $\hat{\mathbf{k}}$ and $\hat{\mathbf{k}}_o$ while the $\hat{\mathbf{p}}_{air}$ polarisation component in air transforms to $\hat{\mathbf{p}}_o$ in the crystal. These components are given by

$$\hat{\mathbf{s}} \propto \hat{\mathbf{k}} \times \hat{\mathbf{k}}_o, \tag{3.33}$$

$$\hat{\mathbf{p}}_{air} = \hat{\mathbf{s}} \times \hat{\mathbf{k}}, \tag{3.34}$$

$$\hat{\mathbf{p}}_o = \hat{\mathbf{s}} \times \hat{\mathbf{k}}_o. \tag{3.35}$$

The ordinary polarisation direction in the crystal and the air must both have the same weightings of s and p components. That is $(\hat{\mathbf{s}}\cdot\hat{\mathbf{o}}) = (\hat{\mathbf{s}}\cdot\hat{\mathbf{o}}_{air})$ and $(\hat{\mathbf{p}}_o\cdot\hat{\mathbf{o}}) = (\hat{\mathbf{p}}_{air}\cdot\hat{\mathbf{o}}_{air})$. Hence it follows that the polarisation components in the air are

$$\hat{\mathbf{o}}_{air} = (\hat{\mathbf{s}}\cdot\hat{\mathbf{o}})\hat{\mathbf{s}} + (\hat{\mathbf{p}}_o\cdot\hat{\mathbf{o}})\hat{\mathbf{p}}_{air}, \tag{3.36}$$

$$\hat{\mathbf{e}}_{air} = \hat{\mathbf{o}}_{air} \times \hat{\mathbf{k}}. \tag{3.37}$$

It is now possible to determine the true angle ρ_a between the extraordinary ray polarisation in air and the horizontal axis. Previously it was assumed this angle was simply ρ (defined from Eq. 3.18) and was independent of α, β and Θ. The geometric relationships $\hat{\mathbf{H}}\cdot\hat{\mathbf{e}} = \cos\rho_a$ and $\hat{\mathbf{H}}\times\hat{\mathbf{e}} = \hat{\mathbf{k}}\sin\rho_a$ can be used to determine ρ_a over the full $(-\pi, \pi]$ range.

The exact solution for ρ_a is therefore,

$$\sin\rho_a = (\hat{\mathbf{H}} \times \hat{\mathbf{e}}) \cdot \hat{\mathbf{k}}, \tag{3.38}$$

$$\cos\rho_a = \hat{\mathbf{H}} \cdot \hat{\mathbf{e}}. \tag{3.39}$$

However it is convenient to use the Taylor approximation about $\alpha = 0$ which gives

$$\rho_a(\rho, \Theta, n_o) = \rho + \frac{\tan\Theta\sin(\beta-\rho)}{n_o}\alpha - \frac{1}{4}\left(\sin 2\beta + \frac{(1+2\tan^2\Theta)\sin(2\beta-2\rho)}{n_o^2}\right)\alpha^2 + O\left(\alpha^3\right). \tag{3.40}$$

Evidently there is a difference between ρ_a and ρ that is usually overlooked. There is a first order term in α when $\Theta \neq 0$ that results in a number of observable effects for displacer waveplates that are described later in the chapter.

The generalised Mueller matrix for a birefringent crystal with arbitrary optic axis and incident angle is then

$$R[-\rho_a].W(\phi).R[\rho_a] \tag{3.41}$$

where ϕ is defined in Eq. 3.19 and ρ_a is defined from Eqs. 3.38 and 3.39. The difference in rotation between $R[\rho]$ and $R[\rho_a]$ leads to a different coupling of the linear Stokes parameters for non-axial rays that is straightforward to determine with a Mueller matrix analysis. It should be noted that ϕ in Eq. 3.19 and ρ_a both contain α terms, however the two can effectively be decoupled as the carrier in ϕ varies much more rapidly across the image than these non-axial effects.

A wire grid polariser only transmits the 'ordinary ray' relative to the wires and is therefore generalised by $R[-\pi/2 - \rho_a(\rho+\pi/2, 0, 1)].P.R[\pi/2 + \rho_a(\rho+\pi/2, 0, 1)]$. Eq. 3.29 can easily be re-derived by evaluating $\rho_a(\pi/2, 0, 1) - \rho_a(0, 0, 1) - \pi/2$.

3.2.3 Implications for a Savart Plate

The effect of non-axial rays explains why carrier sub-harmonics are unavoidable when using a standard Savart plate. The sub-harmonics arise from rays that are delayed by either only the first or second of the Savart's displacers. When $\alpha \neq 0$ the extraordinary ray in the first displacer is not exactly an ordinary ray in the second plate. As a result the Savart plate must be treated as a composite plate and Eq. 3.26 is not exact for rays with $\alpha \neq 0$.

The first order in α sub-harmonics can be alleviated by field-widening the Savart plate with a half-wave plate. In this case the over (under) rotation required to match the axes of the first displacer is mirrored by the half-wave plate so that it is under (over) rotated to match the axes of the second displacer in the Savart plate. This effect can be considered separately to the field-widening effect that leads to straightening of the fringe pattern.

3.2.4 Experimental Measurement of Non-Axial Ray Effects

The rotation difference between ρ and ρ_a for non-axial rays was verified using a Savart plate between polarisers illuminated with an integration sphere and 660nm neon spectral line source. The optical system consisted of a $\rho = 135°$ polariser, a 3mm αBBO $\Theta = 45°$ cut displacer at $\rho = 45°$, a second displacer at $\rho = 135°$ and a final $\rho = 90°$ polariser. To

first order in α the light intensity on the imaging sensor is predicted to be

$$S = \frac{I_0}{4}\Big(\big[1+\frac{2}{n_o}\alpha\sin(\beta+\pi/4)\big]-\frac{2\sqrt{2}}{n_o}\alpha\sin\beta\cos\phi_2+\frac{2}{n_o}\alpha\sin(\beta-\pi/4)\cos(\phi_1-\phi_2)\Big). \quad (3.42)$$

The initial polariser has been deliberately aligned with the first displacer of the Savart plate such that the only spatial carriers in the image have a spatial intensity proportional to α. In the absence of the non-axial ray effect one would expect a smooth image without any carrier fringes, hence this unconventional alignment is optimal for measuring the relatively weak carriers that are typically ignored. An experimental image taken with the system can be compared with the complete theoretical calculation in Fig. 3.9. The fast Fourier transform (FFT) and the spatial frequency filtered components of the image are also shown in the figure.

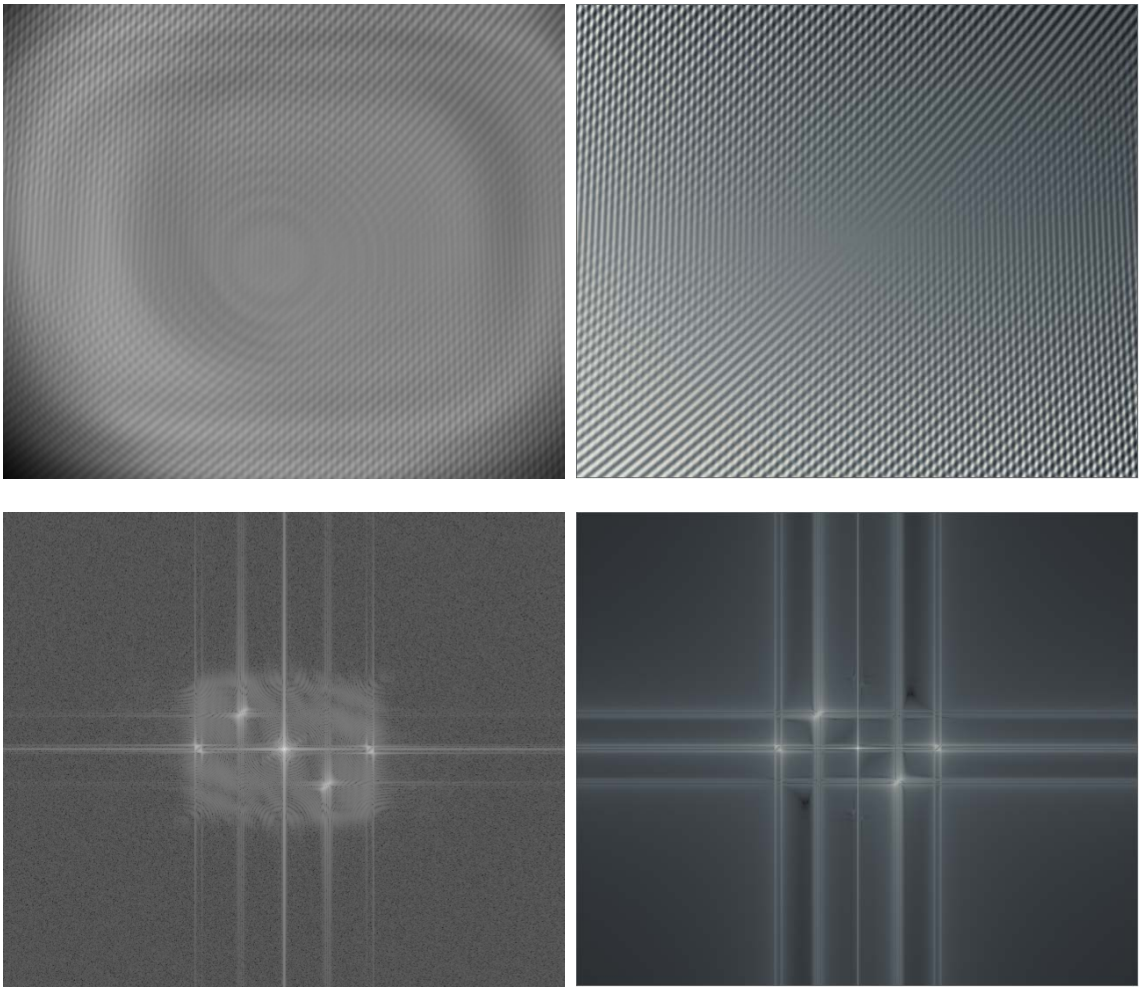

Figure 3.9: (Top Left) Experimental image taken with the Savart plate system illustrating the non-axial ray pattern. (Top Right) Theoretical image calculated for the system. As expected the vertical fringe pattern $\cos(\phi_1 - \phi_2)$ dominates in the left-centre and right-centre of the image and the $\cos\phi_2$ fringe pattern dominates in the left-lower and right-upper parts of the image. (Lower Left) Power spectrum of the experimental image where the single DC intensity peak and 4 AC carriers are evident. (Lower Right) Corresponding power spectrum of the theoretical image.

The illumination intensity profile and instrumental effects must first be considered

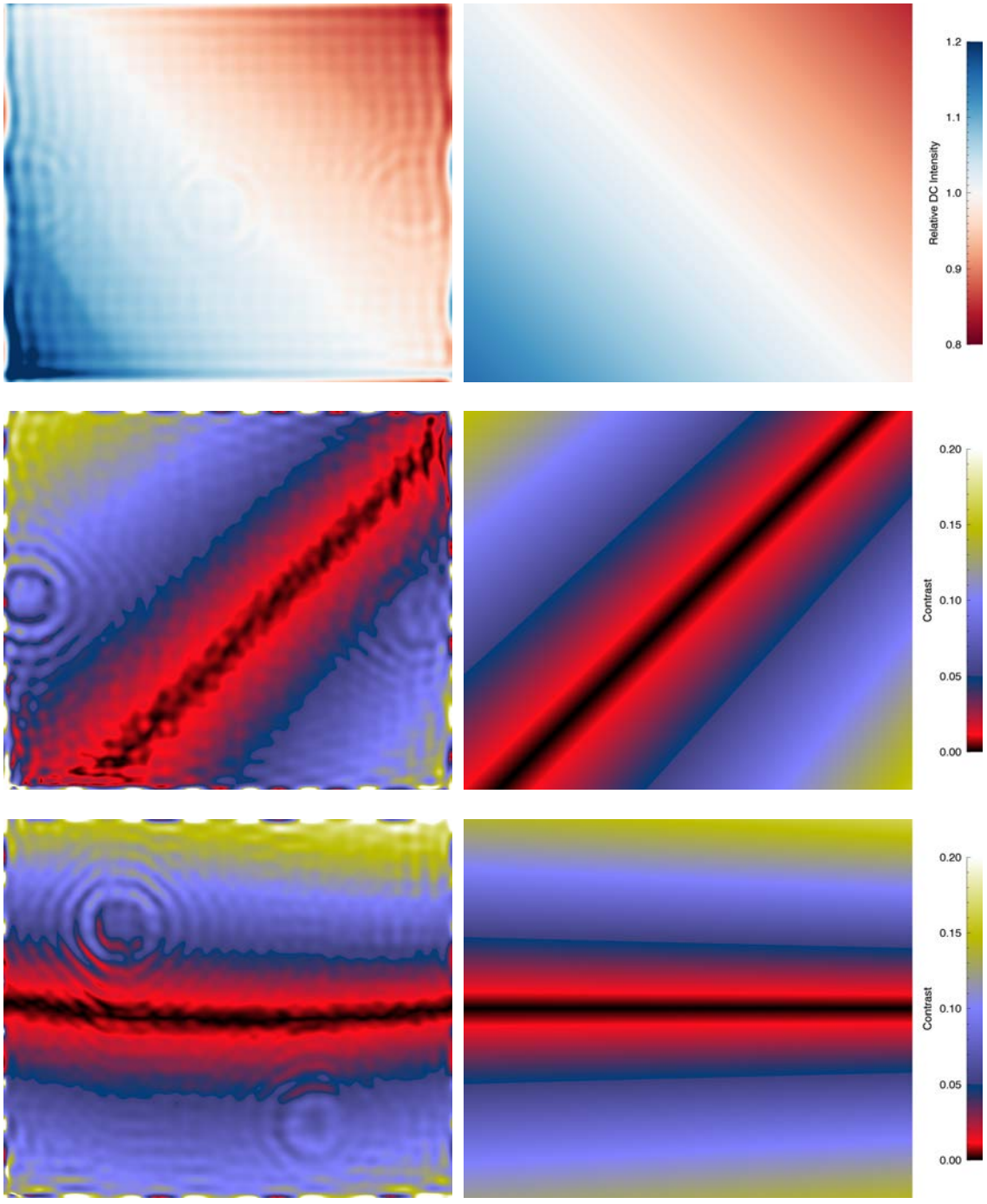

Figure 3.10: (Left Column) Experimental measurement (normalised to coherence imaging with initial polariser at 180°). The Newton's Rings pattern in the raw image evidently has some spectral leakage into the passbands used. (Right Column) Corresponding theoretical predictions from Eq. 3.42. (Top Row) DC intensity. (Middle Row) Contrast of the vertical $\phi_1 - \phi_2$ carrier fringes. (Bottom Row) Contrast of the diagonal ϕ_2 carrier fringes.

before an accurate comparison can be made between the experimental measurement and prediction from Eq. 3.42. I_0 and the instrumental contrast[26] for the system were measured with the initial polariser by 45° to $\rho = 180°$ to produce a conventional 'coherence imaging' spectrometer that is free from first order contributions in α. These values were used to calibrate the relative DC intensity and contrast of the AC carriers in the experimental image. A comparison of these experimental results with the theoretical prediction are shown in Fig. 3.10. All three components of the image are in close agreement. The $\alpha = 0$ position is marginally to the lower-right of the sensor midpoint, indicating a small misalignment between the crystals and camera lens. The contrast of the $\cos\phi_2$ carrier has a clear zero crossing where $\beta = 0, \pi$ ($y = 0$ axis) and the $\cos(\phi_1 - \phi_2)$ carrier where $\beta = \pi/4, 5\pi/4$ ($x = y$ axis) as predicted by the non-axial ray rotation effects. Misalignment of the polarisers and displacers would result in a spatially constant fringe contrast and therefore the non-axial ray effects introduced in this section are needed to account for the effect.

3.3 Polarisation Coherence Imaging

Polarisation coherence imaging is an effective technique for achieving a large net polarisation fraction from a coherent multiplet emission that has underlying polarisation structure but no net polarisation when integrated over the spectrum. Here the principles for achieving a large net polarisation signal are outlined and applied specifically to the MSE emission, however the calculations can easily be adapted to other polarised emission multiplets.

3.3.1 Linear Polarisation Measurement Principle

The polarimeter described by Eq. 3.9 will be sensitive to only the linear polarisation when the initial component is a quarter-wave plate ($\phi_1 = \pi/2$). A displacer with delay $\phi_2 \approx \phi_{offset}(\omega) + k_y(\omega)y$ is used in the polarimeter to provide a interferometric delay and to produce the spatial carrier for the information. This polarimeter is shown in the left of Fig 3.11 and it measures

$$2S = \int_0^\infty \Big(s_0(\omega) - s_1(\omega)\sin\phi_2(\omega, y) + s_2(\omega)\cos\phi_2(\omega, y)\Big) f(\omega) d\omega \tag{3.43}$$

where $f(\omega)$ is the transmission profile of the interference filter used to isolate the multiplet. We see that $\sin\phi_2(\omega)$ *and* $\cos\phi_2(\omega)$ *act as additional periodic filters for* $s_1(\omega)$ *and* $s_2(\omega)$ respectively. Hence the effective polarisation fractions given by $\int s_1(\omega)\sin\phi_2(\omega)d\omega$ and $\int s_2(\omega)\cos\phi_2(\omega)d\omega$ can be maximised with an appropriately chosen displacer thickness.

Calculated interferograms for each of the contributions to the measured signal are shown in Fig. 3.12. For a 'thin' displacer $\phi_2(\omega)$ is approximately constant over the multiplet, leading to a weak signal as the multiplet is net unpolarised i.e. $\int p_{l,MSE}(\omega)d\omega \approx 0$. This is evident in the top right of Fig. 3.12 for small delays where the interferogram contributions from the π and σ components have the same magnitude but opposite phase owing their orthogonal linear polarisation. However with a thicker displacer the periodicity of the sinusoidal filter (ω_T in Eq. 3.14) can be comparable to the 'periodicity' of the spectrum which is approximately the $\pi_{\pm 3}$ spacing given approximately by $3\epsilon/\hbar$. When the period and phase of the sinusoidal filter $\cos\phi_2(\omega)$ matches the 'phase' of the $p_{l,MSE}(\omega)$ spectrum there is a large effective linear polarisation fraction. On the other hand when the filter and spectrum are in 'quadrature' the effective linear polarisation is small. In practice

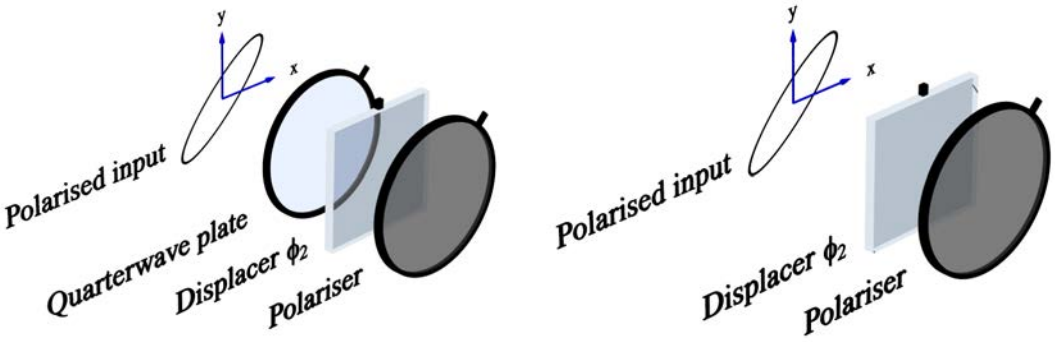

Figure 3.11: (Left) Simple coherence imaging polarimeter for measuring the linear polarisation orientation. The polarimeter has a 45° quarter-wave plate (notch indicates slow axes), a 90° displacer and a 45° polariser. (Right) Simple coherence imaging polarimeter for measuring circular polarisation. The quarter-wave plate on the left is dropped such that it is sensitive to s_3.

the spatial heterodyne interferometer spans many waves of delay (eg left of Fig. 3.5) to establish a spatial carrier wave which encodes the polarimeter response. This is evident in the top right of Fig. 3.12 about the region $3\kappa\epsilon\phi/2\pi\omega_0\hbar = 0.85$ where the interferogram contributions from the π and σ components are in phase, giving rise to a significant signal contrast. This targeted region of the interferogram is highlighted in the lower plot of Fig. 3.12 showing the net measured signal.

When integrating Eq. 3.43 over the MSE spectrum (Eq. 3.2) the polarimeter response can be expressed

$$\begin{aligned}
2S =& \int_0^\infty I(\omega)\big(1 - \cos 2\theta_\sigma p_{l,MSE}(\omega)\sin\phi_2(\omega,y) + \sin 2\theta_\sigma p_{l,MSE}(\omega)\cos\phi_2(\omega,y)\big)f(\omega)d\omega \\
=& I_0\Big(1 - \cos 2\theta_\sigma\zeta_l \sin\big(\phi_0(y)+\alpha_l\big) + \sin 2\theta_\sigma\zeta_l\cos\big(\phi_0(y)+\alpha_l\big)\Big) \\
=& I_0\Big(1 - \zeta_l \sin\big(\phi_0(y)+\alpha_l - 2\theta_\sigma\big)\Big) \qquad (3.44)
\end{aligned}$$

where $\phi_0(y) = \phi_2(\omega_0, y) \approx \phi_{offset}(\omega_0) + k_y(\omega_0)y$ and ζ_l is a slowly varying function of $\phi_0(y)$. The intensity, fringe contrast and phase offset in Eq. 3.44 are given by,

$$I_0 = \int_0^\infty I(\omega)f(\omega)d\omega, \qquad (3.45)$$

$$\zeta_l = \frac{1}{I_0}\left|\int_0^\infty I(\omega)p_{l,MSE}(\omega)f(\omega)e^{i\phi_2(\omega,y)}d\omega\right|, \qquad (3.46)$$

$$\begin{aligned}
e^{i(\phi_0(y)+\alpha_l)} &= \frac{1}{I_0\zeta_l}\int_0^\infty I(\omega)p_{l,MSE}(\omega)f(\omega)e^{i\phi_2(\omega,y)}d\omega \\
&\approx \frac{1}{I_0\zeta_l}\int_{-\infty}^\infty I(\omega)p_{l,MSE}(\omega)f(\omega)\exp\left(i\left(\phi_0(y) + \frac{\kappa\phi_0(y)}{\omega_0}(\omega-\omega_0)\right)\right)d\omega \\
&= \frac{e^{i\phi_0(y)}}{I_0\zeta_l}\int_{-\infty}^\infty I(\omega_0+\upsilon)p_{l,MSE}(\omega_0+\upsilon)f(\omega_0+\upsilon)\exp\left(i\frac{\kappa\phi_0(y)\upsilon}{\omega_0}\right)d\upsilon \qquad (3.47)
\end{aligned}$$

where the change of variable $\upsilon = \omega - \omega_0$ has been applied to centre the integral. The Fourier transform integral of $I(\omega_0+\upsilon)p_{l,MSE}(\omega_0+\upsilon)f(\omega_0+\upsilon)$ in Eq. 3.47 is instructive

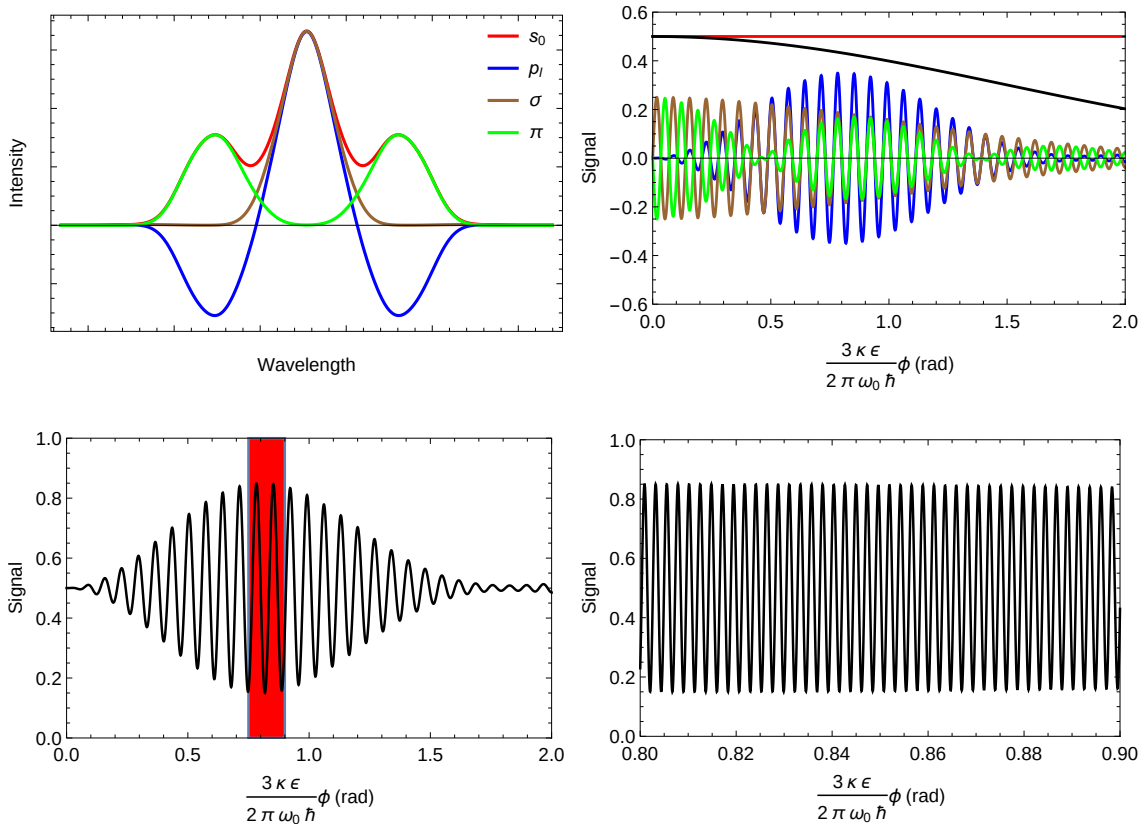

Figure 3.12: (Top Left) Components of the MSE spectrum including s_0 (red), s_1 assuming $\theta_\sigma = 0$ (blue), intensity of σ components (brown) and intensity of π components (green). (Top Right) Individual components of the interferogram in Eq. 3.43, using an unrealistically large linear Stark splitting from a $|\mathbf{E}| = 290\text{MV m}^{-1}$ motional electric field (compares to a representative field strength in Chapter 2 is $|\mathbf{E}| = 5\text{MV m}^{-1}$). The artificially larger splitting requires a smaller delay thereby allowing the carrier wave to be resolved for illustrative purposes. The components are $\int s_0 d\omega$ (red) and -$\int p_{l,MSE} \sin\phi d\omega$ (blue) with the underlying σ contribution in brown and the π contribution in green. The σ and π interferograms sum to the $p_{l,MSE}$ interferogram, i.e. brown+green=blue. The black line indicates the loss in the linear polarisation fraction from line broadening effects $\zeta_S(\phi)$. (Lower Left) Net interferogram for the MSE emission which is effectively the sum of the red and blue components in the previous plot. The red region indicates the range of delays $\phi_2(y)$ across the image. $\kappa = 1$ is assumed here. (Lower Right) Zoomed in version of the left interferogram with a more realistic $|\mathbf{E}| = 9.7\text{MV m}^{-1}$ (1MeV deuterium beam). In this case there is a greater fringe density about the optimal delay for the linear contrast.

for developing an understanding of the phase factor α_l. If the linear polarisation and filter transmission are even functions about ω_0 then the integral will be purely real, implying that $\alpha_l = 0$. Asymmetries in the filter transmission profile and the linear polarisation spectrum, along with higher order crystal dispersion effect can give rise to non-zero α_l. Examples of α_l evolving during a DIII-D plasma shot are shown later in Chapter 4.

Variations in I_0, ζ_l, α_l and θ_σ are all expected to be gradual in the image relative to the carrier $\exp(ik_y y)$ and therefore only contribute to a broadening of the spatial carrier frequency. Similarly the higher order contributions to the displacer delay such as $\phi_{hyperbolic}$ in Eq. 3.25 will contribute to a broadening of the carrier k_y. For this reason only the spatial dependence of the carrier is explicitly retained in Eqs. 3.44 as it varies more rapidly than the other features in the image.

When the filter transmission uniform for each of the individual Stark lines, the value of ζ_l is calculated to be,

$$\zeta_l = \frac{\sum_{n=-8}^{8} a_n I_n \zeta_{S_n} \cos\left(\frac{n\epsilon\kappa\phi_0}{2\hbar\omega_0}\right) \sin^2\psi}{\sum_{n=-8}^{8} I_n(1 + a_n \cos^2\psi)} \quad \text{where} \quad \begin{cases} a_n = 1 \text{ for } \sigma \\ a_n = -1 \text{ for } \pi \end{cases} \tag{3.48}$$

where the sums are taken over each line and the relative intensities I_n of the lines can be taken from Table. 2.11 when upper-states are equally populated, or can be appropriately scaled if they are unequally populated. For simplification it has been assumed that the second order γ/ϵ line splitting terms can be neglected so that the lines are equally spaced. ζ_{S_n} is simply the Fourier transform of the line shape for each individual line[26] (analogous to Eq. 3.46 but for an individual line of the multiplet) and an example is depicted with the black line in the lower left plot of Fig. 3.12. The value of the faction in Eq. 3.48 never reaches 1 (even when $\zeta_{S_n} = 1$) because the π wings and central σ component are each composed of three lines, acting like a broadening mechanism that limits the constructive interference from these lines under the sinusoidal filter. From Eq. 3.48 it can be shown that the signal contrast is maximised by choosing a displacer delay offset that satisfies (assuming equally populated upper-states),

$$\phi(\omega_0) = 0.86 \times \frac{2\pi\omega_0\hbar}{3\kappa\epsilon}. \tag{3.49}$$

This result is comparable to the simplified approximation obtained by solving $\omega_T = 3\epsilon/\hbar$[57] which gives a prefactor of 1 as opposed to 0.86 here. The difference is mainly due to the greater intensity of $\sigma_{\pm1}$ and $\pi_{\pm4}$ compared to $\pi_{\pm2}$. It should be noted that $\zeta_S = 1$ was assumed however when line broadening effects are significant compared to the line splitting the delay required for the maximum contrast will be slightly reduced. Another worthwhile observation is that the first zero crossing in the beating pattern of the π interferogram (green line in top right of Fig. 3.12) occurs near the value 0.5 where the delay is 180° different for the π wings, or more precisely the $\pi_{\pm3}$ lines, giving rise to destructive interference. The crossing is not precisely at 0.5 due to the different intensities of $\pi_{\pm2}$ and $\pi_{\pm4}$.

Eqs. 3.22, 3.24 and 3.49 should be solved simultaneously to determine the displacer thickness L, optic axis cut angle Θ and focal length f that provide the optimal fringe contrast and desired fringe frequency. In practice a fringe frequency approximately 10 pixels per fringe is a good compromise to maximise the spatial resolution without significant

degradation of the fringe contrast resulting from imperfect focusing of the imaging lens.

The polarisation orientation can be determined from Eq. 3.44 when $\phi_0(y) + \alpha_l$ are known and at first glance $\phi_0(y)$ can be determined precisely from Eq. 3.19 with knowledge of the beam voltage (Doppler shift). However precise values for n_e and n_o are difficult to obtain because of temperature dependence, variations in the crystal thickness and stoichiometry. For these reasons the focus in Sections 3.4 and 3.5 will shift to more elaborate IMSE encoding strategies needed for θ_σ to be determined independently of the unknown $\phi_0(y) + \alpha_l$ phase term.

3.3.2 IMSE Circular Polarisation Measurement

From Fig. 2.13 in Chapter 2 it is evident that the linear polarisation fraction of the MSE emission is greater than, but does not necessarily dominate, the circular polarisation fraction. In some IMSE polarimeters s_1 or s_2 share a spatial carrier with s_3 which may potentially corrupt the linear polarisation orientation encoding, therefore the interferometric properties of the circular polarisation s_3 spectrum are considered in this section. Sensitivity to the circular polarisation can be achieved using a polarimeter with $\phi_1 = 0$, as illustrated in the right of Fig. 3.11, such that the general polarimeter described by Eq. 3.9 is now sensitive to s_3 at the expense of s_1. In this case the detector measures

$$2S = \int_0^\infty \big(s_0(\omega) + s_2(\omega)\cos\phi_2(\omega, y) + s_3(\omega)\sin\phi_2(\omega, y)\big) f(\omega) d\omega. \tag{3.50}$$

The interferogram for $\int p_{c,MSE} \sin\phi d\omega$ is shown in the left of Fig. 3.13 and can be compared to the interferogram for the linear component in Fig. 3.12 after scaling by γ/ϵ and appropriate geometric factors. Integrating over the MSE spectrum, the signal reduces to

$$\begin{aligned} 2S &= \int_0^\infty I(\omega)\big(1 + \sin 2\theta_\sigma p_{l,MSE}(\omega)\cos\phi_2(\omega) + p_{c,MSE}(\omega)\sin\phi_2(\omega)\big) f(\omega) d\omega \\ &= \left(1 + \zeta_l \left(\sin 2\theta_\sigma \cos(\phi_0 + \alpha_l) + \frac{\zeta_c}{\zeta_l}\sin(\phi_0 + \alpha_c)\right)\right) \end{aligned} \tag{3.51}$$

where equivalent definitions for ζ_c and α_c, are given earlier in Eqs. 3.46 and 3.47 requiring only a change of subscripts. However the integrand in Eq. 3.47 is now approximately purely imaginary for the circular component, because $s_3(\omega) = p_{c,MSE}(\omega)$ is an odd function about ω_0. Hence *there is an approximately* $\pm 90°$ *phase shift between the linear* α_l *and circular* α_c *terms* and care must be taken to determine the sign of α_c. In Fig. 2.13 where the view has the property $\text{sign}(\mathbf{i} \cdot \mathbf{B}) > 0$ we see that $s_3 > 0$ for $\omega < \omega_0$ and $s_3 < 0$ for $\omega > \omega_0$ such that the Eq. 3.47 integral gives a negative imaginary number when $\phi_0 > 0$. Therefore the phase offset for the circular component can be expressed

$$\begin{gathered} \alpha_c = -m_\pm \pi/2 + \delta_c \\ \text{where } m_\pm = (-1)^n \,\text{sign}\big((\mathbf{i}.\mathbf{B}) \times \phi_0\big), \end{gathered} \tag{3.52}$$

where $\delta_c \approx 0$ and n is the number of zero crossings of ζ_c (not including the crossing at $\phi = 0$). The phase of α_c flips at each zero crossing of ζ_c as evident in Fig. 3.13. Similar to the idealised calculation for ζ_l in Eq. 3.48 the value of ζ_c is

$$\zeta_c = \left| \frac{2\gamma \sin\psi \cos\varphi}{\epsilon} \frac{\sum_{n=-8}^{8} I_n \zeta_{S_n} C_n \sin\frac{n\epsilon\kappa\phi}{2\hbar\omega_0}}{\sum_{n=-8}^{8} I_n} \right| \tag{3.53}$$

where C_n are the circularity of the transitions given in Table. 2.11, correct to second order in γ/ϵ. The sign of $-m_\pm$ in Eq. 3.52 is the same as the sign of the term inside the absolute value brackets of Eq. 3.53. For simplicity the first order γ/ϵ circularity terms have been kept but the second order line splitting terms have been dropped in deriving Eq. 3.53.

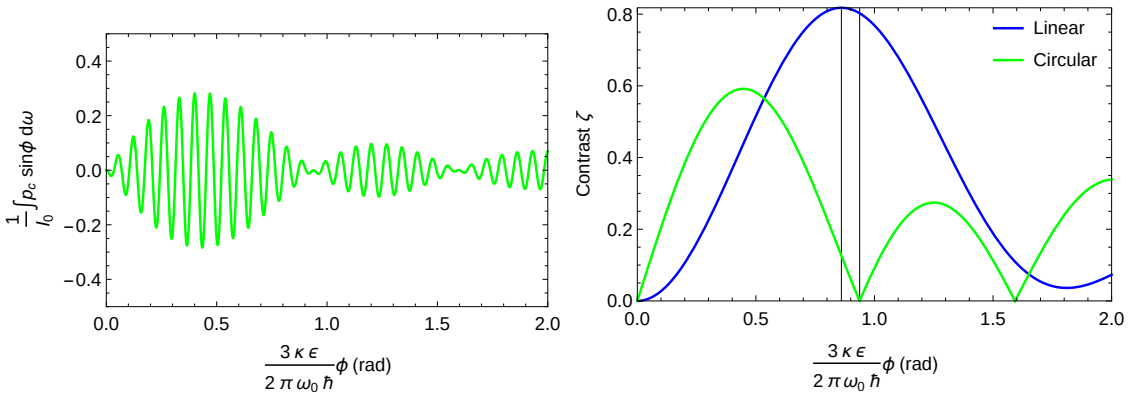

Figure 3.13: (Left) Interferogram of the circular component (unscaled such that $\gamma \sin\psi \cos\varphi/\epsilon = 1$) for a $|\mathbf{E}| = 200\text{MV m}^{-1}$. The phase flip at the zero crossing is evident. (Right) Contrast of linear polarisation (blue) and circular polarisation (green) for the normalised delay. The linear contrast must be scaled by $\sin^2\psi$ and the circular contrast by $\gamma \sin\psi \cos\varphi/\epsilon$, both must be scaled by ζ_S. Gridlines are included for the maximum linear polarisation contrast and the zero crossing of the circular polarisation. Zero crossings in ζ_c are evident near 0.95 and 1.6.

ζ_l and ζ_c are plotted in the right of Fig. 3.13 where it is evident that ζ_c is significantly less than ζ_l after the necessary scaling by γ/ϵ and the $\sin\psi\cos\varphi$ geometric factors are applied. The effective interferometric ellipticity ξ_I for an IMSE system can now be defined with

$$\tan 2\xi_I(\phi_0) = \frac{\zeta_c(\phi_0)}{\zeta_l(\phi_0)}. \tag{3.54}$$

The definition is comparable to Eq. 2.22 where $\tan 2\xi = s_3/\sqrt{s_1^2 + s_2^2}$, however ξ_I is now dependent on the value of ϕ_0 unlike the polarisation orientation θ_σ. For the spectra in Fig. 2.13 and at the delay that maximises ζ_l we have that $\tan 2\xi_I = 0.15\frac{\gamma\cos\varphi}{\epsilon\sin\psi} = 0.023$ or $\xi_I = 0.67°$ when $\gamma/\epsilon = 6.6$, $\psi = \pi/2$ and $\varphi = 0$.

Now that the interferometric ellipticity has been defined Eq. 3.51 can be reduced to

$$2S = I_0\Big(1 + \zeta_l\big(\sin 2\theta_\sigma \cos(\phi_0(y) + \alpha_l) - m_\pm \tan 2\xi_I \cos(\phi_0(y) + \delta_c)\big)\Big). \tag{3.55}$$

Therefore the linear polarisation and circular polarisation carriers are actually out of phase for the MSE spectrum when $\alpha_l = \delta_c$ (or in phase when $m_\pm = -1$). This differs to a monochromatic elliptically polarised source where the carriers would be in quadrature, as seen in Eq. 3.50.

A key result is that *the circular polarisation is 'invisible' to an IMSE polarimeter with delay that satisfies* $\zeta_c(\phi_0) = 0$. For the Stark-Zeeman effect the zero crossing of the circular polarisation contrast occurs when

$$\phi(\omega_0) = 0.94 \times \frac{2\pi\omega_0\hbar}{3\kappa\epsilon}. \tag{3.56}$$

This crossing point is largely independent of the line broadening effects but will depend on

the relative upper-state populations of the different transitions. Importantly the crossing point is close to the maximum of the linear polarisation orientation and therefore can be targeted to eliminate the sensitivity of the polarimeter to circular polarisation without significantly sacrificing the linear polarisation signal. However it should be noted that $\zeta_c = 0$ cannot be precisely satisfied across the field of view due to variations in the Doppler shift ω_0 and line splitting ϵ, with an example given later in Fig. 4.16. Furthermore if some of the half energy multiplet lies in the passband of the IMSE filter or if the filter doesn't uniformly transmit the full energy component then $\delta_c \neq 0$. In this case it is necessary to consider both the phase and magnitude of the interferometric ellipticity and not just the sign and magnitude as considered here. These complications will become clearer in the next chapter where they are applied in a realistic situation.

3.4 Temporally Switched Single Spatial Heterodyne

The temporally switched single spatial heterodyne (TSSSH) IMSE polarimeter[2, 54] outlined below has been deployed on the Textor[60], KSTAR[27] and DIII-D[61] tokamaks. This IMSE encoding technique provides the greatest spatial resolution and its baseline calibration and interpretation are straightforward.

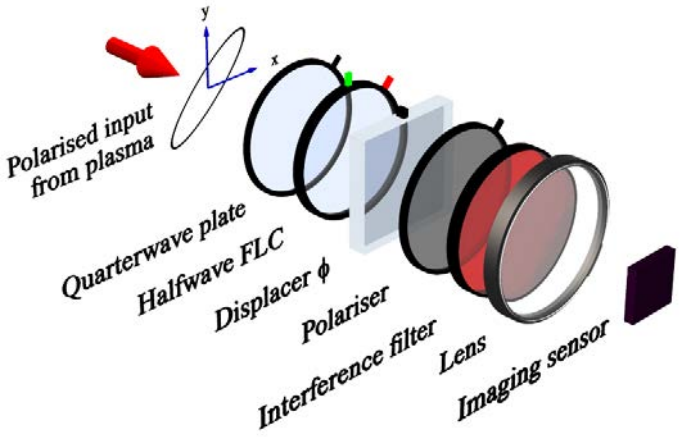

Figure 3.14: Schematic of the switching single spatial heterodyne polarimeter including the interference filter, focusing lens and imaging sensor that are implied in the other polarimeter diagrams in this chapter. The FLC waveplate switches the alignment of its axes from the red $\rho = 45°$ state to the green $90°$ state in between exposures of the camera.

The polarimeter is shown in Fig. 3.14 and is similar to the polarimeter in the left of Fig. 3.11, with the only difference being the inclusion of a half-wave Ferro-electric Liquid Crystal (FLC) waveplate. FLC waveplates ($\Theta = 0$) can quickly switch ($\approx 40\mu s$) the orientation of their optic axes through $\Delta\rho = 45°$ with the reversal of an applied low voltage bias. The fast switching time allows the FLC to completely change states in the readout time between camera exposures allowing the polarimeter to measure two different weightings of the Stokes vector in successive frames.

In the red $\rho = 45°$ FLC state we have that $\phi_1 = 3\pi/2$ and $\phi_2 = \phi(\omega, y)$ in Eq. 3.9 while for the green $\rho = 90°$ state we have that $\phi_1 = \pi/2$ and $\phi_2 = \pi + \phi(\omega, y)$. It follows

that

$$2S_{45^\circ}(\omega) = s_0(\omega) + s_1(\omega)\sin\phi(\omega, y) + s_2(\omega)\cos\phi(\omega, y) \tag{3.57}$$
$$2S_{90^\circ}(\omega) = s_0(\omega) + s_1(\omega)\sin\phi(\omega, y) - s_2(\omega)\cos\phi(\omega, y). \tag{3.58}$$

Integrating over the IMSE spectrum as in Sec. 3.3.1 the signals are found to be

$$2S_{45^\circ} = I_0\Big(1 + \zeta_l(\phi_0)\sin\big((\phi_0(y) + \alpha_l + 2\theta_\sigma\big)\Big) \tag{3.59}$$
$$2S_{90^\circ} = I_0\Big(1 + \zeta_l(\phi_0)\sin\big(\phi_0(y) + \alpha_l - 2\theta_\sigma\big)\Big). \tag{3.60}$$

The phase difference between $\phi_0(y)$ carrier in the $2S_{45^\circ}$ and $2S_{90^\circ}$ images can be demodulated to reveal $4\theta_\sigma$ independently of $\phi_0(y) + \alpha_l$. An example of the $2S_{45^\circ}$ and $2S_{90^\circ}$ signal for a simple model with spatially varying polarisation angle is shown in Fig. 3.15. An actual experimental calibration is shown later in Section. 4.2.1.

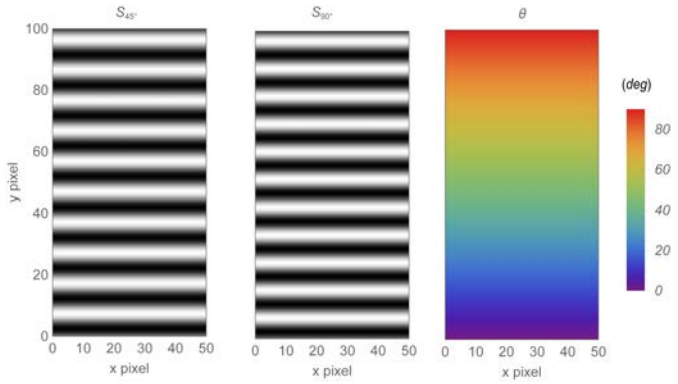

Figure 3.15: Fringe pattern for the red 45° and green 90° FLC orientations with a polarisation orientation varying in the vertical direction. With horizontal or vertical linear polarisation the fringes are in phase and for diagonal linear polarisation the fringes are out of phase.

3.4.1 Non-Ideal Effects

A number of non-ideal effects that occur for the switched single spatial heterodyne system are considered in this section. These non-ideal effects are considered separately to provide a more intuitive understanding of each effect but all should be considered concurrently in the analysis and calibration of a real system.

Dispersive effects in zero-order waveplates

It is generally assumed that the quarter-wave plate retardance is constant across the relatively narrow range of wavelengths of the MSE emission. This is particularly the case for a zero-order waveplate where $\phi = 90^\circ$ as opposed to a multi-order quarter-wave plate where $\phi = 270^\circ, 450^\circ$ etc. Similarly it is assumed dispersive effects in the zero-order half-wave FLC can be neglected. The retardance of the quarter-wave plate can be approximated by $\pi/2(1+\kappa_q \upsilon/\omega_0)$, where $\upsilon = \omega - \omega_0$ is the angular frequency offset relative to the ideal quarter-wave operation occurring at ω_0. Similarly for the half-wave FLC with

$\pi(1+\kappa_f \upsilon/\omega_0)$. To first order in υ the signal in each state of the FLC is now

$$2S_{45^\circ}(\omega) = s_0 + s_2\cos\phi(y) + \left(s_1 + \frac{(2\kappa_f+\kappa_q)\pi\upsilon}{2\omega_0}s_3\right)\sin\phi(y) \tag{3.61}$$

$$2S_{90^\circ}(\omega) = s_0 - \left(s_2 - \frac{\kappa_f\pi\upsilon}{\omega_0}s_1\right)\cos\phi(y) + \left(s_1 + \frac{\kappa_f\pi\upsilon}{\omega_0}s_2 + \frac{\kappa_q\pi\upsilon}{2\omega_0}s_3\right)\cos\phi(y) \tag{3.62}$$

where the ω dependence of the Stokes components and ϕ is implied. When $\upsilon = 0$ the ideal results in Eqs. 3.59 and 3.60 are returned. In the case that the $\zeta_c = 0$ operating point (Eq. 3.56) is targeted the s_3 component can be neglected. The phase difference between the carriers in opposite FLC states is then

$$4\theta_\sigma - \frac{\kappa_f\pi\upsilon}{\omega_0}. \tag{3.63}$$

That is, the inferred polarisation angle θ_σ from the phase difference requires a small correction for the frequency/wavelength of the light. For example with a calibration light source that +1nm from the target σ_0 wavelength an offset of 0.07° will need to be added to the inferred value of θ when $\kappa_f = 1$. An example of the Doppler shift across the field of view of the DIII-D neutral beam is shown later in Fig. 4.12. As would be expected, the offset for the two π wings averages to that of the σ emission. The dispersive effects in the quarter-waveplate only contribute to second order in υ/ω_0 and are therefore negligible. An achromatic quarter-wave plate ($\kappa \approx 0$) could be utilised but depending on its construction this could trade away the angular uniformity of the delay given in Eq. 3.20[62].

Including Non-Axial Ray Effects

The quarter-wave plate and FLC have optic axes with $\Theta = 0$ implying the angle ρ_a in Eq. 3.29 only differs from ρ as a second order effect in α. The quarter-wave plate and half-wave FLC manipulate the initial Stokes vector transforming it to $(s_0, \pm s_3, \pm s_2, -s_1)$ where the positive (negative) sign is taken for the 45° red (90° green) FLC state. The rotation of the coordinate system to correct for the $\rho_a - \rho$ difference angle at the displacer therefore couples the s_2 and s_3 components. Taking a first order approximation in α the signal measured by the system is,

$$2S_{45^\circ}(\omega) = s_0 + 2s_3\frac{\alpha}{n_o}\cos\beta + s_1\sin\phi(y) + \left(s_2 - 2s_3\frac{\alpha}{n_o}\cos\beta\right)\cos\phi(y), \tag{3.64}$$

$$2S_{90^\circ}(\omega) = s_0 - 2s_3\frac{\alpha}{n_o}\cos\beta + s_1\sin\phi(y) - \left(s_2 - 2s_3\frac{\alpha}{n_o}\cos\beta\right)\cos\phi(y), \tag{3.65}$$

where n_o is the ordinary refractive index of the displacer. The DC spatial contribution of the $s_3\alpha$ term will integrate to zero for the MSE spectrum but the $s_3\alpha$ term with the $\cos\phi$ spatial carrier has the potential to contaminate the linear polarisation measurement when $\zeta_c \neq 0$. After integrating over the MSE emission the phase difference between the carriers is found to be

$$4\theta_\sigma + 4\frac{\alpha^2}{n_o^2}\cos^2\beta\sin 4\theta_\sigma\tan^2 2\xi_I + O(\alpha^4). \tag{3.66}$$

Evidently the combined fourth order dependence in ξ_I and α renders the non-axial ray effect negligible for the switched IMSE system, even when $\zeta_c \neq 0$.

Misorientation of Waveplates and Non-Ideal Delays

In reality the waveplates in the system will have some small misalignment and their delays will not be precisely quarter-wave or half-wave. In particular the tolerance limitations in the manufacturing of FLC waveplates have resulted in delays that are generally found to be $\sim 10\%$ from the specified delay. When waveplate misalignments and imperfect delays exist in the temporally switched system the response can be generalised to

$$2S_{45^\circ}(\omega) = DC + (w_{+1}s_1 + w_{+2}s_2 + w_{+3}s_3)\cos\phi(y) + (w_{+4}s_1 + w_{+5}s_2 + w_{+6}s_3)\sin\phi(y) \tag{3.67}$$

$$2S_{90^\circ}(\omega) = DC + (w_{-1}s_1 + w_{-2}s_2 + w_{-3}s_3)\cos\phi(y) + (w_{-4}s_1 + w_{-5}s_2 + w_{-6}s_3)\sin\phi(y) \tag{3.68}$$

where the w weighting terms can be determined from a Mueller matrix analysis that includes the actual delays and misorientations in the system and the positive (negative) sign is taken for the 45° red (90° green) FLC state. The DC spatial component is just s_0 when the displacer is at 45° to the final polariser but can more generally include polarised (s_1, s_2, s_3) components. In any case these low spatial frequency components are not used in the measurement and only have small effect on I_0. While the $s_3(\omega)$ component of the emission is known (apart from broadening and upper-state populations) it is problematic to calibrate given that $\alpha_l \neq \alpha_c$. *Therefore it is prudent to target the delay (Eq. 3.56) that satisfies $\zeta_c = 0$ such that the s_3 contribution can be neglected.* In the general case the integration over the MSE spectrum gives,

$$2S_{45^\circ} = I_0\Big(1 + \zeta_+ \sin\big(\phi_0(y) + \alpha_l + 2\theta_\sigma + 4g\big)\Big), \tag{3.69}$$

$$2S_{90^\circ} = I_0\Big(1 + \zeta_- \sin\big(\phi_0(y) + \alpha_l - 2\theta_\sigma + 4h\big)\Big), \tag{3.70}$$

where the functions ζ_+ and g are given by

$$\begin{aligned}
&\zeta_+\big(\zeta_l(\phi_0), \theta_\sigma, \xi_I(\phi_0), \alpha_c - \alpha_l\big) \\
=&\zeta_l(\phi_0)\Bigg(\big(w_{+1}\cos 2\theta_\sigma + w_{+2}\sin 2\theta_\sigma + \tan 2\xi_I(\phi_0)\big(w_{+3}\cos(\alpha_c - \alpha_l) + w_{+6}\sin(\alpha_c - \alpha_l)\big)\big)^2 \\
&+ \big(w_{+4}\cos 2\theta_\sigma + w_{+5}\sin 2\theta_\sigma + \tan 2\xi_I(\phi_0)\big(w_{+6}\cos(\alpha_c - \alpha_l) - w_{+3}\sin(\alpha_c - \alpha_l)\big)\big)^2 \Bigg)^{1/2}
\end{aligned} \tag{3.71}$$

$$\begin{aligned}
&2\theta_\sigma + 4g\big(\theta_\sigma, \xi_I(\phi_0), \alpha_c - \alpha_l\big) \\
=&\arctan\left(\frac{w_{+1}\cos 2\theta_\sigma + w_{+2}\sin 2\theta_\sigma + \tan 2\xi_I(\phi_0)\big(w_{+3}\cos(\alpha_c - \alpha_l) + w_{+6}\sin(\alpha_c - \alpha_l)\big)}{w_{+4}\cos 2\theta_\sigma + w_{+5}\sin 2\theta_\sigma + \tan 2\xi_I(\phi_0)\big(w_{+6}\cos(\alpha_c - \alpha_l) - w_{+3}\sin(\alpha_c - \alpha_l)\big)}\right),
\end{aligned} \tag{3.72}$$

and the functions ζ_- and h can be obtained with a simple interchange of the subscripts from + to -. The variation of the contrast terms ζ_+ and ζ_- is typically small and only important to the measurement through signal to noise effects. The polarisation orientation is then determined from the phase difference, Δp, of the carrier fringes in either state of

the FLC which is related to the polarisation orientation via,

$$\begin{aligned}\Delta p =&\text{Phase}(S_{45^\circ}) - \text{Phase}(S_{90^\circ})\\ =&4\Big(\theta_\sigma + g\big(\theta_\sigma, \xi_I(\phi_0), \alpha_c - \alpha_l\big) - h\big(\theta_\sigma, \xi_I(\phi_0), \alpha_c - \alpha_l\big)\Big)\\ =&4F\big(\theta_\sigma, \xi_I(\phi_0), \alpha_c - \alpha_l\big)\end{aligned} \tag{3.73}$$

where Phase() is the experimentally measured phase of the carrier fringe. $\Delta p = 4F$ are essentially the same functions but for convenience the Δp notation is used for an experimental measurement and F is used to describe the theoretical/calibrated response function. The equation remains solvable/invertible for θ_σ provided that F remains a monotonic function of θ_σ, which is certainly the case for the typical misalignment and imperfect delays encountered.

For a system with non-ideal 'half-wave' FLC waveplate with delay given by $\pi + \eta$ we have from Eq. 3.9 that $\mathbf{p}_{45^\circ} = (1, \cos\eta\sin\phi, \cos\phi, \sin\eta\sin\phi)$ and $\mathbf{p}_{90^\circ} = (1, \sin(\phi + \eta), -\cos(\phi+\eta), 0)$. Hence $w_{+1} = 0$, $w_{+2} = 1$, $w_{+3} = 0$, $w_{+4} = \cos\eta$, $w_{+5} = 0$, $w_{+6} = \sin\eta$, $w_{-1} = \sin\eta$, $w_{-2} = -\cos\eta$, $w_{-3} = 0$, $w_{-4} = \cos\eta$, $w_{-5} = \sin\eta$ and $w_{-6} = 0$ such that

$$g(\theta, 0, \alpha_c - \alpha_l) = \frac{1}{16}\sin(4\theta)\eta^2 + O(\eta^4), \tag{3.74}$$

$$h(\theta, 0, \alpha_c - \alpha_l) = \frac{1}{4}\eta. \tag{3.75}$$

The non-ideal half-wave FLC therefore introduces a $\eta/4$ offset to the ideal phase difference encoding of the polarisation orientation along with a weak variation with input linear polarisation orientation.

The interpretation is further complicated as the delay of the FLC is not spatially uniform, as seen in Fig. 3.16. The net delay imparted by the FLC is therefore dependent on the ray paths and intensities that illuminate the FLC.

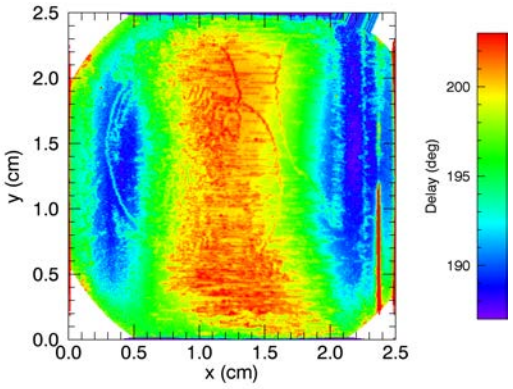

Figure 3.16: Spatial variation of the FLC retardance across the 2.5cm × 2.5cm cell. Ideally the retardance would be uniform and 180°.

The exact form of g and h can be calibrated experimentally or modelled if the characteristics of the entire system are known[40]. Analytic models for the polarimeter response such as in Ref. [40] do not satisfactorily replicate the experimental calibration, particularly when the FLC retardance is dependent on the ray paths through the system. Hence a lookup table generated from a calibration with a linearly polarised light source is the

preferred method for correcting the polarimeter response. A detailed example of this calibration procedure, that also considers ellipticity, is given later in Sections 4.2.1 and 4.2.2. It is essential for the calibration source to replicate the ray paths through the system due to the spatial dependence of the FLC. Ideally for calibration, a linear polariser can be rotated in front of the polarimeter during a plasma shot to accurately reproduce both the wavelength and ray paths as implemented in Ref. [56].

3.5 Alternative IMSE Encoding Strategies

In this section alternative IMSE encoding strategies are outlined, such as a single spatial heterodyne system for measuring ξ_I and amplitude and phase double spatial heterodyne systems for measuring θ_σ. An individual channel, purely temporally modulated polarisation coherence imaging system proposed for ITER to minimise the impact of broadband partially polarised reflections is published in Ref. [57] and is not discussed in this thesis.

3.5.1 Doubly Switched Single Spatial Heterodyne

The standard temporally switched polarimeter detailed in section 3.4 cannot measure circular polarisation. However when the FLC delay significantly deviates from half-wave the linear polarisation measurement can be corrupted by circular polarisation[63]. In an attempt to measure and correct for the elliptical Stark-Zeeman polarisation the front quarter-wave plate can be interchanged with a quarter-wave FLC to allow the polarimeter to also measure the circular polarisation, as tested on the KSTAR tokamak[40]. In this section there are now four different possible combinations from the two different FLCs. The two new combinations introduced from the new second state of the quarter-wave FLC are shown in Fig. 3.17. Alternatively the quarter-wave plate in Fig. 3.14 could be mechanically toggled in and out of the system, with the advantage of avoiding a second non-spatially uniform FLC, but with the drawback of taking longer to switch and possible limitations on repeatability. In the second state of the quarter-wave FLC the system measures

$$2S_{d,45^\circ}(\omega) = s_0 + s_2 \sin\phi(\omega, y) + s_3 \cos\phi(\omega, y), \tag{3.76}$$

$$2S_{d,90^\circ}(\omega) = s_0 + s_2 \sin\phi(\omega, y) - s_3 \cos\phi(\omega, y). \tag{3.77}$$

With an elliptically polarised monochromatic light source the relative magnitude of s_3 to s_2 can be determined from the carrier phase difference between frames with different states of the half-wave FLC. Applying this phase difference calibration procedure naively assumes that the MSE emission has a fixed ellipticity[63], but as formulated in Chapter 2, this is not the case. Integration over the MSE spectrum when $\alpha_l = \delta_c = 0$ gives,

$$2S_{d,45^\circ} = I_0\Big(1 + \zeta_l\big(\sin 2\theta_\sigma + m_\pm \tan 2\xi_I(\phi_0)\big)\sin\phi_0(y)\Big), \tag{3.78}$$

$$2S_{d,90^\circ} = I_0\Big(1 + \zeta_l\big(\sin 2\theta_\sigma - m_\pm \tan 2\xi_I(\phi_0)\big)\sin\phi_0(y)\Big). \tag{3.79}$$

In this case there is no phase difference between alternate images, instead only a change in the relative contrasts/amplitudes of the carrier. Thus the interferometric ellipticity of the light can be measured from the difference in the fringe contrast. However a calibration with monochromatic light does not reproduce this amplitude response to the MSE spectrum and when the half-wave FLC delay significantly deviates from 180° the purely amplitude

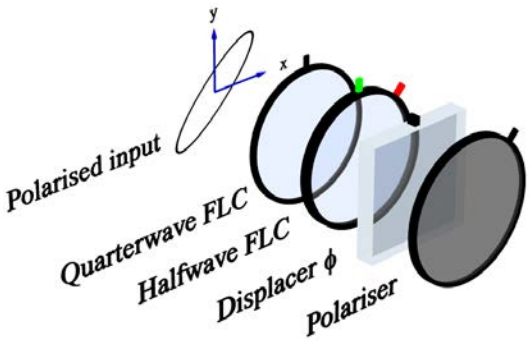

Figure 3.17: Doubly switched single spatial heterodyne showing the new quarter-wave FLC axes position $\rho = 90°$. The other axes position of the quarter-wave FLC is seen in Fig. 3.14.

coupling of the effective interferometric ellipticity is lost. Hence purely experimental or theoretical calibration corrections to obtain the interferometric ellipticity are challenging. For this reason the preferred implementation of a single spatial heterodyne would be to instead target the operating point $\zeta_c(\phi) = 0$ (Eq. 3.56). This way the sensitivity to ξ_I is eliminated/minimised without over complicating the system with a second FLC and sacrificing temporal resolution.

3.5.2 Amplitude Double Spatial Heterodyne

For true snapshot imaging, where all information is contained within a single image, a second carrier fringe pattern is needed to separate θ_σ from the generally unknown spectral term $\phi_0(y) + \alpha_l$. The Amplitude double Spatial Heterodyne (ASH) was first proposed in 2008[2] and the polarimeter response was generalised to include (monochromatic) circular polarisation in Ref. [55]. An ASH has been developed and installed for IMSE measurements on the ASDEX-U tokamak. A review of the experimental performance of the ASDEX-U system is presented in Ref. [56] and plasma measurements are presented in Refs. [64] and [65]. In this section the influence of Stark-Zeeman net circular polarisation and non-axial rays on the ASH are formulated for the first time.

The layout of the ASH polarimeter is presented in Fig. 3.18 and an image produced by the system is seen later in the left of Fig. 3.19. The idealised signal produced by the system is,

$$\begin{aligned} 4S_A(\omega) =& 2s_0 + 2s_2 \cos\phi_D(\omega, y) + s_1\big(\cos(\phi_D(\omega, y) + \phi_S(\omega, x)) - \cos(\phi_D(\omega, y) - \phi_S(\omega, x))\big) \\ &+ s_3\big(\sin(\phi_D(\omega, y) + \phi_S(\omega, x)) + \sin(\phi_D(\omega, y) - \phi_S(\omega, x))\big) \end{aligned} \tag{3.80}$$

where it is understood the terms on the right hand side are functions of ω, $\phi_S(\omega, x) \approx k_x(\omega)x$ is the net delay of the Savart and $\phi_D \approx \phi_{offset}(\omega) + k_y(\omega)y$ is the delay of the

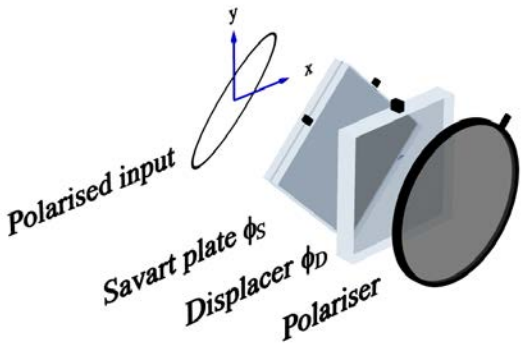

Figure 3.18: Amplitude double spatial heterodyne polarimeter layout with Savart plate axes at 45° and 135°, displacer at 90° and polariser at 45°.

displacer. Integrating over the MSE spectrum gives

$$\begin{aligned}4S_A =& I_0\Big(2 + 2\sin 2\theta_\sigma \zeta_l(\phi_D)\cos(\phi_D(y) + \alpha_l) \\ &+ \cos 2\theta_\sigma\big(\zeta_l(\phi_D + \phi_S)\cos(\phi_D(y) + \phi_S(x) + \alpha_l) - \zeta_l(\phi_D - \phi_S)\cos(\phi_D(y) - \phi_S(x) + \alpha_l)\big) \\ &+ \big(\zeta_c(\phi_D + \phi_S)\sin(\phi_D(y) + \phi_S(x) + \alpha_c) + \zeta_c(\phi_D - \phi_S)\sin(\phi_D(y) - \phi_S(x) + \alpha_c)\big)\Big)\end{aligned} \tag{3.81}$$

where now $\phi_{0,D}(y) = \phi_D(\omega_0, y) \approx \phi_{offset}(\omega_0) + k_y(\omega_0)y$ and $\phi_{0,S}(x) = \phi_S(\omega_0, x) \approx k_x(\omega_0)x$. When $\alpha_l = \delta_c = 0$ the carriers simplify to (using notation in Ref. [56])

$$\begin{aligned}8A(+,\pm) &= \zeta_l(\phi_{0,D} \pm \phi_{0,S})\big(\pm\cos 2\theta_\sigma - m_\pm \tan 2\xi_I(\phi_{0,D} \pm \phi_{0,S})\big)\exp\big(i(\phi_{0,D} \pm \phi_{0,S})\big) \\ 8A(+,0) &= 2\sin 2\theta_\sigma \zeta_l(\phi_{0,D})\exp(i\phi_{0,D}).\end{aligned} \tag{3.82}$$

where the first sign term in A represents the $\phi_{0,D}$ spatial carrier and the second term the $\phi_{0,S}$ spatial carrier. We can see s_1 ($\cos 2\theta_\sigma$) and s_3 ($\tan 2\xi_I$) share the same spatial carriers and are in phase/antiphase for IMSE measurement. This differs to a monochromatic calibration source (Eq. 3.80) where the s_1 and s_3 carriers are in quadrature as $|8A(+,\pm)| = |\pm s_1 - is_3| = \sqrt{s_1^2 + s_3^2}$. When $\alpha_l \neq \delta_c$ there will be some phase difference between the s_1 and s_3 carriers that complicates the interpretation, however the difference is expected to be small ($|\alpha_l - \delta_c| \ll \pi/2$).

As recomended in Ref. [56], a simple demodulation for θ_σ can be obtained by taking the geometric mean of the two s_1 carriers $A(+,\pm)$. This demodulation strategy was suggested to minimise the influence of differences in $\zeta(\phi)$ for each of the carriers ($\phi_{0,D}$, $\phi_{0,D} + \phi_{0,S}$ and $\phi_{0,D} - \phi_{0,S}$), which is most pronounced for larger values of $|\phi_{0,S}|$ towards the left and right of the image. However when the Stark-Zeeman ellipticity is considered the following arithmetic mean demodulation strategy is suggested here, instead of the geometric mean, as it reduces the influence of both variations in $\zeta(\phi)$ as well as interferometric ellipticity coupling effects. The arithmetic mean is (assuming $\cos 2\theta_\sigma > \tan 2\xi_I$)

$$\frac{|A(+,0)|}{|A(+,+)| + |A(+,-)|} = |\tan 2\theta|. \tag{3.83}$$

The arithmetic mean, like the geometric mean, is insensitive to first order variation in $\zeta_l(\phi)$ as the denominator is proportional to $\zeta_l(\phi_{0,D}+\phi_{0,S})+\zeta_l(\phi_{0,D}-\phi_{0,S}) \approx 2\zeta_l(\phi_{0,D})$. The interferometric ellipticity also contributes to the denominator in the term $(\zeta_c(\phi_{0,D}+\phi_{0,S})-\zeta_c(\phi_{0,D}-\phi_{0,S}))$ which is expected to be negligible and zero where $\phi_{0,S}=0$.

With this complete treatment of the Stark-Zeeman circular polarisation *it is evident that the interferometric ellipticity is now encoded in the relative amplitude of the* $A(+,\pm)$ *carriers* and can be determined from (assuming $\cos 2\theta_\sigma > \tan 2\xi_I$),

$$\frac{|A(+,-)|-|A(+,+)|}{\sqrt{|A(+,0)|^2+(|A(+,+)|+|A(+,-)|)^2}} = m_\pm \tan 2\xi_I. \tag{3.84}$$

The numerator contains the term $(\zeta_l(\phi_{0,D}+\phi_{0,S})-\zeta_l(\phi_{0,D}-\phi_{0,S}))\cos 2\theta_\sigma$ that may be of comparable magnitude to the desired ζ_c term in the left and right of the image when ξ_I is small. However along the centre of the image where $\phi_{0,S}=0$ this equation is exact.

It is challenging to calibrate the interferometric ellipticity response of the system because $|A(+,-)|=|A(+,+)|$ for an elliptically polarised monochromatic light source. Similarly the MSE mock calibration spectrum system in Ref. [56] adds a global ellipticity which doesn't recreate the odd symmetry of the MSE circular component. The individual π wings of the mock spectrum would need to be individually elliptically polarised with opposite sign to recreate the effect.

Angular Effects

Here we consider the effect of non-axial rays, as formulated in Sec. 3.2, on an ASH system with displacer cut at general angle $\Theta=\Theta_D$ and the two displacers of the Savart plate cut at $\theta=\pi/4$. To first order in α the carrier pattern is,

$$\begin{aligned}
4S_A(\omega) =& 2s_0 + \big(2s_2 - 4s_1\frac{\alpha}{n_o}\sin(\beta-\pi/4)\big)\cos\phi_D \\
&\Big(s_1 + 2s_1\frac{\alpha}{n_o}\big(\cos\beta\tan\Theta_D - \sin(\beta+\pi/4)\big) + 2s_2\frac{\alpha}{n_o}\sin(\beta-\pi/4)\Big)\cos(\phi_D+\phi_S) \\
&+ s_3\Big(1+2\frac{\alpha}{n_o}\big(\cos\beta\tan\Theta_D - \sin(\beta+\pi/4)\big)\Big)\sin(\phi_D+\phi_S) \\
&- \Big(s_1 - 2s_1\frac{\alpha}{n_o}\big(\cos\beta\tan\Theta_D - \sin(\beta+\pi/4)\big) + 2s_2\frac{\alpha}{n_o}\sin(\beta-\pi/4)\Big)\cos(\phi_D-\phi_S) \\
&+ s_3\Big(1-2\frac{\alpha}{n_o}\big(\cos\beta\tan\Theta_D - \sin(\beta+\pi/4)\big)\Big)\sin(\phi_D-\phi_S) \\
&- 4\frac{\alpha}{n_o}\cos\beta\tan\Theta_D(s_3\sin\phi_S + s_1\cos\phi_S) \\
&+ 2\sqrt{2}s_1\frac{\alpha}{n_o}\sin\beta\big(\cos(\phi_D+\phi_{S_1}) + \cos(\phi_D-\phi_{S_1})\big) \\
&+ 2\sqrt{2}s_3\frac{\alpha}{n_o}\sin\beta\big(\sin(\phi_D+\phi_{S_1}) - \sin(\phi_D-\phi_{S_1})\big) \\
&+ 2\sqrt{2}s_2\frac{\alpha}{n_o}\sin\beta\big(\cos(\phi_D+\phi_{S_2}) - \cos(\phi_D-\phi_{S_2})\big)
\end{aligned} \tag{3.85}$$

where ϕ_{S_1} and ϕ_{S_2} are the delays of the individual displacers that make up the Savart plate such that $\phi_S=\phi_{S_1}-\phi_{S_2}$. It is assumed the displacer and Savart are made of the same material and therefore have a common value for n_o. The carriers in the first five lines (other than the DC s_0 term) in Eq. 3.85 are of interest for the linear polarisation measurement. The remaining carriers result purely from non-axial rays partially delayed

by various combinations of two of the three displacers in the system. The ASH image when including non-axial rays is shown in Fig. 3.19 along with its 2D Fourier transform where the 3 carriers of interest are seen along with the 5 first order in α non-axial carriers. These weaker additional carriers are visible in Fig. 3b) of Ref. [56], are likely due to a combination of this non-axial ray effect along with any possible small misalignments of the plates.

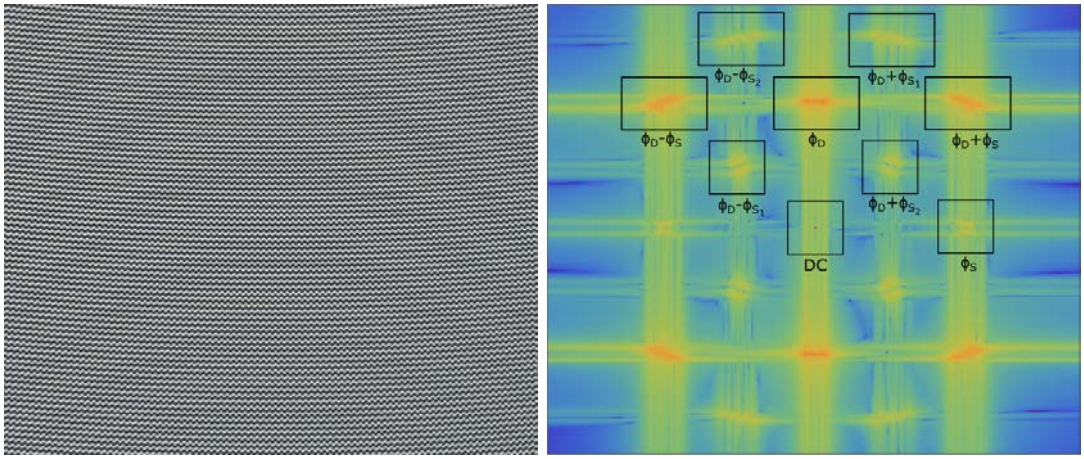

Figure 3.19: (Left) Modelled amplitude double spatial heterodyne fringe pattern with $s_1 = s_0\sqrt{2/3}$, $s_2 = s_0/\sqrt{3}$ and $\lambda = 660$nm from a 2×3mm αBBO Savart plate and a 5mm $\Theta_D = 30°$ αBBO displacer. (Right) Zoomed in Fourier transform (absolute value) showing the 6 main carriers and 10 weaker carriers. A uniform intensity is applied across the image so the DC carrier is not broadened.

When applying the arithmetic mean demodulation strategy to Eq. 3.85 the result is,

$$\arctan\left(\frac{|A(+,0)|}{|A(+,+)|+|A(+,-)|}\right) = 2\theta_\sigma - \arctan\left(2\frac{\alpha}{n_o}\sin(\beta-\pi/4)\right) \tag{3.86}$$

correct to first order in α and s_3. *The second term on the right produces a linear ramp spatial offset that can easily be calibrated.* The offset results from the coupling of s_1 and s_2 due to the difference between the angles ρ and ρ_a occurring at the first displacer of the Savart plate. Difference between the angles occurring further along in the polarimeter result in non-axial carriers that are not used for the measurement. When higher order terms in α are included and s_3 is neglected the response becomes slightly non-linear in θ, but again this can be calibrated. In this case the offset ramp for $\theta = 0$ is shown in the left of Fig. 3.20 and is very similar to the approximation in Eq. 3.86.

It is instructive to consider including an initial quarter-wave plate in the ASH system as an additional example of this non-axial ray effect. When ignoring non-axial ray effects one would expect that including an initial quarter-wave plate aligned with the Savart plate would only offset the phase of the ϕ_S carriers without affecting their amplitude. However the quarter-wave plate first interchanges the s_1 and s_3 positions before the first order in α angle difference $\rho_a - \rho$ occurs at the Savart plate. For linearly polarised light this limits the non-axial ray effect to second order in α. This new offset can be seen in the right of Fig. 3.20. Including the quarter-wave plate serves as an interesting comparison but it is not recommended as the offset can be calibrated in either case.

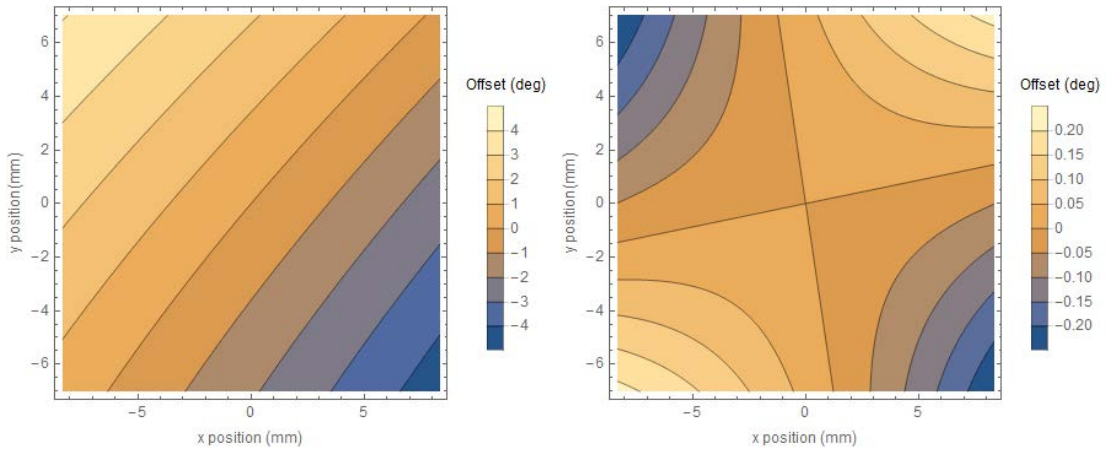

Figure 3.20: (Left) Angle offset due to non-axial ray effects for the amplitude spatial heterodyne with $\theta = 0$ input. (Right) Same as left but with an initial quarter-wave plate included at $\rho = 45°$ to limit the non-axial ray effects on the incident linear polarisation.

Radial Bandwidth

A number of strategies are available for maximising the radial bandwidth of the ASH system. From Fig. 3.19 it is evident that the main ϕ_D and $\phi_D \pm \phi_S$ carriers are at the same vertical position in the power spectrum, hence the radial bandwidth cannot be 'opened' to resolve sharp changes in the radial direction. This is unlike the single spatial heterodyne where ϕ_D and the DC component are the only carriers and the radial bandwidth can be maximised without capturing unwanted carriers. The simplest strategy to increase the ASH radial bandwidth would be to rotate the polarimeter relative to the camera to offset the vertical position of the main carriers. However in this case it is challenging to avoid capturing the non-axial carriers when increasing the bandwidth. A more favourable strategy is to use a field widened Savart in the ASH instead of a regular Savart plate, as illustrated in the left of Fig. 3.21. In this case the non-axial carriers with individual ϕ_{S_1} or ϕ_{S_2} terms are limited to second order in α and the main carriers are automatically offset in the vertical direction. The unobstructed radial bandwidth for the main carriers in the FW ASH is illustrated in the right of Fig. 3.21. It is possible to go even further and align all the carriers along the vertical axis by including another half-wave plate in-between the Savart and displacer, but this case is not shown.

Comparison with Switched FLC system

Here the relative advantages and disadvantages of the TSSSH and ASH are listed. Upper-case roman superscripts are used to indicate challenges that are comparable for the two systems. In approximate order of importance the advantages of the switching FLC system are:

- Greater spatial resolution due to only having a single carrier fringe pattern. To resolve narrow structures in the plasma, such as the edge pedestal, the fringes can be oriented to provide the greatest spatial resolution in the radial direction.
- The non-uniformity in the ASH Savart plate thickness (parallelism) decreases the 'intrinsic contrast' in the $A(+, \pm)$ carrier but not the $A(+, 0)$ carrier, as detailed in

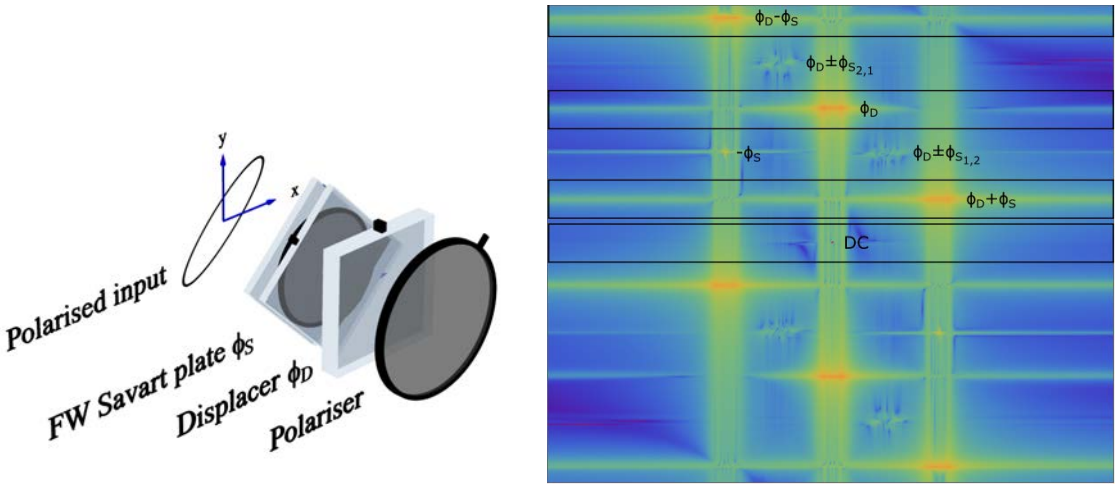

Figure 3.21: (Left) Amplitude spatial heterodyne with a field widened Savart plate. The initial displacer in the Savart is at $\rho = -45°$, the interposed half-wave plate is at $\rho = 0°$ and second displacer is at $\rho = 135°$. (Right) Power spectrum for the FW ASH revealing the different carriers and increased bandwidth in the radial direction. The non-axial ϕ_S carriers is a first order in α while the weak $\phi_D \pm \phi_{S_1}$ and $\phi_D \pm \phi_{S_2}$ carriers are second order in α. The system is modelled with $s_1 = s_0\sqrt{2/3}$, $s_2 = s_0/\sqrt{3}$ and $\lambda = 660$nm from a 2×2mm αBBO FW Savart plate and a 5mm $\Theta_D = 30°$ αBBO displacer.

Ref. [56]. This introduces a dependence on the ray paths through the polarimeter which requires careful calibration.[A]

- The different delays for the $A(+,+)$, $A(+,0)$ and $A(+,-)$ carriers in the ASH system can differ by $\sim 5\%$ in the left and right of the image where $|\phi_S| > 0$. However the geometric and arithmetic mean demodulation strategies significantly reduce any differences.
- With only a single carrier the fast Fourier transform (FFT) can be taken across a single column of the sensor to determine the polarisation angle. This makes the real-time analysis more feasible for the switched system unlike the ASH which requires a 2D FFT.
- The ASH system is weakly sensitive to temporal variations in any temperature gradients across the Savart plate.[B]

The relative disadvantages of the switching FLC system are:

- The simple switching system is sensitive to fluctuations in the neutral beam velocity on the time scale of the exposure, requiring corrections if the fluctuations are large.
- The non-uniformity in the FLC introduces a dependence on the ray paths through the polarimeter which requires careful calibration as outlined in Ref. [61].[A]
- The ASH is a true snapshot imaging system, all information is contained in a single image. The switching system initially requires two exposures to separate the θ_σ and $\phi_0(y) + \alpha_l$ phase terms.
- The switching system is sensitive to the weak temperature dependence of the FLC retardance.[B]

- The retardance inaccuracy of the FLC causes the switching system to be more sensitive to the Stark-Zeeman circular polarisation. This can be alleviated by targeting $\zeta_c = 0$

- The switching system cannot measure the interferometric ellipticity of the MSE emission.

- When the FLC axes are switched in 'rolling shutter' camera readout mode the fringe pattern becomes blurred. In 'global shutter' readout mode this is not an issue as the FLC fully switches during readout.

3.5.3 Phase Double Spatial Heterodyne

Including an initial quarter-wave plate in the amplitude spatial heterodyne system (oriented with $\Delta\rho = 45°$ to the Savart) interchanges the s_2 and s_3 components, such that the polarisation angle becomes encoded in the phase of the carrier[55]. This IMSE polarimeter, known as the Phase double Spatial Heterodyne (PSH), is shown in Fig. 3.22. The general signal produced by the polarimeter is

$$\begin{aligned} 4S_P(\omega) =& 2s_0 + s_1\big(\cos(\phi_D(\omega,y) + \phi_S(\omega,x)) - \cos(\phi_D(\omega,y) - \phi_S(\omega,x))\big) \\ & - s_2\big(\sin(\phi_D(\omega,y) + \phi_S(\omega,x)) + \sin(\phi_D(\omega,y) - \phi_S(\omega,x))\big) + 2s_3\cos\phi_D(\omega,y) \end{aligned} \tag{3.87}$$

and when integrating over the MSE spectrum the signal simplifies to

$$\begin{aligned} 4S_P =& I_0\Big(2 + \zeta_l(\phi_D + \phi_S)\cos\big(\phi_D(y) + \phi_S(x) + \alpha_l + 2\theta_\sigma\big) \\ & - \zeta_l(\phi_D - \phi_S)\cos\big(\phi_D(y) - \phi_S(x) + \alpha_l - 2\theta_\sigma\big) + 2\zeta_c(\phi_D)\cos\big(\phi_D(y) + \alpha_c\big)\Big) \end{aligned} \tag{3.88}$$

where, similarly to the ASH, $\phi_{0,D}(y) = \phi_D(\omega_0, y) \approx \phi_{offset}(\omega_0) + k_y(\omega_0)y$ and $\phi_{0,S}(x) = \phi_S(\omega_0, x) \approx k_x(\omega_0)x$. The polarisation angle can now be demodulated from the phase difference of the $A(+,+)$ and $A(+,-)$ carriers, independent of $\phi_{0,D}$. This phase difference measurement is dependent on the $\phi_{0,S}$ which is less sensitive to spectral and temperature variations than $\phi_{0,D}$ due to the Savart plate having zero net delay. Nevertheless determination of $\phi_{0,S}$ requires a neutral beam like calibration source such as beam into gas calibration and temperature stability is required between the calibration and plasma measurement. The phase double spatial heterodyne is not currently favoured for IMSE measurements due to these calibration challenges.

The effective interferometric ellipticity ξ_I is straightforward to measure with the phase double heterodyne from the relative amplitudes of $A(+,0)$ and $A(+,\pm)$. A monochromatic elliptical polarisation calibration remains valid for the IMSE emission as the measurement is independent of carrier phases.

The PSH quarter-wave plate could be interchanged with a quarter-wave FLC for a combined phase and amplitude spatial heterodyne polarimeter, as described in Ref. [56]. In one state the FLC axes are aligned with the Savart plate to effectively recreate the ASH and the axes in the second state are aligned at $\rho = 90°$, as per Fig. 3.22, to recreate the PSH.

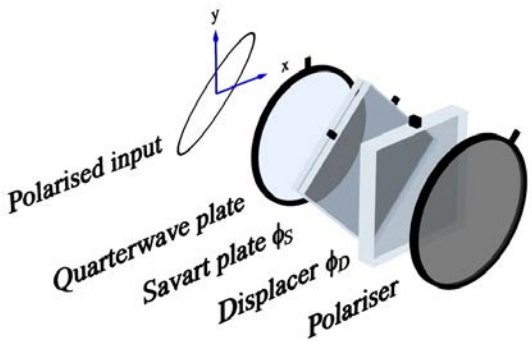

Figure 3.22: Phase double spatial heterodyne polarimeter layout. The system is the same as the ASH but with an initial quarter-wave plate at 90°.

3.6 Conclusion

Polarisation coherence imaging, in particular IMSE, is a powerful technique for measuring the polarisation of a net unpolarised spectral multiplet. Spectral discrimination is achieved by coupling the spectral and polarisation information to achieve a large net linear polarisation fraction. The challenge then remains to separate polarisation orientation from the spectral information, which can be achieved with a number of different encoding strategies. The temporally switched single spatial heterodyne and amplitude double spatial heterodyne are presently the favoured encoding strategies.

In some instances IMSE polarimeters encode the s_3 circular polarisation in the same carrier as the s_1 or s_2 linear polarisation, hence consideration must be given to the interferometric properties of the significant Stark-Zeeman circular polarisation fraction that was formulated in Chapter 2. Fortunately the Stark-Zeeman net circular polarisation fraction is significantly reduced by the sinusoidal spectral filter width that maximises the linear polarisation fraction and with careful selection of the sinusoidal filter width the interferometric ellipticity can be negated. The ASH system cannot easily measure the circular polarisation of monochromatic light but can measure the effective interferometric circular polarisation of the MSE emission owing to the odd symmetry of the s_3 spectra about ω_0.

The TSSSH system delivers the greatest spatial resolution and has been used to resolve the H-mode edge pedestal when implemented on the KSTAR tokamak[63, 27]. A number of calibration corrections are outlined to account for non-ideal waveplates/FLC orientations and retardances, spatial non-uniformity in the FLC delay and differences between calibration and plasma wavelength.

It has been shown that the 'angle difference' for non-axial rays, when incident on a $\Theta > 0$ waveplate, leads to an additional coupling of the s_1 and s_2 linear Stokes components. An unexpected implication is that non-axial carriers and a spatial offset ramp in the ratio of the carrier amplitudes are unavoidable for the ASH polarimeter.

Chapter 4

Imaging MSE on DIII-D

A temporally switched single spatial heterodyne (TSSSH) imaging MSE system[2], introduced in Section 3.4, was successfully operated on the DIII-D tokamak for a two month period in early 2016 (shots 165676-166617). The IMSE system was tested concurrently with well-established conventional MSE polarimeters and demonstrated good agreement for shots with plasma current and toroidal field in the standard direction. The properties of the radial view utilised by the IMSE system is outlined in Section 4.1 and the calibration of the polarimeter are detailed in Section 4.2. A comparison of the IMSE and conventional MSE measurements is presented in Section 4.3 along with interesting results that demonstrate the operating principles and self-consistency of the IMSE measurements.

4.1 Viewing Geometry and Design Considerations

Conventional photoelastic modulator (PEM) MSE polarimeters[1] have been used on the DIII-D tokamak for over 25 years[16, 66] and have since been expanded to 69 channels, viewing two different beams from four different directions[49]. The IMSE polarimeter was installed on the radial 15° MSE viewing port, shown in Fig. 4.1, that was previously used for a dual-view measurement of both the radial and motional electric fields with conventional polarimeters[12, 67]. The port has a direct view of the plasma without any need for a mirror, one of the common sources of error for polarimetric MSE measurements. Two neutral deuterium beam sources, known as 30L (thirty left) and 30R (thirty right), are observable in the IMSE view. The narrowband filters in the conventional PEM polarimeters are tuned to the σ component of the 30L beam which is usually operated at 81keV ($2.79 \times 10^6 \mathrm{m\,s^{-1}}$). The 30R beam is often derated to 75keV ($2.68 \times 10^6 \mathrm{m\,s^{-1}}$) or less to decrease the Doppler shift at the 'edge' 45° and 'tangential' 315° views, to avoid overlap of the 30L and 30R full energy MSE multiplets. On the other hand at the 15° port the Doppler shift is relatively stronger for the 30R beam compared with the 30L beam, hence *derating 30R increases the overlap of the two spectra for the IMSE view such that the IMSE system can measure from either the 30L or 30R beams.* However the disadvantage is that the interpretation of the IMSE measurement is, at the very least, complicated when the beams are operated simultaneously as the sightlines intersect the beams at different radial positions and with different Doppler shifts.

Consideration must be given to the harsh environment presented by radiation and strong electromagnetic fields when installing a camera system on a fusion device. DIII-D is usually operated with deuterium fuel. The cross section for the $^2\mathrm{D}+^2\mathrm{D}\rightarrow{}^3\mathrm{T}+^1\mathrm{H}$ and $^2\mathrm{D}+^2\mathrm{D}\rightarrow{}^3\mathrm{He}+^1\mathrm{n}$ fusion reaction is ~ 100 times smaller than the deuterium-tritium reaction. However with up to 8 heating neutral beams the tail of the plasma velocity

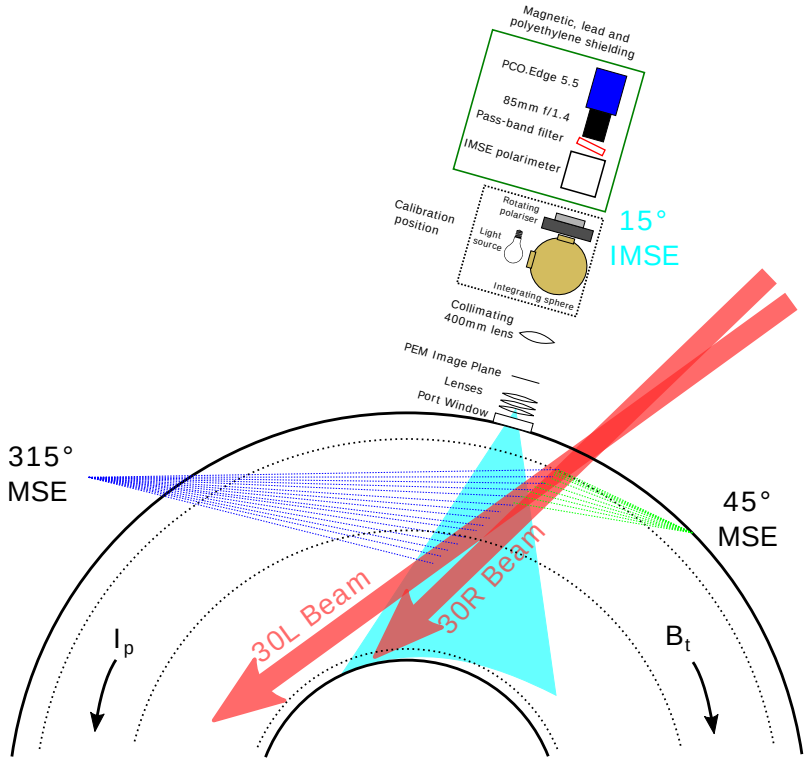

Figure 4.1: Diagram of the IMSE viewing positions and the relevant neutral beams for the measurement. The conventional MSE systems view discrete radial positions on the midplane of the 30L beam. The imaging MSE system is operable with either the 30L or 30R beam. The curved dotted lines indicate the standard position of the inner and outer separatrix at the midplane, and the magnetic axis. The direction of 'normal' plasma current ($I_p > 0$) and 'normal' toroidal magnetic field ($B_t < 0$) are indicated. The IMSE calibration optics in the dashed box are not present for plasma measurements. The calibration procedure is detailed later in Section 4.2 and a basic ray trace of the optical system is shown in Fig. 4.26. The 400mm lens and further downstream optics are on an optical rail detached from the tokamak, as seen later in Fig. 4.2.

distribution is sufficiently energetic for a considerable reaction rate and neutron flux. These neutrons and gamma rays (produced by the interaction of neutrons with reactor materials) can cause short term hot-pixel noise and long term damage on the sCMOS camera sensor. For this reason the camera was housed in a boronated polyethylene box to attenuate the neutron flux and the box was lined with lead bricks to further attenuate gamma rays. The camera was also housed in an iron box to limit the magnetic field strength at the camera which has the potential to saturate its electronic components. These shielding components can be seen in the photos taken during the installation of the system in Fig. 4.2.

4.1.1 Spatial Registration

With high resolution imaging it is straightforward to register the location and view direction of the camera by fitting the location of known objects in the camera image. A significant region of the inner wall tiles structure was captured favourably in the IMSE images. A fit of the tiles in the image to their known location is shown in Fig. 4.3 and the inferred camera position and view direction are given in Table 4.1. Some small distortions

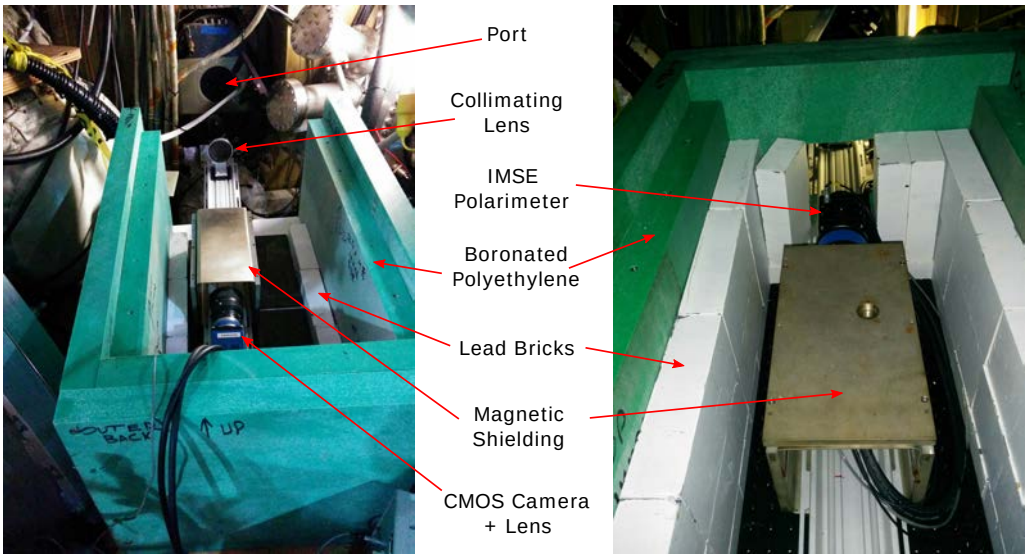

Figure 4.2: Photos taken during the installation of the IMSE system on DIII-D. The shielding and key optical components are highlighted.

exist in the imaging properties of the lenses but the spatial offsets are small.

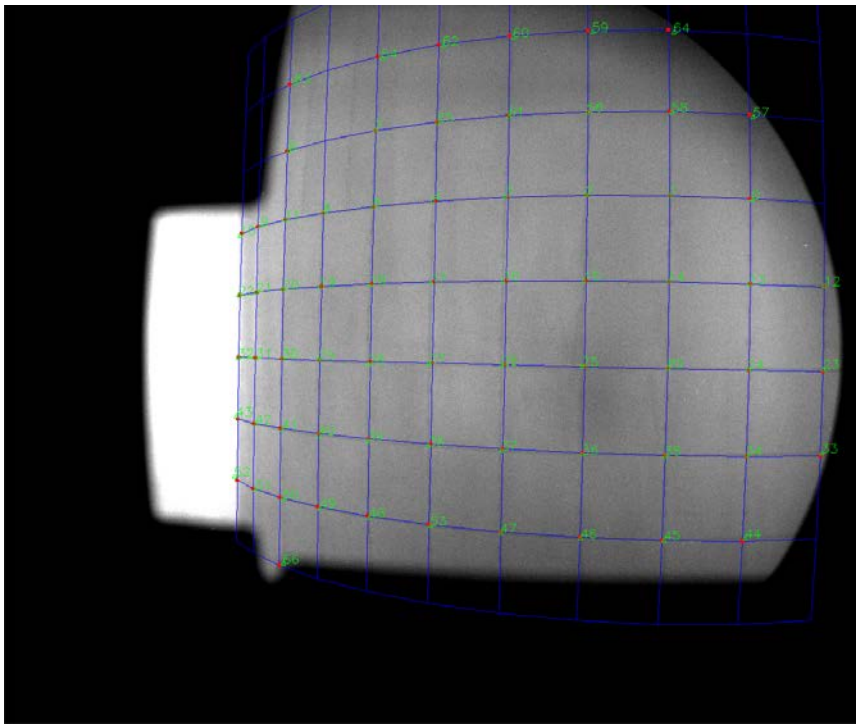

Figure 4.3: Spatial registration of IMSE view showing the outline of tiles on the inner wall. The outline of the port structure is evident from the dark region with no light.

From the registration of the camera geometry it is possible to convert between the camera pixel coordinates and the (R, Z) coordinates of the intersection of the neutral beam and sightlines. These coordinate mappings for both the 30L and 30R beams are shown in Fig. 4.4. The spatial coverage of the 30R beam is significantly greater than that of the 30L owing to the different injection angles of the neutral beams and greater distance

Pinhole location (r, ϕ, z)	$(2634\text{mm}, 74.62°, 15\text{mm})$
Effective Focal Length	19.62mm
Pitch	$-0.56°$
Yaw	$10.89°$
Roll	$1.17°$

Table 4.1: Camera location and view direction using a pinhole lens approximation. The negative pitch signifies that the view has a slight declination, the positive yaw signifies the centre of the view looks to the left of the centre post and the roll indicates the camera rail is rotated slightly anti-clockwise from the horizontal.

from the camera to the 30R beam. Measurements of the 30L beam cover $R = 1.6 - 2.1$m with high pixel density (~ 0.3mm per pixel in the radial direction). The 30R view provides spatial coverage from the inner wall to $R = 2$m but there is an associated reduction in the pixel density (~ 0.6mm per pixel in the radial direction) and signal strength due to beam attenuation.

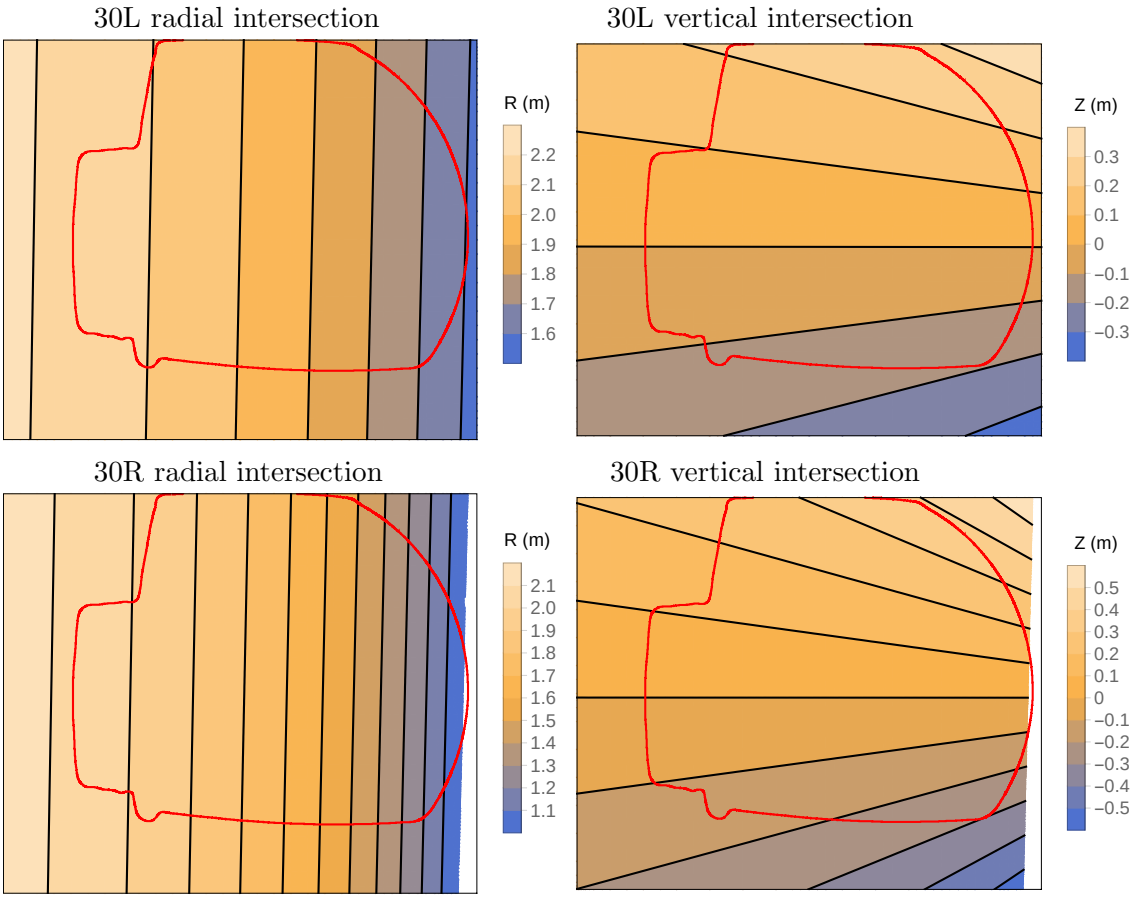

Figure 4.4: Mapping of the (R,Z) intersection with the 30L (top) and 30R (bottom) neutral beam to camera coordinates. The red outline encloses the region of the view that is not obscured by the port structure. The 30R beam centre-line intersects the inner wall, hence coordinates inside $R < 1.01$m are excluded from the plot and represented white.

Using the camera view registration and properties of the displacer waveplate it is possible to calibrate any tilt offset that may exist between the polarimeter and tokamak.

Firstly the polarimeter can be aligned with high accuracy relative to the camera sensor by referencing the interference fringes produced by the displacer. Secondly the relative tilt between the camera sensor and the tokamak, given by the 'Roll' in Table 4.1, is known from the spatial calibration using the fiducial markers in the tokamak.

4.1.2 Beam Divergence and Radial Resolution

Once the viewing coordinates have been determined it is possible to model the relevant parameters for the view. Firstly the polarisation angle expected for either view can be modelled by calculating the direction of the motional electric field from an EFIT equilibrium of the toroidal and poloidal magnetic fields. Line integration effects from the IMSE view are significant given that the neutral beams have a non-negligible 14cm full width at half maximum in the horizontal direction[12]. The radial sightlines from the 15° port intersect the neutral beam over a large range of radii and flux surfaces unlike the 315° view, as evident in Fig. 4.1 and later in Fig. 4.6. An indicator of this line integration width is given in Fig. 4.5 for the IMSE view of both the 30L and 30R beams as well as a comparison with the tangential 315° MSE view of the 30L beam. The plot is comparable to the plot in Ref. [68] that compares the radial resolution of the 315° and 45° MSE ports. It is well known that views of the neutral beam that are approximately tangent to the flux surfaces are preferred, such as the 315° view which is tangent to the flux surfaces at $R = 1.67$m and therefore the radial resolution is optimal. On the other hand the $\delta r \sim 20$cm range of flux surfaces that are integrated/averaged over for the IMSE sightlines will blur any sharp features in the q-profile. While the radial resolution inherent to the IMSE port is far from ideal, it should be noted that the port was chosen for this experiment due to port availability and the view having a relatively straightforward window calibration (using previous Faraday rotation measurements and the view is free of mirrors) given in-vessel or beam-into-gas calibration opportunities weren't possible for the short campaign.

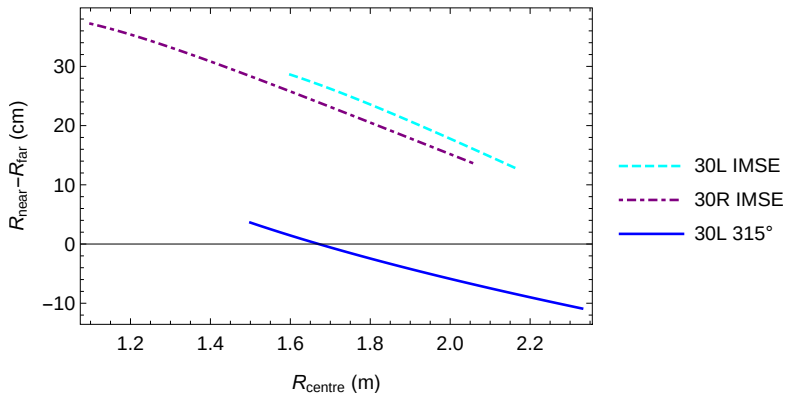

Figure 4.5: Radial resolution of the IMSE view with the 30L and 30R beams compared with the 315° conventional MSE view. The x-axis gives radius of the sightline intersection with the beam centre-line, while the y-axis gives the difference between the radial coordinate for the near and far edges of the beam-sightline intersection assuming a 14cm wide neutral beam.

The neutral beam properties must be considered in greater detail to better understand the line integration effects. The neutral beams are accelerated and neutralised before entering the beam duct through a 0.48m high, 0.12m wide aperture at which point they are modelled as a continuous spatial grid of beamlets (as opposed to discrete beamlets as on

MAST[13]). The extended nature of the source leads to a beam velocity distribution that is a five dimensional function of vertical and horizontal velocity angles and three spatial coordinates[13]. The beamlets have a focal length of 10m with a FWHM divergence of 3.1° in the vertical direction and are focused at infinity with a FWHM divergence of 1.2° in the horizontal direction[69]. The beam aperture is only 6m from the edge of the plasma but the divergence of the beamlets overcomes the vertical focusing of the beam such that the average beam velocity is diverging from the central beam axis by the time it reaches the plasma. Based on these beam parameters the calculated density and divergence angles of the beam along the vertical centre-plane and horizontal tokamak midplane are shown in Figs. 4.6 and 4.7, in the case where attenuation of the beam is neglected (the apparent intensity decrease in the plots is purely due to beam divergence).

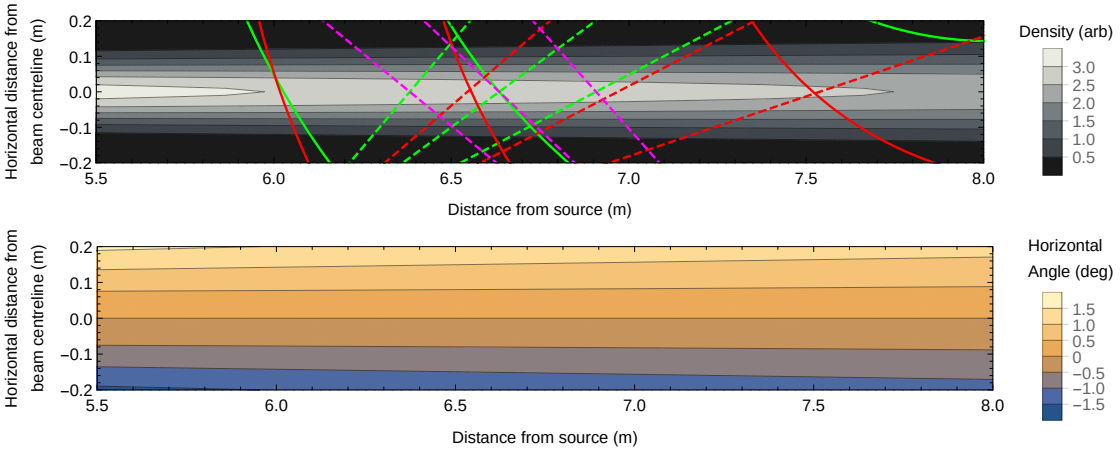

Figure 4.6: (Top) Density of the neutral beam(s) on the horizontal midplane of the beam. The 30L and 30R beams are injected at different angles hence different coloured contours are used to represent the geometry in the different frame of reference for the two beams. Curved green contours represent the radii 2.3m, 1.8m and 1.01m for the 30L beam. Comparable contours for the more steeply injected 30R are in red. The IMSE sightlines that intersect the 30L centre-line at $R = 2$m, 1.8m and 1.6m are shown with dashed green lines and the identical sightlines in the 30R frame of reference are in red ($R = 1.81$m, 1.44m and < 1.01m). The purple dashed lines show the intersection of the 315° MSE sightlines with the 30L beam. (Bottom) Horizontal angle of the average neutral beam velocity.

The vertical divergence of the beam velocity above and below the midplane is inconsequential for conventional MSE measurements that only measure on or near the midplane. However to interpret the information captured by IMSE above and below the midplane the assumption that $\mathbf{v}$ is horizontal (Eq. 1.12) is evidently invalid. The vertical divergence essentially introduces the need for two additional 'A coefficients' for the B_r and B_ϕ components in the numerator of the polarisation orientation equation of Ref. [12]. Furthermore the A_2 and A_3 coefficients also require adjustment and the calculations in Chapter 1 and Eq. 1.13 become more complicated. The net effect of the vertical divergence of the beam velocity can be seen in the MSE polarisation orientation images in Fig. 4.8 for the 30L and 30R beams. The 0° polarisation contour which occurs where $B_z = 0$ is common to both beams in (R,Z) coordinates but the geometric factors in Eq. 1.16 must be considered to relate the measurements from different beams. Similarly polarisation orientation images are given in Fig. 4.9 for the 30L beam for a shot with reverse toroidal field and a shot with reverse plasma current. The most obvious change when either the toroidal field or plasma

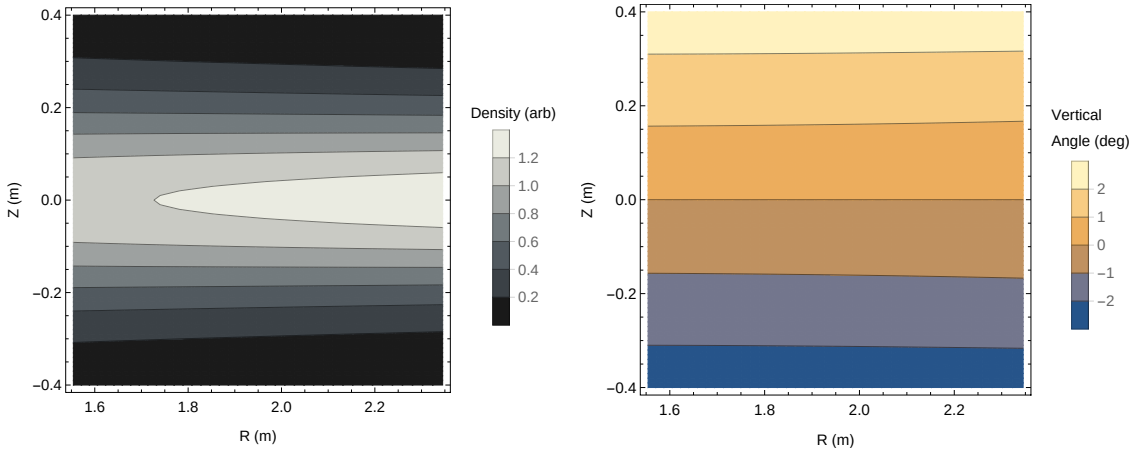

Figure 4.7: (Left) Density of the 30L neutral beam in tokamak coordinates along the central vertical plane of the beam. The (R,Z) coordinates are slightly different for the 30R beam but the trend is similar. (Right) Inclination angle of the average neutral beam velocity.

current are reversed is that the slope of the polarisation orientation $d\theta/dR$ changes. The case with both field and current reversed was not encountered and is therefore not shown, however it would be expected to have similar trends to the case where both are in the standard direction.

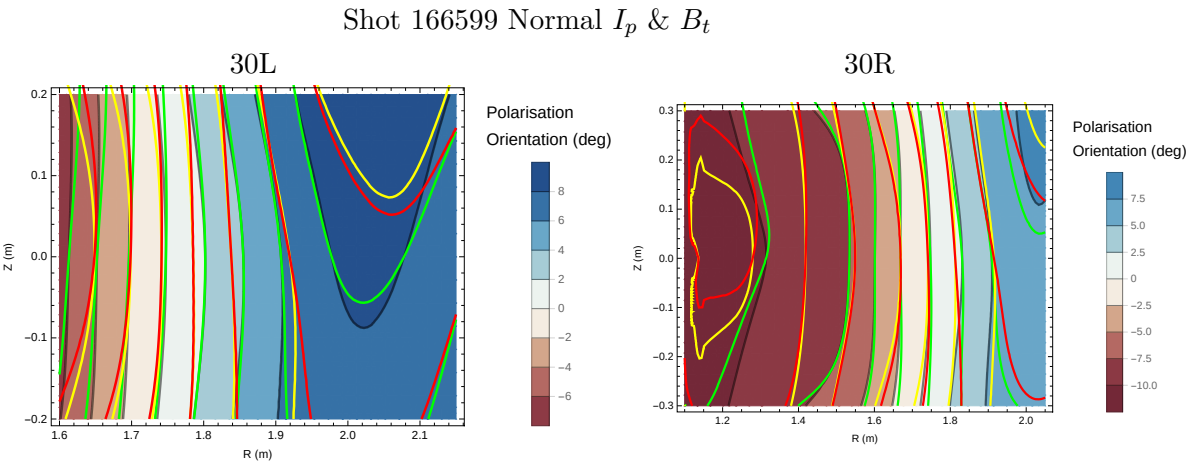

Figure 4.8: EFIT forward model of the polarisation orientation images for the 30L (Left) and 30R beams (Right) for shot 166599 at 2.2s. The black contours and colour scale assumes an infinitesimally thin horizontally injected beam, green contours assume an infinitesimally thin beam with vertical divergence, yellow contours assume a thick horizontally injected beam and red assumes a thick beam with vertical divergence.

With the approximation that the neutral beam velocity is purely horizontal, the contours of constant polarisation are up-down symmetric in regions where B_z is small. Away from the magnetic axis near $R = 2$m some up-down asymmetry is evident and this is produced by the B_z contribution (A_4 coefficient). When the vertical divergence of the beam is included, the up-down symmetry of these contours is further reduced. The vertical divergence increases the polarisation orientation in the low R, $Z < 0$ and high R, $Z > 0$ regions and decrease the polarisation orientation in the opposite two regions. *In the case*

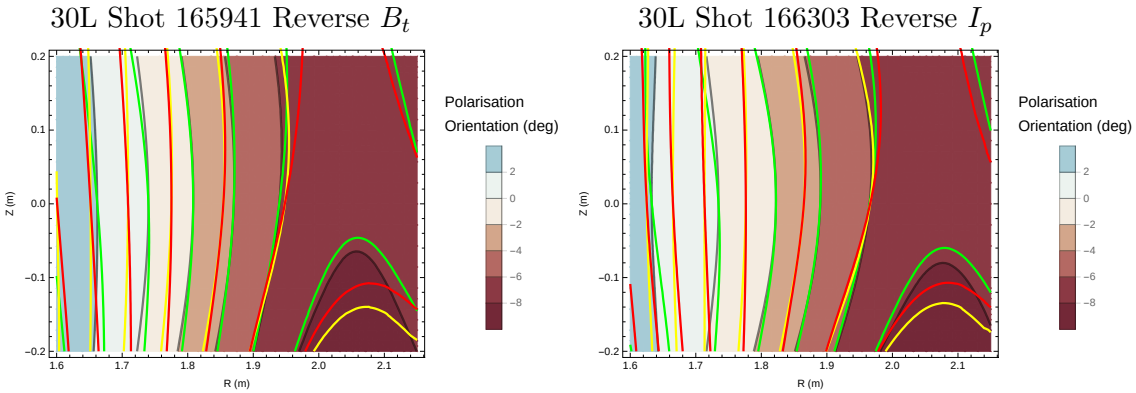

Figure 4.9: Polarisation angle modelled for the 30L beam in for shot 165941 at 3s with reverse toroidal field (Left) and shot 166303 at 1.8s with reverse plasma current (Right). The contours are the same as in Fig. 4.8.

of normal field and current directions this effectively causes the contours to slightly fan outwards from the top of the image. In the opposite case, *when either the plasma current or toroidal field (but not both) are reversed, the contours of constant polarisation orientation fan outwards slightly from the bottom of the image.* This is evident when comparing the black and green contours in Figs. 4.8 & 4.9.

A second effect relates to the finite width of the neutral beam and the horizontal divergence. Account of this effect requires a weighted Stokes vector line-integration that includes the varying Doppler shift due to the horizontal divergence of the beam velocity, small variations in $|\mathbf{E_L}|$ and variation in the orientation of $\mathbf{E_L}$ along the line of sight. However a complete account of this effect is particularly complicated for the IMSE radial view because the weighting depends on the relative attenuation of the beam which further depends on the density of the plasma. On the far side of the sightlines the beam will be more attenuated as it has: entered the plasma earlier than on the nearside; has travelled a greater distance before it intersects the sightline; and has encountered higher density plasma, as can be seen in the top of Fig. 4.6. An example of the complete line-integration calculation in the absence of any attenuation is given in Ref. [61]. Here an approximation for the horizontal extent of the beam is made here to give a simplified understanding of this effect. This simplifying approximation treats the beam as two separate infinitesimal beams that are 5cm either side of the beam centre-line and have a velocity diverging horizontally at 0.3°. Examples that show the effect of line integration are shown for midplane cross sections in Figs. 4.10, 4.11 and later in 4.29. *The polarisation orientation measured from the near and far portions of the beam are seen to be* $\sim 5°$ *from the polarisation at the centre-line of the beam. Evidently the average of the near and far contributions is often different from the centre-line expectation by up to* 1°. In particular for the $30R$ the polarisation orientation is heavily weighted to the near side of the beam for lower values of R, especially once the far side of the beam reaches the separatrix and strikes the inner wall. Meanwhile the polarisation orientation seen at the tangential 315° view from the near, centre-line and far sides of the neutral beam is almost identical, as expected.

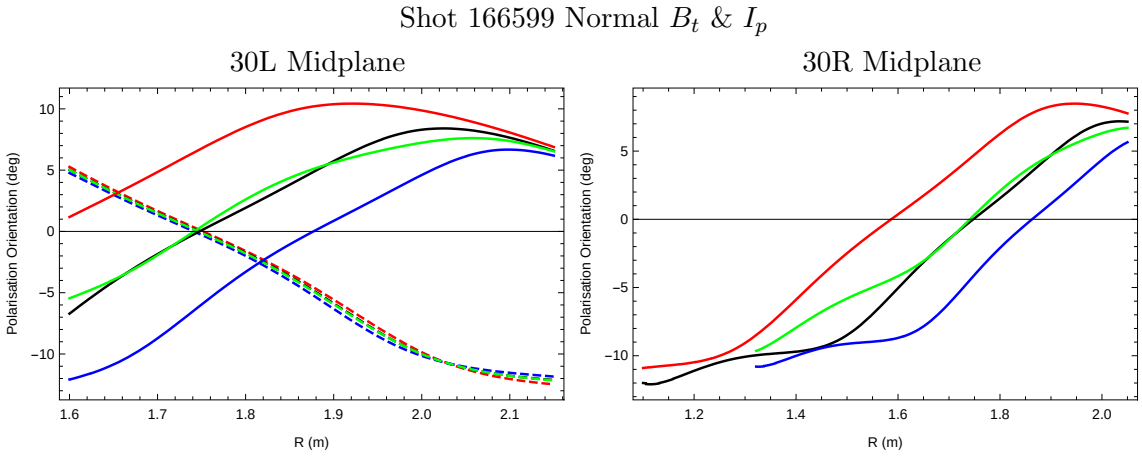

Figure 4.10: EFIT modelled polarisation angle at $Z = 0$m for shot 166599 at 2.2s for the IMSE view (solid lines) and 315° conventional MSE (dashed lines) for the 30L (Left) and 30R beams (Right). The polarisation angle on the beam centre-line is in black, the near side of the beam is red, the far side is blue and near/far average is in green.

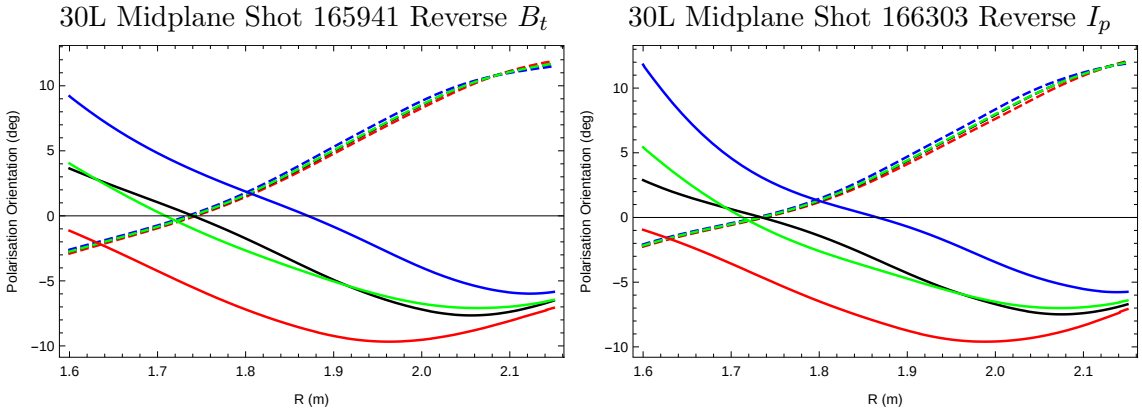

Figure 4.11: Polarisation angle modelled for the 30L beam in shot 165941 at 3s with reverse toroidal field (Left) and shot 166303 at 1.8s with reverse plasma current (Right). The lines are the same as in Fig. 4.10.

4.1.3 Modelled Parameters for the View

The Doppler shift of the neutral beams can be calculated precisely once the spatial registration of the view is known. The modelled wavelengths at the centre-line of the 30L and 30R beams are shown Fig. 4.12 where it is evident that the 30R is more redshifted than 30L particularly at larger values of R in the left of the image. Ideally the IMSE filter will transmit all of the full-energy multiplet while blocking impurity emissions (expected to be unpolarised) and the emission from half and third energy neutral beam components. The IMSE filter is deliberately placed in a collimated region of the optical system and tilted, as seen in Fig. 4.1, to partially track the variation in the Doppler shift across the field of view. The angle of incidence and resulting offset in the central wavelength of the filter are shown in the lower part of Fig. 4.12.

From Fig. 4.12 it is evident that the beams are less red-shifted than the centre of the filter transmission at the larger radii in the left of the image. As a result the π_+ wing (here defined as the higher energy/lower wavelength wing) of the full energy component

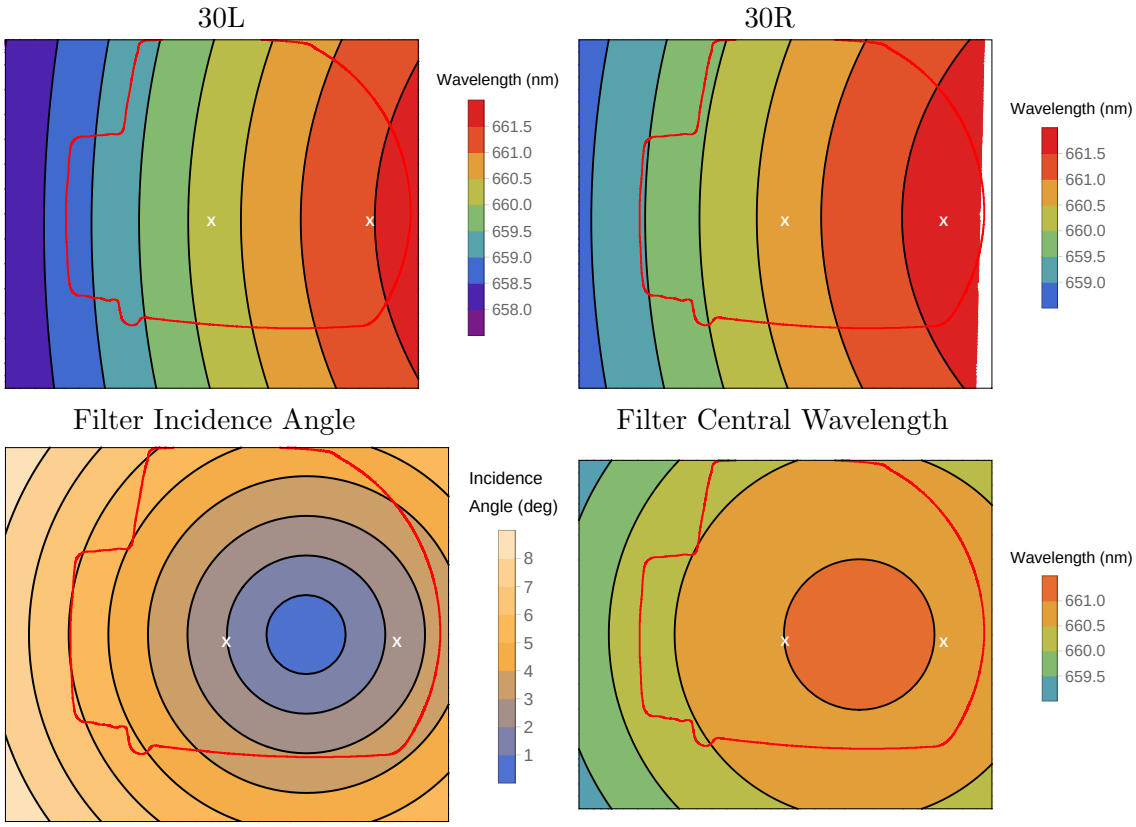

Figure 4.12: (Top Left) Doppler shifted σ_0 wavelength for the 30L beam in camera coordinates (assuming thin beam with horizontal velocity). The white crosses are used to indicate the sightlines used in Fig. 4.13. (Top Right) Doppler shifted σ_0 wavelength for the 30R beam. (Lower Left) Angle of incidence of the rays to the filter normal in camera coordinates. The filter is attached to the camera lens in a region where the light is collimated. (Lower Right) Central wavelength of the filter resulting from the angle of incidence.

becomes clipped by the filter, more so in the case of the 30L neutral beam. This is evident in the left of Fig. 4.13 where the filter transmission profile and various components of the spectrum are plotted. Meanwhile in the right of the images at lower radii the spectra are more redshifted relative to the centre of the filter transmission. In this case the half energy components of the spectra are partially transmitted by the filter. Transmission of the half energy components is not a major concern to the experiment as the motional electric field only has a different magnitude but still has the same orientation and therefore also produces the same polarisation orientation. As a consequence the contrast term ζ_l in Eq. 3.46 is expected to decrease but the value of the net linear polarisation signal $I_0\zeta_l$ may even increase depending on the precise Doppler shift and delay at that point in the image. The Stark-Zeeman circular polarisation and radial electric fields have different relative magnitudes for the full and half energy components and are considered in more detail later in Sections 4.1.5 and 4.2.2.

To verify the effect of the tilted filter the experimentally measured light intensity is compared with a modelled intensity in Fig. 4.14 for the 30L beam and two different energies of the 30R neutral beam. The two 30R cases roughly agree but the beam attenuation and line integration effects make quantitative comparisons challenging. Notably the signal

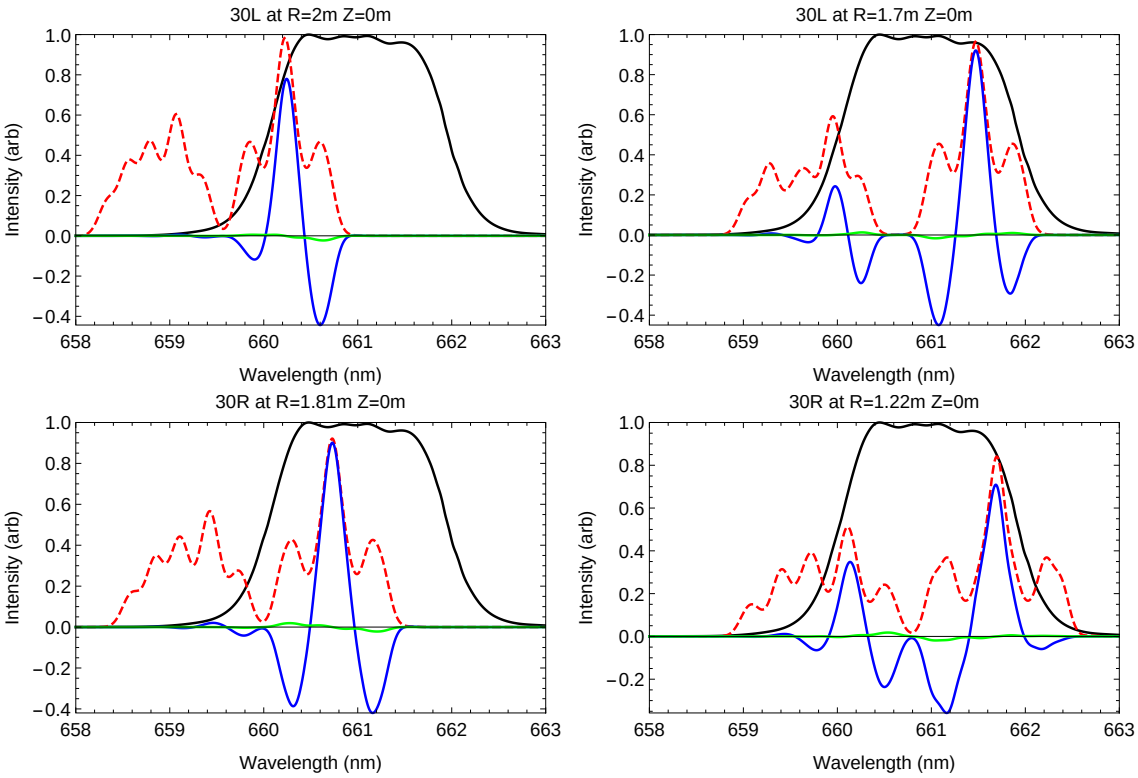

Figure 4.13: Spectra for the 30L and 30R beams at two different points in the image for a normal B_t shot. The filter passband is in black, the unfiltered total intensity for all energy components is in red, the filtered linear polarisation fraction is in blue ($I(\lambda)p_{l,MSE}(\lambda)f(\lambda)$) and the filtered circular polarisation fraction is in green ($I(\lambda)p_{c,MSE}(\lambda)f(\lambda)$). It should be noted the central wavelength of the filter is similar as the two sightlines chosen are roughly equidistant from the point of normal incidence on the filter. Equally populated upper-states are assumed such that the line ratios in Chapter 2 can be used. The half and third energy components are taken to respectively have 53% and 29% the intensity of the full energy component[70]. The maximum transmission of the filter is 72.5% but this has been normalised to 1 for simplicity. Some artificial Gaussian broadening has been added to each of the transitions.

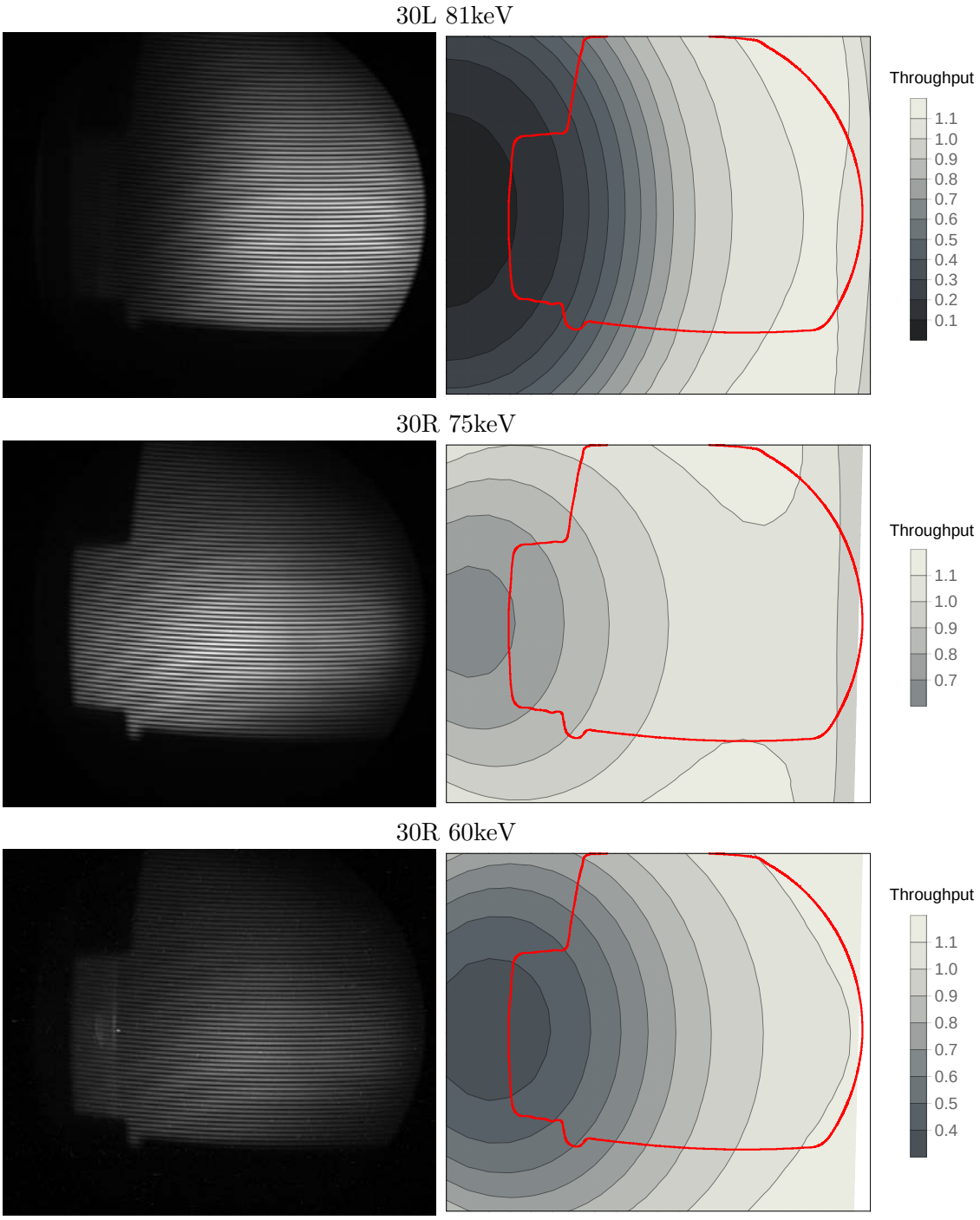

Figure 4.14: (Left) Experimental measured beam emission intensity in camera coordinates. (Right) Theoretically predicted intensity ignoring beam attenuation. Intensities are scaled according to the intensity of the full energy component. Values greater than one occur when some half energy component also leaks into the filter passband. Top) 30L beam at 81keV. Middle) 30R beam at 75keV. Bottom) 30R beam at the less common energy of 60keV.

from the 30L beam is weak at high values of R due to the smaller Doppler shift. The filter was originally designed for IMSE measurements on the KSTAR tokamak with a tangential view where the Doppler shift has a smaller range across the field of view. Evidently a more permanent installation of the experiment here would have benefited from a greater tilting of the filer to approximately 4° to increase the signal from 30L at high values of R. Additionally, for this measurement a filter with slightly higher/redder wavelength would also be beneficial for compensating for the Doppler shift variation with the tilt of the filter.

4.1.4 Displacer Waveplate

The system uses the same displacer that has previously been used on the KSTAR tokamak[40, 27]. The 5mm $\Theta = 30°$ αBBO displacer oriented at $\rho = 90°$ imparts the delay given in Fig. 4.15. As per Eq. 3.22 the offset delay is $\phi_{offset} = 684$ waves at 660nm. With a 2560×2160 6.5µm pixels and an 85mm lens the fringe frequency is $2\pi/k_y = 27$ pixels per wave. This fringe frequency is notably less than the 10 pixels per wave recommended in Chapter 2, as it was originally designed for use with a shorter focal length lens and therefore the vertical resolution is decreased. The interference fringes of the IMSE polarimeter are oriented to give the maximal spatial resolution in the radial direction, however in reality, the radial resolution from the port is limited by line of sight integration, as outlined in Section 4.1.2. When the IMSE polarimeter is illuminated with the neutral beam source, the Doppler shift and the phase offset $\phi_0(y)$ in Eq. 3.44 change across the field of view. This effectively tilts the interference fringes such that they slope downward toward the more red Doppler shifted right hand side of the image, as seen in the right Fig. 4.15.

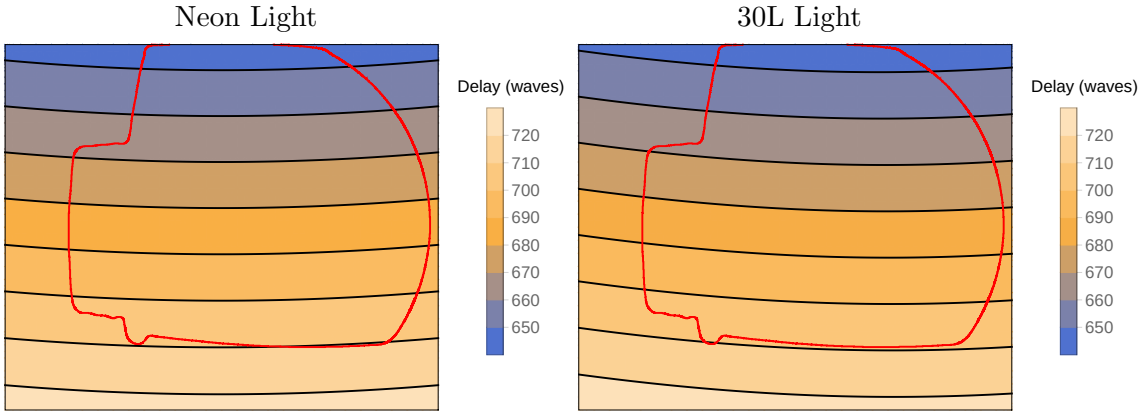

Figure 4.15: Delay of the displacer in camera coordinates with a 660nm neon spectral line (left) and 30L neutral beam σ_0 (right).

In Chapter 3 the dimensionless parameter $3\kappa\epsilon\phi_0/2\pi\hbar\omega_0$ is introduced to describe the interferometric contrasts of the linear and circular polarisation components (ζ_l and ζ_c in Fig. 3.13). Now that the Doppler shift and delay used for the DIII-D system have been outlined it is useful to illustrate the variation of the dimensionless parameter across the image, shown for the 30L and 30R beams in Fig. 4.16. It is evident that there is around 40% variation in this parameter across the field of view due to variations in ϵ (mainly resulting from B_ϕ increasing towards the high field side and changes in the angle between $\mathbf{B}$ and $\mathbf{v}$) and $\phi_0(y)$. The peak in the linear polarisation contrast is broad hence a significant $\sim 50\%$ contrast is achieved across the entire image.

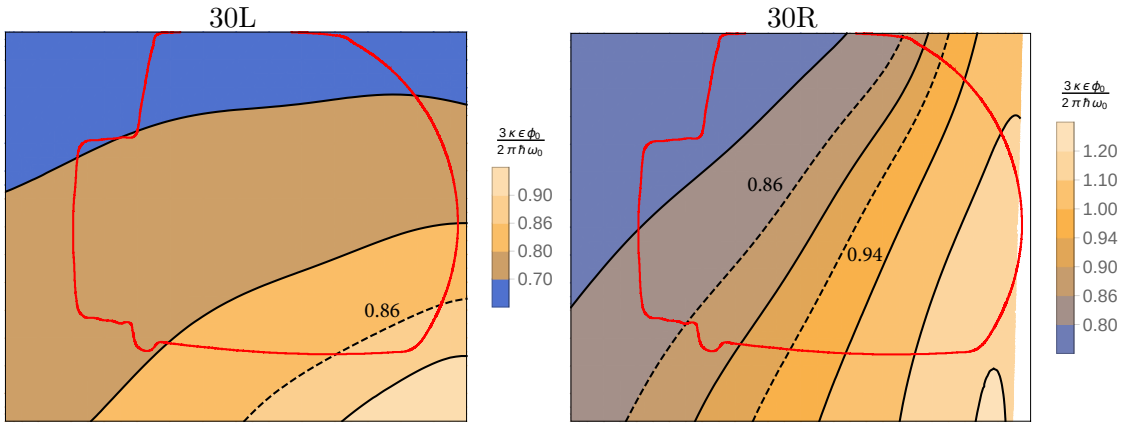

Figure 4.16: Normalised delay for the 30L and 30R beams in camera coordinates. The dashed lines indicate the value of 0.86 in Eq. 3.49 where the linear polarisation contrast is maximised and for 30R the line at value of 0.94 in Eq. 3.56 indicates where the circular polarisation contrast will be zero.

	I_0	ζ_L	ζ_l	α_l	ζ_C	ζ_c	α_c
30L R=2m	0.71	0.66	0.65	2.2°	0.010	0.013	−130°
30L R=1.7m	1.11	0.69	0.54	−12.5°	0.006	0.002	66°
30R R=1.81m	0.99	0.70	0.65	−1.2°	0.003	0.003	−91°
30R R=1.22m	1.03	0.54	0.40	−13.0°	0.009	0.009	−89°

Table 4.2: Relative intensity, interferometric contrast and phase for the spectra in Fig. 4.13. The intensity is normalised to the unfiltered full energy intensity. The upper case L and C subscripts are used for the contrast factors under the assumption the filter only transmits the full energy components. In this case the phase offset would be $\alpha_L = 0$ and $\alpha_C = \pm 90°$ (sign depends on viewing angle relative to $\mathbf{B}$). Lower case subscripts are used for the case where the true filter profile and half/third energy components are considered.

The intensity, interferometric contrast and phase for the spectra shown earlier in Fig. 4.13 are tabulated in table 4.2. The linear polarisation contrast is $\approx 50\%$ smaller at the high field side of the 30R view where the dimensionless delay is 1.2, compared to the optimal value of 0.86, but is still easily measurable. Overall the linear polarisation contrast and phase do not change significantly when the effects of the filter passband and half/third energy components are considered. In the case of the circular polarisation the contrast and phase are more susceptible to the filter passband and lower energy components but for this IMSE view the contrast is small because the sightlines are largely perpendicular to the magnetic field such that the Stark-Zeeman circularity is not manifest.

4.1.5 Sensitivity to $\mathbf{E_r}$

It is important to consider the possibility for radial electric fields within the plasma to alter the polarisation orientation expected with only a motional electric field. Indeed the 15° port was originally commissioned for a conventional MSE polarimeter for the purpose of measuring and validating the superposition of the radial and motional electric fields due to the different relative sensitivities of the views[12]. For the radial electric field to alter the polarisation orientation more than 0.1° it must have a magnitude relative to the motional electric field of at least 0.2% in the direction perpendicular to the sightline

and motional electric field. The influence of the radial electric field on the measured polarisation orientation is shown in Fig. 4.17 for the 30L and 30R beams using a radial electric field profile like that in Ref. [12]. In that example the radial electric field reaches up to 200kV m^{-1} which compares to the typical motional electric field strength of $\sim$ 4MV m^{-1}. This is considered to be a worst case scenario and sets approximate bounds for the effect. Importantly for an IMSE measurement any leakage of the half energy multiplet into the filter passband will have a polarisation orientation offset $\sqrt{2}$ of that in Fig. 4.17. In this example for the 30L beam the half energy component would be at most $40\% \times 1^\circ = 0.4^\circ$ from the full energy polarisation orientation so if 25% of the half energy component is transmitted the polarisation orientation will only deviate an extra 0.1°.

In the IMSE view there are a number of important features that cause it to be insensitive to the radial electric field in some places. A vertical contour through the magnetic axis exist where $B_z = 0$, in which case both the motional and radial electric fields are purely in the vertical direction and the polarisation orientation is therefore unaffected. There is also a point where the sightline is normal to the flux surface and therefore insensitive to the radial electric field. A contour through this point exists in the image where the motional and radial fields are aligned. As a result the 15° view of the 30L and 30R beams is largely insensitive to the radial electric field, although at the higher R positions the contribution from the radial electric field becomes more significant. The zero crossing contour where $B_z = 0$ magnetic axis is to the left of the $\mathbf{i} \times \mathbf{E_r} = 0$ contour for the 30R beam while the two contours approximately overlap for the 30L beam.

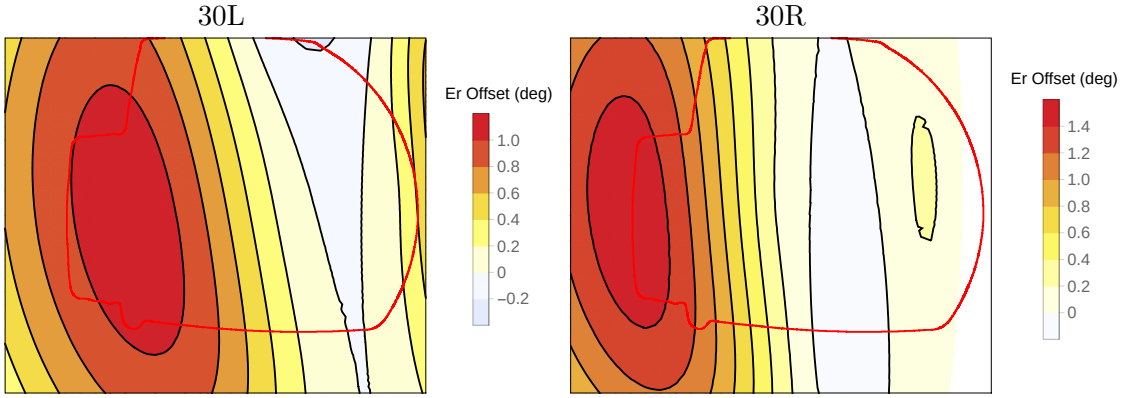

Figure 4.17: Offset in the polarisation orientation expected from a purely motional electric field as a result of including a radial electric field for the 30L (left) and 30R (right) beams.

4.2 Temporally Switched IMSE Polarimeter Calibration

In this section the calibration of the individual components of the IMSE polarimeter is presented along with the calibration procedure used for the complete polarimeter. The four main calibration challenges discussed are the influence of the Stark-Zeeman circular polarisation, Faraday rotation, possible partially polarising elements in the polarimeter and the influence of ray paths on the polarimeter response resulting from the non-spatially uniform FLC. Many of the calculations are specific to this particular IMSE implementation but can be adapted for other implementations. Furthermore three of the four effects can be overcome with an FLC or similar switching waveplate, having spatially uniform retardance closer to the ideal half-wave delay. Further corrections resulting from non-ideal

effects discussed in the previous two chapters, such as the Stark-Zeeman angle defect and waveplate dispersion effects, are also considered.

4.2.1 Polarimeter Components

The orientation and delay of each individual component in the polarimeter was determined by placing the element between a fixed polariser and a digitally controlled rotating polariser. Either a neon 660nm spectral line or bandpass filtered white light source is directed into an integrating sphere to provide a roughly uniform intensity through the optics and is then focused onto the camera. As the polariser is rotated the light intensity is measured and can be fitted to a theoretical curve. For example with an input polariser orientated at θ, a general waveplate with delay ϕ at angle ρ and a fixed polariser at 45° the light intensity is given by,

$$S = \frac{I_0}{4}\Big(1 + \sin 2\rho \cos(2\theta - 2\rho) + \cos\phi \cos 2\rho \sin(2\theta - 2\rho)\Big) \tag{4.1}$$

The orientation and delay of the individual components in the DIII-D IMSE polarimeter measured using this technique are presented in Table 4.3. At first glance Eq. 4.1 is insensitive to the sign of the delay ϕ but it is possible to resolve the sign of ϕ by carefully considering the angular dependence of the delay given in Eq. 3.20 and non-axial ray effects in Eq. 3.40. The theoretical Stokes vector weighting factors for the polarimeter based on these measured orientations and delays are given in Table 4.4. A theoretical description of these weighting factors was presented in Section 3.4.1. It should be noted that the quarter-wave plate fast and slow axes are swapped relative to that outlined in Eq. 3.4 such that the $\approx 45°$ FLC orientation now delivers the $S_{90°}$ like phase response $(+2\theta + g)$ and the $\approx 90°$ FLC orientation the $S_{45°}$ like phase response $(-2\theta + h)$.

Component	Orientation ρ	Delay ϕ
Quarter waveplate	134.6°	89°
FLC -5V	43.2°	$\approx 195°$, Fig. 3.16
FLC +5V	90.9°	$\approx 195°$, Fig. 3.16
Displacer	89.9°	5mm $\Theta = 30°$ αBBO, Fig. 4.15
Polariser	135°	NA

Table 4.3: Orientation and delay of the optics in the IMSE polarimeter measured using the rotating polariser calibration technique.

	w_1	w_2	w_3	w_4	w_5	w_6
-5V FLC	-0.031	-0.994	0.106	0.961	-0.001	0.275
+5V FLC	0.271	0.959	0.083	0.962	-0.272	0.005

Table 4.4: Stokes vector weighting factors for polarimeter. The interferometric phase of the -5V state is given by $\phi_0 + \alpha_l + 2\theta + 4g(\theta, \xi_I, \alpha_l - \alpha_c)$ where the function g can be determined using these weight functions in Eq. 3.67. Similarly the interferometric phase of the +5V state is given by $\phi_0 + \alpha_l - 2\theta + 4h(\theta, \xi_I, \alpha_l - \alpha_c)$.

It is possible to predict the response of the polarimeter based on the values for the individual components in Tables. 4.3 and 4.4, however invariably the experimental response of the combined polarimeter differs slightly and has a complicated spatial dependence.

Hence an experimental calibration through the entire polarimeter is preferred. The experimental response of the carrier fringe phase to the input polarisation θ (i.e. the functions g and h in Eqs. 3.69 and 3.70) is calibrated using a bandpass filtered white light source that fills an integration sphere before passing through a linear polariser on the digitally controlled rotation stage. The 0.3nm wide, 660nm bandpass filtered white light source is preferred over using a 660nm Ne I spectral line for the polarisation calibration because the longer coherence length of the spectral line is found to contribute a weak Newton rings interference pattern to the image. The Newton rings are created by multiple reflections between coatings in the system and have a broad spatial frequency spectrum that can contaminate the spatial fringe carrier. However to absolutely calibrate the displacer delay there is a trade-off using the white light source as the central wavelength of the bandpass filter has an angular dependence that must be considered. Therefore, depending on the magnitude of the Newton rings pattern, it may also be worthwhile to use the neon spectral line. This absolute calibration of the delay is not the primary purpose of the measurement but it is a useful self-consistency check and can be used to measure the vertical divergence of the beam (Fig. 4.7) using the Doppler effect[54].

The fringe pattern can be demodulated to determine phase difference Δp between alternate states of the FLC which is related to the polarisation orientation by the function $\Delta p/4 = F(\theta, 0, 0) = \theta + g(\theta, 0, 0) - h(\theta, 0, 0)$, as per Eq. 3.73 with linearly polarised calibration light such that $\xi_I = 0$. The experimentally measured $F(\theta, 0, 0)$ is not a constant function across the image and is essentially a three dimensional function of θ and camera pixel coordinates, that is $F_{ij}(\theta, 0, 0)$ for horizontal pixel i and vertical pixel j. To visualise the function it is straightforward to individually fit a function of θ to the experimental data for each pixel. The values obtained for a linear fit to the experimental calibration are shown in Fig. 4.18 where it is evident there is an offset of 3.3° in the response that primarily results from the non-ideal delay of the FLC waveplate[40]. The gradient of the function is close to one and therefore the inverse function is well conditioned. Hence a measurement of the phase difference can be used to determine the polarisation orientation i.e. $\theta = F^{-1}(\Delta p/4)$. This procedure assumes that there is no circular polarisation, however considerations are made for the circular polarisation and the complete form of $F(\theta, \xi_I, \alpha_c - \alpha_l)$ are described in the next section.

It was noticed that there was a small offset in the phase difference measured after each 90° rotation of the input polariser, as seen in Fig. 4.19. Ideally the system response to linear polarisation should repeat every 90° as this is simply a transformation of the stokes vector $(s_1, s_2) \rightarrow (-s_1, -s_2)$ but there are differences of $\sim 0.5°$. The quoted accuracy of the rotation stage is 0.08°. Such an effect could result if the axis of the rotation stage is not parallel to the surface normal of the polariser, however the misalignment needed for this non-axial ray effect seems unlikely to be the cause of the inconsistency every 90°. It is more likely to be a component in the system that is weakly polarising, arising from small differences between the reflection/transmission of orthogonal polarisations at some surface in the system. To correct the experimental IMSE data a quadratic fit is made for $F^{-1}(\Delta p/4)$ using an average of the four different calibrations shown in Fig. 4.19. The predicted $g - h$ response of the polarimeter based on the calibration of the individual components is approximately 1° above experimentally measured phase difference. Overall the deviation from this average is within ±0.25° and it should be remembered the IMSE system also performs a similar average over perpendicular σ and π emissions. The 1° offset likely results from the uncertainty in the ray-path weighted average of the non-spatially uniform FLC retardance. For this reason the experimental calibration is preferred to the

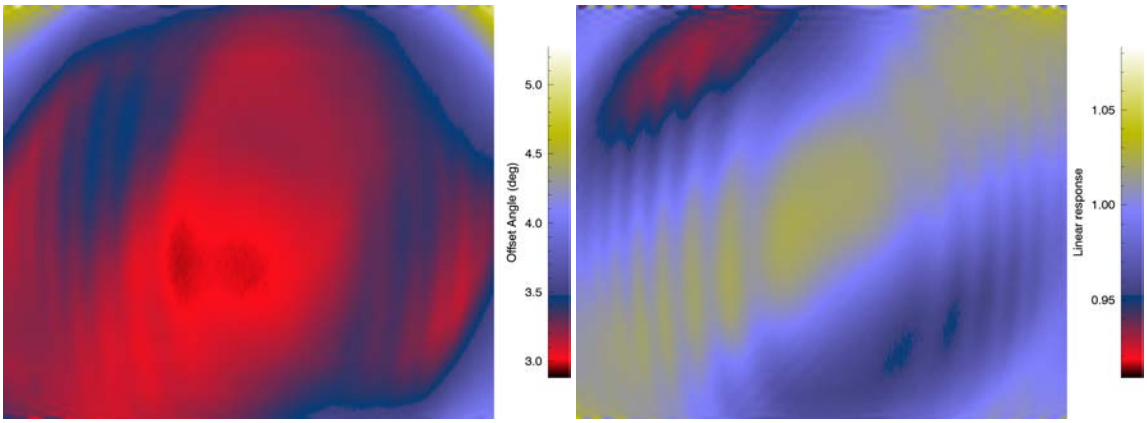

Figure 4.18: Calibration correction used to for the non-ideal response of the polarimeter. The left hand plot is a fixed offset which represents $g(0,0,0) - h(0,0,0)$. The right plot describes the linearity of the response given by $1 + d(g(\theta,0,0) - h(\theta,0,0))/d\theta|_{\theta=0}$. Spatial variations are mainly thought to result from the non-uniformity of the FLC shown in Fig. 3.16.

theoretical prediction based on the individual components. Nevertheless the theoretical calculation remains useful for understanding perturbations to the system, such as the effects of circular polarisation or changes in the effective FLC retardance, which will be discussed in the following two sections.

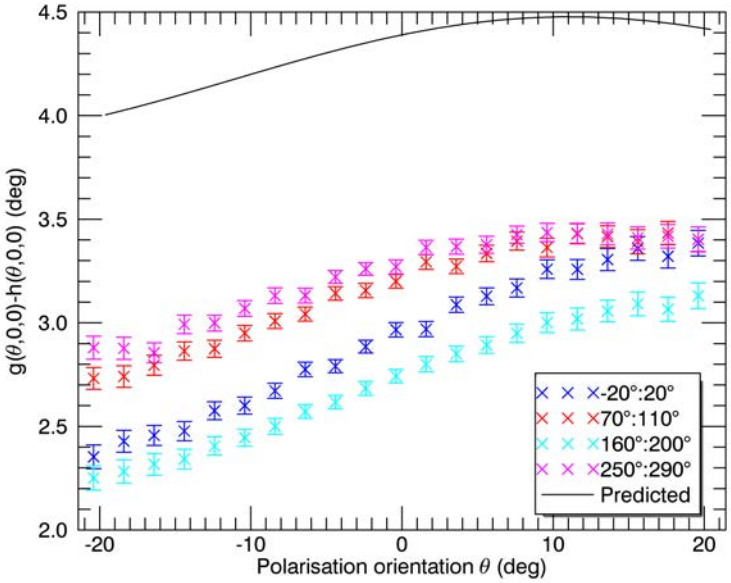

Figure 4.19: Calibration data taken in the ±20° range about horizontal (180° & 180°) and vertical (90° & 270°) linear polarisation. The theoretical prediction is based on the weighting coefficients in Table 4.4 established from the calibration of the individual components.

4.2.2 Stark-Zeeman Interferometric Ellipticity

Given the tolerance limitations in achieving half-wave FLC retardance it is imperative to consider the validity of the linear polarisation calibration for the TSSSH for measurements having some circular polarisation. The sightlines from the 15° port are largely perpendicular to the magnetic field ($\varphi \approx \pm\pi/2$ in Chapter 2 and Section 3.3.2) and therefore the Stark-Zeeman circular polarisation is relatively small (easily seen when comparing Fig. 4.13 with the parallel view modelled earlier in Fig. 2.13). However to put the theory developed in the preceding two chapters into practice it is worthwhile presenting a full description of the effects here, with the understanding that the corrections can be significant for standard tangential views when the FLC retardance is non-ideal. The theoretical basis for this is outlined earlier in Section 3.4.1 where the phase correction functions g and h depend on the input polarisation orientation θ, the interferometric ellipticity angle ξ_I and the relative phase of the linear and circular interferograms given by $\alpha_c - \alpha_l$. For the amplitude spatial heterodyne the effects of the circular polarisation were outlined in Section 3.5.2 but here the further complication of the phase term $\alpha_c - \alpha_l$ is elucidated.

The idealised approximation for the effective interferometric ellipticity, obtained from Eqs. 3.54, 3.53 and 3.48, is plotted for the 30L and 30R views in Fig. 4.20. The zero crossing in ζ_c, where the sightlines are exactly perpendicular to the magnetic field ($\varphi = \pm\pi/2$), is evident for both beams. Additionally for the 30R beam there is a zero crossing where the circular polarisation contrast is zero, occurring where the dimensionless delay is 0.94 as per Eq. 3.56 and seen in Fig. 4.16. For the 30L view the interferometric ellipticity remains below $|\xi_I| < 1.2°$ and $|\xi_I| < 1°$ for 30R, indicating the effect will be small. However this approximation only applies when upper-states are equally populated and the full energy multiplet is uniformly transmitted by the filter while the half and third energy components are completely blocked. This is certainly not the case for this IMSE system, as evident from the spectra plotted in Fig. 4.13. Even though the approximation could be more closely satisfied with a new filter design, there will likely still be some clipping of the full energy spectrum or partial transmittance of the half energy component.

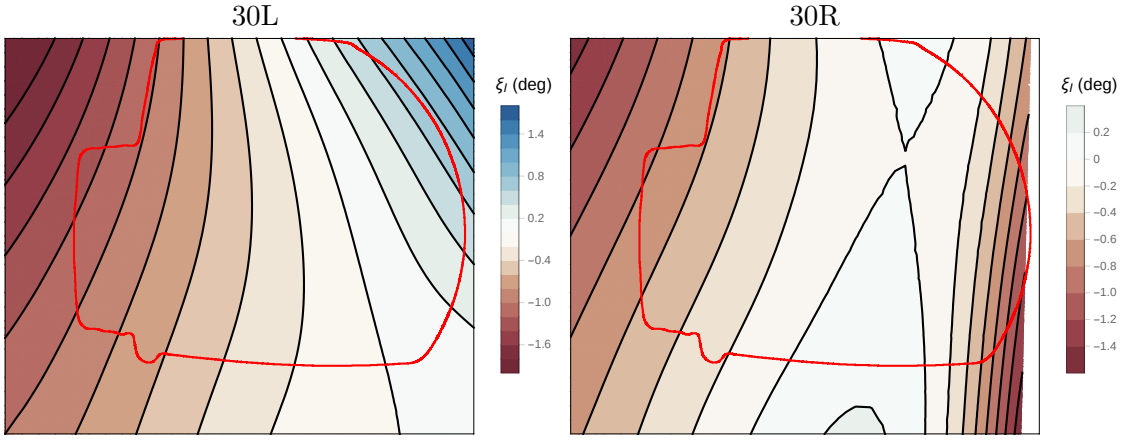

Figure 4.20: Effective interferometric ellipticity for the view of 30L and 30R when assuming the filter transmits only the full energy multiplet such that Eqs. 3.53 & 3.48 are valid.

It is expected that $\alpha_l = 0$ due to the even symmetry of the linear polarisation about σ_0 and that $\alpha_c = \pm\pi/2$ due the odd symmetry of the Stark-Zeeman circular polarisation. The interferometric delay has been deliberately chosen to match the periodicity of the linear polarisation spectrum to deliver the maximum polarisation fraction ζ_l, as outlined

in Section 3.3.1, and therefore the α_l interferometric phase factor is relatively tolerant to changes in the spectrum due to the filter passband and half energy components. However this delay lies near the zero crossing of the circular polarisation interferometric contrast ζ_c for the full energy spectrum and the phase α_c is therefore more susceptible to changes in the spectrum. This is further compounded by leakage of the half energy component which has $\sqrt{2}$ greater circular:linear polarisation fraction ratio due to the fact that $\gamma/\epsilon \propto 1/|\mathbf{v}|$. The complete spatial structure of the effective interferometric ellipticity and phase terms is presented in Fig. 4.21. To conceptualise the link between these plots and the spectral domain it is worthwhile to reconsider the spectra in Fig. 4.13 and their associated contrasts and phases given in Table 4.2. It should be noted that the terms will also have a dependence on relative upper-state populations, with the circular contrast and phase having greater sensitivity. It is evident that the interferometric ellipticity $|\xi_I|$ has increased in the left of the images (more so for 30L) relative to the simple case shown in Fig. 4.20. This increase results from the filter blocking the π_+ wing and transmitting only the circular polarisation peak near the π_- wing, essentially eliminating the beating pattern in the interferogram (Fig. 3.13) leading to an increase in the coherence of the circular polarisation spectrum. Additionally the phase α_c shifts by over 45° from the idealised value of 90°. The second $\zeta_c = 0$ crossing for the 30R beam, seen in Fig. 4.20, is lost for the full calculation but the value remains close to zero.

In the previous section the calibration of the polarimeter with a linearly polarised source was outlined. This calibration neglects the circular polarisation in the MSE emission that the polarimeter is sensitive to due to non-ideal components (mainly the FLC). In a previous experiment, before the properties of the Stark-Zeeman circular polarisation were fully understood, a range of monochromatic elliptical polarisations were used to calibrate a doubly switched single spatial heterodyne system[40]. With the monochromatic source $\alpha_c = \alpha_l$, however it is seen in Fig. 4.21 that this is certainly not the case. Any calibration strategy developed must be able to account for phase difference $\alpha_c - \alpha_l \neq 0$. The most obvious calibration strategy is to experimentally measure the full spatial dependence of the 12 weighting factors in Table 4.4 by inputting a complete set of Stokes vectors (e.g. horizontal linear $\mathbf{s} \propto (1, 1, 0, 0)$, diagonal linear $\mathbf{s} \propto (1, 0, 1, 0)$ and circular polarisation $\mathbf{s} \propto (1, 0, 0, 1)$). However this strategy is complicated by the weak partially polarising element in the polarimeter that implies the weighting factor analysis is over-simplified. Care would be required with this calibration method as the phase and contrast can drift in-between each different Stokes vector measurement if the temperature of the displacer or ray paths change. Once the weighting factors are determined a forward model of the circular and linear spectra that includes line-integration and filter passband effects could be used to remove the interferometric ellipticity effects by subtracting the expected fringe pattern contributed by the circular polarisation.

The interferometric ellipticity calibration strategy suggested in the previous paragraph is not possible for the DIII-D IMSE polarimeter because no calibrations were taken with purely circular polarised light and experimental values for the w_3 and w_6 weighting factors are therefore unknown. It can be seen from Fig. 4.19 that the polarimeter response predicted from the calibration of the individual components is not absolutely accurate. However it is still useful to apply these weighting functions to get an estimate of the relative perturbation produced from the Stark-Zeeman circular polarisation fraction. The phase offset functions g and h for TSSSH can be calculated from Eq. 3.72 using the necessary weighting factors in Table 4.4. From these functions it is possible to calculate the difference between the polarisation orientation θ_l inferred assuming the linear calibration

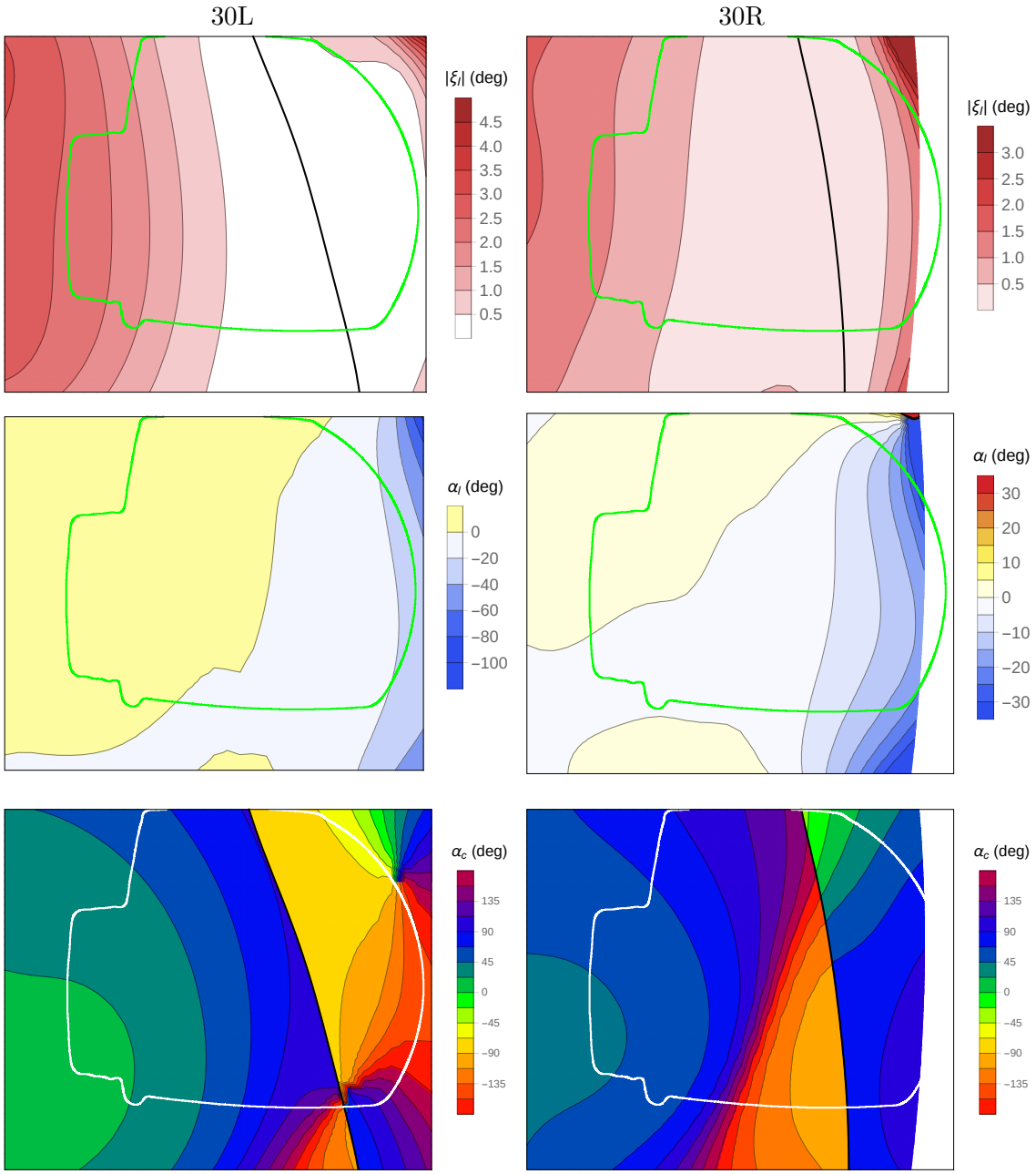

Figure 4.21: Individual components of the interferometric ellipticity including filter passband effects and half/third energy components seen in Fig. 4.13. (Left Column) 30L calculations. (Right Column) 30R calculations. (Top Row) Magnitude of the interferometric ellipticity. The zero crossing where $\varphi = \pm\pi/2$ is marked with the dark black line. (Middle Row) α_l for each beam. (Bottom Row) α_c for each beam. There is a 180° phase jump where $\varphi = \pm\pi/2$ and it should be noted that α_c is plotted for a shot with normal B_t and I_p but will flip 180° if the field is reversed.

is valid and the true polarisation orientation θ_σ, by solving the following equation for θ_l,

$$\theta_l + g\big(\theta_l, 0, 0\big) - h\big(\theta_l, 0, 0\big) = \theta_\sigma + g\big(\theta_\sigma, \xi_I(\phi_0), \alpha_c - \alpha_l\big) - h\big(\theta_\sigma, \xi_I(\phi_0), \alpha_c - \alpha_l\big) \quad (4.2)$$

The true orientation θ_σ can be estimated from an EFIT forward model while the interferometric ellipticity ξ_I and the phase difference $\alpha_c - \alpha_l$ are already shown in Fig. 4.21. The difference between the true and inferred polarisation orientation, given by $\theta_l - \theta_\sigma$, is shown in Fig. 4.22. The offset remains under 0.25° for this view. If the same non-ideal components were used on a more typical tangential view the offset would be larger and possibly $> 1°$. Therefore *it is essential to source components with ideal retardances and/or select the displacer delay to target $\zeta_c = 0$ so that these corrections are not needed or sufficiently small that corrections will be reliable.*

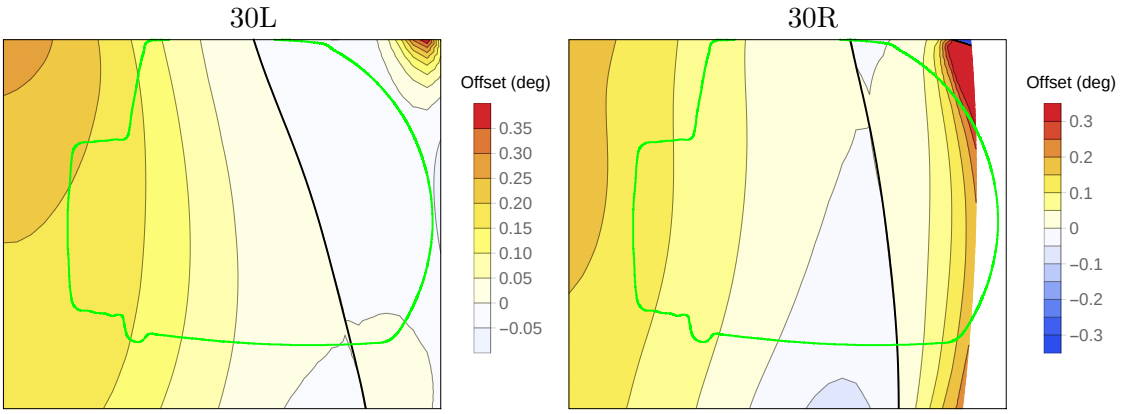

Figure 4.22: Offset error in the polarisation orientation measurement resulting from the Stark-Zeeman partial circular polarisation fraction when using the non-ideal TSSSH with the weighting factors given in Table 4.4.

Stark-Zeeman Angle defect

The 'angle defect' resulting from the elliptical Stark-Zeeman transitions, formulated in Section 2.6.3, is plotted in Fig. 4.23. The defect remains $< 0.1°$ for the IMSE view thanks to the sightlines having a significant component perpendicular to both the motional electric field ($\psi = \pi/2$) and magnetic field ($\varphi = \pi/2$). The defect is larger than the example for the more tangential KSTAR IMSE view given in Fig. 2.12 because ψ and φ span a greater range for the 15° DIII-D port. Both the interferometric ellipticity offset and angle defect are smaller than uncertainties arising from line integration effects and ray path effects (discussed in the next section) and are therefore left uncorrected in results presented later.

4.2.3 Sensitivity to Ray Paths

A linear polariser was inserted in front of the polarimeter during a plasma shot to verify the integrity of the calibration procedure outlined in Section 4.2.1. Ideally the two FLC orientations produce two unique but well defined Stokes vectors that take the same ray paths through the displacer. The spectral and delay properties introduced by the displacer, carried in the $\phi_0 + \alpha_l$ term in Eqs. 3.69-3.70, are therefore common to both states of the

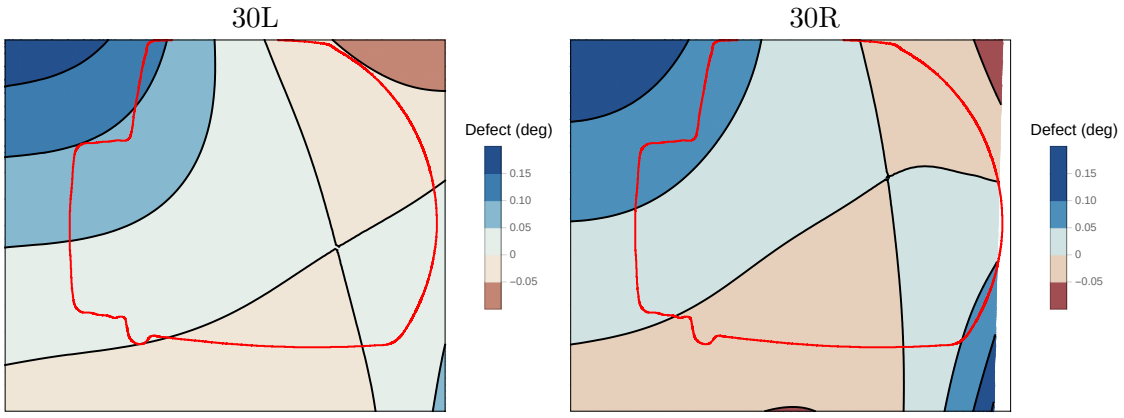

Figure 4.23: Weighted angle defect for the 30L (left) and 30R (right) beams from the 15° view for a normal B_t and I_p shot.

FLC, hence it is expected that this verification test should be independent of any non-uniformity in the thickness or temperature of the displacer. However *the neutral beam illumination measurement was found to be different from the bandpass filtered white light calibration measurement*. Essentially the phase difference Δp between the carrier fringes in opposite FLC states was not only dependent on the input Stokes vector and spatial coordinate in the image but also dependent on the distribution of ray paths illuminated by the light source. The measured value of $\Delta p_{plasma}(\theta_0, 0, 0) - \Delta p_{sphere}(\theta_0, 0, 0)$ across the image is displayed in Fig. 4.24 where Δp_{source} is the calibration function measured with either neutral beam or integration sphere illumination and θ_0 is the orientation of the polariser (close to horizontal).

The retardance of the FLC varies spatially by 15° (Fig. 3.16), but it must be remembered the FLC lies in a region of the optical system where the rays are collimated. Thus an average must be taken over the ray paths through the system to determine the effective FLC delay at each point in the image. This averaging effect results in a variation significantly less than the 15° spatial variation and if the FLC is uniformly filled the effective retardance will be the same across the image. This test with the calibration polariser demonstrates that the effective retardance of the FLC is different between the neutral beam and integration sphere as the rays fill the polarimeter with different spatial distributions. Previously it had been assumed that the FLC retardance spatial variation was small, in which case the polarisation measurement is independent of the ray paths through the polarimeter. It was only with later testing that the cause of this illumination source dependence was pinpointed to the spatial non-uniformity in the FLC delay.

This neutral beam measurement is applied as a zeroth order correction to the integration sphere bandpass filtered white light calibration, however the precise dependence on the input polarisation orientation θ is unknown. It is possible to approximate the higher order polarisation orientation terms by applying a perturbation to the weighting factor model, in a similar manner to the interferometric ellipticity correction. For an offset in the polarimeter response of ±1°, the approximate magnitude evident in Fig. 4.24, requires the FLC delay to change by approximately ±4° (Eqs. 3.74 and 3.75). When the FLC delay is adjusted by this amount to produce new weight factors (Table 4.4), the higher order θ terms of the perturbation to $g(\theta, 0, 0) - h(\theta, 0, 0)$ are found to be within $< 0.2°$ for all polarisation orientations.

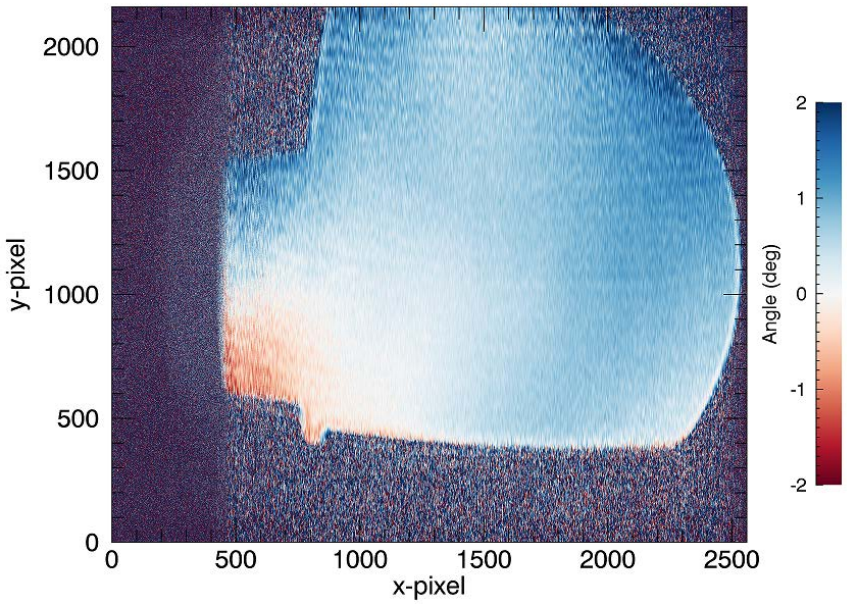

Figure 4.24: Difference in the response between a fixed polariser illuminated with the neutral beam and integration sphere in camera coordinates. The outline of the viewing port is evident in the image.

4.2.4 Dispersive Effects in Waveplates

The neutral beam Doppler shift varies across the field of view and therefore the central wavelength of the multiplet will inevitably be different from the calibration source (here narrowband filtered white light or neon light). In Section 3.4.1 the effect of the quarter waveplate and FLC dispersion on the polarimeter response is considered. The linear approximation of a $0.07°\text{nm}^{-1}$ correction for the ideal system remains fairly accurate for the DIII-D IMSE polarimeter with non-ideal weighting factors in Table 4.4. The offset in the polarisation orientation response relative to the 660nm narrowband filtered calibration is shown in Fig. 4.25.

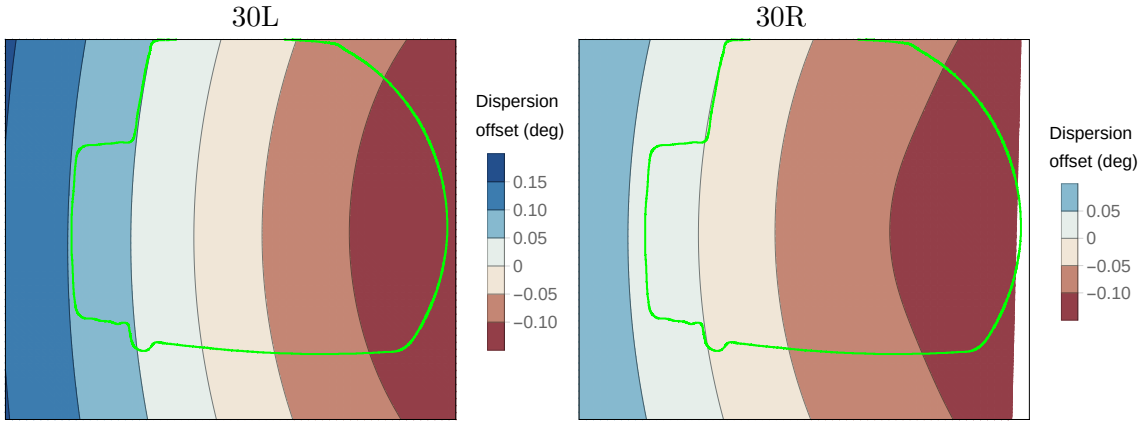

Figure 4.25: Offset in the polarisation orientation resulting from the different wavelengths of the calibration source and the 30L beam (left) or 30R beam (right) in camera coordinates. The model assumes the dispersion factor $\kappa_f = 1$ for the FLC and $\kappa_q = 0$ for the achromatic quarter waveplate.

4.2.5 Faraday Rotation

Experimental measurements of the Faraday rotation through the port window and front end optics have been obtained at 10 radial locations across the field of view from the previously installed conventional MSE system. The image plane of the conventional MSE system was relayed as an intermediate image in the IMSE system, as seen in Fig. 4.1. In Fig. 4.26 it is seen that the angle of incidence of the rays at the port window has a dependence on their origin in the plasma. As the port window is in between the toroidal field coils the magnetic field is significant, resulting in a $\sim 0.4°\mathrm{T}^{-1}$ variation in the Faraday rotation across the field of view. The Faraday rotation at the 10 points was extrapolated to the full IMSE view under the assumption that the toroidal field is the dominant influence. Faraday rotation contributions from the poloidal field are expected to be small, particularly near the midplane where the sightlines and poloidal field are perpendicular. *The* 300mm *and camera lenses that are additional to the IMSE system are not captured in this calibration* but the toroidal magnetic field drops off rapidly beyond the field coils so any additional Faraday rotation is not anticipated to be significant.

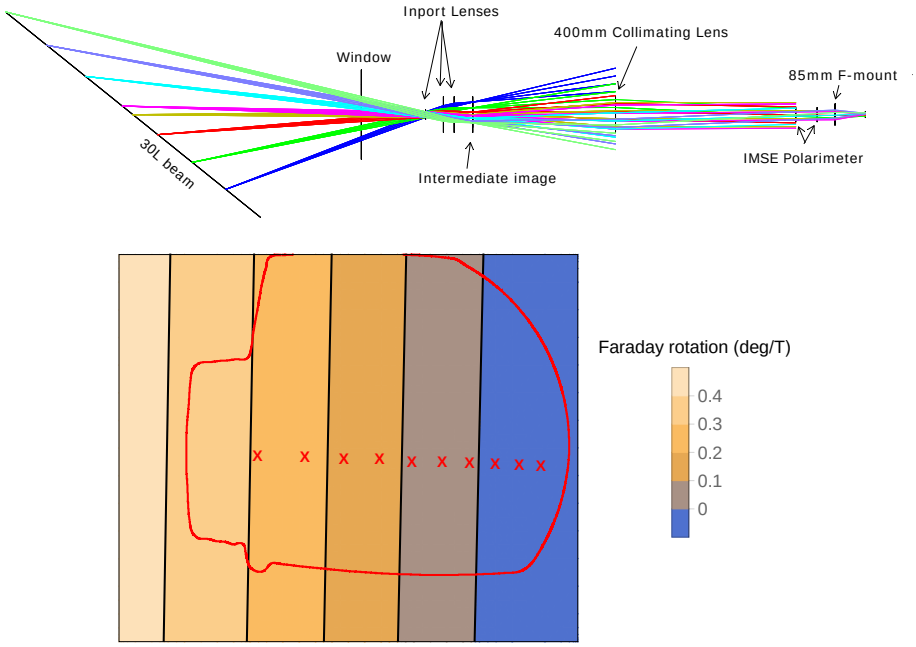

Figure 4.26: (Top) Ray trace of the optical system revealing the toroidal component of the rays through the port window. (Bottom) Extrapolated Faraday rotation produced by the port window and in port lenses, based on previous measurements with the 15° conventional MSE polarimeter at the ten locations shown with red crosses.

4.2.6 Calibration Summary

Overall the calibration procedure used for the MSE measurements can be summarised by

$$\theta_\sigma = F^{-1}\Big(\Delta p - \big(\Delta p_{plasma}(\theta_0, 0, 0) - \Delta p_{sphere}(\theta_0, 0, 0)\big)\Big) - \frac{\Delta\theta}{\Delta B_t} B_t + \theta_{roll} \tag{4.3}$$

where F^{-1} is the inverse calibration function formulated in Section 4.2.1, Δp is the phase difference between alternate states of the FLC, $\Delta p_{sphere} - \Delta p_{plasma}$ is given in Fig. 4.24, the Faraday rotation ratio in the second term is given in Fig. 4.26 and θ_{roll} is roll angle

of the camera rail in Table 4.1. Interferometric ellipticity ($< 0.25°$, Fig. 4.22), angle defect ($< 0.1°$, Fig. 4.23), wavelength corrections ($< 0.1°$, Fig. 4.25) and higher order FLC ray filling corrections ($< 0.2°$ uncertainty, Section 4.2.3) could be included but they are neglected because they are small compared to the included corrections. The Faraday correction is extrapolated from pre-existing measurements which don't include optics new to the IMSE installation but these differences are expected to be much less than the rotation in the port window. The partially polarising element in the polarimeter (Fig. 4.19) contributes an uncertainty ($< 0.25°$). Evidently to achieve a TSSSH measurement with accuracy better than $0.2°$ requires consideration of many different effects. However it is important to keep in mind that using an FLC (or a similar time step modulating element) with spatially uniform retardance close to half-wave will remove the need for the more complicated corrections, namely the interferometric ellipticity and ray path corrections.

4.3 Spectro-Polarimetry Results

For the IMSE plasma measurements the camera was generally operated in full frame readout mode with 10ms exposure and 10ms readout, overall resulting in an acquisition rate of 50Hz and duty cycle of 50%. There was enough light to operate with shorter exposures but this would come at the expense of the duty cycle and was therefore not favoured. Speeds of 500Hz with ~ 100 photoelectron counts per pixel (~ 200 amplitude fringes with 2x2 binning) were obtained when operating the camera with rolling shutter mode, in which case the switching frequency of the FLC was reduced to limit blurring produced when exposing during the 50µs FLC switch time.

There was significant variety in the shots during the campaign with different magnetic field configurations and beam modulation patterns. For reliable data to be obtained with the IMSE system it is preferable for only one of the 30L or 30R neutral beams to be on. Additionally separate exposures with the FLC in opposite states are required to extract the polarisation independently of the spectral and delay information carried in the phase term $\phi_0 + \alpha_l$.

4.3.1 Comparison with Conventional MSE

Conventional MSE provides the most reliable benchmarking tool for the IMSE measurements and the tangential 315° view is the most trusted of these views as it does not use any mirrors. The polarisation orientations measured with the IMSE and 315° conventional MSE derive from different viewing geometries and therefore cannot be directly compared. However geometric factors can be applied for a comparison of the tilt of the motional electric field θ_E using Eq. 1.16, under the assumption that the radial electric field is negligible. This can then be converted to the more standard magnetic field pitch angle, given by $\arctan(B_z/B_\phi)$, under the assumption $B_r = 0$ on the midplane. The 315° MSE channels all lie near the midplane of the device and are spaced approximately every 5cm radially. The IMSE data can be reduced to a number of discrete channels with spatial location matching the conventional MSE channels but it must be remembered that the two views have dramatically different radial resolutions resulting from line-integration effects, as highlighted in Section 4.1.2. A comparison of the temporal evolution of the pitch angles measured by the IMSE and 315° conventional MSE is presented in Figures 4.27-4.30, for three different shots with normal B_t and I_p. These shots have been selected as they contain some large and fast changes in the pitch angle which are useful for comparisons

but also demonstrate the limited radial resolution of the IMSE view. Nevertheless there is good agreement between the two systems for these shots.

In shot 165748, shown in Fig. 4.27, the line integration effects are most evident for the $R = 2.03$m channel for the L to H-mode transition occurring at 3s. For this channel the pitch angle measured by the conventional MSE, which has a radial resolution of ≈ 5cm, remains approximately constant while the $R = 1.98$m channel shows a drop in pitch angle of $\approx 1^\circ$ and the $R = 1.93$m channel shows a drop in pitch angle of $\approx 2^\circ$. Effectively there is a redistribution of the toroidal current occurring near $R = 1.98$m at 3s. Meanwhile the radial resolution for the IMSE view is only ≈ 16cm at $R = 2.03$m and is therefore more sensitive to this drop in the pitch angle occurring for $R < 2$m unlike the conventional MSE view. The Doppler 'angle' $\phi_0 + \alpha_l$ also deviates during the mode transitions, a further indication that the weighting of the line integral changes during the transitions leading to a change in the measured polarisation angle. The oscillation and other trends seen in the Doppler angle are considered in more detail in section 4.3.6.

A more gradual effect occurs in shot 165858, shown in Fig. 4.28, a 'profile control' shot where the q-profile is deliberately adjusted during the shot. Particularly near $R = 1.8$m the IMSE pitch angle is initially greater than the conventional measurement but later in the shot the pitch angle measured by IMSE is lower than the conventional MSE. These channels are near the magnetic axis and therefore E_r is expected to be negligible for both systems. This effect is highlighted in Fig. 4.29 where an MSE constrained EFIT forward model for the IMSE polarisation orientation is shown for the infinitesimally thin beam approximation and the near/far beam example introduced in Section 4.1.2. The polarisation orientation zero crossing (magnetic axis position) for the near/far beam average approximation approaches the conventional MSE measurement later in the shot. Additionally as the plasma density and beam attenuation increase during the shot the polarisation angle will become more weighted to the near side of the beam with smaller polarisation angles.

In shot 166582 there is good agreement between the systems for the large scale features in the shot, particularly during the current ramp down. However, in a similar fashion to shot 165858 the difference in the pitch angle between the conventional MSE and IMSE measurements subtly changes as the shot progresses. For all shots with normal B_t and I_p the relative differences between the measured IMSE and conventional MSE pitch angles generally fluctuates in the range $\pm 1^\circ$. All IMSE and conventional MSE calibration effects are expected to remain constant during a shot and these relative changes are therefore thought to result from the different intrinsic radial resolution of the two views. E_r is the only contribution that is expected to change during the shot but the 30L IMSE view is centred near the magnetic axis where E_r is zero. For this reason the small scale changes are most likely to result from changes in the q-profile and changes in the relative weightings of the line integration as the density of the plasma and beam attenuation evolve.

4.3.2 Imaging Data Above and Below the Midplane

The polarisation orientation measured above and below the midplane is an important feature of the IMSE technique. While there are no direct measurements to benchmark IMSE in this region it is reasonable to use a conventional MSE constrained EFIT equilibrium reconstruction for comparison with the imaging data. The IMSE polarisation orientation measured from the 30L beam is shown in the left of Fig. 4.31 accompanied by contours showing the EFIT forward modelled polarisation orientation for each different simplified

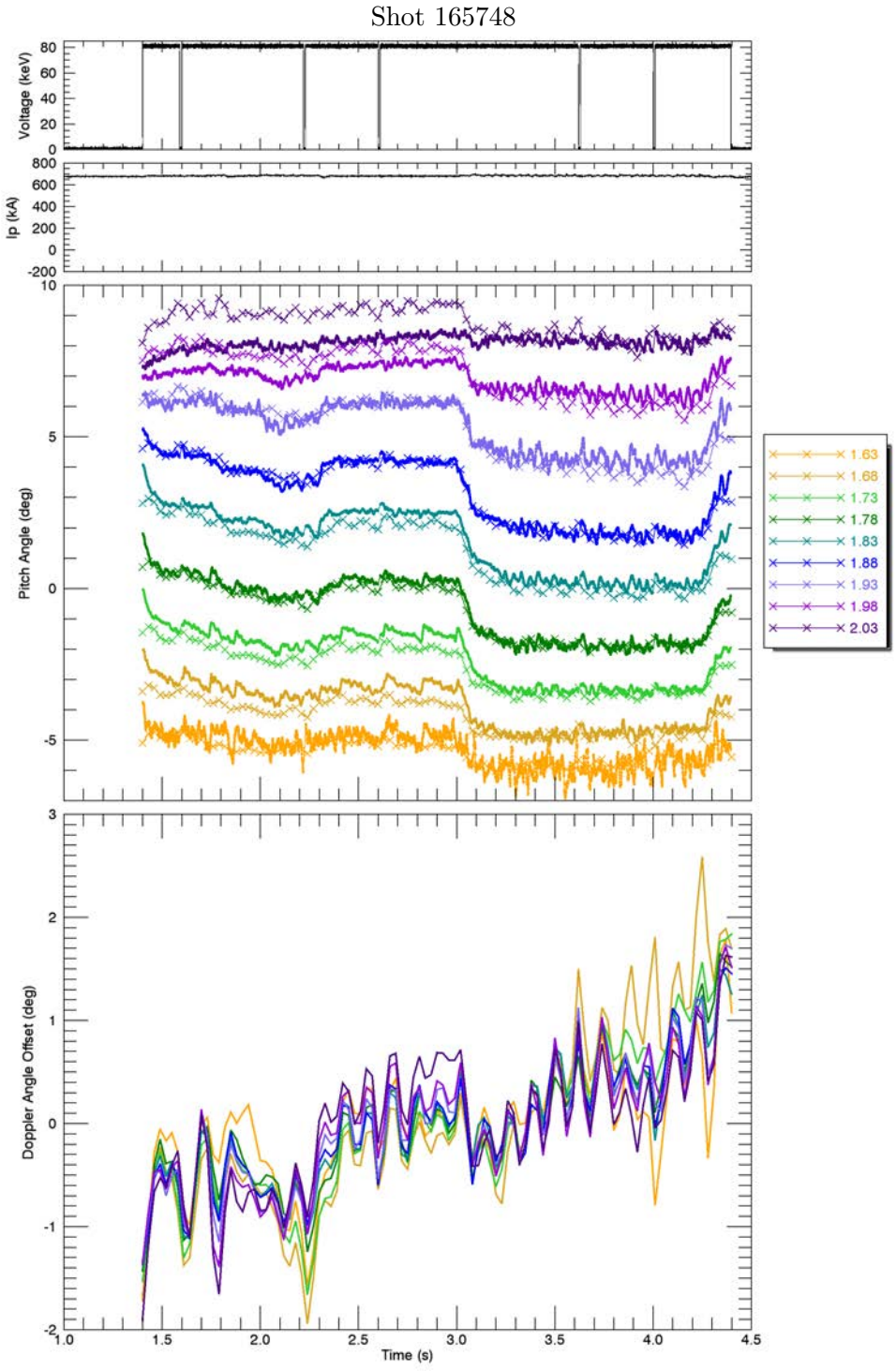

Figure 4.27: Pitch angle evolution for shot 165748. The IMSE measured pitch angle is shown with crosses and the 315° conventional MSE measurements are shown with dots which effectively looks like a thicker line. A 10ms averaging window is applied to the conventional MSE data. The Doppler angle offset tracks the IMSE phase $\phi_0 + \alpha_l$ (offset to average value during shot) and is discussed in greater detail in Section 4.3.6. At 2.3s the plasma transitions from H to L-mode and then at 3s the total neutral beam power is increased leading to a transition back to H-mode. The IMSE exposure time is 20ms with 10ms readout. There are no corrections for E_r applied for either view.

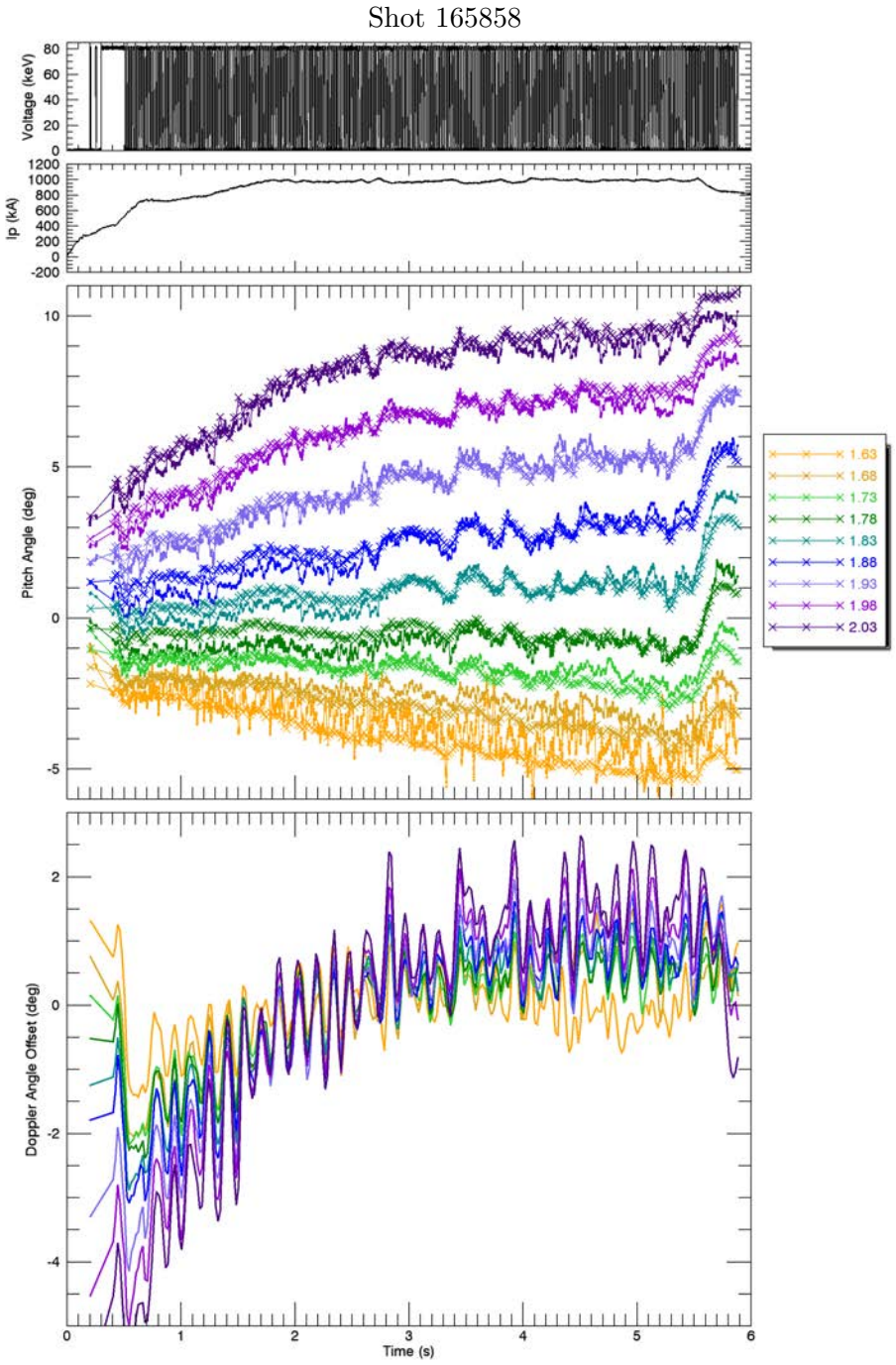

Figure 4.28: Pitch angle evolution for shot 165858. From 0.5s onward the camera exposure is synchronised with the 10ms 30L beam blips at 50% duty cycle. The oscillation seen in the Doppler angle is due to a small vibration between the polarimeter and tokamak discussed in Section 4.3.6.

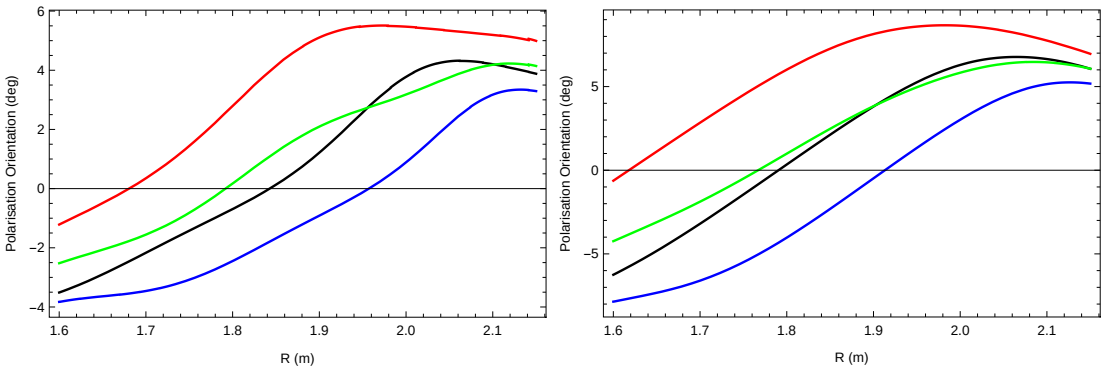

Figure 4.29: EFIT IMSE midplane polarisation orientation forward model for shot 165858 for beam centre-line (black), far side of beam (blue), near side of beam (red) and average approximation (green) at 805ms (left) and 5005ms (right).

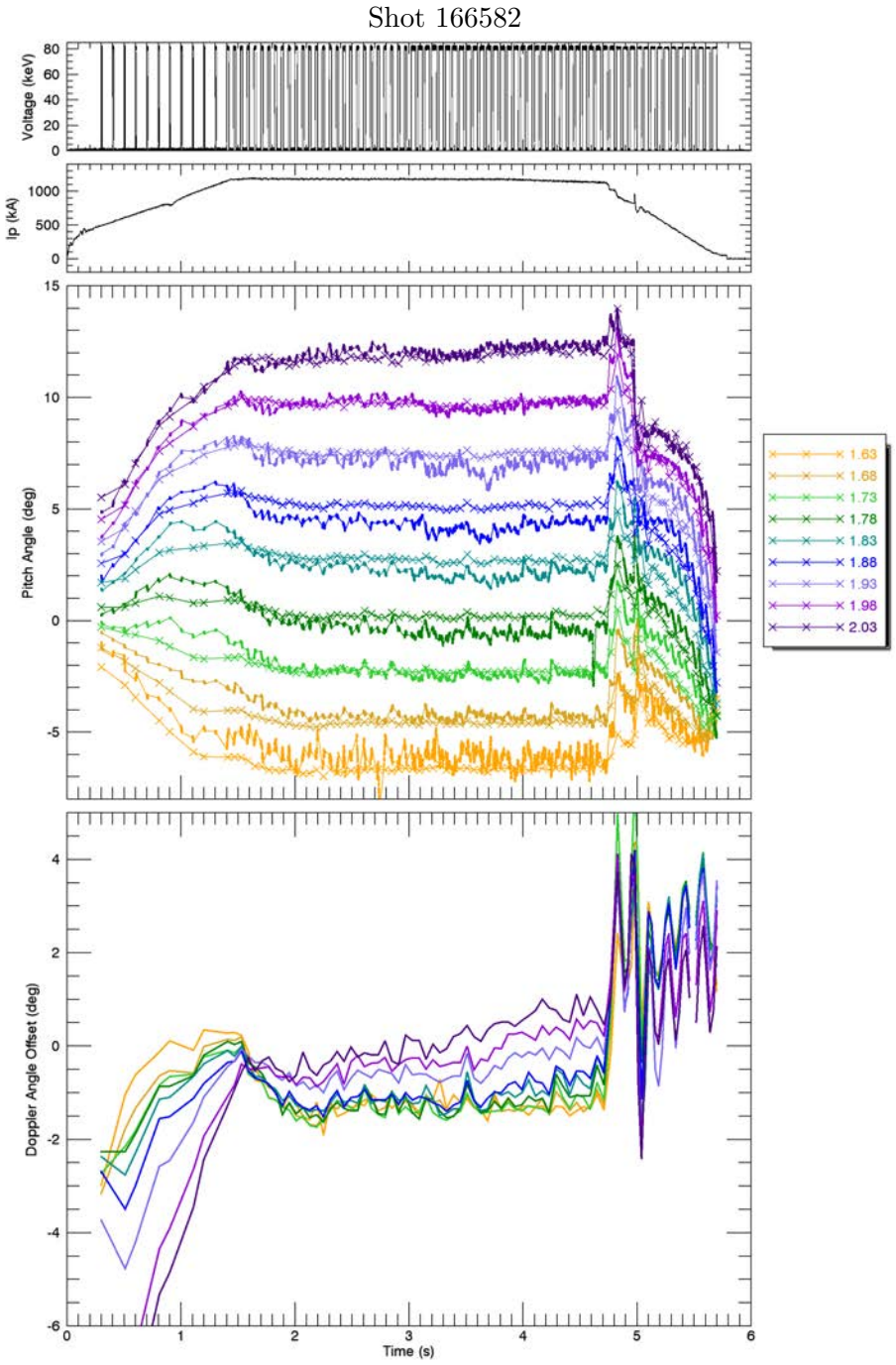

Figure 4.30: Pitch angle evolution for shot 166582 where the beam remains on during the current ramp down. The camera exposure is 20ms with 10ms readout. The 30L neutral beam initially has 10ms 10% duty cycle blips followed by 20ms 33% duty cycle blips and finally 40ms 67% duty cycle blips.

beam model (with/without horizontal and vertical divergence similar to Fig. 4.8). The residual difference between the IMSE measurement and EFIT prediction (without beam divergence) is shown in the right of the figure. The most notable difference between the two is that the contours of constant polarisation predicted from EFIT are reasonably vertical while the IMSE contours are more strongly tilted. This additional tilt and curvature is not consistent with the predictions when considering any of the beam divergence effects. The IMSE contours fan outward from the bottom of the image in the experimental measurement but in the forward model they are expected to fan outward from the top of the image. If in fact the beam were vertically converging then the effect would be somewhat replicated but the magnitude of the tilt cannot even be reproduced in an adapted neutral beam model given the physical limitations imposed by the beam aperture. Line-integration through the beam, approximated by the near/far beam model, contributes a small fraction of the tilt seen here but the vertical divergence effect is anticipated to be a stronger effect. These trends in the IMSE/EFIT residual difference are consistent for shots with normal B_t and I_p which indicates that there is some systematic error in the IMSE measurement above and below the midplane that has not been captured in the calibration. Beam-into-gas calibrations would be ideal to calibrate possible distortions in the IMSE images but was not available during the campaign.

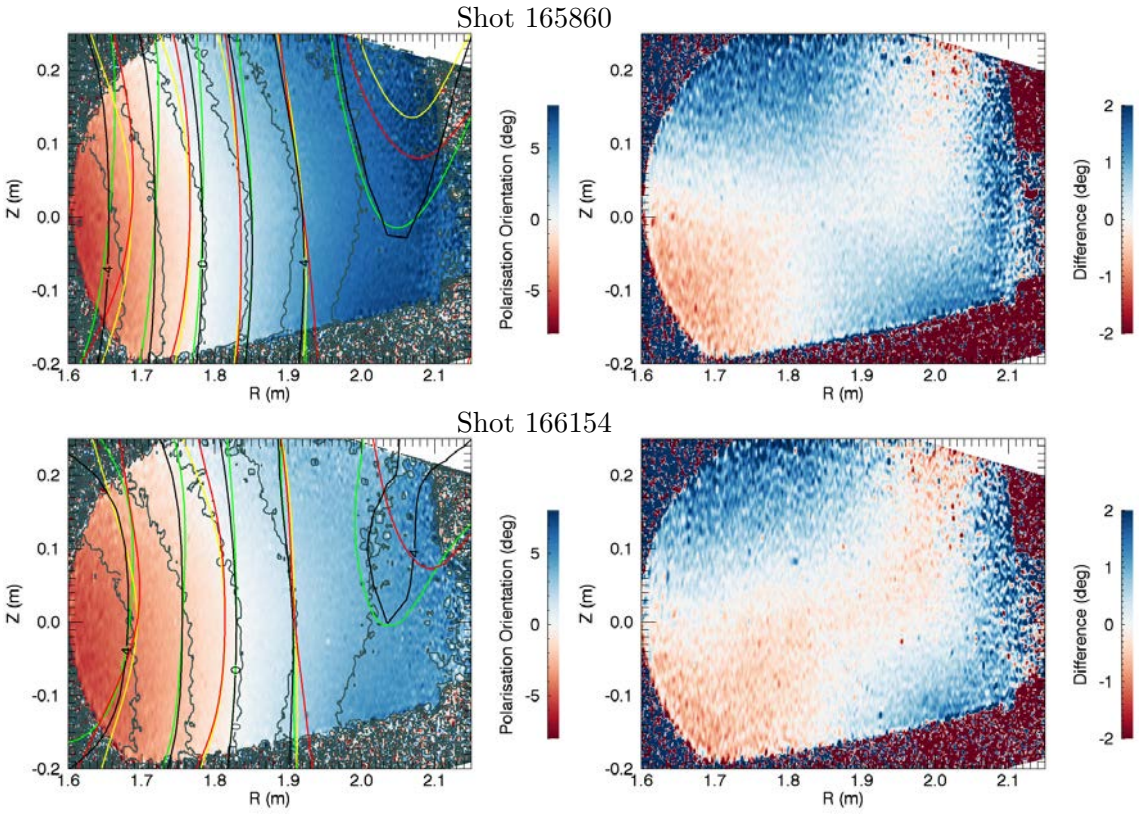

Figure 4.31: (Top) Polarisation orientation for shot 165860. (Bottom) Polarisation orientation for shot 166154. (Left) Colour map and dark grey contours depict the experimental IMSE measurement while similarly to Fig. 4.8 the EFIT forward modelled polarisation orientation for a thin non diverging beam is in black, a thin vertically diverging beam in green, a thick beam with no vertical divergence in yellow and thick diverging beam in red. (Right) Residual difference between the IMSE measurement and EFIT forward model (thin beam, no divergence).

4.3.3 Comparison with Conventional MSE for Reverse B_t or I_p Shots

In about 100 shots during the IMSE campaign the toroidal magnetic field direction was reversed and for another 100 shots the direction of the plasma current was reversed. There weren't any shots with both the current and field reversed. When either the magnetic field or toroidal field is reversed the pitch of the magnetic field flips compared to the normal I_p and B_t case, as seen earlier in Fig. 4.11. In Fig. 4.32 the IMSE pitch angle is compared with the 315° conventional MSE measurement for a shot with reverse toroidal field. The $R = 2.03$m IMSE and conventional MSE channels show good absolute agreement. However for channels at lower radii there is a discrepancy between the two measurement of $1 - 2°$. This offset remains fairly constant throughout the shot and is similar for other shots with reverse B_t. The pitch angle is expected to be zero for all channels at the very beginning of a shot when the toroidal field is on but there is no plasma current, however only once the neutral beam turns on later in the shot are MSE measurements possible. By visually extrapolating the pitch angles in Fig. 4.32 to the start of the shot it appears the conventional MSE measurements originate from approximately $-1.5°$ while the IMSE channels appear to originate from closer to 0° pitch as expected. The extrapolation technique is not definitive and when applied to a number of other shots having early neutral beams both measurements appear to originate from near 0°.

An example of the MSE measurements for a shot with reverse plasma current is shown in Fig. 4.33. In this case there is a more dramatic offset between the IMSE and the conventional MSE of $2 - 3°$ pitch angle or alternatively a $\sim$ 8cm shift in the radial location of the channels. Again this difference is fairly consistent across the range of shots where IMSE was operational. This difference is surprising given the good agreement demonstrated with normal B_t and I_p shots. The relevant sightlines from both views are almost horizontal so that Faraday rotation coming from the poloidal field is not expected. If the pitch angle is visually extrapolated to the start of the shot for the reverse B_t shots, the conventional MSE measurements seem to originate from $-2.5°$ while the IMSE measurements are not inconsistent with a 0° origin as expected. More details of this discrepancy are considered in Section 4.3.4 where the magnetic axis locations measured with the MSE systems are compared for the different shot types.

The 2D nature of the IMSE measurement for shots with reverse toroidal field and reverse plasma current are shown in Fig. 4.34 and can be compared with the earlier plots in Fig. 4.31 for shots with normal B_t and I_p. For both 'reverse' shots the contours of constant polarisation orientation appear to be fanning outward from the top of the image relative to the EFIT forward modelled contours. Similarly to the 'normal' shots the direction of the tilt is inconsistent with a vertically diverging beam and too large to result from line-integration effects. The residual difference between the IMSE and EFIT forward model, shown in the right of the figures, is similar for shots with normal B_t but differences are more pronounced for the cases with reverse B_t. A possible systematic error in the Faraday rotation correction is the most obvious cause that would change for the IMSE measurement between normal and reverse B_t shots. However the magnitude of any error in the Faraday rotation correction is expected to be relatively small. When changing the sign of the $\sim$ 2T toroidal field the Faraday rotation in the IMSE view is expected to change by $\sim 1°$ in the high R positions while at $R = 1.8$m the Faraday rotation is expected to remain zero. As noted earlier there may be some additional Faraday rotation in the 300mm lens used for the IMSE system that is not included in the Faraday correction. Given there is some consistency between the offsets for the different shot types it seems likely that some

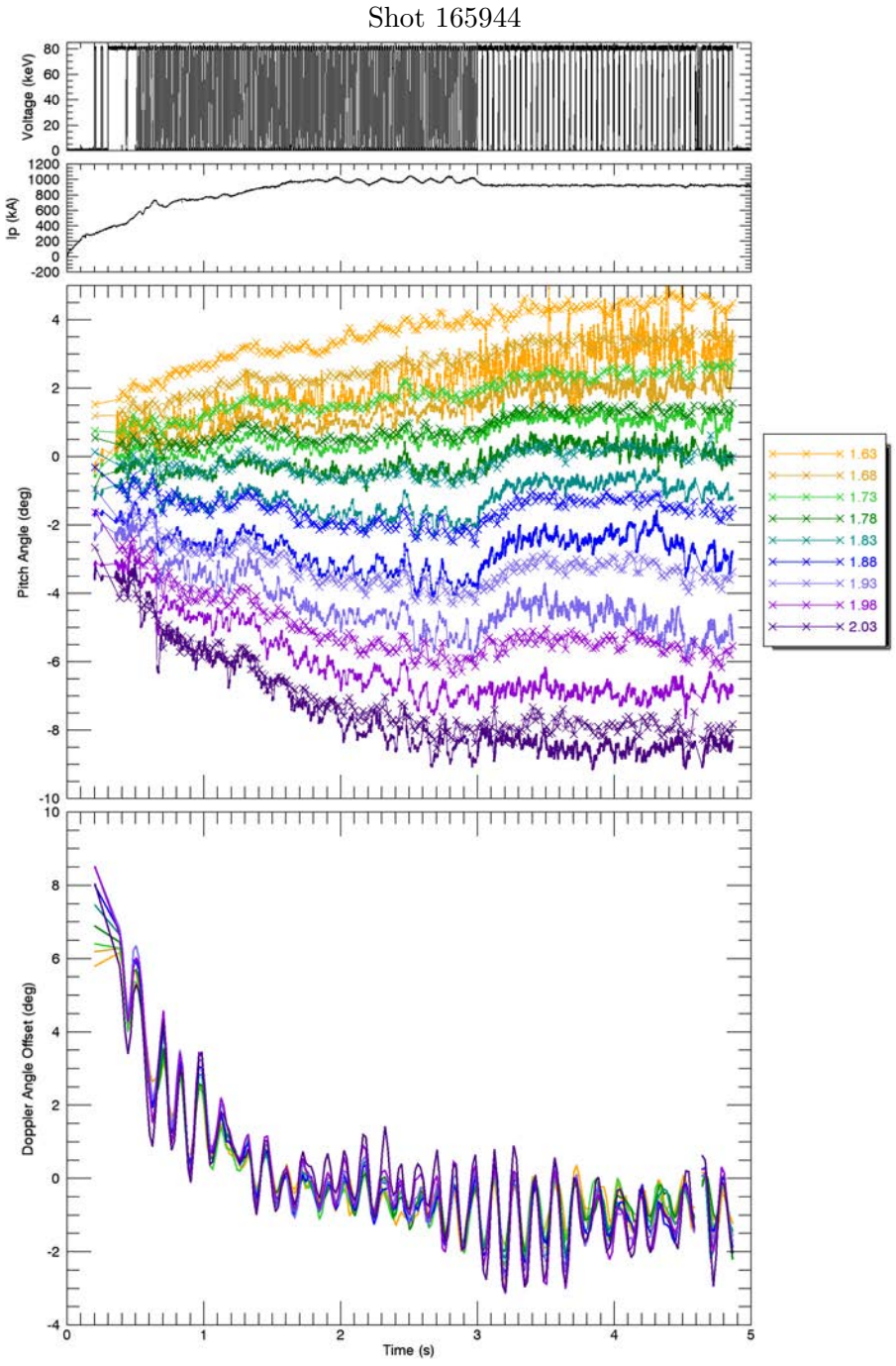

Figure 4.32: Evolution of shot 165944 with reverse toroidal field. The camera exposure is 20ms with 10ms readout. From $0.5 - 3$s the 30L neutral beam operates with 10ms 50% duty cycle blips which is followed by 32ms 80% duty cycle blips.

distortions exist in the MSE images, however it must also be remembered that EFIT is not constrained with any measurements off the midplane. It is hypothesised that Faraday rotation likely contributes some distortion when B_t is reversed and a fixed distortion also exists, most likely originating from a shortcomings in the illumination source calibration correction described in Section 4.2.3. It is possible that the aperture of the calibration polariser used for the calibration correction was insufficiently wide. *An in-vessel or beam-*

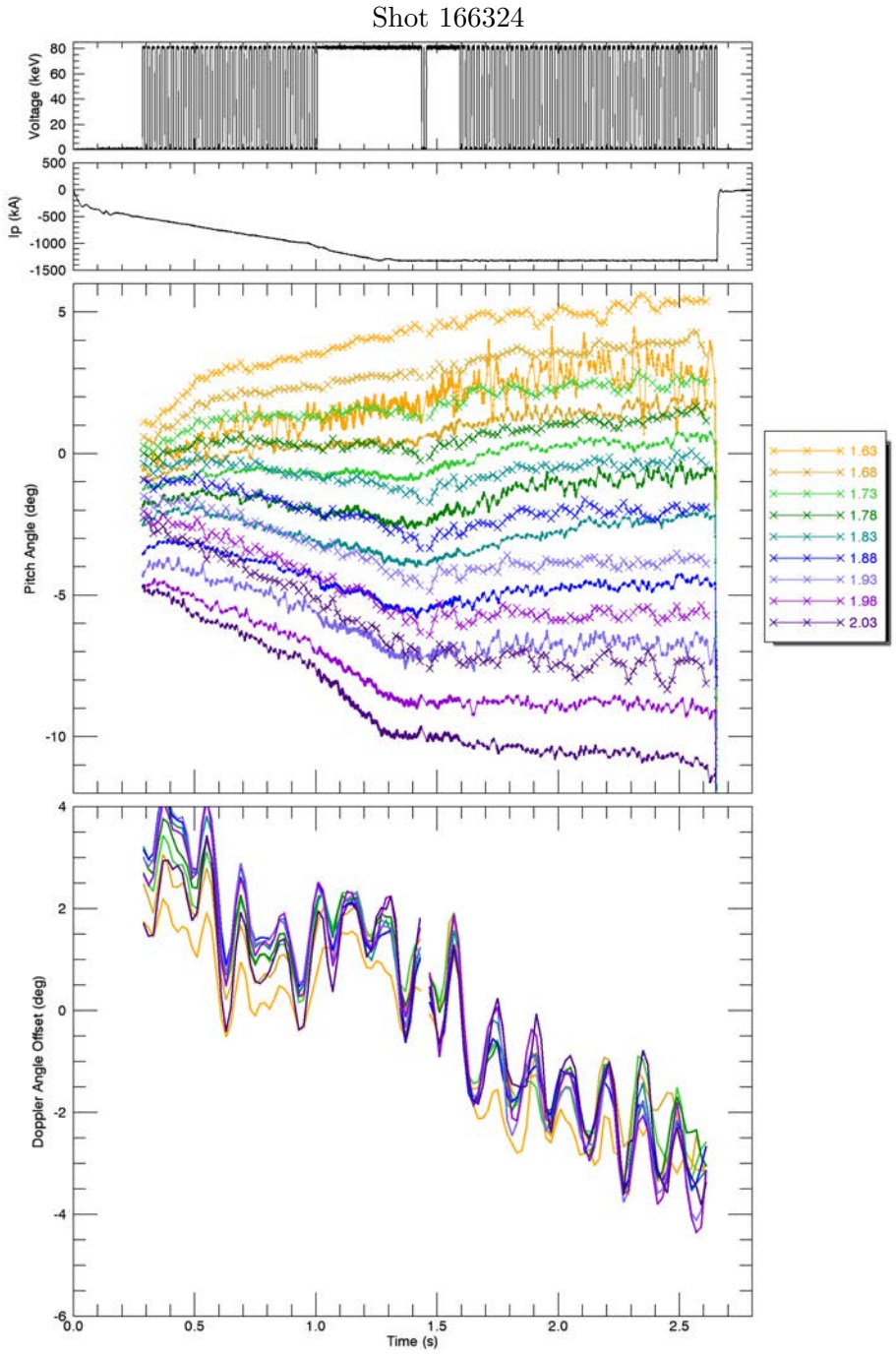

Figure 4.33: Evolution of shot 166324 with reverse plasma current. Other than the steady beam period the 30L is operated with 10ms blips with 50% duty cycle. The camera is synchronised with these blips.

into-gas calibration would be ideal for ruling out or correcting these uncertainties in any future IMSE installation.

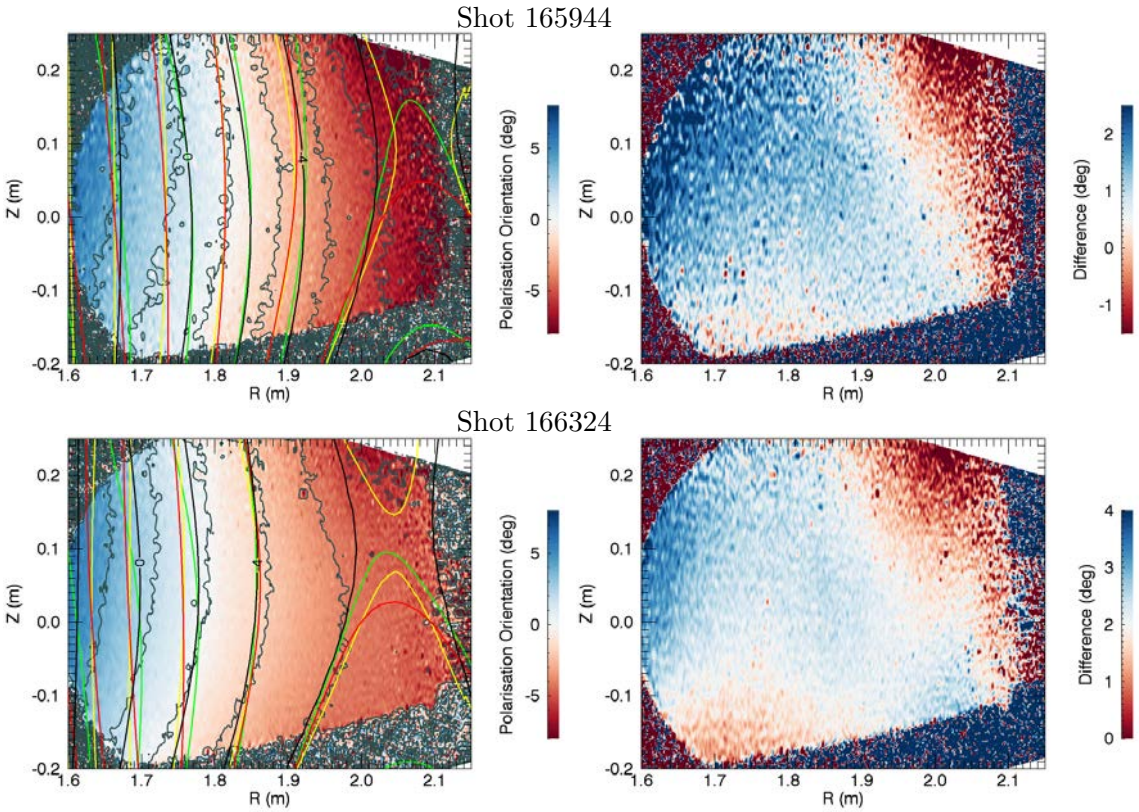

Figure 4.34: (Top) Polarisation orientation image for shot 165944 with reverse toroidal field and (Bottom) for shot 166324 with reverse plasma current. The layout is the same as in Fig. 4.31 except with an offset in the colour scale.

4.3.4 Consistency of Magnetic Axis Calculations

It is instructive to compare measurements of the magnetic axis that are independent of MSE to corroborate the inconsistencies between the IMSE and conventional MSE for different shot types. The magnetic axis is an excellent comparison point because ambiguity between different MSE views is removed as $E_r = 0$ and measurements of other plasma parameters such as electron temperature are expected to peak on the axis. The 'EFIT1' equilibrium reconstruction is constrained with external magnetic pickup coils and directly provides a prediction of the magnetic axis independent of MSE. The electron cyclotron emission (ECE) diagnostic measures the electron temperature with channels spaced closer than 3cm along the midplane and the peak temperature indicates the position of the magnetic axis. Other diagnostics such as 'soft x-rays' or charge exchange ion temperature measurements could also be used to measure the magnetic axis position but ECE offered the greatest resolution. Calculation of the magnetic axis position from MSE measurements is straightforward as the polarisation orientation profile is roughly linear and the magnetic axis corresponds to the zero crossing. 'EFIT2' is constrained with the conventional MSE and is therefore expected to indicate the same axis position. The location of the magnetic axis using these various diagnostics is shown in Fig. 4.35 for three shots covering the different combinations of B_t and I_p directions. Small differences $\sim 1^\circ \cong 2$cm are to be expected between the IMSE and conventional MSE measurements due to line-integration and beam attenuation effects.

As expected the MSE constrained EFIT2 magnetic axis location agrees with the 315° MSE measurements. Definitive measurements of the axis position from the ECE electron temperature are challenging as the peak is often too broad to provide the resolution needed to make a conclusive assessment. Furthermore with non-inductive current drive the electron temperature signal is often peaked on both sides of the axis. Therefore ECE data is only shown when there is a clear peak. As detailed earlier, for shots with normal toroidal field and plasma current there is close agreement between the IMSE and conventional MSE, this is again evident in the top plot of Fig. 4.35. Typically the EFIT1 and ECE measurements are in agreement for the ohmic part of the discharge and when supplementary heating is applied the ECE and MSE data suggests that EFIT1 underestimates the magnetic axis position. In shot 166153 there is a discrepancy between the IMSE and conventional MSE after 1.8s but this likely results from a line-integration effect from the IMSE view. The ECE peak identification is also noisier during this period.

For the reverse toroidal field shots with IMSE measurements there is limited consistency in the ECE data to corroborate the accuracy of the IMSE and conventional MSE measurements. This is evident in Fig. 4.35 for shot 166093 where initially the ECE data is in agreement with the conventional MSE near $t = 800$ms before it more closely follows the IMSE axis measurements near $t = 2000$ms. At other periods during the shot there is no clearly resolvable peak in the ECE data, either because it is too broad or too noisy. The EFIT2 axis position in this case is inside the EFIT1 prediction which is opposite to the normal B_t example.

For shot 166263 with reverse plasma current, both the EFIT1 and ECE measurements suggest that the axis position measured by the conventional MSE is too low and the IMSE is too high. In particular the EFIT2 axis position is well below the EFIT1 position, which is the opposite of the case with normal B_t and I_p when there was agreement between all internal measurements. Furthermore in Fig. 4.35 for the reverse I_p shot, it can be seen that there are a limited number of EFIT2 equilibrium reconstructions available. When

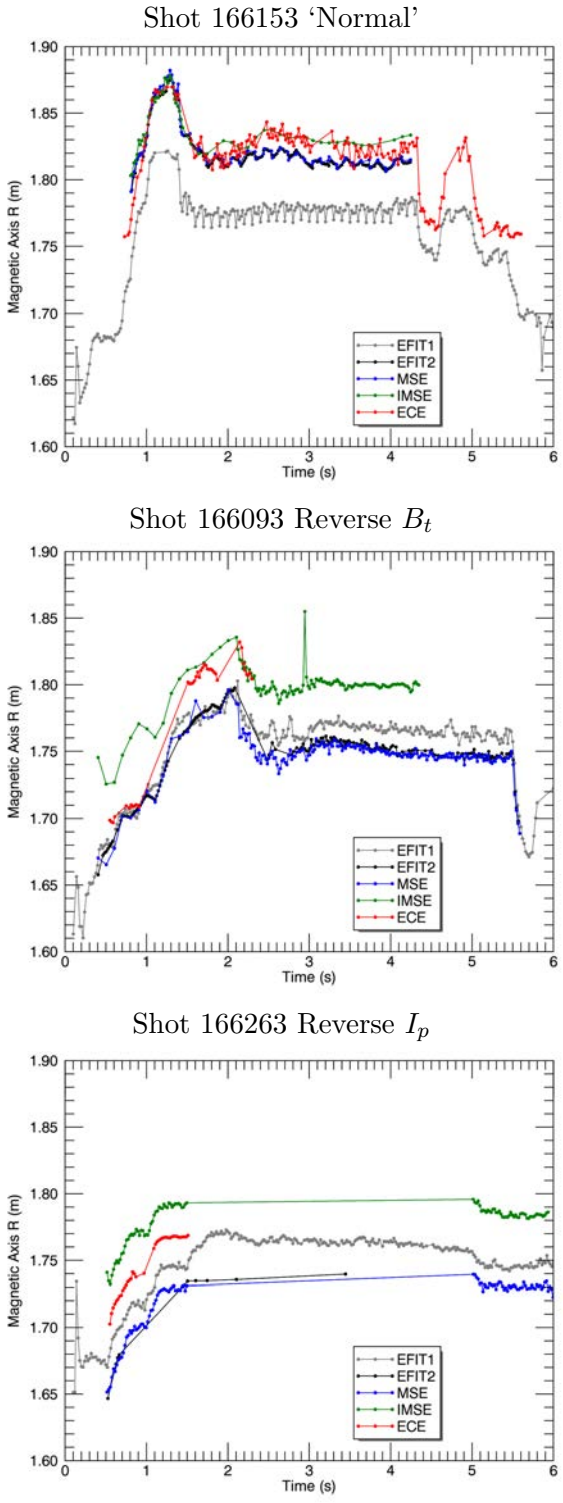

Figure 4.35: Comparison of the magnetic axis position measured using EFIT (EFIT1 magnetics only, EFIT2 MSE constrained), 315° MSE, IMSE and electron cyclotron emission. (Top) Shot 166153 with normal I_p and B_t. (Middle) Shot 166093 with reverse B_t (the 2.94s IMSE data point is noisy due to a failed beam blip shorter than 1ms). (Bottom) Shot 166263 with reverse I_p.

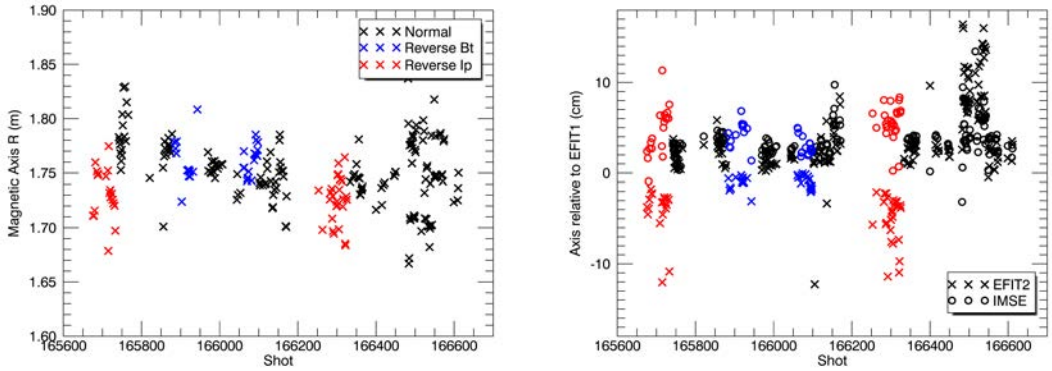

Figure 4.36: (Left) Position of magnetic axis given from EFIT1 for normal, reverse toroidal field and reverse plasma current shots. (Right) Magnetic axis position for EFIT2 (conventional MSE constrained) and IMSE relative to EFIT1 (external magnetics only). The median value is taken from points in time where all three measurements are available.

	'Normal'	Reverse B_t	Reverse I_p
EFIT1	1.751m	1.755m	1.729m
EFIT2	1.784m	1.749m	1.691m
IMSE	1.785m	1.799m	1.787m

Table 4.5: Median magnetic axis position inferred with EFIT1 (magnetics only), EFIT2 (MSE constrained) and IMSE for different shot types.

there is an inconsistency between the external magnetic measurements and conventional MSE the equilibrium solver will struggle to converge to a solution.

Given the challenges in obtaining routine measurements of the magnetic axis from ECE it was decided that EFIT1 provides the most unbiased and consistent comparison point. In the left of Fig. 4.36 the average magnetic axis position given by EFIT1 for each shot is shown. The average is only taken during time intervals in a shot where EFIT1, EFIT2 and IMSE are all available and therefore the intervals are different for each shot. Then in the right hand side of Fig. 4.36 the position of the magnetic axis measured with EFIT2 and IMSE is plotted relative to the EFIT1 measurement. In this plot there is a clear discrepancy between the IMSE and conventional MSE for the reverse I_p measurements and to a lesser degree for the reverse B_t shots. This trend is quantified in Table 4.5 where the median value from all shots of a given type is displayed, confirming the general trends seen in Fig. 4.35.

The shots with reverse I_p have the greatest discrepancy between the MSE diagnostics for the magnetic axis measurements and while there are a number of uncertainties for the IMSE measurement the discrepancy is significant. The possibility of a systematic error in the conventional MSE measurement for reverse I_p shots should be further investigated given that: EFIT2 struggles to converge to a solution; the discrepancy with the ECE, IMSE and EFIT1 measurements of the magnetic axis position; and the conventional MSE pitch angles do not appear to be originating from 0° pitch at the start of the shot. However there is no obvious source of error that would arise with only a change in the direction of the plasma current. Less commonly considered effects such as stress induced birefringence in the port window or Faraday rotation from a poloidal field coil may change with direction

of the current. For example ramped currents used to induce the plasma current may cause changes in magnetic flux through the port window resulting in stresses from any metal enclosing the window, however any fringing fields near the midplane will not have a significant component normal to the window. Movements between the beams, tokamak and collection optics are unlikely but could possibly give rise to a current dependent offset. IMSE has the advantage that the any movement can be seen in the images and some minor movements that were observed with the IMSE optics are discussed in the next section. There are smaller discrepancies between the different measurements for shots with reverse B_t and there is less evidence casting doubt over the well-established conventional MSE measurements for these shots.

4.3.5 Consistency of Data with the 30L and 30R Beams

Measurements from the 30R neutral beam deliver new information inside the magnetic axis in a region that has not previously been measured while also delivering a cross validation of the 30L measurements. However the radial resolution from the 15° port with the 30R beam is even poorer than the 30L beam. Furthermore the far side of the 30R beam reaches the inner wall for measurements inside $R \approx 1.3$m resulting in a polarisation orientation more heavily weighted to the near side of the beam, as highlighted in Fig. 4.10. This effectively reduces the measured value of $|\theta_\sigma|$ and pitch angle in this region. An example of the polarisation orientation image measured with the 30R beam is shown in Fig. 4.37. Interestingly the tilt/fanning pattern of the experimental polarisation contours is comparable to that in the 30L images and also in the opposite direction to that expected from the vertical divergence of the beam. Again this indicates there is some small remaining distortion in the IMSE images.

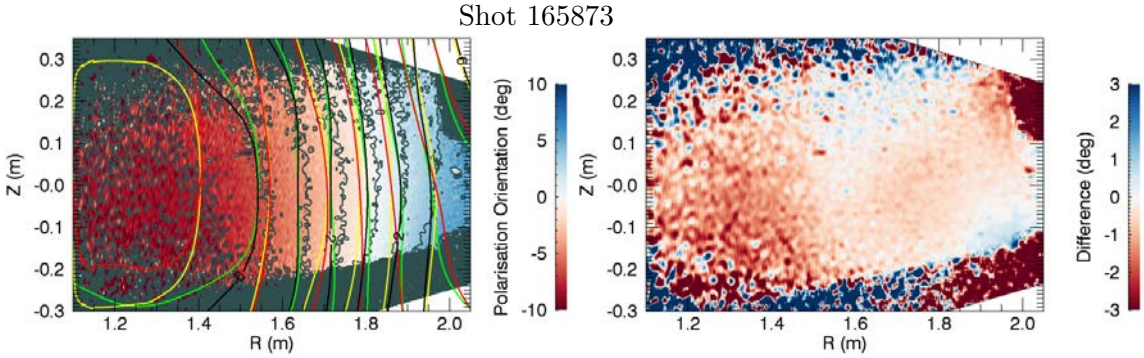

Figure 4.37: Polarisation orientation image for shot 165873 with the 30R beam. The EFIT forward modelled contours assume a horizontally injected infinitesimally thin neutral beam.

Given the significant line integration and drifts in the Doppler angle it is not possible to simultaneously compare measurements from the 30L and 30R beams because reliable IMSE measurements are only available when one of the beams is injected. However with some of the beam modulation strategies used there were periods when the beams were somewhat interleaved allowing for a comparison at similar times. An example of such a beam modulation strategy is shown in Fig. 4.38 for a shot with normal B_t and I_p. There is close agreement between the IMSE measurements from both beams and the conventional MSE. It should be noted that the beams will perturb the current profile but any changes are small, particularly given the limited radial resolution of the IMSE view.

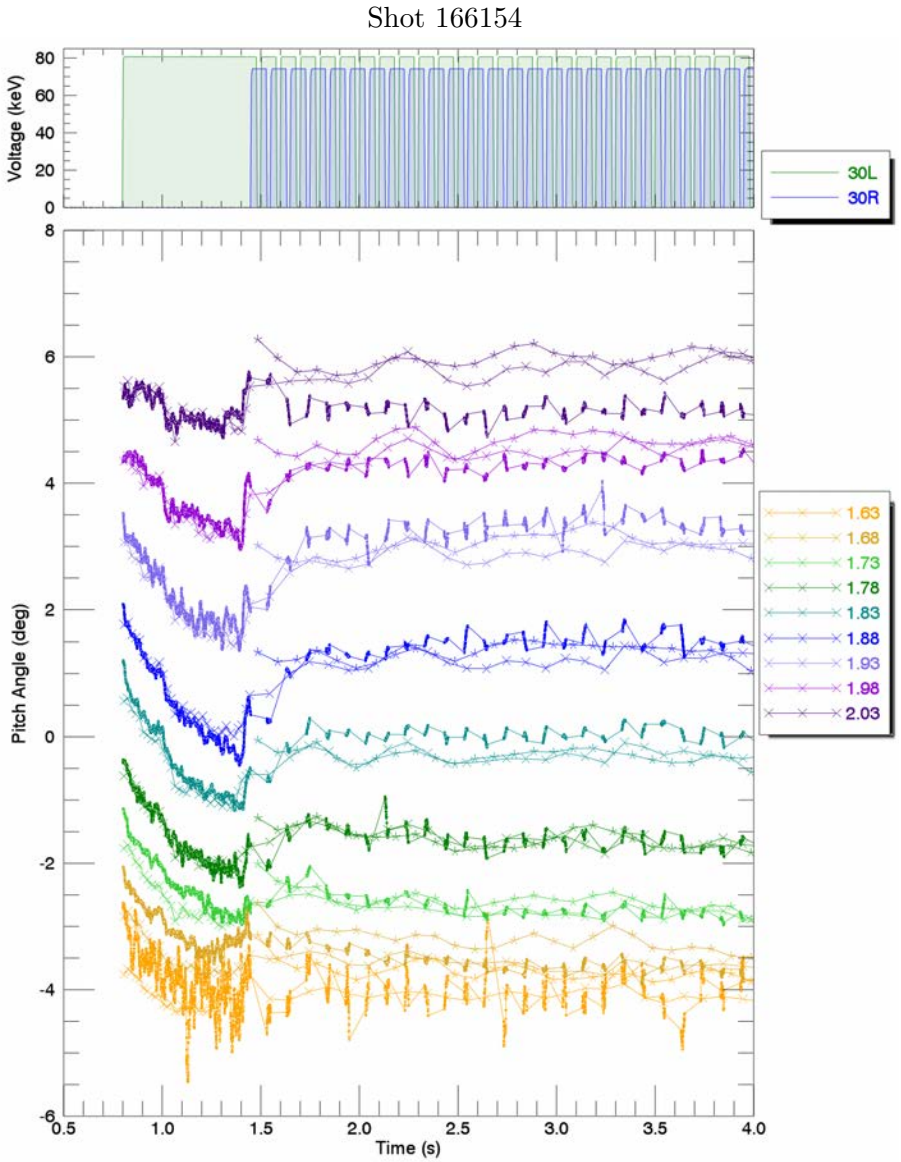

Figure 4.38: Temporal evolution of the pitch angle for shot 166154 with 30L (crosses) and 30R (asterisk) beams interleaved. Between $1.5-4$s the 30L and 30R have 80ms blips where only the opposite beam is on during the downtime. The camera exposes for 10ms during each blip to deliver a 10Hz acquisition rate from each beam.

To compare the imaging data from the different beams requires a correction for geometric factors and assumptions to be made about B_r. While it is may be possible to directly infer B_r from gradients in an MSE image (Eq. 1.18) and boundary constraints, it remains to be seen if sufficient resolution and accuracy can be obtained from the IMSE measurements and whether the average vertical velocity of the beam can be modelled or measured with sufficient accuracy. Nevertheless on the midplane the approximation that $B_r = 0$ is generally valid and midplane pitch angle measurements are shown in the left column of Fig. 4.39 under the assumption of an infinitesimally thin beam for comparison of the MSE measurements. In the middle and right columns of the figure $\arctan(B_z/B_\phi)$ 'pitch angles' are shown for $Z = 0.15$m and $Z = -0.1$m. The relationship $B_z/B_\phi = \tan\theta_E(\sin\alpha B_\phi + \cos\alpha B_r)/B_\phi$ is used, where $\tan\theta_E$ (Eq. 1.16) is calculated from

the IMSE measurement assuming $E_r = 0$ and the remaining scaling correction $\approx \sin\alpha$ is determined from EFIT to make minor corrections for B_r in a self-consistent manner.

In all three midplane cross sections the agreement between IMSE measurements from the two beams is remarkable and demonstrates the self-consistency of the IMSE system. There are some noteworthy features in these midplane pitch angle comparisons. For the 30R beam the line integration effects, indicated in Fig. 4.10, are expected to bring the measured IMSE pitch angle closer to zero for $R < 1.6$m. While this is somewhat evident in the region $1.4\text{m} < R < 1.6\text{m}$ the opposite occurs for $R < 1.4$m. A similar discrepancy occurs for $R < 1.4$m in the shots with reverse B_t and I_p but in the reverse current shot the EFIT2 pitch angles look non-physical in this region. The pitch angles measured from the 30L IMSE in the region $R > 2.05$m look to be incorrect, particularly for the reverse B_t example. The weak Doppler shift and signal in this region (evident in Fig. 4.14) may result in the measurement being susceptible to systematic errors and noise.

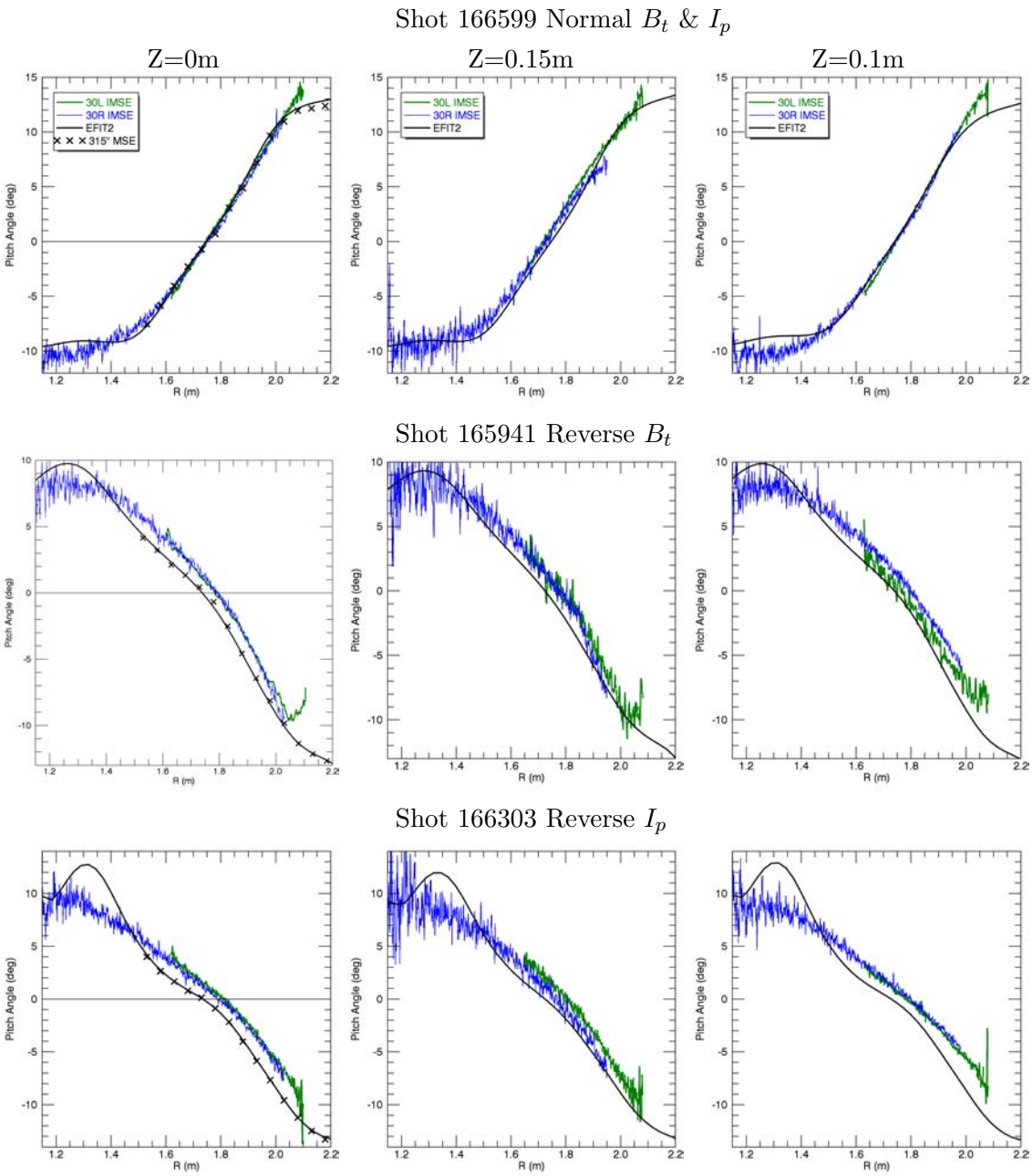

Figure 4.39: Pitch angle measured with 30L IMSE (green), 30R IMSE (blue), EFIT2 (black line) and conventional MSE (black crosses). (Top) Shot 166599 with normal B_t and I_p near t = 2200ms. (Middle) Shot 165941 with reverse B_t near t = 3000ms. (Bottom) Shot 166303 with reverse I_p near t = 1800ms. (Left) At midplane with the 0° intersection indicating the magnetic axis position, (Centre) Z=0.15m and (Right) Z=−0.1m. Line integration effects for the polarisation orientation in the same shots are shown in Figs. 4.10 and 4.11.

4.3.6 Instrumental Effects Related to the 'Doppler angle' $\phi_0 + \alpha_l$

The primary goal of a MSE diagnostic is to measure the linear polarisation orientation, however in the case of IMSE it is also worthwhile to understand and measure the 'Doppler angle' $\phi_0 + \alpha_l$ in the carrier phase, for potentially calibrating the effects of vertical beam

divergence and Stark-Zeeman effective interferometric ellipticity. In Section 4.2.2 it was emphasised that the interferogram phase factors α_l and α_c are needed to calculate and correct for the Stark-Zeeman circular polarisation fraction in an IMSE measurement. For the radial view used here the effective interferometric ellipticity of the MSE emission is expected to be small, however there are a number of interesting effects relating to the Doppler angle that highlight some of the challenges that must be considered when making corrections for a more tangential IMSE view. In a number of the examples the Doppler angle is shown to vary during the shot, potentially contaminating the decoding of θ_σ. To limit contamination of the IMSE θ_σ measurement the carrier fringe phase difference is calculated using one image and its two nearest neighbours in time having the opposite FLC state.

Absolute Measurement of the Beam Velocity

The phase offset ϕ_0 measured in the IMSE phase is dependent on the wavelength of the multiplet and can therefore be used to measure the Doppler shift of the beam. An example illustrating the difference in the displacer delay between a calibration at fixed wavelength and the neutral beam emission is seen in Fig. 4.15 where the fringes become tilted due to the Doppler shift increasing across the field of view. This measurement is important to validate the vertical divergence of the beam and give certainty in the unfolding of the magnetic field orientation from the cross product $\mathbf{v} \times \mathbf{B}$. To measure the Doppler shift of the beam it is essential that the delay of the displacer does not change between the calibration and plasma measurement and for the spectral contribution in the α_l term to be known. Such a measurement of the beam Doppler shift has previously been made on Textor in Ref. [54] with some success.

For the DIII-D IMSE measurements the delay of the waveplate was found to drift by up to a wave between the calibration and the plasma shots, preventing an accurate measurement of the absolute Doppler shift. This drift is caused by two different effects. The first is that the temperature of the displacer crystal is likely to have changed between the day it was calibrated and the day of the plasma measurement, leading to a shift in the delay from thermal expansion and the temperature dependence of the thermo-optic coefficients[71]. The second effect is that the displacer surfaces inevitably have some non-parallelism and thickness non-uniformity. Consequently the effective delay is dependent on the distribution of ray-paths through the crystal which is not the same for the calibration and plasma measurement. This is related to the situation where the non-uniformity in the FLC delay influences the polarisation response (Fig. 4.24) but it is important to note that the displacer non-uniformity is not expected to affect the polarisation orientation measurement. For the relatively short time scales within a shot the displacer temperature drift is negligible and the ray paths through the system do not change implying is still possible to make a measurement of the relative Doppler shift during a shot. Hence the experimental plots of the Doppler angle presented in this chapter have been arbitrarily offset but relative changes are valid.

Oscillation

In a large number of shots there is a 6.7Hz oscillation in the measured Doppler angle with an amplitude of around $\sim 2°$. This oscillation is evident for shot 165748 in Fig. 4.27 (8Hz in this case), shot 165858 in Fig. 4.28, shot 165944 in Fig. 4.32 and shot 166324 in Fig. 4.33. This oscillation is caused by a vibration of the optical rail relative to the

tokamak that is also evident in the background features in the image moving during the shot. The amplitude of the oscillation can be measured from movement in the background features in the IMSE image or directly from this Doppler shift oscillation. The gradient of the neutral beam Doppler shift is approximately in the horizontal direction (Fig. 4.12). Hence from the $\sim 2^\circ$ oscillation it is calculated that there is a horizontal shift in the image of around 3 pixels or $\Delta R = 0.8$mm for the 30L beam. This shift is not inconsistent with the movement of the fiducial markers in the image during the shot. The Doppler angle is insensitive to vertical oscillations provided that the camera lens remains fixed relative to the camera sensor. The oscillation is relatively slow compared to the exposure rate and therefore the effect on the polarisation orientation encoding is not significant. By tracking the movement of background features in the image it would be possible to correct for this oscillation in both the phase of the carrier and in the spatial calibration. However routinely correcting for such an effect is not straightforward and it is therefore best to minimise or prevent such vibrations in future implementations of the system. It should also be noted that a mechanical shift/drift of the fringe pattern on the CCD will more significant when using aggressive fringe frequencies.

There is also a trend for Doppler angle to increase during shots with normal I_p and B_t while the Doppler angle decreases during shots with reverse I_p or B_t. This trend is also linked to a relative horizontal movement between the camera rail and tokamak, which typically leads to a 9 pixel movement for reverse B_t shots and 14 pixel movement for reverse I_p shots relative to the normal shots. This requires the radial position of the IMSE channels to be increased by ≈ 2.7mm for the reverse B_t shots and increased by ≈ 4.2mm for reverse I_p shots. These corrections are small compared to the discrepancies between the IMSE and conventional MSE discussed in Section 4.3.4 and have not been corrected for in the data.

Variation in α_l with $|\mathbf{E}|$

The interferometric phase $\phi_0 + \alpha_l$ of the linearly polarised spectrum can be calculated from Eq. 3.47, where it is seen that the phase depends on both the profile of the transmitted spectrum and the delay of the displacer. Furthermore the transmitted spectrum is complicated by the filter profile, the neutral beam velocity, the total electric field strength, neutral beam divergence, line integration, Doppler broadening due to the range of rays through the lens and the relative upper state populations of the transitions. Ideally $\alpha_l = 0$ when the spectrum is symmetric about the σ_0 emission, but even when a small subset of these spectral effects are included this is not the case, as evident in Fig. 4.21. The $\phi_0 + \alpha_l$ phase term is carried in both states of the FLC and therefore the polarisation measurement is expected to be independent of its value when the circular polarisation fraction is negligible (which is true here but less valid for more tangential views) or the polarimeter is ideal (requiring a true half-wave FLC). The $\phi_0 + \alpha_l$ term is also important for the amplitude spatial heterodyne to determine the relative contribution of the circular polarisation to the $\phi_D \pm \phi_S$ carriers (Section 3.5.2).

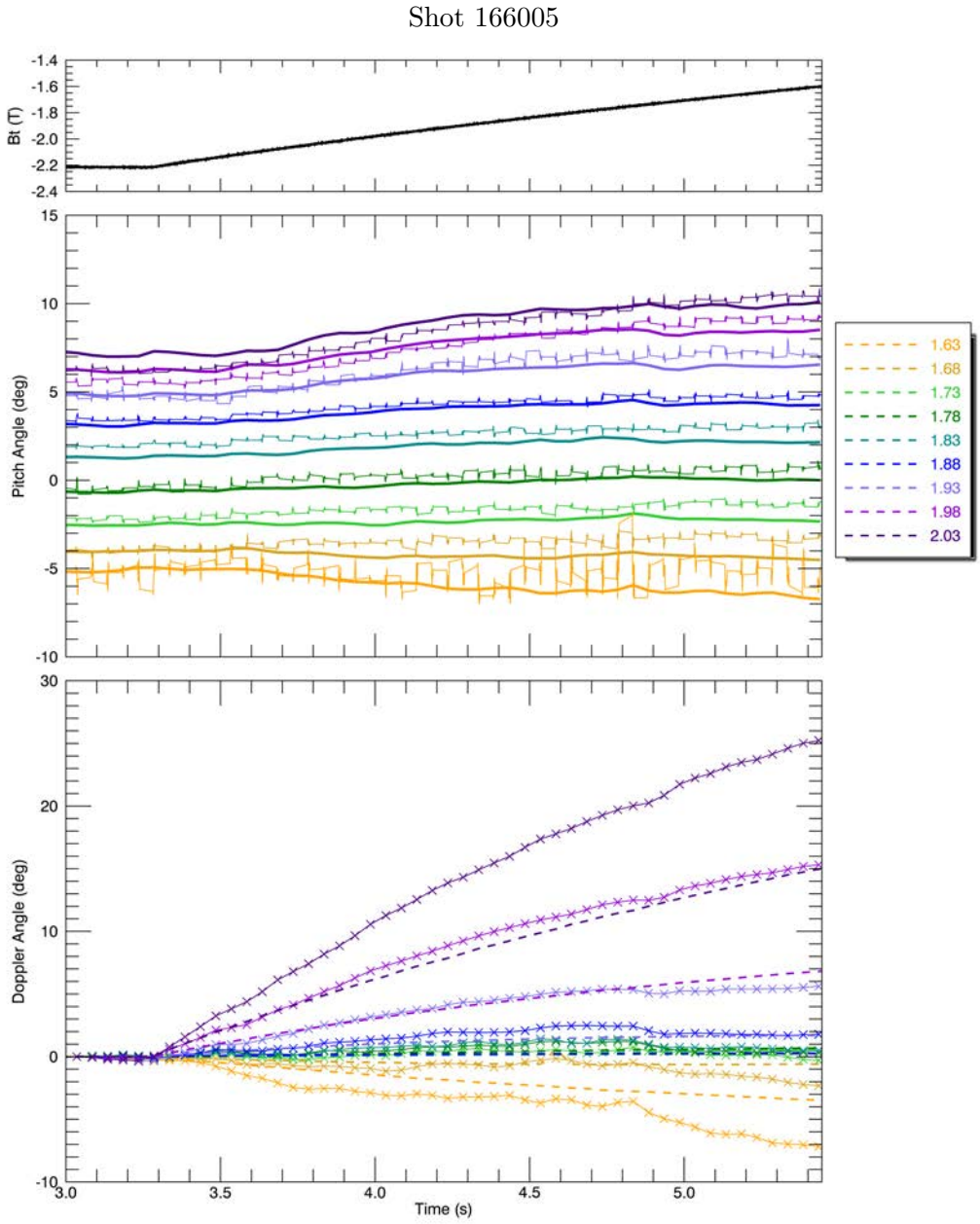

Figure 4.40: Evolution of α_l for shot 166005. The plasma current remains constant over the displayed time period. The lines with crosses represents the experimentally measured value of α_l while the dashed line gives the EFIT prediction assuming equally populated upper-states and an infinitesimally thin beam as in Fig. 4.13.

It was noticed that $\phi_0 + \alpha_l$ suddenly began drifting by up to 30° within a plasma shot while the beam velocity was constant. This was found to coincide with an increase or decrease in the toroidal field strength, with an example given for shot 166005 in Fig. 4.40. A decrease in the toroidal field strength leads to an increase in the pitch angle and decrease in the Stark splitting but has no effect on the Doppler shift. At first glance this is not expected to have a noticeable effect on the $\phi_0 + \alpha_l$ term, but for this measurement in regions where the full energy component is at the edge of the filter passband the change in the Stark splitting will shift the 'centre of mass' of the spectrum. Qualitatively the trend in the Doppler angle in Fig. 4.40 agrees for the IMSE and EFIT prediction but the

magnitude of the drift is underestimated by a factor of roughly 2. It is anticipated that a more complete model of the spectrum would improve the quantitative agreement. This model would have to consider line-integration effects; upper-state populations; full, half and third energy intensity ratios; and Doppler broadening from the range of ray paths through the collection optics. However this example is important for highlighting that α_l can take values significantly different to 0°. Experimental validation of the circular polarisation fraction is needed to give similar confidence in calculations of α_c which is expected to be more susceptible to changes and may be needed to predict and correct the IMSE data for the Stark-Zeeman circular polarisation fraction.

Variable Beam Voltage Shots

In one of the experimental sessions the 30L neutral beam voltage was deliberately varied during the shots. This effectively decreases the Doppler shift and Stark splitting without changing the direction of the motional electric field (there may be small changes due to the change in current profile with injected power). The IMSE system is tolerant to changes in the beam energy unlike the conventional MSE where the central σ component shifts under the passband leading to a mixture of π and σ emissions with a low polarisation fraction, as seen earlier in Fig. 2.11. An example of the IMSE measurement during one of these shots is shown in Fig. 4.41. A change in the beam energy from 82keV to 72keV reduces the beam velocity by $176\mathrm{km\,s^{-1}}$ in turn decreasing the Doppler shift by 0.25nm at $R = 2$m. From Eq. 3.22 this corresponds to a change in phase of $\Delta\phi_0 = 100°$. There is a zig-zag pattern in the IMSE polarisation orientation measurement that arises because the 1Hz oscillation in the beam velocity is large enough to noticeably disrupt the phase encoding of the polarisation orientation, unlike the relatively low amplitude oscillation discussed earlier. It would be straightforward to include corrections for the known velocity of the beam to correct for this coupling. The right hand side of the figure shows the difference between the experimentally measured phase offset $\phi_0+\alpha_l$ compared with forward modelled values for ϕ_0 and $\phi_0 + \alpha_l$. The model that includes the α_l effects gives a better fit to the data (apart from at $R = 2.03$m), however there is still some noise, likely resulting from the incomplete spectral model discussed in the previous section and the vibration between the optical rail and tokamak.

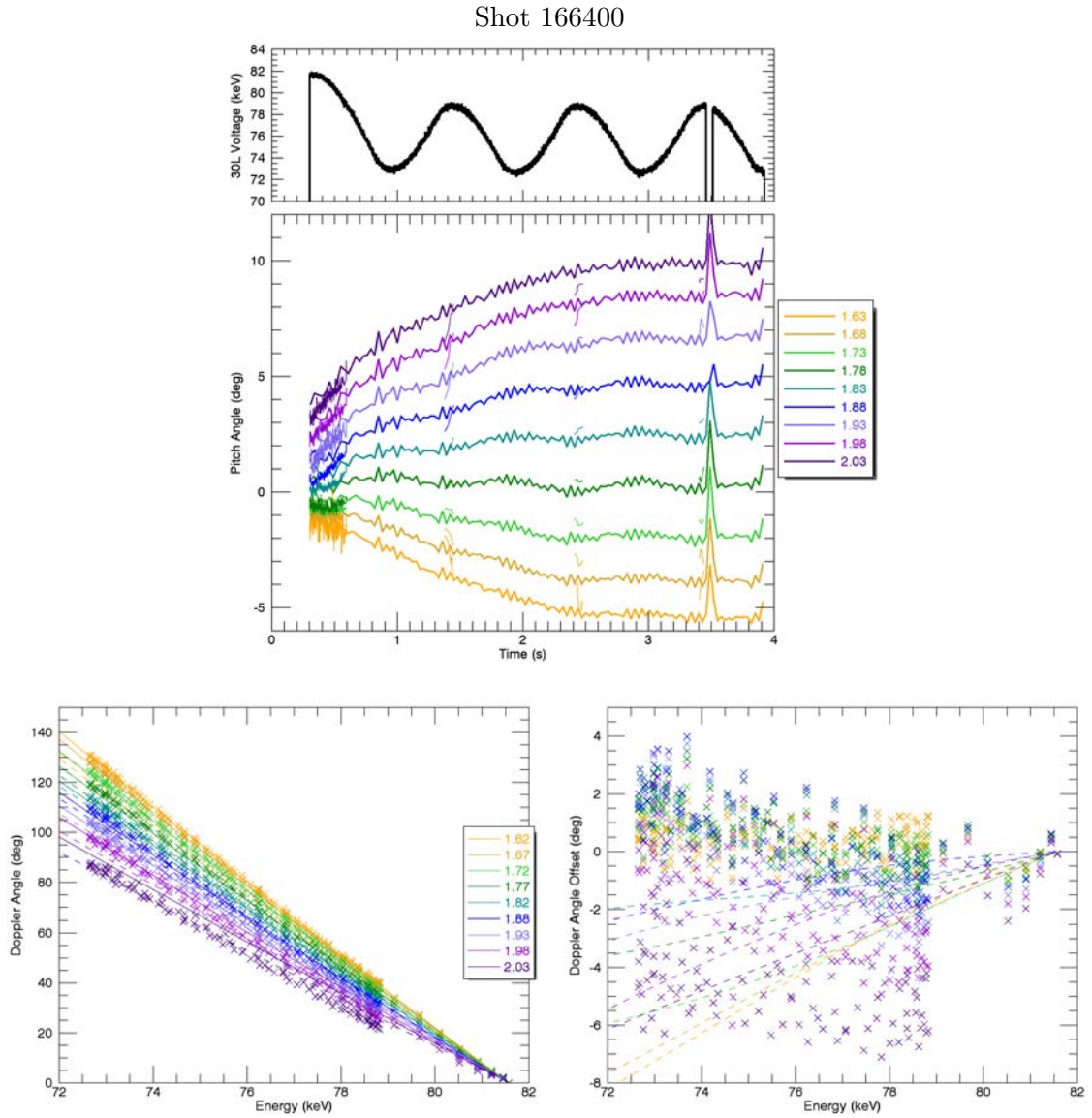

Figure 4.41: (Top) Evolution of the 30L voltage, IMSE pitch angle (solid line) and conventional MSE pitch angle (thin line/dots) for shot 166400. (Bottom Left) Measured offset in the Doppler angle $\phi_0 + \alpha_l$ (crosses) compared with a prediction of the Doppler angle based on measured accelerator voltage when including (solid line) and excluding (dashed line) the influence of α_l. (Bottom Right) Same as left plot only with the removal of the modelled $\phi_0 + \alpha_l$ Doppler angle ramp.

30R Beam Velocity Rise Time

The velocity stabilisation time of the 30L beam has been measured with spectrometers to be faster than $<$ 1ms[72]. However the 30R neutral beam is known to have a slower beam velocity rise time[73]. This slow rise time is evident in the IMSE data when the camera exposure period in a series of images occurs at different times relative to the beam blips. For example in shot 166300 the 30R beam blips were operated with 30ms on period and 10ms off period (25Hz 75% duty cycle) while the IMSE camera was operated with an exposure time of 10ms and readout of 15ms (40Hz 40% duty cycle). By assuming that the polarisation orientation and α_l are constant it is straightforward to extract the average

beam velocity during the exposure from variations in ϕ_0. The Doppler angle and beam energy measured with this strategy are shown in Fig. 4.42. After the initially slow rise time the velocity remains relatively stable, unlike fluctuations that have previously been observed using IMSE on TEXTOR[54].

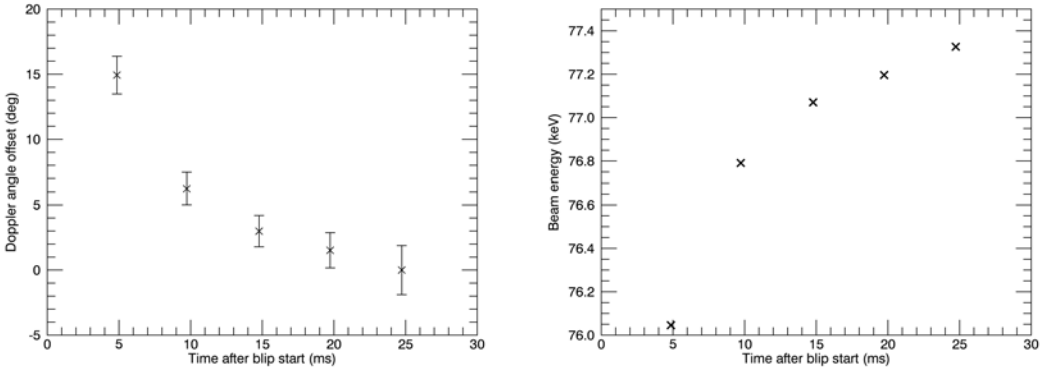

Figure 4.42: (Left) Dependence of the measured Doppler angle relative to overlap between the camera exposure and the beam blip in shot 166300. The time variable is averaged across the exposure time, for example the 5ms data point is for an exposure that started with the beam blip and ended 10ms into the beam blip. The uncertainty bars show the standard deviation which is noisy due to the vibration and changes in the polarisation orientation. (Right) Average beam voltage during the exposure inferred from the Doppler angle. This is a relative measurement offset to the data point at $t = 25$ms.

4.3.7 Summary

Table 4.6 summarises the IMSE data presented for each shot considered in this chapter. The IMSE system was installed on the 15° port on DIII-D, a view with limited radial resolution due to line-integration across the beam. For shots with toroidal field and plasma current in the normal direction the IMSE measurements were fairly consistent with the conventional MSE measurements, particularly after considerations were made for the line-integration effects using a simplified model of the beam. Some small systematic errors and remaining calibration uncertainties are evident towards the extremities of the 2D images, hence the data could not reliably be exploited to directly measure the toroidal current as per Eq. 1.18. The IMSE results for shots with reversed toroidal field direction, and particularly reversed plasma current, were inconsistent with the conventional MSE measurements. Other independent diagnostics such as ECE and magnetics only EFIT were considered in an attempt to understand the discrepancy but the cause remains unclear. While the IMSE system was able to measure relative Doppler shifts from neutral beam velocity, absolute measurement were not possible and would require a between shot calibration source and/or temperature stabilisation of the displacer.

4.4 Challenges and Future Implementations

The measurements presented here demonstrate the utility of the temporally switched IMSE system and the wealth of data contained in the images. While MSE is a mature diagnostic technique the data presented highlights that MSE is an exacting measurement

Shot	B_t	I_p	Fig.	Summary details
165748	N	N	4.27	Inferred pitch angle line-integration effects for L-H transition
165858	N	N	4.28	Variation in inferred pitch angle during a q-profile control shot
			4.29	Midplane EFIT forward model revealing line-integration effects
165860	N	N	4.31	2D IMSE/EFIT comparison revealing offset either side of midplane
165873	N	N	4.37	2D EFIT comparison with 30R IMSE measurement
165941	R	N	4.39	Midplane pitch angle comparison between 30L IMSE, 30R IMSE and EFIT highlighting offset with EFIT
165944	R	N	4.32	Inferred IMSE and conventional pitch angles revealing that offsets remain approximately constant and are greater at lower R
			4.34	2D IMSE/EFIT comparison highlighting spatial differences
166005	N	N	4.40	Highlights the dependence of the IMSE 'Doppler angle' on the multiplet lineshape as B_t (Stark splitting) decreases
166093	R	N	4.35	Magnetic axis position inferred with a range of diagnostics, ECE/EFIT are consistent early but ECE/IMSE later in the shot
166153	N	N	4.35	Magnetic axis position inferred with a range of diagnostics showing reasonable consistency between all internal measurements
166154	N	N	4.31	2D IMSE/EFIT comparison showing similarities to 165860
			4.38	Comparison of 30L IMSE, 30R IMSE and conventional MSE with interleaved 30L and 30R beam blips
166263	N	R	4.35	Magnetic axis position inferred with a range of diagnostics showing offsets between all internal measurements
166303	N	R	4.39	Midplane pitch angle comparison between 30L IMSE, 30R IMSE and EFIT highlighting offset with EFIT, particularly near 1.3m
166324	N	R	4.33	Inferred IMSE and conventional pitch angles with noticeable offsets
			4.34	2D IMSE-EFIT comparison highlighting spatial differences
166400	N	N	4.41	Highlights capability for IMSE to measure both the polarisation angle and Doppler shift for a range of beam voltages
166582	N	N	4.30	Comparison between systems including current ramp up and down
166599	N	N	4.39	Midplane pitch angle comparison between 30L IMSE, 30R IMSE and EFIT with close agreement between 1.5-1.95m

Table 4.6: Summary of the data presented for each shot, including the toroidal field and plasma current directions (Normal [N] or Reverse [R]).

with limited benchmarking options and self-consistency checks. However it is clear that the additional information available in IMSE provides some self-consistency and cross validation techniques. Additionally the IMSE system effectively averages across the entire MSE spectrum and is therefore more tolerant of filter misalignment and partially polarised broadband background light. The key highlights of these IMSE measurements include:

1. Availability of measurements on the high field side of the plasma to better constrain the equilibrium and measurements from different beams across a range of beam energies.

2. Revealing inconsistencies between the magnetic axis position inferred from ECE, EFIT1, IMSE and conventional MSE measurements, particularly for reverse I_p shots.

However there are remaining uncertainties in the polarimeter response and line-integration from the radial view that limit the extent to which the high resolution imaging data can be fully utilised. Many challenges encountered in this IMSE implementation can be overcome with experimental improvements, theoretical modelling and data analysis improvements that are outlined in the following sections.

View

The well-known challenges presented by the radial view have already been discussed. It should be noted that a tangential view that includes the plasma edge will deliver opportunities for resolving structures in the H-mode pedestal resulting from radial electric fields and toroidal currents[27]. However often tangential views comes at the expense of including a mirror which, as highlighted in Ref. [20], can lead to coupling between the linear polarisation and the Stark-Zeeman circular polarisation fraction and therefore cannot be adequately calibrated with only a linearly polarised source.

Modelling and Data Analysis Improvements

The optical modelling of the system does not contain enough detail of the apertures and lenses to precisely predict the ray paths through the system. More detailed modelling of the optical assembly is essential to deliver a more complete understanding and calibration of the Faraday rotation in the port window and lenses and to verify the accuracy of the extrapolation used. Furthermore this modelling could be used to determine the ray paths through the non-spatially uniform FLC and the ray path weighted average retardance at each point in the image. If this averaged delay could accurately reproduce the dependence on illumination source, seen in Fig. 4.24, it would improve the confidence in the calibration. Currently this ray path effect seems the most likely source of systematic distortions in the IMSE images.

The spectral model used in the calculations here is oversimplified but more accurate modelling will likely be required to correct for (and measure in the case of the amplitude spatial heterodyne or doubly switched single spatial heterodyne) the Stark-Zeeman circular polarisation. Some of the more straightforward improvements could include line-integration (ignoring beam attenuation), using intensity ratios from a collisional radiative model such as Ref. [28] and Doppler broadening from the etendue of the optical system. It is likely these improvements, along with a well-designed filter, would be sufficient to estimate α_l and α_c with enough accuracy to calibrate the ellipticity effects with small uncertainty, particularly for a more tangential view with a better suited bandpass filter.

Spectrometer measurements, particularly of the s_3 component, would be important for benchmarking the modelled spectra.

For simplicity a number of smaller correction factors were not applied to the polarisation orientation measurement such as those related to the vibration, beam voltage effects on ϕ_0, spectral changes, interferometric ellipticity, the angle defect and waveplate dispersion. It is possible to include all of these factors self-consistently but given the line-integration effects and calibration uncertainties the benefit of including these effects was not considered to be critical. Ideally the $\phi_0 + \alpha_l$ phase term can be accurately calculated, in which case each image of the TSSSH delivers an independent measurement of the polarisation orientation and no FLC would be needed. More realistically the first two images with the FLC in opposite states can be used to determine θ_σ and $\phi_0 + \alpha_l$ and thereafter a new value of $\theta_\sigma(t)$ is available from each subsequent image. Hence there are $n-1$ independent polarisation orientation measurements available from n images when the exact delay of the displacer is not precisely known (due to some temperature instability or ray path effects) but remains steady within a shot. This would only require the FLC to switch once during the shot. However here the Doppler angle was drifting, due to changes in the spectrum under the filter passband and the vibration of the camera relative to the tokamak. To limit the coupling of Doppler angle drifts to the polarisation orientation it was essential to obtain images regularly in both states of the FLC.

Experimental Improvements

An obvious improvement would be to procure an FLC with improved spatial uniformity and retardance closer to half-wave, however it is unclear if this is possible. The FLC could be replaced with any other discrete switching waveplate, be it one that rotates its axes or one that steps the delay between two values. The 'holy grail' of spatial uniformity, uniformity of delay with angle of incidence and fast switching speeds may not be achievable with current liquid crystal technology.

The limitations of the FLC therefore prompt the need for a calibration that replicates the optical paths illuminated by the plasma. The easiest way to achieve this is to gradually rotate a large aperture linear polariser in front of the IMSE polarimeter during a plasma shot over the expected range of polarisation orientations, as has been implemented on ASDEX-U[56] and KSTAR. Ideally beam-into-gas or in-vessel calibrations are preferred but they are a less readily available options. These calibrations also have the advantage that Faraday rotation and mirror effects can also be included.

It is suspected that there is a weakly polarising element in the polarimeter (Fig. 4.19) that compromised the repeatability of the calibration every 90°. Further investigation of the anti-reflective coatings on the polarimeter components and the accuracy of the rotation stage are considered worthwhile. Improving the temperature stability for the polarimeter is also desirable. The polarimeter used here was not insulated but it could be placed in an oven with temperature control. Stabilising the displacer temperature (possibly with passive thermal stabilisation[71]) in combination with an in-vessel calibration, would be optimal for an absolute measurement the neutral beam Doppler shift. Measurements of the vertical divergence of the beam from the Doppler shift are useful for improving the interpretation of the imaging data off the midplane but high accuracy is required to measure this second order effect. The temperature stability of the FLC was not thought to have a significant effect on the measurements here, however the FLC delay does have a weak temperature dependence so stabilising the FLC temperature would only be beneficial.

The neutral beams on DIII-D are often operated with rapid blips. The timing system used to trigger the camera and FLC had a fixed exposure and readout time throughout the shot. Often data was missed when the beam timing changed mid-shot or sometimes only every second exposure would contain a neutral beam leading to sampling of only one FLC state. For a future implementation of the TSSSH it would be worthwhile using the neutral beam drive signal, with appropriate modifications, to control the camera timing.

Elimination of the vibration between the camera rail and tokamak would benefit both the spatial calibration and the absolute Doppler measurement. Software corrections are less desirable as inevitably some noise is introduced and often background structures are difficult to identify in the images. Improvements to the filter have already been outlined but this will depend on the viewing port that is used. Both the radiation shielding and magnetic shielding were essential for the experiment. Some short term hot pixel noise and long term pixel damage were evident and will degrade the quality of the data if they are not minimised. Both the camera and data acquisition hardware were susceptible to magnetic saturation for some shot configurations even though magnetic shielding was used, this is different to our experience on KSTAR where the magnetic field has not been an issue[74].

Chapter 5

Synchronous Imaging of RF Heating Waves on the H-1 Heliac

The initial goal of the H-1 experiments was to use polarisation imaging techniques similar to IMSE for measuring the 7MHz radio-frequency (RF) electric field in the vicinity of the H-1 antenna via the Stark effect. The atomic modelling and experimental design for this experiment are detailed in Section 5.1. Unfortunately there was insufficient signal to measure the RF field, however while attempting the measurement it was observed that the plasma light emission intensity was weakly modulated at the frequency of the antenna. The spatial dependence of the light intensity perturbation manifests as a propagating wave that is thought to result from density perturbations associated with an ion cyclotron wave launched by the H-1 antenna. The details of this measurement and the characteristics of the measured waves are detailed in Section 5.2.

5.1 Stark Effect in the RF Sheath

The propagation and absorption of RF waves in fusion plasmas is generally well understood, with good agreement between experiments and theory. However evanescent electric fields near the antenna-plasma interface are less well understood, due to the complexity of the sheath dynamics and experimental challenges encountered in this high electric field region. The high voltages applied to the antenna and resulting electric fields in the vicinity of the antenna are important to consider as they can promote sputtering of antenna materials, leading to gradual damage of the antenna and radiative losses from these injected impurities will decrease the confinement of the plasma energy. Measurements of the electric field in the vicinity of the antenna are therefore vital to validate models and understand the interaction. Fortunately spectroscopic measurements are possible as the strong electric field in the vicinity of the antenna preclude the use of probes.

First time non-perturbative spectroscopic measurements of the RF electric field in the vicinity of a 3.7GHz lower-hybrid wave launcher have been made on the Tore Supra tokamak[75, 76, 77]. For that particular experiment a single sightline was used to obtain a time-averaged D_β spectrum. A theoretical model of the dynamic Stark effect spectrum was fitted to the experimental spectrum to deduce the direction and amplitude of the dynamic electric field ($1.5\mathrm{kV\,cm^{-1}}$). The atomic modelling for these measurements was developed in the thesis by Martin (Ref. [78]) where the dynamic Stark effect is considered because the lower-hybrid RF period of 0.27ns is relatively short compared to the 33ns average lifetime of the $n = 4$ hydrogen/deuterium levels. Additionally Martin developed a 1D spatially resolved diagnostic to measure the electric field in the sheath near a 13.56MHz

RF electrode in a dedicated magnetised plasma device. In this case the 73ns RF period is sufficiently gradual to make time resolved measurements and is comparable to the 33ns H_β lifetime, such that the energy level shifts are approximately adiabatic, implying that the static Stark effect is a valid approximation. Furthermore at this lower frequency possible rectification of the electrode potential must be considered because more electrons are extracted from the sheath during the 'positive' half cycle of the RF voltage due to their greater mobility relative to the hydrogen ions, leading to a negative DC bias. Martin considered the option of attempting intensified CCD based spectrometer time resolved measurements, however due to signal to noise ratio (SNR) constraints, only time averaged spectra were measured. These spectra were fitted to a quasi-static Stark effect model under the assumption that electric field evolution is well approximated by a Fourier expansion with a single temporal harmonic i.e. $|\mathbf{E}(z)| = E_0(z) + E_1(z)\cos(\omega t + \theta_1(z))$ where ω is the antenna angular frequency, z is the distance from the electrode and E_0, E_1 and θ are the fit parameters. At the electrode surface the electric fields were found to peak at $10\text{kV}\,\text{cm}^{-1}$ and at 7mm from the electrode surface the fields peaked at $\approx 2\text{kV}\,\text{cm}^{-1}$.

IMSE like imaging techniques offer a number of advantages that improve the prospects for making time resolved measurements on H-1 with H_α light. The imaging techniques described in Chapter 3 are free of a narrow slit and therefore have the greater light throughput than spectrometer measurements while still capturing polarimetric information and low-order moments of the spectroscopic information. The imaging polarimeter can be designed so that the fringe contrast is sensitive to either the linear or circular polarisation spectrum while the phase is sensitive to the polarisation orientation. Furthermore the $n = 3$ levels (H_α upper-states) have an average lifetime of only 10ns and the 7MHz RF frequency typically used on H-1 effectively doubles the duty cycle relative to measurements at 13.56MHz.

The potential in the centre of the H-1 plasma is small compared to the large voltages $\sim$ kV applied to the RF heating antenna. Consequently there are large electric fields in the sheath of the plasma near the antenna. The width of the plasma sheath where the voltage drop occurs can be estimated from the Child-Langmuir law given by

$$d = \frac{2}{3}\left(\frac{2e}{m_e}\right)^{1/4} V^{3/4}\sqrt{\frac{\epsilon_0}{J_e}}, \tag{5.1}$$

where e is the electron charge, m_e the electron mass, V is the potential difference between the antenna and bulk plasma, ϵ_0 is the vacuum permittivity and the saturation current is given by

$$J_e = en_e\sqrt{\frac{2k_BT_e}{m_e}}. \tag{5.2}$$

when k_B is the Boltzmann constant, T_e is the electron temperature and n_e the electron density. As an example 1eV electrons with density $n_e = 1\times10^{17}/\text{m}^3$ will have a saturation current of $J_e = 9\text{kA}/\text{m}^2$ and with an antenna voltage of $V = 2\text{kV}$ the sheath width will be $d = 4.7\text{mm}$ corresponding to an average electric field of $4.3\text{kV}\,\text{cm}^{-1}$.

In the left of Fig. 5.1 phase resolved spectra for anticipated H-1 conditions are presented and the corresponding circular and linear polarisation interferometric contrast are shown in the right of the figure. A delay of approximately $\kappa\phi_0 = 30\,000\text{rad} = 4800$ waves is expected to maximise the linear polarisation over the range of expected magnetic fields. This delay corresponds to an αBBO delay plate of thickness 25mm or a lithium niobate delay plate of 30mm. For fields greater than $2\text{kV}\,\text{cm}^{-1}$ the linear polarisation contrast

should be greater than 10% which is expected to be easily resolvable in the images. The direction of the electric field is not expected to change over the RF cycle, hence the time averaged spatial carriers will constructively interfere allowing for time average measurements with greater duty cycle and further improved SNR.

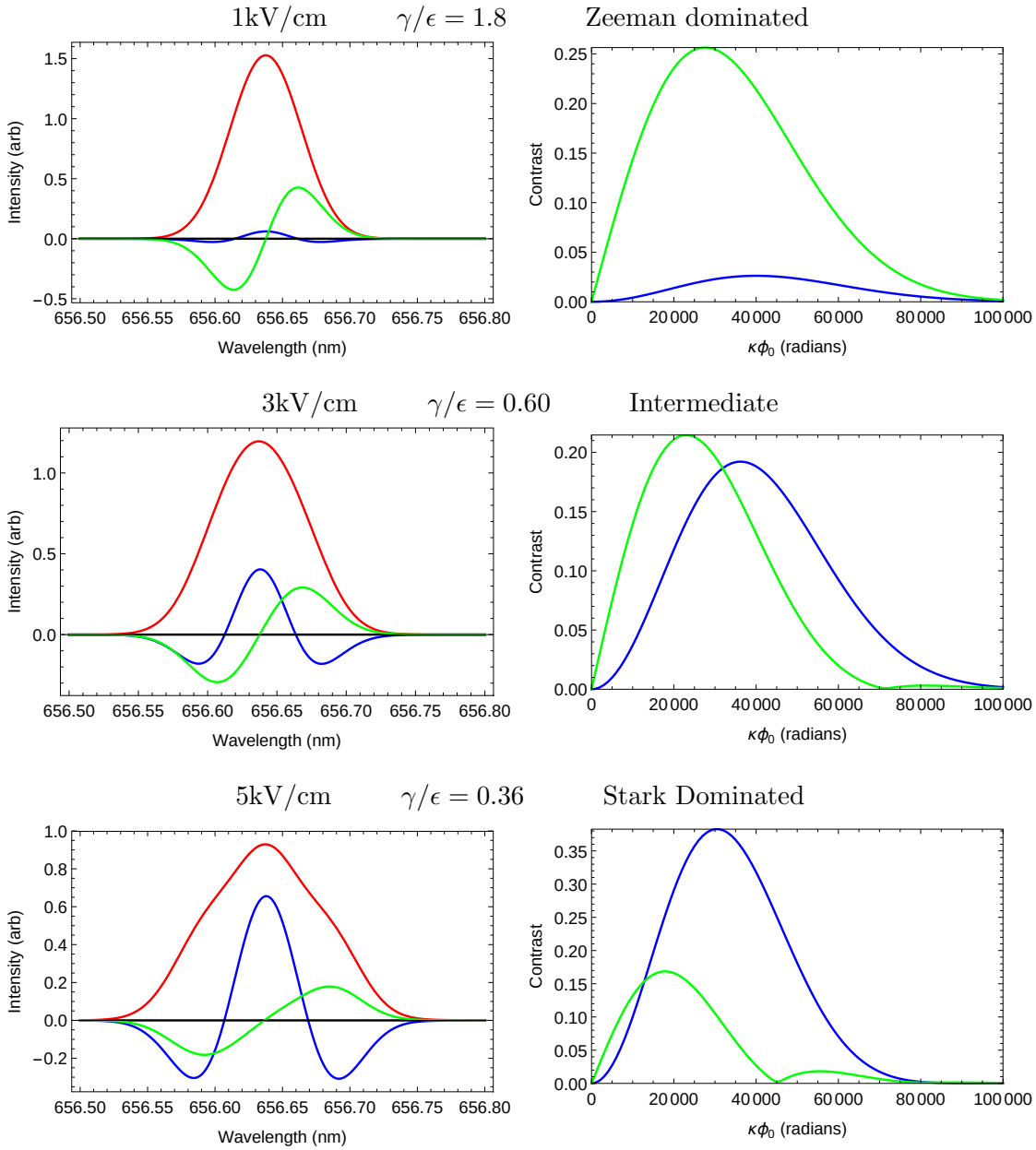

Figure 5.1: (Left) Spectra for s_0 (red), s_1 (blue) and s_3 (green) when including the Stark effect, Zeeman effect and fine structure (outlined in Chapter 2). (Right) Interferometric fringe contrast of the linear (blue) and circular (green) polarisation calculated from Eq. 3.46. (Top) $1\,\mathrm{kV\,cm^{-1}}$, (Middle) $3\,\mathrm{kV\,cm^{-1}}$ and (Bottom) $5\,\mathrm{kV\,cm^{-1}}$ with 1eV hydrogen atoms. It is assumed the view is perpendicular to the electric field and parallel to the magnetic field. The model includes fine structure and assumes equally populated upper-states.

5.1.1 Experimental Design

Temporally resolved measurements on RF time scales (7MHz frequency or $T = 143$ns period) are not feasible with high-speed cameras. However when the desired signal is periodically reproducible, as is the case here, intensified cameras can be used to gradually build up an image on the camera sensor over 1000s of $\sim$ 50ns intensifier gatings. The accumulated image can then be digitised with sufficient signal to overcome readout noise. A low voltage duplicate of the 7MHz H-1 antenna waveform was accessible and used to trigger the camera at the same point in the RF cycle, as depicted in Fig. 5.2. The Princeton Instruments PI-MAX3 1024i intensified CCD camera used for the experiments has a maximum intensifier gating repetition rate of 1MHz. To give the most reliable camera performance a downsampling counter was developed in Labview to produce a rising edge for the camera every 8^{th} cycle of the RF (875kHz) as there were repeatability issues when pushing the limit of every 7^{th} cycle. The counter has a sampling rate of 80 MS/s that causes a 12.5ns jitter in the intensifier gating window. This jitter is averaged over $\sim$ 50 000 intensifier gatings and is therefore insignificant. For each image the delay between the rising edge and intensifier gate opening are carefully selected in the camera software (Lightfield) to target a particular window in the RF cycle. Only a single phase in the RF cycle was sampled for each plasma shot as the $\approx$ 40ms full-frame readout time of the camera is comparable to the 100ms duration of typical H-1 plasma shots. H-1 shots are usually sufficiently repeatable that a full set of phases in the RF cycle can be targeted in the subsequent shots. Typically 4 (as in Fig. 5.2) or 8 equally spaced phases in the RF cycle were used to obtain a time resolved sequence. It is advantageous to measure 8 or more equally spaced phases in the RF cycle when higher order harmonics are important, however if only the first harmonic is of interest there are no SNR disadvantages in taking two sets of 4 phases instead of a single set of 8. Indeed in rare cases where the shots are not repeatable it is often advantageous to take a smaller number of phases per set so any outliers can be discarded without fracturing the completeness of the sequence. The optimal intensifier gate width can be determined by maximising the value of (assuming only shot noise and that the desired signal only contains a first harmonic component)

$$\frac{\sin(2\pi T_{gate}/T)}{\sqrt{T_{gate}/T}}. \tag{5.3}$$

The solution is a gate width of $T_{gate} = 0.371T = 53$ns in which case there is some overlap of the gatings for each phase, as shown in Fig. 5.2. In the presence of camera readout noise the optimal gate width will be slightly longer but shorter gate widths are necessary if it is also desirable to measure the second and higher order harmonics.

The linear polarisation sensitive imaging polarimeter used for the RF Stark effect measurement is shown in the left of Fig. 5.3 and is comparable to that in the left of Fig. 3.11, only with the inclusion of delay plates to increase the delay without increasing the carrier fringe frequency. For the H-1 measurements two 15mm lithium niobate delay plates and a 2.5mm αBBO Savart plate were used. The delay plates are crossed with an intervening half-wave plate at 45° to deliver a more uniform delay across the field of view [79]. This field-widening is more critical for this measurement, compared with the IMSE measurements, because more delay is required to achieve the optimal contrast due to the weaker electric field and shorter focal length lens. A 'reentrant' port (port 113), shown in the right of Fig. 5.3, was designed to provide an optimised view of the H-1 antenna. To relay the image to the camera it was necessary to incorporate a mirror and optical

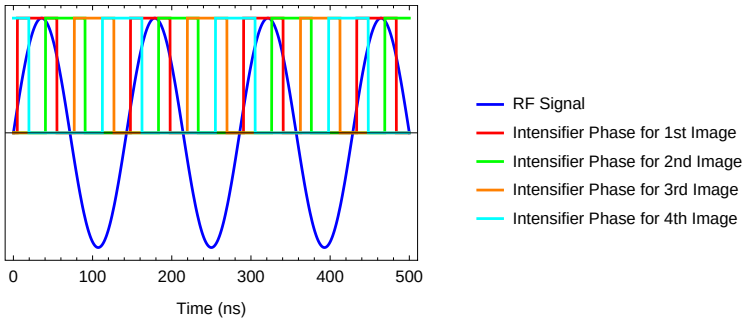

Figure 5.2: Timing of the intensifier gatings relative to the RF waveform for synchronous imaging. Each image is built up by opening the intensifier at the same point in the RF cycle before the phase is offset for subsequent images to build up a complete phase resolved measurement (in this example using 4 different phases). In reality only every 8^{th} RF cycle was sampled, yielding a duty cycle of $\sim 4\%$.

imaging fibre bundle into the assembly. The dielectric mirror in the system is optimised for polarisation preservation at 660nm so any possible coupling between linear and circular polarisation is expected to be small. To measure the polarisation information it is essential for the polarimeter to be located before the imaging optical fibre bundle resulting in some degradation of the carrier fringe fidelity.

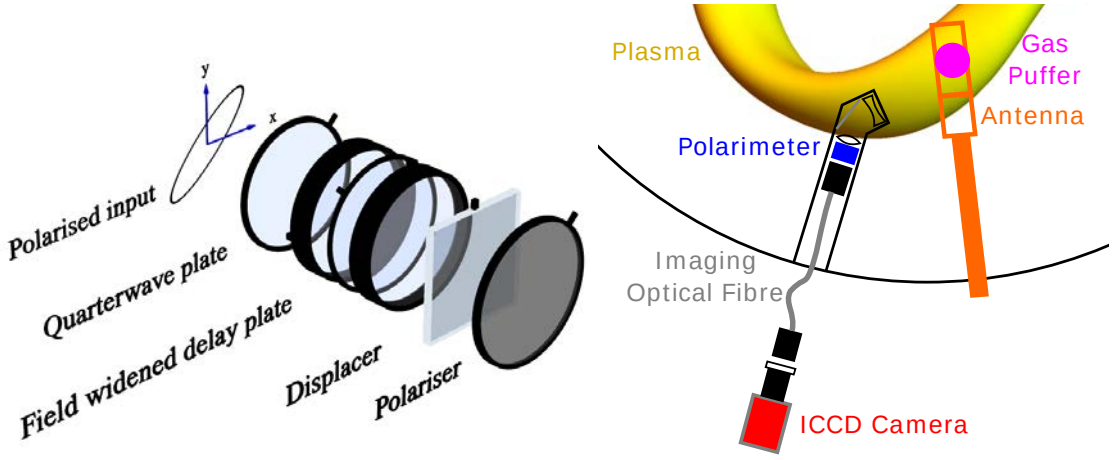

Figure 5.3: (Left) Polarimeter used for the linear polarisation measurement. The delay plate is field-widened to produce a more uniform delay across the image. In reality a Savart plate was used instead of the displacer as it delivered the best carrier fringe frequency of the available plates, but in the most straightforward implementation a displacer is sufficient. The lenses, interference filter and camera sensor are implied but not shown. (Right) Viewing geometry used for the RF Stark measurement. The plasma is shown in yellow and the edge of the vacuum vessel is depicted with the curved black line. A negative lens (−60mm) near the window of the reentrant assembly enhances the field of view. The plasma light is then reflected by a dielectric mirror and collimated with a 150mm lens. The polarisation information is encoded by the polarimeter before it is focused onto the 8mm × 10mm imaging optical fibre bundle with a 35mm C-mount lens. The fibre bundle relays the light to the ICCD camera outside the H-1 vacuum vessel where the light is refocused onto the camera with a 50mm and 85mm F-mount lens combination and the H_α line of interest is isolated with a 656nm interference filter.

A supersonic gas puffer was installed on H-1 specifically for this RF electric field measurement[80]. The gas puffer is located above the antenna and injects any desired gas species into the region under the antenna with a FWHM cone angle of 33°. The gas species can be the same as the background plasma to enhance the light intensity (eg hydrogen puff into hydrogen plasma) or an alternative species to enhance the localisation of the measurement (eg neon into hydrogen plasma).

5.1.2 Null Result

Both time resolved and time averaged measurements did not reveal any carrier fringe contrast in the sheath below the antenna, indicating that the electric field was not measurable from this view. Time averaged measurements are expected to be more sensitive to the RF electric field compared to the time resolved technique given the 25× improvement in duty cycle. In the narrow region just under the antenna there were approximately 2000 counts above background on the camera sensor (shot noise dominated) for the time averaged measurements. Simulations with 2000 counts indicate that carrier fringes with contrast greater than 1% would be visually observable in the region of the sheath. Possible reasons that the electric field was not resolvable are:

- The sightlines are not precisely tangent to magnetic field at the antenna and consequently intersect a significant region of plasma before reaching the sheath near the relatively narrow antenna. The line integration of this additional non-Stark split light with negligible linear polarisation fraction will not produce any carrier fringes and therefore decrease the contrast of the desired signal from the region directly underneath the antenna. The signal from the antenna region is expected to have a cold background gas and hot charge exchange components in an unknown ratio. The thermal Doppler broadening of the hot component may dominate the Stark splitting such that the linear polarisation fraction is negligible. Furthermore reflections off the metallic surfaces inside H-1 will also contribute to a decrease in the signal contrast. It is plausible that the desired emission region contributes $\ll 10\%$ of the total light in which case a time averaged $4\mathrm{kV\,cm^{-1}}$ amplitude RF electric field will not be resolvable. In the dedicated experiment designed by Martin[78] great care was taken to design a limiter that eliminated plasma in the region adjacent to the RF sheath to maximise the signal to background emission ratio. To boost the prospects for measuring the electric field it would be worthwhile improving the tangency of the port 113 reentrant view but a carefully designed limiter assembly may also be necessary to deliver sufficient contrast of the signal to background emission.
- The electric field may be weaker than anticipated.
- Limited spatial resolution: At the antenna the pixel density is approximately 3 $\mathrm{pixels mm^{-1}}$ leading to an apparent sheath width of approximately 14 pixels on the camera. Even with some imperfect focusing and imaging degradation from the optical fibre bundle it is expected that this would be sufficient to resolve interference fringes that are oriented perpendicularly to the antenna.

5.2 Imaging of RF Heating Waves

In the process of attempting the RF electric field measurement a temporal modulation was noticed in the light intensity at the antenna frequency. Further analysis revealed that the

RF temporal modulation had spatial characteristics of a propagating wave. In this section the RF wave measurements from four different views are presented and interpreted. Firstly in Section 5.2.1 an overview is given of ion cyclotron heating and the main electromagnetic wave types in the ion cyclotron range of frequencies. The viewing geometries from the 4 ports used to make the measurements are outlined in Section 5.2.2 before the experimental measurements and characteristics of the wave are discussed in Sections 5.2.4 - 5.2.8.

5.2.1 Ion Cyclotron Heating

Non-inductive heating is essential to achieve the temperatures required for 'ignition' of the fusion reaction. The objective of any plasma heating scheme is to externally launch energy near the edge of the plasma that will be absorbed near the centre of the plasma to maximise the energy confinement time. Fortunately plasmas can support a variety of electromagnetic waves that are capable of propagating to the centre of the plasma and depositing their energy at a targeted resonant surface. Ion Cyclotron Radio-Frequency (ICRF) heating is a widely used technique where the launched wave frequency is tuned to resonate with the plasma ions at a desired surface in the plasma that has magnetic field strength satisfying the relationship

$$\omega_{ci} = \frac{Z_i e|\mathbf{B}|}{m_i}, \tag{5.4}$$

where ω_{ci} is the ion cyclotron angular frequency, Z is the ion charge, e is the electron charge and m_i the ion mass. In the case of H-1 the standard RF frequency used is $\nu = 7$MHz ($\omega = 4.4 \times 10^7 \mathrm{rad\,s^{-1}}$ angular frequency) which is resonant with hydrogen ions where the magnetic field is $|\mathbf{B}| = 0.46$T. Usually on large tokamaks the RF antennas are located on the low field side of the plasma for accessibility reasons. In this case, for the wave to be resonant at the centre of the plasma, the launched frequency must obey $\omega > \omega_{ci}$ at the edge of the plasma. On the low field side where $\omega > \omega_{ci}$ the only electromagnetic wave supported by the ('cold') plasma is the compressional (aka fast magnetosonic) wave. The wave is capable of propagating across field lines and travels at (or near) the Alfvén velocity

$$V_A = \frac{|\mathbf{B}|}{\sqrt{\mu_0 \sum n_s m_s}}, \tag{5.5}$$

where μ_0 is the vacuum permeability, n_s is the density of each plasma species and m_s is the mass of each species. For H-1 the typical density is $n \sim 1 \times 10^{18}/\mathrm{m^3}$ and magnetic field is ≈ 0.5T leading to a Alfvén velocity of $V_A = 7 \times 10^6 \mathrm{m\,s^{-1}}$ for a H^+/He^+ mixed plasma or equivalently a wavelength of $\lambda = 1.0$m at $\nu = 7$MHz.

In a single ion species plasma the compressional wave is right hand circularly polarised at $\omega = \omega_{ci}$ whereas the positively charged ions orbits the magnetic field in a left handed sense and therefore the resonance is non-existent. However when the plasma contains two different ion species an ion-ion hybrid resonance exists between the cyclotron frequencies for each species. When the 'minority' species has a concentration of a few percent then the ion-ion hybrid and minority cyclotron resonance layers are very close. In this case the wave will have a significant left hand circularly polarised component near the minority cyclotron layer leading to significant heating of the minority species, in what is known as the minority heating scheme. An approximately 50% : 50% H^+:He^+ ratio is usually used on H-1 for minority ICRF heating[81]. This ratio is far greater than the optimal minority hydrogen concentration such that the ion-ion hybrid resonance surface at 0.9T lies well

outside the plasma. In this case the left hand circularly polarised component of the wave will be small and the minority heating is therefore weak.

On the high field side of the ion cyclotron layer, where $\omega < \omega_{ci}$, there is a second electromagnetic plasma wave supported by the plasma known as the ion cyclotron (aka finite frequency shear Alfvén[82]) wave[83]. The cross sectional area of the H1 plasma is relatively small (minor radius ~ 0.2m) and consequently *the antenna straps traverse both sides of the* $|\mathbf{B}| = 0.46$T *ion cyclotron layer*. Therefore it is possible for the component of the antenna on the high field side of the plasma to launch both the compressional and ion cyclotron waves. At low frequencies the compressional wave is preferentially launched by antenna currents perpendicular to the background magnetic field and the shear Alfvén wave by antenna currents parallel to the field. However at higher frequencies the launching becomes more complicated as the ion cyclotron wave is no longer polarised with a purely transverse magnetic field at finite frequencies relative to ω_{ci} ($\omega \lesssim \omega_{ci}$). The phase velocity of the ion cyclotron wave is[82]

$$v_p^2 = \frac{\omega^2}{k^2} = \frac{2V_A^2(1 - \frac{\omega^2}{\omega_{ci}^2})\cos^2\theta}{1 + \cos^2\theta + \sqrt{\sin^4\theta + 4\frac{\omega^2}{\omega_{ci}^2}\cos^2\theta}} \tag{5.6}$$

where $k = |\mathbf{k}|$ is the wave vector magnitude and θ is the angle of propagation relative to the static magnetic field. *The group velocity of the ion cyclotron wave has a dominant component in the direction of the static magnetic field resulting in the wave energy being confined to field lines and unable to significantly cross flux surfaces. Consequently the energy launched by an external antenna is deposited near the plasma edge instead of the centre of the plasma as desired.* At frequencies near ω_{ci} the ion cyclotron wave develops a $B_\parallel$ to the static magnetic field resulting in some compression of the plasma $\nabla \cdot \mathbf{v}$ ($\mathbf{v}$ is the average plasma velocity) and observable density fluctuations.

Unexplained hollow (i.e. edge peaked) electron temperature profiles have previously been observed on H-1 using a helium line ratio measurement technique[84]. Notably, one of the two RF waves discovered here only propagates near the last closed flux surface (LCFS) in the region where $\omega < \omega_{ci}$ and only on magnetic field lines intersecting the antenna. This is consistent with the interpretation that an ion cyclotron wave is launched by the H-1 antenna straps lying on the high field side of the ion cyclotron layer and this wave is thought to be the likely cause of the edge heating and associated hollow temperature profile, as outlined later in Section 5.2.8.

5.2.2 Viewing Geometry

The propagation direction of the RF wave first observed from the port 113 reentrant view was not clear from a single 2D projection image. For this reason three additional views were utilised to investigate the characteristics of the observed wave. The layout of these views is shown in Fig. 5.4. The toroidally directed port 113 reentrant view is complimented by two radially directed views (ports 207 and 222) that observe smaller regions of plasma that overlap with the port 113 view. The toroidal view has the advantage that it captures a larger region of the plasma, however the measurement is therefore significantly volume integrated and lacks localisation. The gas puffer above the antenna can be used to enhance the contrast in the region of plasma near the antenna, while ports 207 and 222 are also valuable as they deliver greater spatial resolution in the regions underneath and beyond the antenna respectively. Port 215 was utilised to survey the toroidal extent of the intensity

modulation as it is $\approx -120°$ toroidally from the antenna and the other three views.

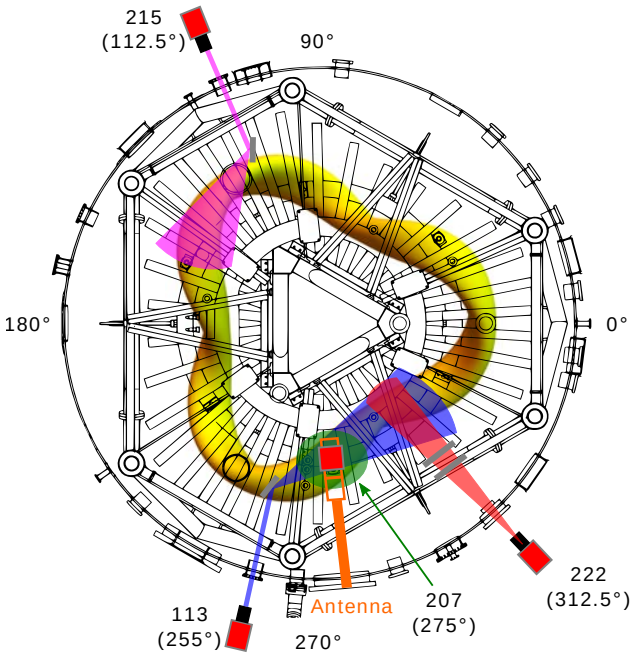

Figure 5.4: Layout of the four different camera views used for the H-1 measurements. The port 113 reentrant view depicted in blue was shown in more detail earlier in Fig. 5.3. The radial view from port 222 depicted in red is 40° toroidally displaced from the antenna and incorporates two in-vessel mirrors. The toroidal view from port 215 depicted in pink includes an in-vessel lens and mirror. Port 207 depicted in green provides a downward view of the antenna from the roof of H-1.

The positions of the toroidal, helical and poloidal magnetic field coils in H-1 are accurately known and are easily identifiable in the images. A fit of the magnetic field coils to images from the four different views is shown in Fig. 5.5 and the corresponding coordinates and orientation of the view are in Table. 5.1. The view from port 207 was designed to capture three different gaps between the toroidal field coils however the two side gaps are largely obscured by various components in the H-1 vessel. The central gap gives the best view of the plasma but it is also partially obscured by the antenna and gas puffer. The radial view from port 222 uses two mirrors and the region of interest is relatively small.

5.2.3 Electron Beam Imaging

Electron beam imaging is an essential technique for verifying the accuracy of the image registrations and magnetic field models. A thermionic filament can be inserted into H-1 to inject electrons that remain confined to the magnetic field line they originated on[85] (curvature and gradient drifts are negligible). After several toroidal orbits the electron beam density becomes attenuated due to collisions with background atoms, with these collisions leading to the measureable light emission from the background atoms. Thus the camera images capture a trace of several toroidal rotations of a particular magnetic field line which can be compared with a model of the magnetic field. The H-1 vacuum magnetic field topology is calculated using an existing Biot-Savart computer code that is based on the best estimated geometry of the magnetic field coils. A VMEC code[86] is

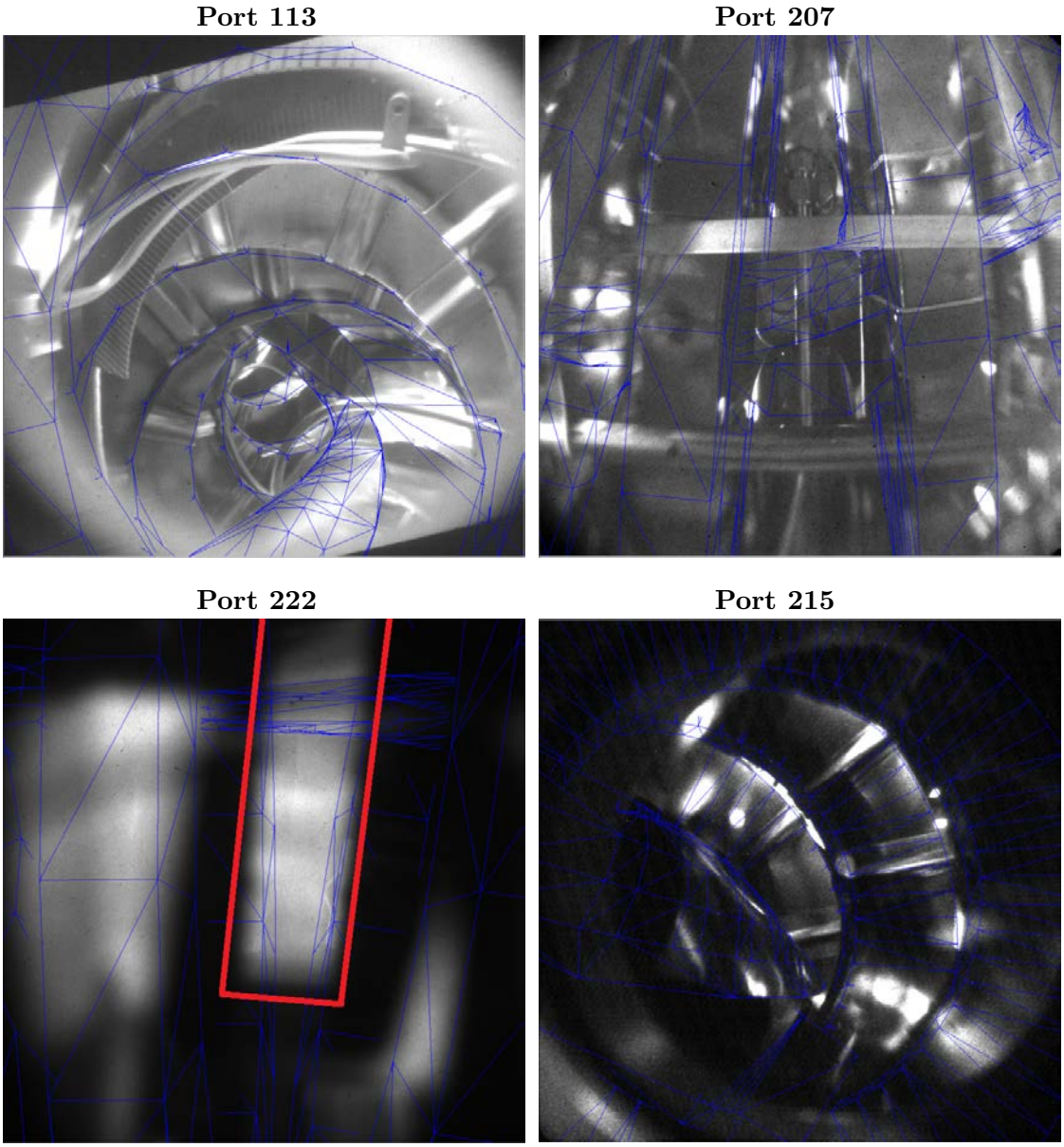

Figure 5.5: Registration for the port 113 reentrant view, port 207 roof view, port 222 radial view and port 215 toroidal view. The fitted outlines of the magnetic field coils are shown in blue. The image from port 222 is illuminated with plasma light and the region of interest restricted by the mirrors is outlined in red (some reflections and unfocused emission are evident in other parts of the image). The three remaining views are illuminated with background lighting with stopped down lenses to maximise the depth of field.

also available for H-1 that represents the equilibrium magnetic flux surfaces in a reduced toroidal Fourier series and is built upon the magnetic field input from the Biot-Savart code. The differences between the vacuum and equilibrium magnetic field are expected to be small given that the pressure and currents in H-1 are relatively small. While the Biot-Savart magnetic field lines are expected to be more accurate than the VMEC field lines, the VMEC representation is more convenient and therefore used for calculations in later sections. In Fig. 5.6 the electron beams imaged from the four different ports are shown with a comparison to the magnetic field lines modelled using the Biot-Savart

View	113	207	222	215
Effective Focal Length	18.12mm	35.06mm	52.30mm	19.66mm
R	1.287m	0.977m	1.844m	1.442m
ϕ	255.5°	275°	311.4°	116.5°
Z	0.373m	1.732m	−1.377m	0.016m
Pitch	−14.1°	−89.8°	50.6°	10.6°
Yaw	−43.7°	87.0°	0.5°	−40.6°
Roll	19.1°	272.8°	3.9°	35.0°
Decenter	(0.659,0.397)	NA	NA	NA

Table 5.1: Registration for H-1 views with parameters similar to Table 4.1. A 'decenter' parameter for the camera sensor offset is worthwhile for the port 113 view as the two intermediate images in the optical system allow the original image to be offset from the centre of the camera sensor each time it is refocused. The value represents the horizontal and vertical position on the camera sensor intersected by the optical axis defined from the pinhole location and viewing angles. For the remaining views the decenter is simply (0.5,0.5). The yaw and roll for port 207 are less straightforward to conceptualise as the yaw and roll become singular when the pitch approaches ±90°.

and VMEC codes. Some small inconsistencies between the magnetic field line codes are evident, most notably in the upper section of the port 215 view the registration appears to be inaccurate. Nevertheless the image registration is acceptable for the purposes of interpreting the wave imaging experiments presented here, especially in the main regions of interest. The measurements were undertaken with the H-1 magnetic configuration having equal currents in the helical and toroidal field coils ($\kappa_H = 1$) and the vertical and toroidal field coils ($\kappa_V = 1$).

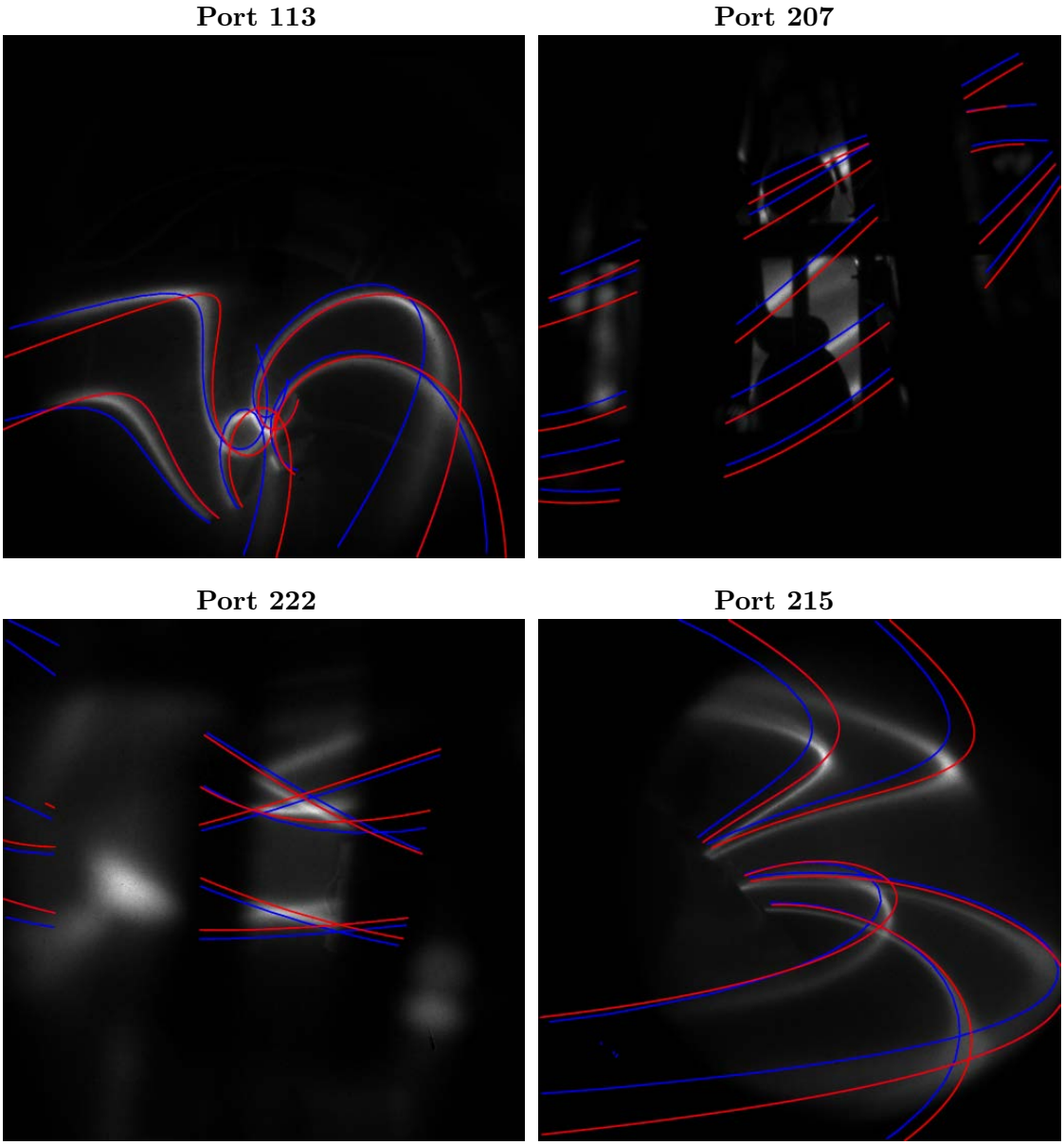

Figure 5.6: Electron beam mapping the four different views. The electrons follow the magnetic field lines and give rise to light emission when they collide with the low pressure background gas in H-1. The VMEC model field lines are shown in red and the Biot-Savart code field lines in blue.

5.2.4 Wave Imaging

The synchronous imaging technique outlined in Fig. 5.2 was used to obtain the RF phase resolved measurements. A temporal oscillation in the s_0 light intensity with $\sim 1\%$ contrast (not to be confused with spatial carrier fringe contrast considered in other parts of the thesis) is seen in some regions of the plasma. The polarimeter was dispensed with for these measurements to improve the throughput, given that the light intensity oscillation is unpolarised. *The phase of the temporal intensity perturbation for the four different views is shown in Fig. 5.7 where the spatial characteristics of the propagating wave are evident. The intensity perturbation was observed from all four views and with a range of emission sources* including H_α (τ = 10ns), both 514nm (τ = 11ns) and 658nm (τ = 9ns) C II ,

660nm Ne I (τ = 18ns) and broadband emission. The contrast for each of the emission lines is similar and the lifetimes are short relative to the RF period, indicating the light intensity modulations are generated from electron density fluctuations in the plasma. The second and higher order temporal harmonics of the intensity are negligible for all of the views.

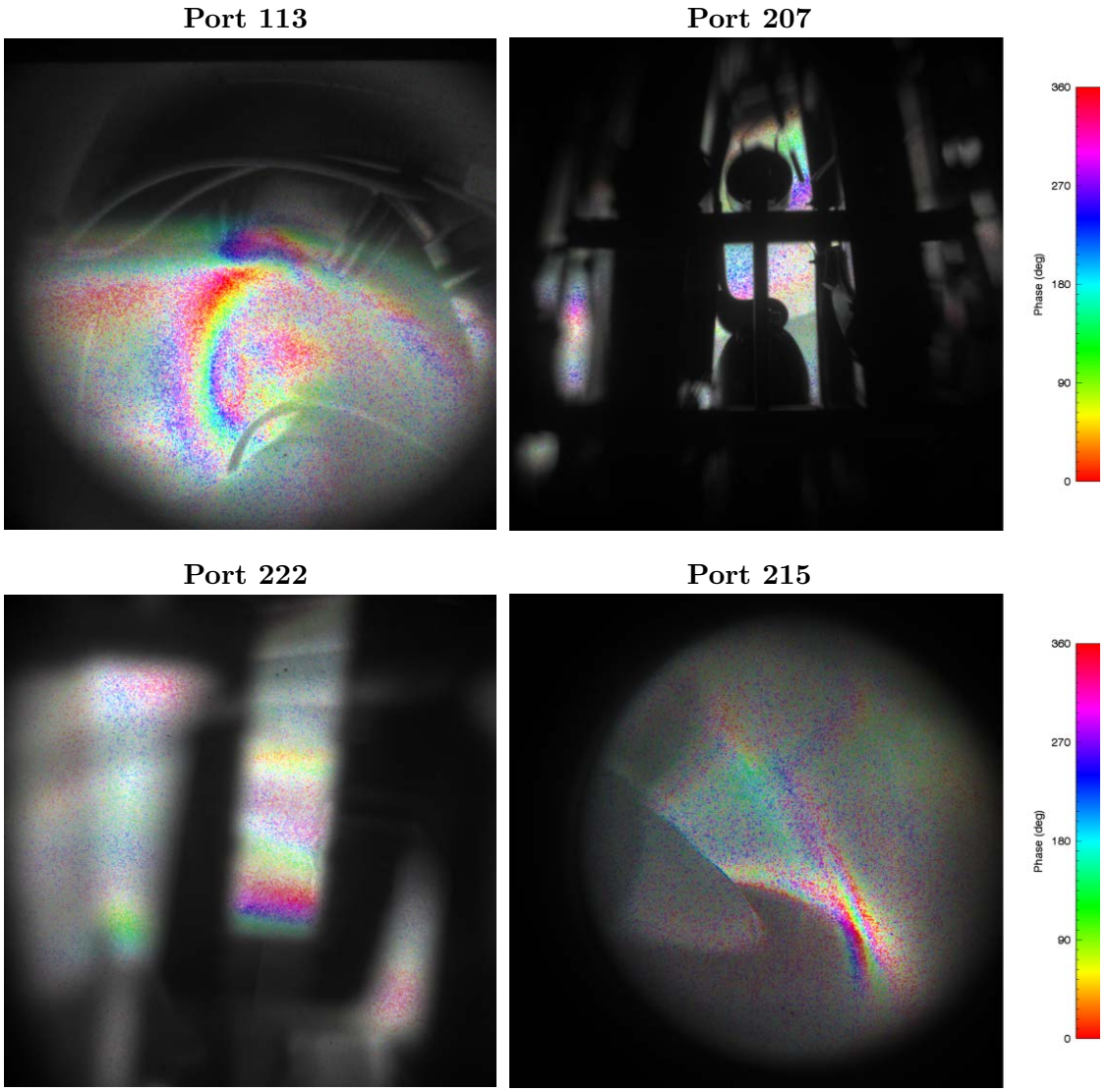

Figure 5.7: Phase of the 7MHz light intensity in 514nm C II seen from the four different views. Each phase image is constructed from 8 plasma images obtained with intensifier gatings at equally spaced points in the RF cycle i.e. 32 shots needed for all 4 views. The data is displayed in the HSV colour scheme with the hue representing the phase, the colour saturation representing the relative amplitude of the temporal modulation and the value/brightness representing the relative intensity. Consequently regions with no light appear blacker and regions with weak harmonic signal have less colour saturation. The wave propagates in the direction of increasing phase and care has been taken to ensure the absolute phase is consistent for all of the views.

In the port 113 reentrant view the wavelike structure exists in the centre of the image just below the antenna and extends downwards from that region. In the left and right of the image the first harmonic component is weak and dominated by noise. It is not

immediately possible from just the port 113 view to understand the propagation direction of the wave, i.e. from the line-integrated image it is not clear if the wave is only in the region directly underneath the antenna or if it extends toroidally beyond the antenna. For the port 113 view the contrast in the region closest to the antenna is around 5% and in the region of the image further below the antenna the contrast drops to around 2%.

The views from port 207 and 222 (shown relative to the port 113 view in the right of Fig. 5.8) were installed to clarify the spatial extent of the wave seen from port 113. In the downward view from port 207 there is a coherent wavelike structure in the upper half of the central TFC gap near the antenna with contrast of approximately 1%. In the lower part of central TFC gap the contrast is weak and in the side TFC gaps the visible regions are too small to clearly observe the wave. Port 222 provides evidence that the wave extends at least 40° toroidally from the antenna with a wavelike structure evident in the lower part of the image. There are a number of features that are common to the three views (ports 113, 207 and 222) that are consistent with the interpretation that the wave is localised near the LCFS and propagates in the negative poloidal direction. Further details and evidence of this surface wave interpretation are considered in Section 5.2.5 and the dependence of the wave on the magnetic field strength is detailed is Section 5.2.6.

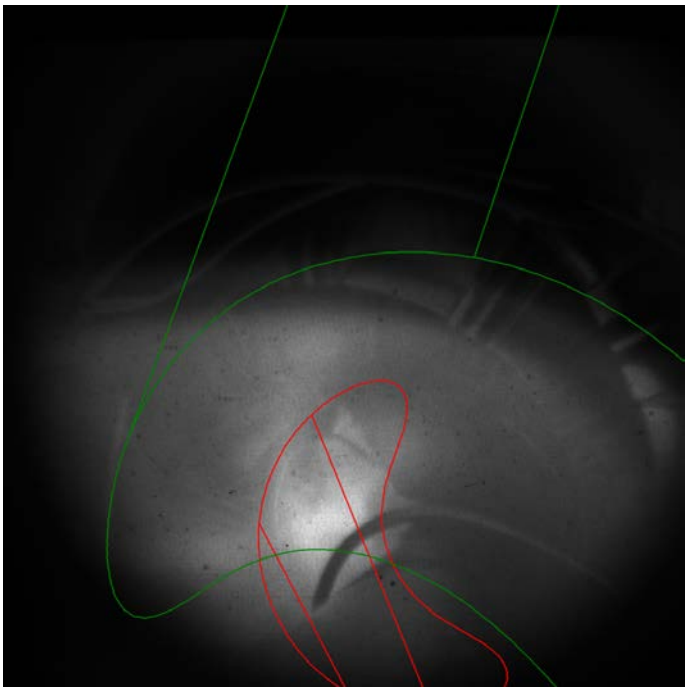

Figure 5.8: View from port 113 during a plasma shot. The plasma cross section under the antenna at $\phi = 275°$ and two sightlines from the downward port 207 view are shown in green. The plasma cross section at $\phi = 312.5°$ and two sightlines from port 222 are shown in red.

The view from port 215 ($-120°$ toroidally displaced from the antenna) was used to further investigate the toroidal extent of the RF wave. A temporal perturbation in the light intensity was also observed from this view, mainly seen in the lower right of the image. In this region of the plasma the wave appears to be propagating radially inwards with a shorter wavelength than the wave observed from the other three ports. Further analysis and modelling of this wave are presented in Section 5.2.7.

5.2.5 Mapping to Flux Coordinates

Here a mapping from image coordinates to flux coordinates is applied to relate the measurements from ports 113, 207 and 222, and confirm the wave is localised near the LCFS. To assess the propagation direction of the wave relative to the magnetic field direction it is convenient to use Boozer magnetic coordinates[87] which can be calculated from the VMEC coordinates. In the skewed Boozer coordinates, labelled with $(\psi_p, \phi_B, \theta_B)$ or (poloidal flux, Boozer toroidal angle, Boozer poloidal angle), the magnetic field lines for each flux surface are straight with direction given by $\hat{\phi}_B + \iota\hat{\theta}_B$ where ι is the rotational transform ($\iota = 1.41$ on the LCFS). The sightlines from most pixels generally intersect a flux surface at two points, hence it is possible to attempt mapping pixels to coordinates (ϕ_B, θ_B) for any desired flux surface. The mapping is only valid when the wave is localised in a narrow range of surfaces and the contribution from one side of the sightline-surface intersection dominates the opposite intersection. In Fig. 5.9 the temporal phase is mapped to the LCFS Boozer coordinates for the port 113 view and compared with the overlapping regions viewed from port 207 and port 222. In the region underneath the antenna between $110° < \theta_B < 160°$ the temporal phase seen from the port 113 and 207 views is approximately in agreement. There is some coherent signal in the small region near $(\phi_B, \theta_B) = (275°, 100°)$ in the port 207 view but in other regions where $\omega > \omega_{ic}$ the harmonic signal is weak and dominated by noise. Likewise in the region near $\phi_B = 308°$ between $160° < \theta_B < 210°$ the phase is in agreement for the port 113 and 222 views, although the measurement from port 113 becomes noisy due to the lower spatial resolution and increased volume integration through the bulk plasma. In the region of between $140° < \theta_B < 160°$ the harmonic signal is weak in both views however there is a region of noticeable harmonic signal near $\theta_B = 135°$ only in the port 222 view that is colour yellow-red. It may be the case that this signal originates from the near side of the LCFS intersection near $(\phi_B, \theta_B) = (318°, 305°)$ or elsewhere inside the LCFS given that it is not evident in the port 113 reentrant view and has a different slope to the wavelike structure evident between $160° < \theta_B < 210°$ thought to originate from the far side intersection of the LCFS. The phase measured from the overlapping views is compared in Fig. 5.10, *highlighting the correlation between views under the assumption of a surface wave.* While there is some noise and offsets (possibly resulting from uncertainties in the registration of the views or line integration effects) the correspondence is clear.

Evidently from Fig. 5.9 the intensity perturbation is localised near the LCFS and the phase velocity is mainly perpendicular to the magnetic field in the negative poloidal direction. *The wave is only apparent in the region where* $0.85\omega_{ci} \lessapprox \omega < \omega_{ci}$ *and is localised to magnetic field lines that intersect near the antenna, an indication that the group velocity and wave energy are propagating along the magnetic field lines near the LCFS.* In the region $290° < \phi_B < 320°$ the wavelength and propagation direction are fairly consistent, whereas *in the region closer to the antenna the wave structure is more complicated.* The view from port 222 provides the greatest spatial resolution for resolving the wavelength of the wave. In the region the wave is evident in the port 222 view the pixel→Boozer mapping scales approximately by $1° \equiv 3$mm in the poloidal direction. The wavelength of the observed RF wave is measured to be about $\lambda = 94$mm, corresponding to a phase velocity of $v_p = 6.6 \times 10^5 \mathrm{m\,s^{-1}}$. From the port 113 reentrant view it appears that the wave also has a small component of the propagation vector parallel to the field. The angle of propagation is measured to be approximately $\theta = 85°$ but it should be noted there is some uncertainty in the registration of the view that may affect this value. Given the

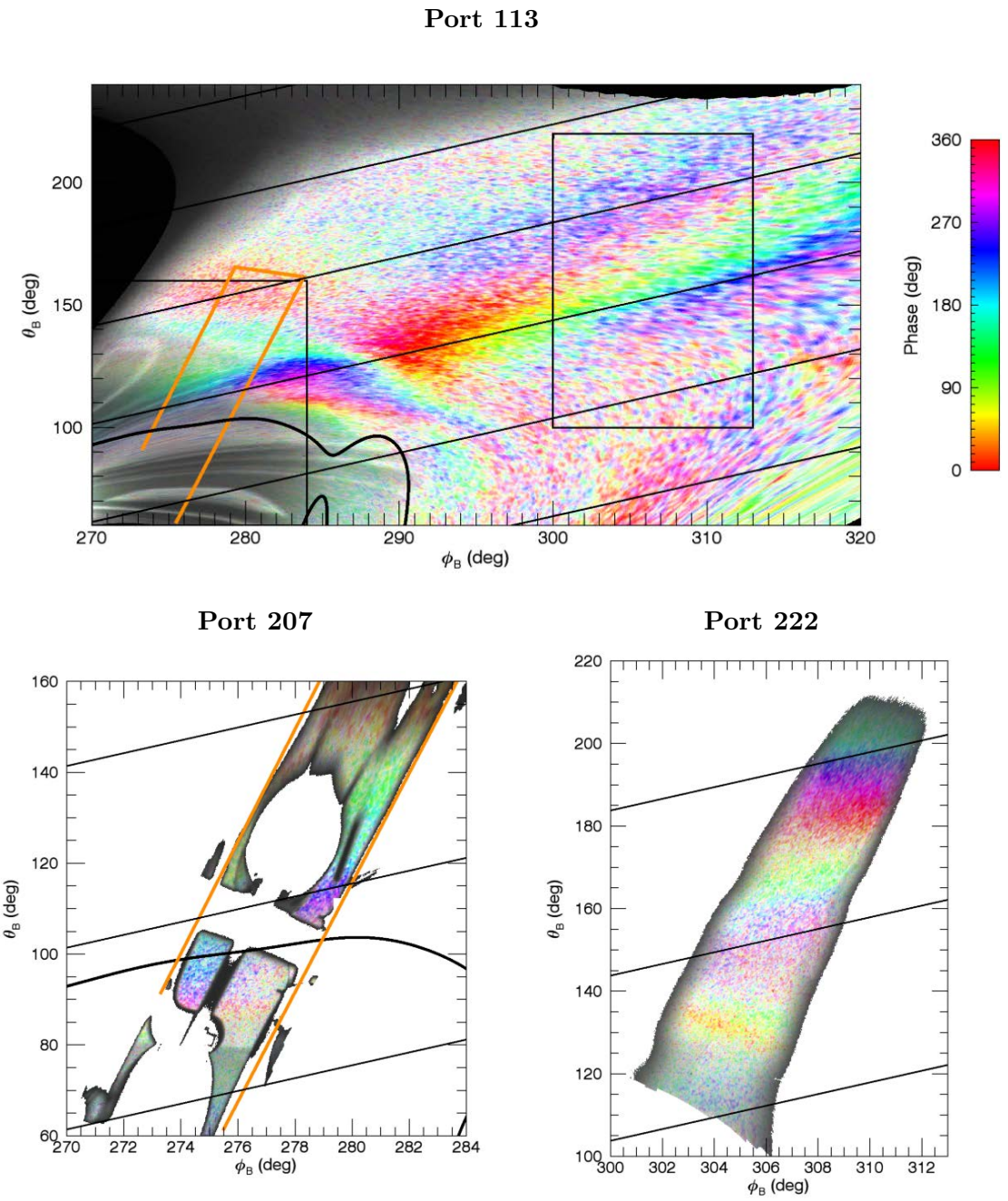

Figure 5.9: Phase images from Fig. 5.7 projected into Boozer coordinates assuming the wave is concentrated on the LCFS. The port 113 view is shown in the top plot with the black rectangles showing the common intersection with the views from port 207 and port 222. The straight black lines represent the magnetic field direction and the thick black lines trace the ion cyclotron layer ($\omega < \omega_{ci}$ in the upper region). The orange lines approximately trace the antenna straps, where the high voltage side is on the left and grounded side on the right. The mapping is not one to one and the resolution is particularly low where the sightline is tangent to the surface. In the lower left corner of the port 113 mapping some reflections off the antenna and other surfaces leave imprints in the brightness.

wave is propagating in a region near $\omega/\omega_{ci} \approx 0.8$ it is possible to calculate the theoretical velocity of the ion cyclotron wave in this region from Eq. 5.6 to be $v_p = 3.6 \times 10^5 \mathrm{m\,s^{-1}}$

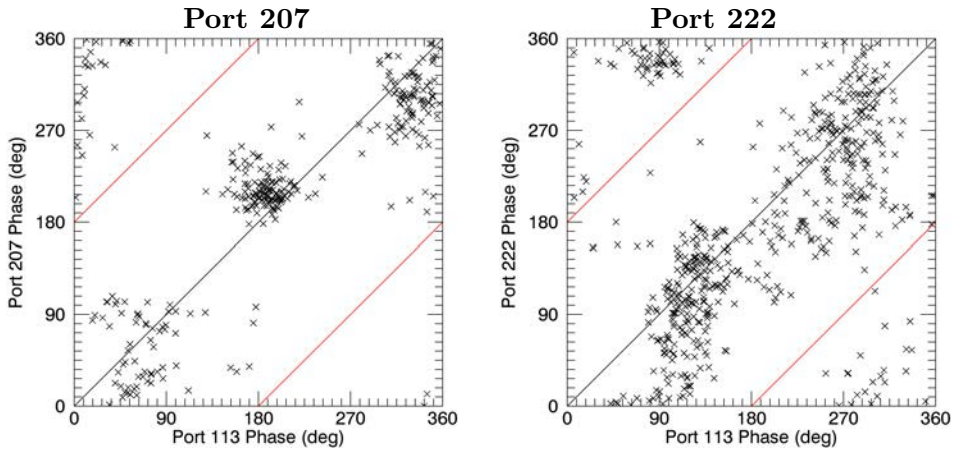

Figure 5.10: Phase measured at port 113 compared with phase measured in overlapping region of (Left) port 207 and (Right) port 222. Only regions where the wave structure is clear are sampled. The black and red lines indicates points exactly in phase and antiphase respectively. Points in the top left and bottom right of the plots are almost in phase.

equivalent to $\lambda = 51$mm. This value is of similar magnitude to the measured value and if a propagation angle of $\theta = 81°$ had been used the values would agree.

A heuristic model was developed to verify the location and propagation direction of the surface wave and to interpret the measured contrast. The light intensity is modelled to take the form

$$I = I_0\Big(1 + \frac{I_1}{I_0}\cos\big[m(\theta_B - \iota\phi_B) + n\phi_B - \omega t\big]\Big) \text{ with } I_1 \neq 0 \text{ for } \begin{array}{l} 0.91 < \rho < 1 \\ 64° < \theta_B - \iota\phi_B < 130°. \end{array} \tag{5.7}$$

where the plasma emissivity I_0 is assumed to be uniform across the plasma, I_1 is the magnitude of the emissivity perturbation caused by the wave, m is the poloidal/perpendicular mode number and n is the toroidal/parallel mode number. $\theta_B - \iota\phi_B$ is constant along the field lines such that its gradient is in the direction perpendicular to the magnetic field while ϕ_B is approximately constant in the direction perpendicular to the field given there is negligible toroidal current. The perpendicular mode number of $m \approx -11$ and parallel mode number $n \approx 6$ reproduce the observed wave well in the region $290° < \phi_B < 320°$. The perturbation I_1 is modelled to only be present on the outer flux surfaces in the range $0.026\text{Wb} < \psi_p < 0.031\text{Wb} = \psi_{p,LCFS}$ ($\psi_p = 0$ on axis) or in terms of a normalised radial coordinate $0.91 < \rho < 1$ where $\rho = \sqrt{\psi_p/\psi_{p,LCFS}}$. The modelled phase images for the three views are seen in Fig 5.11 and can be compared with the experimental measurements shown earlier in Fig. 5.7. In the model the wave only propagates on field lines that intersect near the antenna, however the experimentally observed restriction that the wave only has appreciable amplitude where $0.85\omega_{ci} \lessapprox \omega < \omega_{ci}$ is not included as the magnetic field strength ($\propto \omega_{ci}$) can be varied, as considered in Section 5.2.6. In the region directly under the antenna the spatial structure of the wave is more complicated and the model and experimental data are less consistent.

The amplitude of the temporal intensity perturbation I_1 is thought to be caused by a modulation of the electron density which is related to the observed contrast via $I_1/I_0 \approx n_{e1}/n_{e0}$, where n_{e0} is the unperturbed electron density and n_{e1} is the electron density perturbation produced by the wave. *A density fluctuation of* $n_{e1}/n_{e0} \approx 1/10$ *delivers the best agreement with the experimental data.* In this case a comparison of the modelled contrast and experimentally measured contrast is seen in Fig. 5.12. In the port 113 view the magnetic field lines near the antenna are largely parallel to the sightlines resulting in significant constructive interference of the perturbation intensity. Further along the surface toroidally beyond the antenna the sightlines have a greater component normal to the LCFS and greater line integration contribution from the bulk plasma resulting in a $\sim 3\times$ lower contrast. Similarly the contrast is also lower from the views from ports 222 and 207 as they are largely perpendicular to the field lines and volume integrated though the bulk plasma.

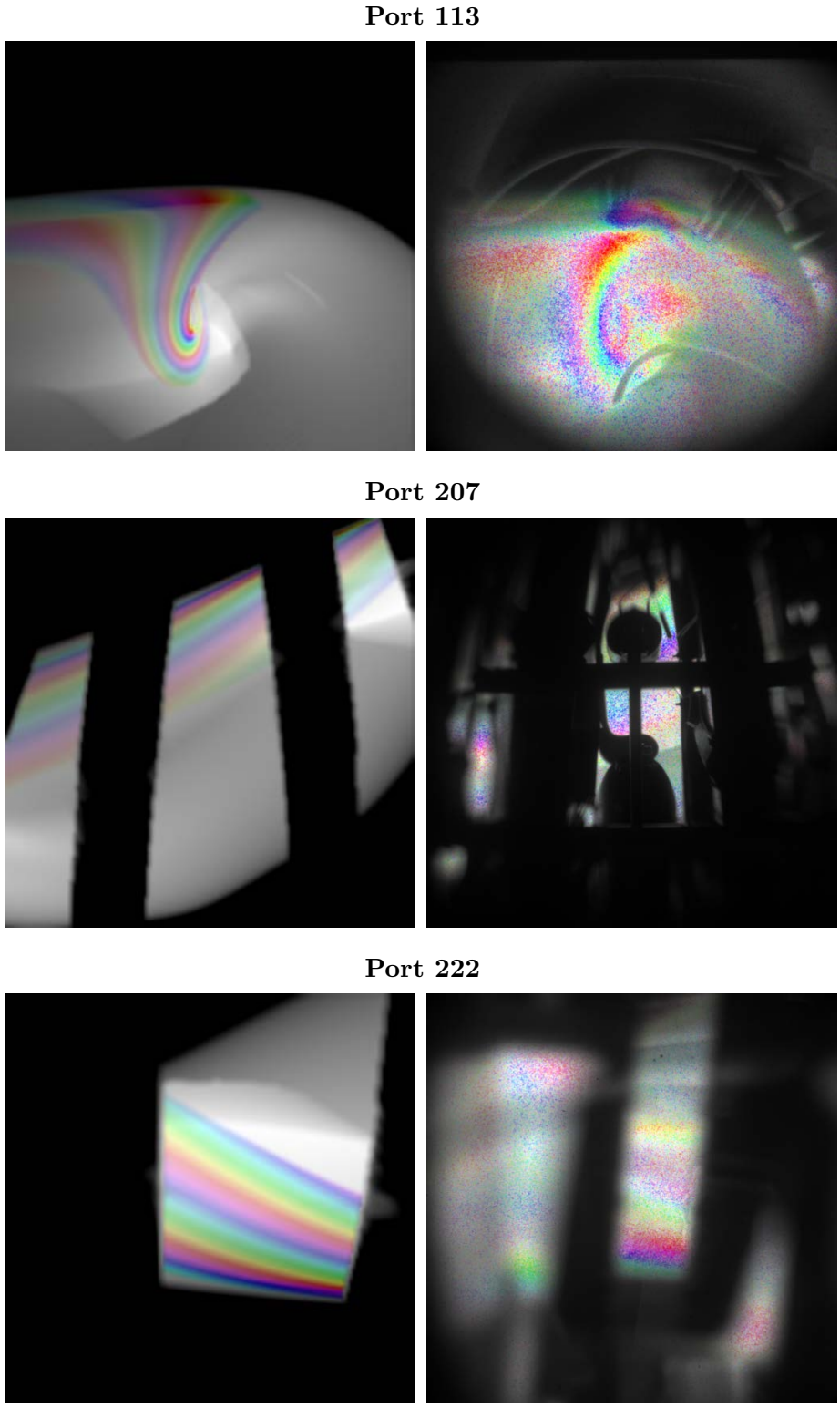

Figure 5.11: (Left) Forward model of the RF wave from ports 113, 207 and 222 modelled using Eq. 5.7 with $m = -11$ and $n = 6$. The model assumes the wave is localised near the last closed flux surface ($0.91 < \rho < 1$) and localised to field lines that intersect the upper antenna strap. The constraint $0.85\omega_{ci} \lessapprox \omega < \omega_{ci}$ is not applied as it is dependent on the magnetic field strength. The model includes field coil obstructions but does not contain other obstructions such as the antenna, gas puffer and other structures that restrict the side gaps in the experimental port 207 view or the edges of mirror that limit the view from port 222. Reflections off the field coils and other metallic surfaces will tend to decrease the contrast are not considered in the model. (Right) Copy of the experimental measurement in Fig. 5.7 for comparison.

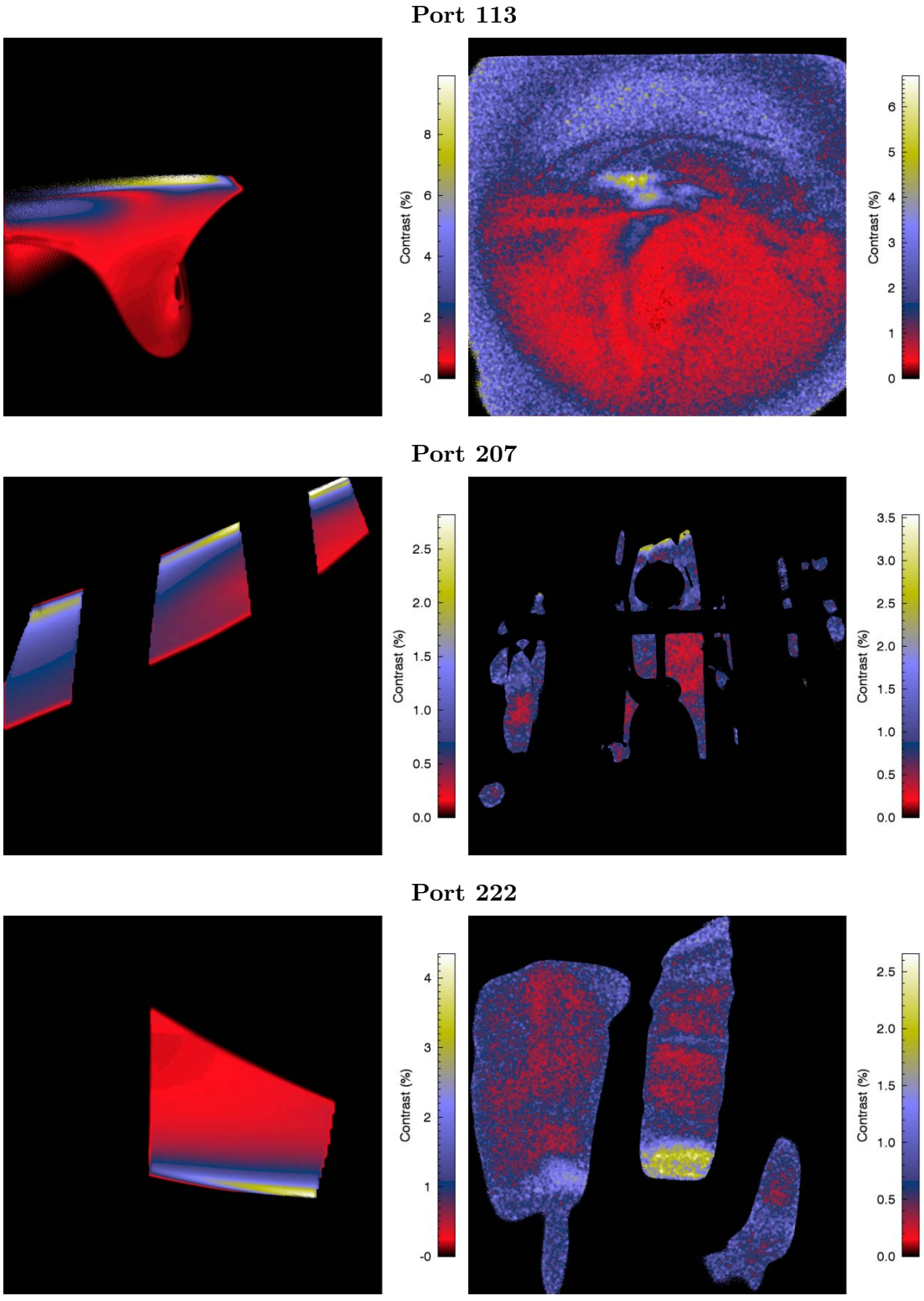

Figure 5.12: (Left) Forward modelled contrast seen from port 113 (top), port 207 (middle) and port 222 (bottom) applying Eq. 5.7 with $I_1/I_0 = 1/10$ (Right) Experimentally measured contrast.

Experiments puffing neon gas into a hydrogen/helium plasma were undertaken to confirm that the wave is localised near the LCFS. In this case the RF intensity perturbation was only visible in the region directly under the antenna where the neon is puffed and not in the region of the LCFS toroidally extended beyond the antenna that is free of any gas puffing, as seen in Fig. 5.13. Similar results were observed with hydrogen puffing into hydrogen/helium plasmas resulting in slightly increased contrast near the antenna and more significantly reduced contrast in the region further toroidally extended from the antenna.

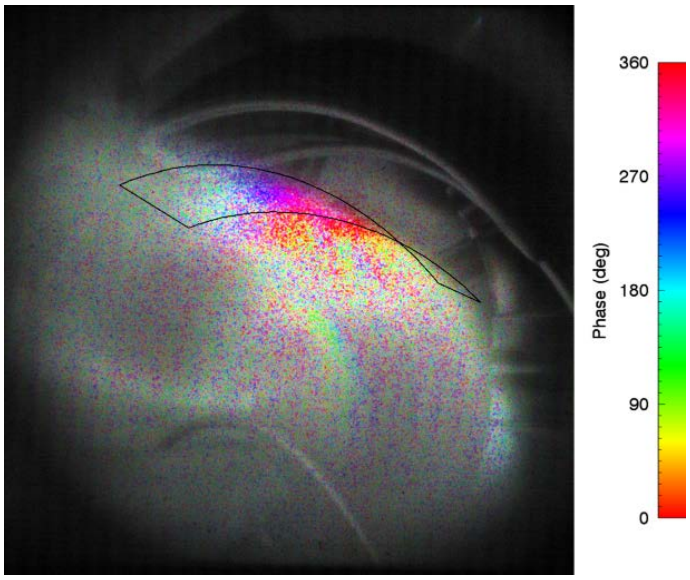

Figure 5.13: Phase of the RF intensity perturbation seen from port 113 with neon puffing into a hydrogen/helium plasma. The neon emission is isolated with a 660nm Ne I filter. The black lines indicate the region of the last closed flux surface directly under the antenna. The reduced helical current of $\kappa_H = 0.55$ used for this sequence produces a slightly different plasma shaping compared to all other shots presented here with $\kappa_H = 1$.

5.2.6 Relation to the Ion Cyclotron Layer

In Fig. 5.11 it appears the surface wave is limited to the high field side of the ion cyclotron layer ($\omega < \omega_{ci}$). To further investigate the relationship between the wave and the ion cyclotron layer the magnetic field strength was changed by regulating the current in the magnetic field coils. Four different currents (5.7kA, 6.1kA, 6.5kA and 6.9kA) were used to shift the position of the ion cyclotron layer (for all other shots presented here the current through the field coils was 6.5kA) and the RF phase measured from port 113 for each of the field strengths is shown in 5.14. As the current/field strength is increased the high field side of the ion cyclotron layer expands to the right in the images and the location of the wave is also seen to move to the right. It should be noted that the 6500A example has the same magnetic configuration as the example in Fig. 5.7. There are however some differences in the structure of the surface wave that are not related to the different light source (same day C II and H_α measurements are very similar). These difference may be due to wall conditions, gas fill ratios or slight changes to the precise antenna position that may have occurred when it was removed and reinserted for maintenance in the 16 months between the two measurements.

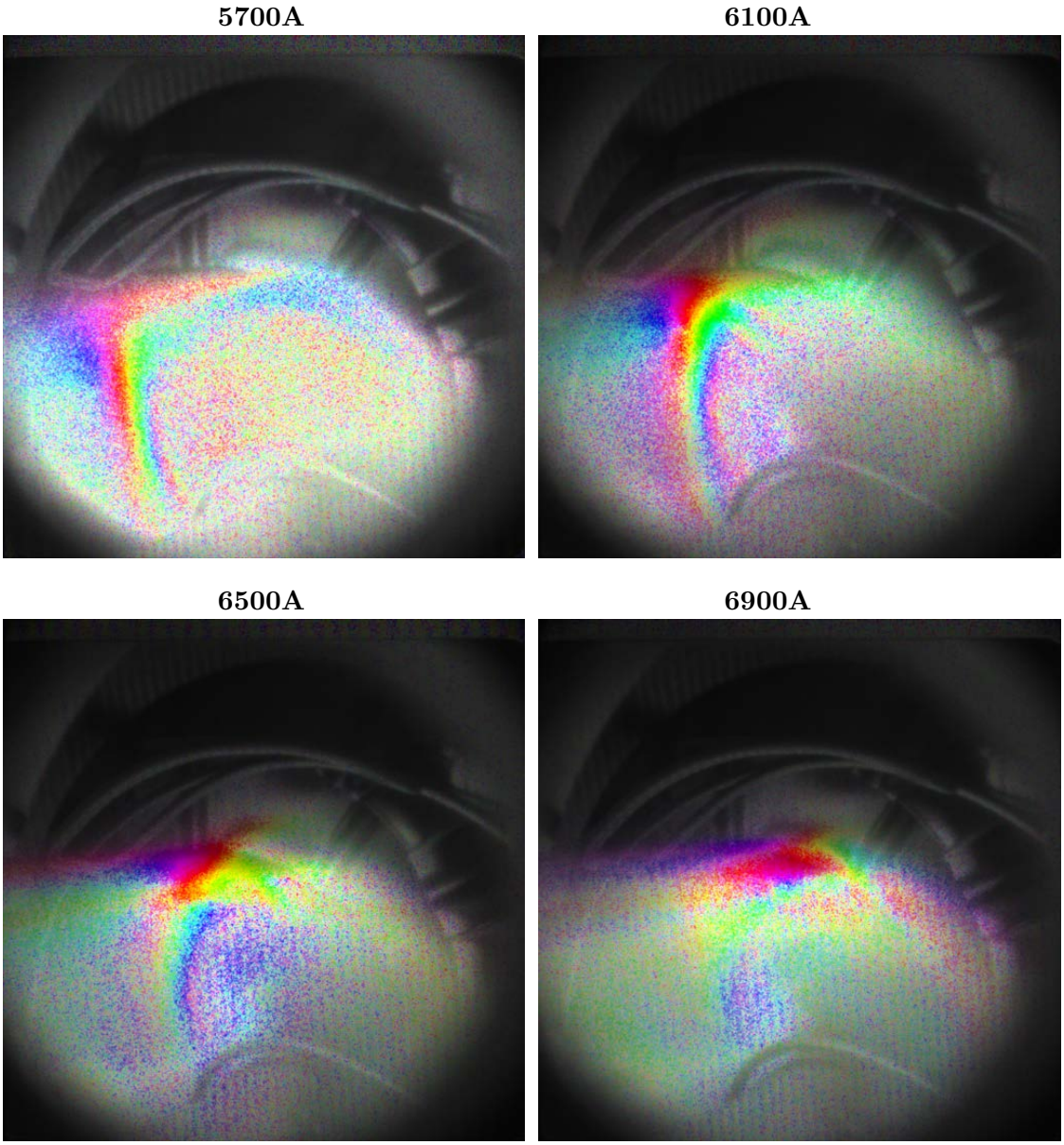

Figure 5.14: Phase of the 7MHz H_α light intensity for ring currents of 5700A, 6100A, 6500A and 6900A. Hydrogen was puffed into the hydrogen plasma so the contrast of the toroidally extended component of the wave is reduced due to enhanced weighting of the line integral in the region directly underneath the antenna. The weak interference fringes visible in the images are produced by the polarimeter that was in place (but not necessary) for the measurements.

The magnetic field coils are connected in series and therefore changing the current only scales the magnetic field strength, without changing the direction of the magnetic field or the shape of the flux surfaces (pressure effects are negligible). Consequently the same transformation can be applied from camera coordinates to Boozer coordinates as done earlier for Fig. 5.9 under the assumption that the wave is concentrated near the LCFS (although the camera registration requires some small corrections due to minor shifts in the lens positions). The Boozer coordinates transformation of these variable field shots is plotted in Fig. 5.15 revealing the phase of the wave in relation to the ion cyclotron

layer and $\omega = 0.85\omega_{ci}$. It is evident in these plots that *the observed wave location shifts in tandem with the ion cyclotron layer and is restricted to the high field side of the layer.* In regions where $\omega < 0.85\omega_{ci}$ the amplitude of the wave, or more precisely the electron density perturbation associated with the wave, drops off such that the observed wave is weak or unresolvable. In the 6.9kA case the upper strap of the antenna is almost completely on the high field side of the ion cyclotron layer but the component of the wave that extends beyond $\phi_B = 290°$ is not visible because ω_{ci} becomes too large relative to the fixed ω. Unfortunately measurements with different magnetic field strengths were not obtained from port 222 to further corroborate these measurements from port 113.

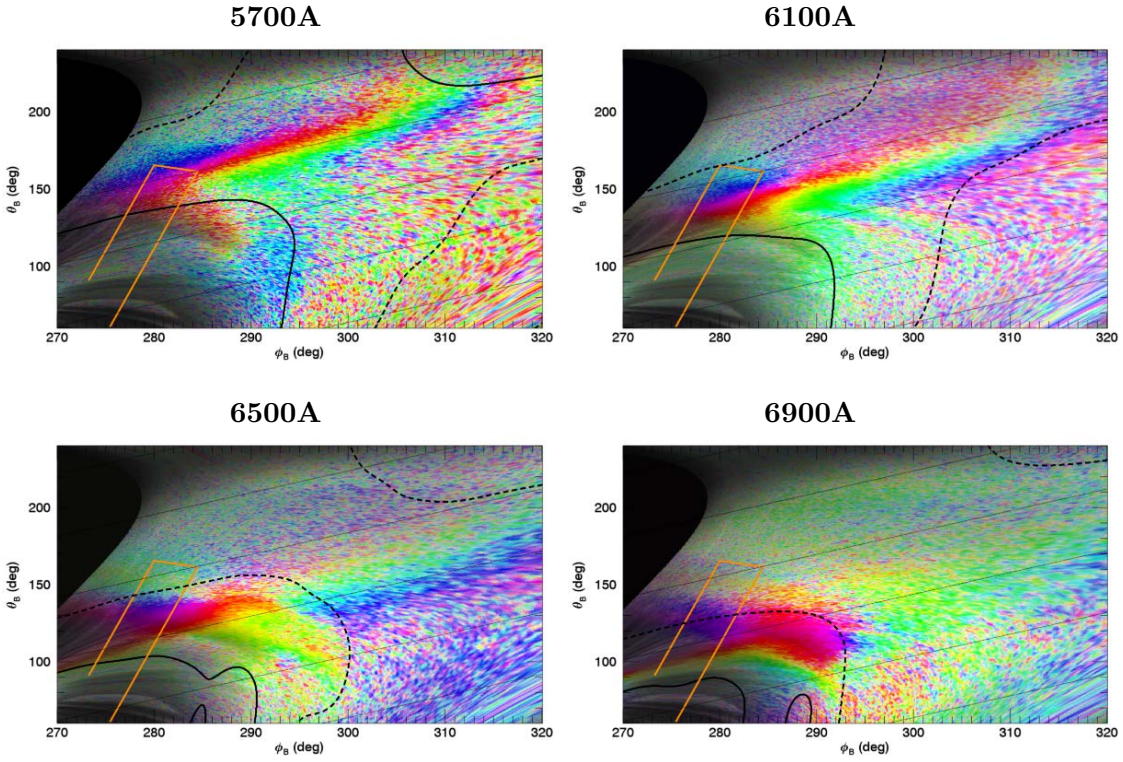

Figure 5.15: Same as Fig. 5.14 but converted into Boozer coordinates. The curved black line depicts the magnetic field strength where $\omega = \omega_{ci}$ and the dashed black line where $\omega = 0.85\omega_{ci}$.

5.2.7 Wave from Port 215

The wave structure seen from port 215 is inconsistent with the poloidally propagating surface wave observed from the other three ports. The wave observed at port 215 has a shorter wavelength and the phase velocity is not in the poloidal direction. From the registration of the view and the VMEC flux surface model it was realised that the wave is only evident near a contour where the LCFS is tangent to the camera sightlines. Furthermore the wavefronts are perpendicular to this contour indicating that the wave is propagating radially inwards. To model the radial propagation of this wave the heuristic model defined in Eq. 5.7 can be adapted to the form,

$$I = I_0\Big(1 + \frac{I_1}{I_0}\cos(k_\rho \rho - \omega t)\Big) \quad \text{with } I_1 \neq 0 \text{ for } \begin{array}{l} 0.71 < \rho < 1 \\ 34° < \theta_B - \iota\phi_B < 130°. \end{array} \tag{5.8}$$

A forward modelled image of the wave with $k_\rho = 40$ is shown in Fig. 5.16 in relation to the sightline-flux surface tangency contour and reproduces the main features of the experimental measurement in Fig. 5.7. The model function is line integrated leading to *constructive interference only near where the sightline is tangent to the flux surface* and destructive interference elsewhere, due to the short wavelength and sightlines having a component normal to the surface. Hence the location that the wave is observed in the plasma is strongly dependent on the viewing location. In Fig. 5.16 it is clear that the wave is not observed near the tangency contour on field lines that do not intersect the antenna, indicating that the wave is limited to the field lines that intersect near the antenna. To match the experimentally observed poloidal range of the wave, the modelled lower limit for flux surfaces intersecting the antenna ($\theta_B - \iota\phi_B$) has been extended by 30° relative to Eq. 5.7. It is fortunate that both the tangency contour and fieldlines intersecting the antenna coincided from the port 215 view, otherwise the wave would not have been observed. In the region the wave is observed $k_\rho = 40$ corresponds to a radial wavelength $\lambda \approx 29$mm.

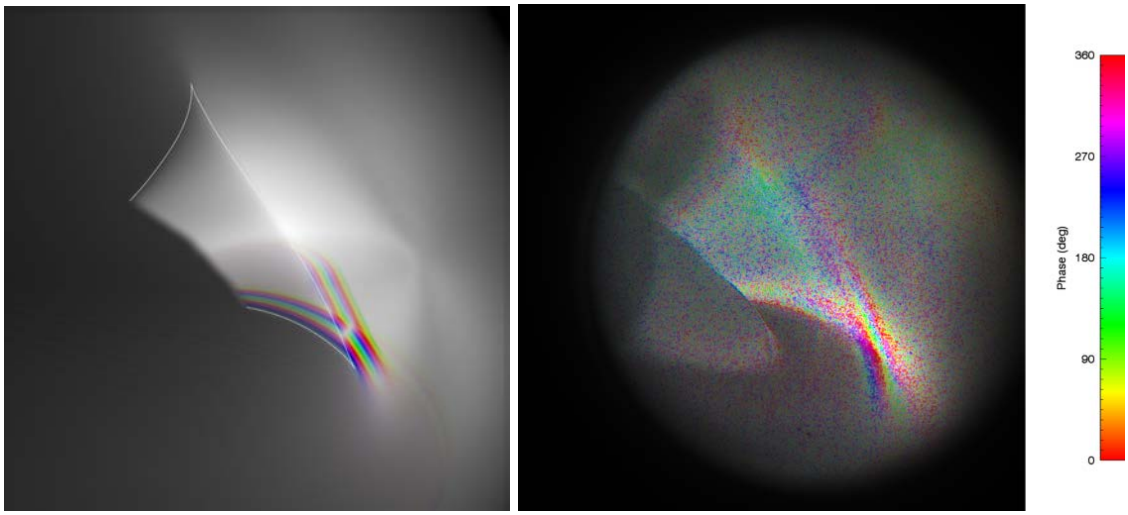

Figure 5.16: (Left) Forward modelled phase seen from port 215 for a radially inwards propagating wave with 29mm wavelength. The white contour traces where the last closed flux surface is perpendicular to the camera sightlines. It is assumed that the wave only exists on field lines that intersect with the antenna. (Right) Copy of the experimental measurement in Fig. 5.7 for comparison.

The maximum experimental contrast of $I_1/I_0 = 1.25\%$, seen in Fig. 5.17, corresponds to *a density fluctuation of* $n_{e1}/n_{e0} \approx 1/25$. The comparison between the model and experimental data highlights that the signal from this view is particularly weak, with $\sim 0.5\%$ noise coming from regions of the plasma where the wave is not apparent. The modelled width of the wave ranges from $0.71 < \rho < 1$ suggesting that the wave energy is absorbed near $\rho = 0.7$. However the cause of the drop off in the intensity perturbation near $\rho = 0.7$ is unclear, particularly because in the observed region of the wave the gradient in $|\mathbf{B}|$ is small and it does not correspond to the position of the ion cyclotron layer. There is no obvious poloidal or toroidal component to the experimentally observed wave and tolerance testing with the forward model suggests that they are limited to the range $|m| < 4$ and $|n| < 10$. Hence *with just a single view it is not possible to precisely measure the parallel component of the propagation vector or the propagation angle* θ.

The observed RF waves propagating in H-1 are summarised in Fig. 5.18 on a LCFS

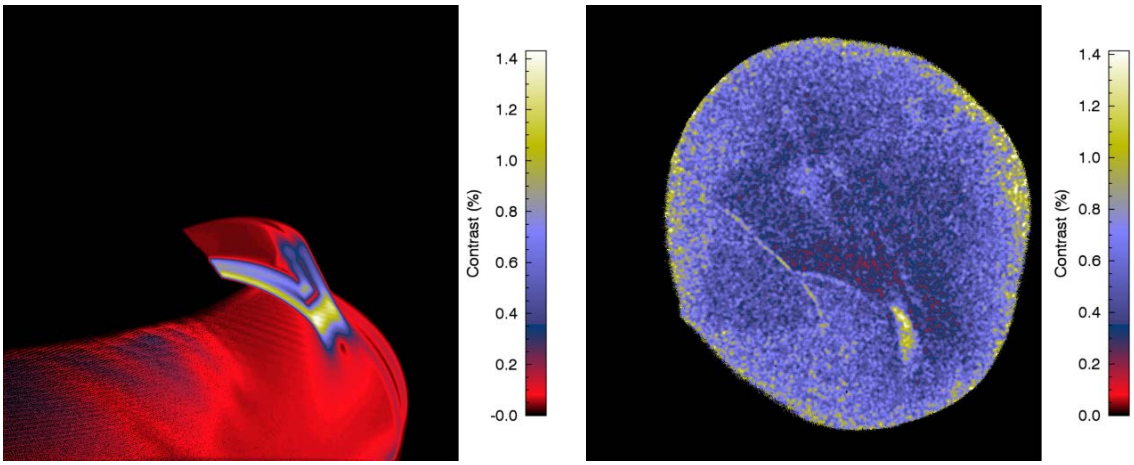

Figure 5.17: (Left) Forward modelled contrast seen from port 215 applying Eq. 5.8 with $I_1/I_0 = 1/25$ (Right) Experimentally measured contrast from port 215.

Boozer coordinates plot. If the RF wave seen from port 113 is restricted to magnetic field lines intersecting near the antenna, then it must propagate through a low field side ($\omega > \omega_{ci}$) region of the ion cyclotron layer near $\phi_B = 220°$ before coming into view from port 215. However in Section 5.2.6 it is evident that the surface wave near the antenna does not propagate on the low field side of the ion cyclotron layer, suggesting *the RF wave observed at port 215 has been mode converted or is unrelated to the surface wave near the antenna.* Possibly the wave visible from port 215 is an electrostatic wave however from a single view with weak signal it is not possible to accurately measure the propagation direction relative to the background magnetic field for studies of the dispersion relationship.

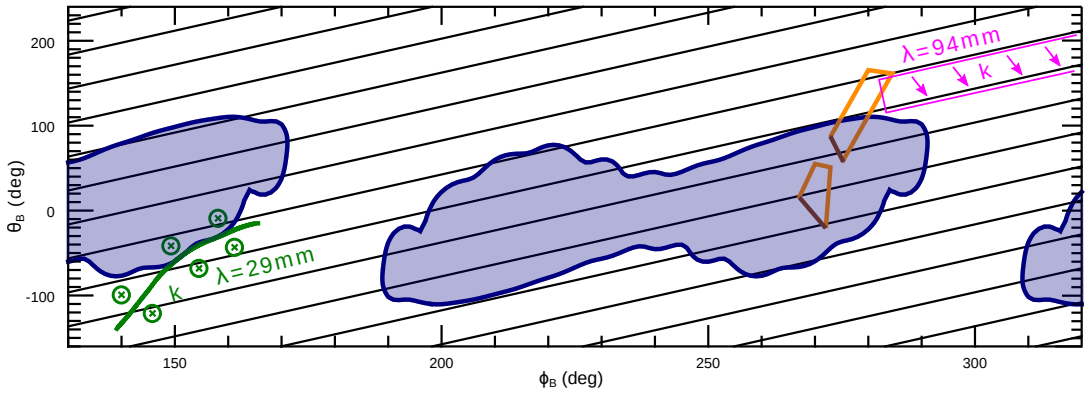

Figure 5.18: Summary plot of the two observed RF waves on H-1 mapped onto the last closed flux surface of H-1 in Boozer coordinates. The ion cyclotron layer $|B| = \omega m_i/e$ for the standard 6.5kA shots is depicted in blue (the $\omega > \omega_{ci}$ low field side is shaded) and the antenna straps in orange. The RF wave (pink) observed from ports 113, 207 and 222 has phase velocity along the surface. The sightline-flux surface tangency contour where the RF wave observed from port 215 is shown in green with crosses, to indicate that the wave is propagating radially inwards in the region close to this contour. The full extent of the green wave is unknown and therefore a bounding box is not shown.

5.2.8 Discussion

Two different RF waves have been observed in different regions of H-1. In the vicinity of the antenna a 7MHz 94mm surface wave is observed to be propagating along the LCFS in the negative poloidal direction at $\approx 85°$ to the magnetic field. The characteristics of the wave are consistent with an ion cyclotron wave. Furthermore given that the H-1 antenna straps have a significant component parallel to the magnetic field capable of launching an $E_{\|}$ component, it is expected that an ion cyclotron wave will indeed be launched. $-120°$ toroidally from the antenna a 7MHz 29mm wave is observed propagating radially inward.

Further experimental measurements in the region near $\phi_B = 220°$ may be valuable to understand the transition between the two RF waves that were observed with different characteristics. The simplified treatment of the ion cyclotron wave (Eq. 5.6) neglects the possibility of mode conversion and does not include the effects of the multiple ion species plasma. Furthermore kinetic effects, finite resistivity and finite electron mass effects may play an important role in the wave propagation. The development of a full-wave ICRF model to understand the wave propagation on H-1 would be the most credible option for not only validating and interpreting the measurements but also for understanding the heating mechanisms on H-1.

The launching of an ion cyclotron wave near the edge of the H-1 plasma appears to be the likely heating source for the previously unexplained hollow electron temperature profile[84]. The $20 - 60$eV electron temperatures observed at the edge of H-1 correspond to a thermal velocity of $v = 2.7 - 4.6 \times 10^6 \mathrm{m\,s^{-1}}$. This is comparable to the parallel phase velocity $v_{\|} = \lambda\nu/\cos\theta = 4 \times 10^6 \mathrm{m\,s^{-1}}$ of the wave observed from port 113. Therefore electron Landau damping of the wave appears to be the likely heating mechanism giving rise to the hollow temperature profiles. It is well known that ion cyclotron waves can deliver significant electron heating via electron Landau damping. For example, on the C Stellarator the observed electron temperatures and heating rates were found to be consistent with electron Landau damping of an ion cyclotron wave[88]. On Alcator C-Mod ion cyclotron waves have been detected with phase contrast imaging that is complemented with full-wave ICRF simulations[89]. Analysis of Alcator C-Mod electron cyclotron emission temperature profiles showed the ion cyclotron wave could produce significant electron heating and was in qualitative agreement with simulations[90].

These measurements on H-1 are the first time ion cyclotron range of frequency waves have been directly imaged and *the technique is certainly worth investigating on other devices*. As part of this research a similar synchronous imaging experiment was attempted on the KSTAR tokamak to look for intensity perturbations in the neutral beam emission at 30MHz caused by ICRF heating. Unfortunately no intensity perturbations were evident in these preliminary 'piggyback' tests, possibly due to non-steady state plasma conditions, the $\times 4$ reduction in duty cycle due to the higher RF frequency and the $90°$ toroidal offset between the neutral beam and ICRF antenna.

Conclusion

Fortuitously the unsuccessful H-1 RF electric field measurements led to arguably the two most important discoveries of this research, the first being the polarisation effects related to the Stark-Zeeman degeneracy[45] and secondly the RF wave imaging measurements. The advances in the instrumental and theoretical understanding of IMSE diagnostics and successful DIII-D measurements are also considerable and make up the greatest portion of the thesis. Many of the insights in this thesis are contained in generalised analytic equations and physical descriptions that serve as useful starting points or benchmarking tools for future calculations. It is beneficial to present a synopsis of the key findings of each chapter to conclude the thesis.

In Chapter 2 the focus is on atomic modelling of the Balmer-α emission in (approximately) crossed electric and magnetic fields. It was discovered that the degenerate Stark-Zeeman states have a degree of freedom that can affect both the state populations and polarisation of the emission. This is of importance because it is well known that upper-states are non-statistically populated, especially for beam-into-gas (BIG) calibrations. The predictions of any Stark-Zeeman model are therefore sensitive to further weaker splitting mechanisms that eliminate the degeneracy and its associated degree of freedom. When the fine structure of the atom is considered, the degeneracy is split such that the quantum states are similar to the Stark-Zeeman $|n,k,m\rangle_L$ states formulated in Section 2.5.3. However microscopic electric fields that exist in the plasma prevent the fields from being precisely crossed, further complicating the situation. With non-orthogonal fields the degeneracy is also split but in this case the quantum states become similar to the $|n,k,m\rangle_C$ states given in Tables 2.5 and 2.6. The distribution of microscopic electric field strengths in a plasma has a large range that includes zero and therefore inevitably some mixture of $|n,k,m\rangle_C$ and $|n,k,m\rangle_L$ similar states will exist. More work is needed to completely model all effects, however it is possible to draw a number of conclusions from these two physically relevant sets of Stark-Zeeman states.

- The σ_0 polarisation orientation is not sensitive to the upper-state populations[1] for either the $|n,k,m\rangle_C$ or $|n,k,m\rangle_L$ states, an important correction to previous studies that found σ BIG calibrations would not be accurate[30, 31].
- With the $|n,k,m\rangle_L$ states the $\sigma_{\pm1} : \pi_{\pm3}$ intensity ratio is sensitive to upper-state populations (Eq. 2.62), contradicting the key assumption of the MSE line ratio measurement technique[42].
- With the $|n,k,m\rangle_L$ states the $\sigma_{\pm1}$ polarisation orientation is sensitive to upper-state populations (Eq. 2.52). Fortunately many factors contribute to drastically limit, and

[1] Ignoring weaker effects relating to the ellipticity of the transitions

likely negate, this sensitivity by either driving the relevant degenerate state pairs to have similar populations ($\delta = 0$ via electron density, beam injection angle ρ and beam velocity effects) or with geometric viewing angle effects (ψ and φ).

Therefore, in the absence of secondary neutrals[34], BIG is expected to be a valid calibration technique for MSE polarisation measurements. Spectrally resolved linear polarisation BIG measurements are needed to validate the $\sigma_{\pm 1}$ polarisation orientation upper-state population dependence, however such a measurement would be challenging given the large range of limiting factors involved.

The work by Yuh[31] highlighted the need for fully polarimetric modelling of the MSE emission but unfortunately this notion has not been embraced and the circular polarisation is often still disregarded. In Section 2.6 equations for the Stark-Zeeman circular polarisation are given, correct to second order in γ/ϵ, that are straightforward to apply for calculating and understanding the s_3 component of the MSE emission. The circular polarisation fraction of the π wings is typically $\sim 20\%$ and is essential to consider in the following circumstances,

- Upon reflection from a non-ideal mirror the linear and circular polarisation will become coupled. This can lead to systematic errors in the polarisation orientation measurement, as realised on DIII-D[20], and will likely be a considerable effect on ITER.

- IMSE polarimeters such as the amplitude spatial heterodyne (ASH) and non-ideal temporally switched single spatial heterodyne (TSSSH) carry s_3 at the same spatial frequency as either s_1 or s_2. These effects are considered in greater detail in Chapter 3.

- The circular polarisation is zero for the σ_0 emission and is therefore a useful indicator for ensuring that σ measuring narrowband filters are centred correctly. The circular polarisation also carries information about the magnetic field direction, additional to that encoded in the polarisation orientation.

Non-optimised 'filter scan' measurements of the circular polarisation on DIII-D were found to be in qualitative agreement with the theoretical circular polarisation calculations, however the spectral resolution and range of the measurement was limited (Fig. 2.11). Higher resolution spectrometer measurements are still needed to validate the accuracy of the calculations.

The concepts and measurement principles involved in polarisation coherence imaging are the focus of Chapter 3. Significant advances are made in quantifying the impacts of the Stark-Zeeman circular polarisation fraction (Section 3.3.2) and non-axial ray effects that give rise to spatial carriers that have previously been observed but not understood (Section 3.2).

The choice of displacer waveplate is the most important consideration when implementing an IMSE diagnostic. The ideal displacer thickness L and optic axis cut angle Θ can be obtained by solving Eqs. 3.49, 3.22 and 3.24 for a given Stark line splitting ϵ and desired spatial carrier fringe frequency k_y. The precise interferometric delay of the displacer, more specifically $\phi_0 + \alpha_l$ (Eq. 3.47), is generally not precisely known and therefore further encoding strategies are needed to separate the delay from the desired polarisation orientation information. For this reason several different IMSE polarimeter designs exist, each with different advantages.

The TSSSH IMSE system delivers the greatest radial resolution, making it possible to resolve H-mode edge pedestal structures in KSTAR[27]. The system was also used for the DIII-D measurements presented in this thesis, however the plasma edge was not in the field of view in this case. Calibration wavelength corrections, non-axial ray effects and non-ideal effects for the TSSSH are considered in theoretical detail in Section 3.4. It is essential to ensure the orientations and retardances of the waveplates in the system are as close to ideal as possible to minimise any coupling of s_3 to s_1 and s_2. Nevertheless, if needed, the displacer delay can be selected to ensure the interferometric ellipticity ξ_I is minimised (via Eq. 3.56) without severely affecting the strength of the desired linear polarisation signal.

The ASH has been preferred for IMSE measurements on ASDEX-U[64] and is also considered in detail. The ASH is intrinsically sensitive to the Stark-Zeeman circular polarisation however it can be decoupled from the measurement to give both the polarisation orientation θ_σ and the interferometric ellipticity ξ_I (Eqs. 3.83 and 3.84). The non-axial ray model is applied to the ASH to reveal the sub-harmonic spatial carriers generated by the system that have not previously been understood and they are predicted to encode usable polarimetric information (Eq. 3.85).

In Chapter 4 the viewing geometry, calibration and results from a two month IMSE campaign on the DIII-D tokamak are presented. After considering the availability of ports and pre-existing Faraday rotation calibrations a decision was made to install the IMSE system on a port with a radial view of the neutral beam, having limited radial resolution of $\sim$ 20cm owing to significant line integration across flux surfaces[67].

The experimental considerations needed for a successful TSSSH IMSE implementation are characterised in detail. The design of the interference filter passband is crucial for maximising the desired signal while ensuring complicating factors such as the relative increase in E_r/E_L and Stark-Zeeman circularity for the half energy component are minimised and therefore straightforward to correct. It was discovered that the retardance of the 'half-wave' FLC switching waveplate in the polarimeter was spatially non-uniform, in addition to being offset from the ideal half-wave delay[40, 61]. The spatial non-uniformity causes the polarisation orientation measurement to be sensitive to the precise ray paths illuminated through the system. Therefore accurate calibration of the polarimeter requires a light source that replicates the illumination of the neutral beam, leading to the recommendation that BIG or in-vessel calibrations are imperative. In this instance the Stark-Zeeman circular polarisation was weak due to the sightlines being largely perpendicular to $\mathbf{B}$. Nonetheless the influence of the circular polarisation on the measurement is described in detail, primarily for the benefit of future IMSE systems with more typical viewing geometries having sightlines largely tangential to the flux surfaces and parallel to $\mathbf{B}$.

Two neutral beams were visible in the IMSE view, one of which intersects with the inner wall allowing for first time measurements on the high field side of the plasma. The close agreement demonstrated between the IMSE measurements from both beams gives confidence in the measurements. The IMSE system was operated simultaneously with conventional MSE polarimeters, viewing the neutral beam from different ports, and was the first time IMSE has been directly benchmarked against conventional measurements. Close agreement was demonstrated for shots with magnetic field and plasma current in the standard direction, particularly after considerations are made for the lower radial resolution of the IMSE view. However the agreement is lost for shots with either reversed

field or current direction. This disagreement is not anticipated to be inherent to the differences between the measurement techniques but is possibly due to residual uncertainties in the IMSE calibration, or effects intrinsic to the ports such as Faraday rotation or stress induced birefringence that were inadequately calibrated.

The original intention of the experiments conducted on the H-1 heliac, covered in Chapter 5, was to apply polarisation coherence imaging techniques to measure the RF electric field in the vicinity of the ICRF antenna. It was anticipated that the measurement technique would deliver improved spatial resolution and sufficient SNR for time resolved measurements compared to spectrometer based measurements. It appears likely that the background light emission from regions either side of the antenna dominated the desired RF Stark split emission, preventing any observation of the electric field. However an oscillation was noticed in the RF time resolved light intensity images and consequently the aim of the H-1 experiments shifted to studying this unexpected phenomena. The weak intensity perturbation at 7MHz has a wave like structure and is thought to result from n_e perturbations produced by a wave propagating in the plasma. Four different viewing ports were used for the measurements and two RF waves with different characteristics were observed, one in the vicinity of the antenna and the other 120° toroidally from the antenna. The RF wave observed near the antenna only propagates on the high field side of the ion cyclotron layer in the region $0.85\omega_{ci} \lessapprox \omega < \omega_{ci}$, as confirmed by a scan of the magnetic field strength (Fig. 5.15). Furthermore the wave is only evident near the last closed flux surface on magnetic field lines that intersect near the antenna, indicating the wave energy propagates along the magnetic field lines. These wave characteristic, along with the measured wavelength and propagation direction, are consistent with an electromagnetic ion cyclotron wave and notably the geometry of the unshielded H-1 antenna does not preclude the launching of an ion cyclotron wave. The parallel velocity of this observed RF wave is comparable to the electron thermal speed and therefore Landau damping of the wave energy to electrons can be expected. Consequently these measurements appear to solve the longstanding anomaly of edge peaked electron temperatures observed on H-1[84]. The other RF wave, observed 120° toroidally from the antenna, also appears to be restricted to magnetic field lines that intersect near the antenna. However this RF wave propagates radially inwards with a shorter wavelength and is possibly a mode converted wave produced from the ion cyclotron wave. This is the first time this wave imaging technique has been used to measure RF heating waves and further investigation of the technique on other devices may be warranted, depending on the anticipated amplitude of the density perturbations produced by the targeted wave.

In summary, polarisation coherence imaging has been demonstrated as a versatile high resolution technique for spectroscopic measurements of electric and magnetic fields. Successful experiments were carried out to measure the magnetic field pitch angle on DIII-D and RF heating waves on H-1. Challenges relating to atomic and optical effects have been investigated and opportunities for improvements in modelling and optical components capable of overcoming these challenges are highlighted.

Bibliography

[1] F. M. Levinton, R. J. Fonck, G. M. Gammel, R. Kaita, H. W. Kugel, E. T. Powell, and D. W. Roberts, "Magnetic field pitch-angle measurments in the PBX-M tokamak using the motional Stark effect," *Physical Review Letters*, vol. 63, no. 19, p. 2060, 1989.

[2] J. Howard, "Snapshot-imaging motional Stark effect polarimetry," *Plasma Physics and Controlled Fusion*, vol. 50, no. 12, p. 125003, 2008.

[3] IEA, *Key World Energy Statistics*. Paris: International Energy Agency, 2016.

[4] IPCC, *Climate Change 2014: Synthesis Report. Contribution of Working Groups I, II and III to the Fifth Assessment Report of the Intergovernmental Panel on Climate Change*. Geneva, Switzerland: IPCC, 2014.

[5] F. Romanelli, *Fusion Electricity: A roadmap to the realisation of fusion energy*. European Fusion Development Agreement, 2012.

[6] E Cartlidge, "Fusion energy pushed back beyond 2050." http://www.bbc.com/news/science-environment-40558758, 2017.

[7] J. Wesson, *Tokamaks*. New York: Oxford University Press, fourth ed., 2011.

[8] A. Boileau, M. Von Hellerman, W. Mandl, H. P. Summers, H. Weisen, and A. Zinoviev, "Observations of motional Stark features in the Balmer spectrum of deuterium in the JET plasma," *Journal of Physics B: Atomic, Molecular and Optical Physics*, vol. 22, no. 7, p. L145, 1989.

[9] H. A. Bethe and E. E. Salpeter, *Quantum Mechanics of One- and Two-Electron Atoms*. Boston, MA: Springer US, 1977.

[10] C. C. Petty, W. R. Fox, T. C. Luce, M. A. Makowski, and T. Suzuki, "Analysis of current drive using MSE polarimetry without equilibrium reconstruction," *Nuclear Fusion*, vol. 42, no. 9, p. 1124, 2002.

[11] B. W. Rice, K. H. Burrell, and L. L. Lao, "Effect of plasma radial electric field on motional Stark effect measurements and equilibrium reconstruction," *Nuclear Fusion*, vol. 37, no. 4, p. 517, 1997.

[12] B. W. Rice, K. H. Burrell, L. L. Lao, and Y. R. Lin-Liu, "Direct Measurement of the Radial Electric Field in Tokamak Plasmas using the Stark Effect," *Physical Review Letters*, vol. 79, no. 14, p. 2694, 1997.

[13] M. F. De Bock, N. J. Conway, M. J. Walsh, P. G. Carolan, and N. C. Hawkes, "Ab initio modeling of the motional Stark effect on MAST," *Review of Scientific Instruments*, vol. 79, no. 10, p. 10F524, 2008.

[14] J. C. Kemp, "Piezo-Optical Birefringence Modulators: New Use for a Long-Known Effect," *Journal of the Optical Society of America*, vol. 59, no. 8, p. 950, 1969.

[15] J. C. Kemp, G. D. Henson, C. T. Steiner, and E. R. Powell, "The optical polarization of the Sun measured at a sensitivity of parts in ten million," *Nature*, vol. 326, no. 6110, p. 270, 1987.

[16] D. Wróblewski, K. H. Burrell, L. L. Lao, P. Politzer, and W. P. West, "Motional Stark effect polarimetry for a current profile diagnostic in DIII-D," *Review of Scientific Instruments*, vol. 61, no. 11, p. 3552, 1990.

[17] N. C. Hawkes, K. Blackler, B. Viaccoz, C. H. Wilson, J. B. Migozzi, and B. C. Stratton, "Design of the Joint European Torus motional stark effect diagnostic," *Review of Scientific Instruments*, vol. 70, no. 1, p. 894, 1999.

[18] J. Chung, J. Ko, H. Wi, M. Messmer, S. Schenkelaars, M. Scheffer, and R. J. E. Jaspers, "Initial operation of a newly developed multichord motional Stark effect diagnostic in KSTAR," *Review of Scientific Instruments*, vol. 87, no. 11, p. 11E503, 2016.

[19] P. Lotte, M. H. Aumeunier, P. Devynck, C. Fenzi, V. Martin, and J. M. Travre, "Wall reflection issues for optical diagnostics in fusion devices," *Review of Scientific Instruments*, vol. 81, no. 10, p. 10E120, 2010.

[20] B. S. Victor, C. T. Holcomb, S. L. Allen, W. H. Meyer, M. A. Makowski, and A. Thorman, "Asymmetries in the motional Stark effect emission on the DIII-D tokamak," *Review of Scientific Instruments*, vol. 87, no. 11, p. 11E126, 2016.

[21] W. Mandl, R. C. Wolf, M. G. Von Hellermann, and H. P. Summers, "Beam emission spectroscopy as a comprehensive plasma diagnostic tool," *Plasma Physics and Controlled Fusion*, vol. 35, no. 10, p. 1373, 1993.

[22] D. Voslamber, "Self-calibrating magnetic field diagnostics in beam emission spectroscopy," *Review of Scientific Instruments*, vol. 66, no. 4, p. 2892, 1995.

[23] F. M. Levinton, "The motional Stark effect: Overview and future development (invited)," *Review of Scientific Instruments*, vol. 70, no. 1, p. 810, 1999.

[24] R. C. Wolf, A. Bock, O. P. Ford, R. Reimer, A. Burckhart, A. Dinklage, J. Hobirk, J. Howard, M. Reich, and J. Stober, "Motional Stark Effect measurements of the local magnetic field in high temperature fusion plasmas," *Journal of Instrumentation*, vol. 10, no. 10, p. P10008, 2015.

[25] R. T. Mumgaard and R. T. Mumgaard, "Review of results from mse diagnostics," tech. rep., Massachusetts Institute of Technology, Cambridge MA, 2015.

[26] J. Howard, C. Michael, F. Glass, and A. Danielsson, "Time-resolved two-dimensional plasma spectroscopy using coherence-imaging techniques," *Plasma Physics and Controlled Fusion*, vol. 45, no. 7, p. 1143, 2003.

[27] J. Howard, C. Michael, H. Chen, R. Lester, A. Thorman, and J. Chung, "Spectropolarimetrc optical systems for imaging plasma internal fields, structures and flows," *Journal of Instrumentation*, vol. 10, no. 9, p. P09023, 2015.

[28] O. Marchuk, Y. Ralchenko, R. K. Janev, W. Biel, E. Delabie, and A. M. Urnov, "Collisional excitation and emission of Hα Stark multiplet in fusion plasmas," *Journal of Physics B: Atomic, Molecular and Optical Physics*, vol. 43, no. 1, p. 11002, 2010.

[29] O. Marchuk, Y. Ralchenko, and D. R. Schultz, "Non-statistical population distributions for hydrogen beams in fusion plasmas," *Plasma Physics and Controlled Fusion*, vol. 54, no. 9, p. 95010, 2012.

[30] M. F. Gu, C. T. Holcomb, R. J. Jayakuma, and S. L. Allen, "Atomic models for the motional Stark effect diagnostic," *Journal of Physics B: Atomic, Molecular and Optical Physics*, vol. 41, no. 9, p. 95701, 2008.

[31] H. Y. H. Yuh, *The Motional Stark Effect Diagnostic on Alcator C-Mod*. PhD thesis, Massachusetts Institute of Technology, 2005.

[32] R. C. Isler, "Profiles and polarizations of the Balmer-α line from high-temperature hydrogen atoms in strong magnetic fields," *Physical Review A*, vol. 14, no. 3, p. 1015, 1976.

[33] F. M. Levinton and H. Yuh, "The motional Stark effect diagnostic on NSTX," *Review of Scientific Instruments*, vol. 79, no. 10, p. 1, 2008.

[34] H. Y. Yuh, F. M. Levinton, S. D. Scott, and J. Ko, "Simulation of the motional Stark effect diagnostic gas-filled torus calibration," *Review of Scientific Instruments*, vol. 79, no. 10, p. 10F523, 2008.

[35] F. M. Levinton, S. H. Batha, and M. C. Zarnstorff, "Calibration of the upgraded motional Stark effect diagnostic on TFTR," *Review of Scientific Instruments*, vol. 68, no. 1, p. 926, 1997.

[36] N. J. Conway, M. F. M. De Bock, C. A. Michael, M. J. Walsh, P. G. Carolan, N. C. Hawkes, E. Rachlew, J. F. G. McCone, S. Shibaev, and G. Wearing, "The MAST motional Stark effect diagnostic," *Review of Scientific Instruments*, vol. 81, no. 10, p. 10D738, 2010.

[37] J. Ko and J. Chung, "Direct measurements of safety factor profiles with motional Stark effect for KSTAR tokamak discharges with internal transport barriers," *Review of Scientific Instruments*, vol. 88, no. 6, p. 063505, 2017.

[38] S. M. Hamberger, B. D. Blackwell, L. E. Sharp, and D. B. Shenton, "H-1 Design and Construction," *Fusion Technology*, vol. 17, no. 1, p. 123, 1990.

[39] G. G. Borg, B. D. Blackwell, S. M. Hamberger, D. Rudakov, D. A. Schneider, L. E. Sharp, M. Shats, and B. C. Zhang, "The H-1 radio frequency system and an initial study of plasma formation," *Fusion Engineering and Design*, vol. 26, no. 1-4, p. 191, 1995.

[40] A. Thorman, C. Michael, and J. Howard, "A high spatial resolution Stokes polarimeter for motional Stark effect imaging," *Review of Scientific Instruments*, vol. 84, no. 6, p. 063507, 2013.

[41] J. Chung, J. Ko, J. Howard, C. Michael, G. von Nessi, A. Thorman, and M. De Bock, "Motional Stark effect diagnostics for KSTAR," *Journal of the Korean Physical Society*, vol. 65, no. 8, 2014.

[42] N. A. Pablant, K. H. Burrell, R. J. Groebner, C. T. Holcomb, and D. H. Kaplan, "Measurements of the internal magnetic field using the B-Stark motional Stark effect diagnostic on DIII-D," *Review of Scientific Instruments*, vol. 81, no. 10, p. 10D729, 2010.

[43] A. Iwamae, A. Sakaue, M. Atake, K. Sawada, M. Goto, and S. Morita, "Alignment creation and deviation from statistical population distribution in hydrogen n = 3 levels observed on MSE spectra of LHD plasma," *Plasma Physics and Controlled Fusion*, vol. 51, no. 11, p. 115004, 2009.

[44] E. K. Souw and J. Uhlenbusch, "Calculation of the combined Zeeman and translational Stark effect on the Hα-multiplet," *Physica B+C*, vol. 122, no. 3, p. 353, 1983.

[45] A. Thorman, "Polarisation of the Balmer-α emission in crossed electric and magnetic fields," *Journal of Quantitative Spectroscopy and Radiative Transfer*, vol. 207, p. 8, 2018.

[46] R. Reimer, A. Dinklage, R. Fischer, J. Hobirk, T. Löbhard, A. Mlynek, M. Reich, L. Sawyer, and R. Wolf, "Spectrally resolved motional Stark effect measurements on ASDEX Upgrade," *Review of Scientific Instruments*, vol. 84, no. 11, p. 113503, 2013.

[47] A. E. Kramida, "A critical compilation of experimental data on spectral lines and energy levels of hydrogen, deuterium, and tritium," *Atomic Data and Nuclear Data Tables*, vol. 96, no. 6, p. 586, 2010.

[48] O. Marchuk, Y. Ralchenko, D. R. Schultz, E. Delabie, and A. M. Urnov, "Non-statistical simulations for neutral beam spectroscopy in fusion plasmas Non-Statistical Simulations for Neutral Beam Spectroscopy in Fusion Plasmas," *AIP Conference Proceedings*, vol. 169, no. 1, p. 169, 2012.

[49] C. T. Holcomb, M. A. Makowski, R. J. Jayakumar, S. A. Allen, R. M. Ellis, R. Geer, D. Behne, K. L. Morris, L. G. Seppala, and J. M. Moller, "Motional Stark effect diagnostic expansion on DIII-D for enhanced current and Er profile measurements," *Review of Scientific Instruments*, vol. 77, no. 10, p. 10E506, 2006.

[50] E. Stambulchik, "FAC Changelog." https://github.com/fnevgeny/fac/blob/master/ChangeLog, 2017.

[51] R. Reimer, O. Marchuk, B. Geiger, P. J. Mc Carthy, M. Dunne, J. Hobirk, and R. Wolf, "Influence of non-local thermodynamic equilibrium and Zeeman effects on magnetic equilibrium reconstruction using spectral motional Stark effect diagnostic," *Review of Scientific Instruments*, vol. 88, no. 8, p. 083509, 2017.

[52] H. R. Griem, *Spectral Line Broadening by Plasmas.* New York: Academic Press, 1974.

[53] S. Scott and H. Yuh, "Effect of Zeeman Splitting on MSE Analysis," tech. rep., Massachusetts Institute of Technology, 2004.

[54] J. Howard, "Coherence imaging spectro-polarimetry for magnetic fusion diagnostics," *Journal of Physics B: Atomic, Molecular and Optical Physics*, vol. 43, no. 14, p. 144010, 2010.

[55] J. Howard and J. Chung, "Spatial heterodyne Stokes vector imaging of the motional Stark-Zeeman multiplet," *Review of Scientific Instruments*, vol. 83, no. 10, p. 10D510, 2012.

[56] O. P. Ford, J. Howard, and R. C. Wolf, "The prototype imaging motional Stark effect diagnostic for ASDEX upgrade," *Review of Scientific Instruments*, vol. 86, no. 9, p. 093504, 2015.

[57] A. Thorman, C. Michael, M. De Bock, and J. Howard, "A photoelastic-modulator-based motional Stark effect polarimeter for ITER that is insensitive to polarized broadband background reflections," *Review of Scientific Instruments*, vol. 87, no. 7, p. 073504, 2016.

[58] K. Kato, "Second-harmonic generation to 2048 Å in β-BaB2O4," *IEEE Journal of Quantum Electronics*, vol. 22, no. 7, p. 1013, 1986.

[59] F. E. Veiras, L. I. Perez, and M. T. Garea, "Phase shift formulas in uniaxial media: an application to waveplates," *Applied Optics*, vol. 49, no. 15, p. 2769, 2010.

[60] J. Howard, A. Diallo, R. Jaspers, and J. Chung, "Spatial heterodyne spectro-polarimetry systems for imaging key plasma parameters in fusion devices," *Plasma and Fusion Research*, vol. 5, p. S1010, 2010.

[61] A. Thorman, C. Michael, J. Howard, B. Victor, C. Holcomb, and S. Allen, "Motional Stark effect imaging first results on the DIII-D tokamak," *Review of Scientific Instruments*, vol. 89, no. 10, p. 10D124, 2018.

[62] S. Guimond and D. Elmore, "Designing effective crystal waveplates requires understanding the engineering tradeoffs.," *Oemagazine*, p. 26, 2004.

[63] A. R. Thorman, *Motional Stark Effect Imaging of Plasma Currents in the KSTAR Tokamak*. Honours thesis, Australian National University, 2012.

[64] O. P. Ford, A. Burckhart, R. McDermott, T. Pïtterich, and R. C. Wolf, "Imaging motional Stark effect measurements at ASDEX Upgrade," *Review of Scientific Instruments*, vol. 87, no. 11, p. 11E537, 2016.

[65] A. Burckhart, O. Ford, A. Bock, R. Fischer, M. Reich, D. Rittich, and R. Wolf, "The new Imaging Motional Stark Effect diagnostic at ASDEX Upgrade," in *2nd European Conference on Plasma Diagnostics*, (Bordeaux), 2017.

[66] D. Wróblewski and L. L. Lao, "Polarimetry of motional Stark effect and determination of current profiles in DIII-D (invited)," *Review of Scientific Instruments*, vol. 63, no. 10, p. 5140, 1992.

[67] B. W. Rice, "q profile measurements with the motional Stark effect diagnostic in the DIII-D tokamak," *Fusion Engineering and Design*, vol. 34-35, p. 135, 1997.

[68] B. W. Rice, D. G. Nilson, and D. Wróblewski, "Motional Stark effect upgrades on DIIID," *Review of Scientific Instruments*, vol. 66, no. 1, p. 373, 1995.

[69] W. W. Heidbrink, D. Liu, Y. Luo, E. Ruskov, and B. Geiger, "A code that simulates fast-ion Dα and neutral particle measurements," *Communications in Computational Physics*, vol. 10, no. 3, p. 716, 2011.

[70] D. M. Thomas, B. A. Grierson, J. M. Muñoz Burgos, and M. A. Van Zeeland, "Determination of neutral beam energy fractions from collisional radiative measurements on DIII-D," *Review of Scientific Instruments*, vol. 83, no. 10, p. 10D518, 2012.

[71] R. Lester, Y. Zhai, C. Corr, and J. Howard, "Coherence imaging for ion temperature and flow measurements in a low-temperature helicon plasma source," *Plasma Sources Science and Technology*, vol. 25, no. 1, p. 015025, 2016.

[72] B. A. Grierson, K. H. Burrell, B. Crowley, L. Grisham, and J. T. Scoville, "High speed measurements of neutral beam turn-on and impact of beam modulation on measurements of ion density," *Review of Scientific Instruments*, vol. 85, no. 10, p. 103502, 2014.

[73] B. A. Grierson, "Private communication," 2017.

[74] J. Chung, D. K. Lee, D. Seo, and M. C. Choi, "Installation of a fast framing visible camera on KSTAR," *Review of Scientific Instruments*, vol. 79, no. 10, p. 1, 2008.

[75] C. Klepper, D. Hillis, R. Isler, J. Hillairet, E. Martin, L. Colas, A. Ekedahl, M. Goniche, P. Lotte, G. Colledani, V. Martin, S. Panayotis, B. Pegourié, and J. Harris, "Direct, spectroscopic measurement of electric fields in a plasma-RF antenna interaction region in Tore Supra," *Journal of Nuclear Materials*, vol. 438, p. S1232, 2013.

[76] C. C. Klepper, R. C. Isler, J. Hillairet, E. H. Martin, L. Colas, A. Ekedahl, M. Goniche, J. H. Harris, D. L. Hillis, S. Panayotis, B. Pegourié, P. Lotte, G. Colledani, and V. Martin, "Dynamic stark spectroscopic measurements of microwave electric fields inside the plasma near a high-power antenna," *Physical Review Letters*, vol. 110, no. 21, p. 215005, 2013.

[77] E. H. Martin, M. Goniche, C. C. Klepper, J. Hillairet, R. C. Isler, C. Bottereau, L. Colas, A. Ekedahl, S. Panayotis, B. Pegourie, P. Lotte, G. Colledani, J. B. Caughman, J. H. Harris, D. L. Hillis, S. C. Shannon, F. Clairet, and X. Litaudon, "Electric field determination in the plasma-antenna boundary of a lower-hybrid wave launcher in Tore Supra through dynamic Stark-effect spectroscopy," *Plasma Physics and Controlled Fusion*, vol. 57, no. 6, p. 065011, 2015.

[78] E. H. Martin, *Electric field measurements of the capacitively coupled magnetized RF sheath utilizing passive optical emission spectroscopy.* PhD thesis, North Carolina State University, 2014.

[79] W. H. Steel, *Interferometry.* Cambridge: Cambridge University Press, 1983.

[80] B. Frost, *Diagnostic Development of Gas Delivery and Viewing System for Analysing the Electric Field Stark Effect on H-Alpha Light Emissions close to a Plasma Excitation Antenna.* Masters thesis tbp, Australian National University.

[81] J. H. Harris, M. G. Shats, B. D. Blackwell, W. M. Solomon, D. G. Pretty, S. M. Collis, J. Howard, H. Xia, C. A. Michael, and H. Punzmann, "Fluctuations and stability of plasmas in the H-1NF heliac," *Nuclear Fusion*, vol. 44, no. 2, p. 279, 2004.

[82] R. Cross, *An Introduction to Alfven Waves.* Bristol: IOP Publishing, 1988.

[83] T. H. Stix, *Waves in plasmas.* New York: American Institute of Physics, 1992.

[84] S. Ma, J. Howard, B. D. Blackwell, and N. Thapar, "Measurements of electron density and temperature in the H-1 heliac plasma by helium line intensity ratios," *Review of Scientific Instruments*, vol. 83, no. 3, p. 033102, 2012.

[85] R. F. Gandy, M. A. Henderson, J. D. Hanson, G. J. Hartwell, and D. G. Swanson, "Magnetic surface mapping with an emissive filament technique on the Auburn torsatron," *Review of Scientific Instruments*, vol. 58, no. 4, p. 509, 1987.

[86] S. P. Hirshman and J. C. Whitson, "Steepest-descent moment method for three-dimensional magnetohydrodynamic equilibria," *Physics of Fluids*, vol. 26, no. 12, p. 3553, 1983.

[87] A. H. Boozer, "Guiding center drift equations," *Physics of Fluids*, vol. 23, no. 5, p. 904, 1980.

[88] S. Yoshikawa and H. Yamato, "Observation of Collisionless Electron Heating by Ion Cyclotron Waves," *Physics of Fluids*, vol. 9, no. 9, p. 1814, 1966.

[89] E. Nelson-Melby, M. Porkolab, P. T. Bonoli, Y. Lin, A. Mazurenko, and S. J. Wukitch, "Experimental Observations of Mode-Converted Ion Cyclotron Waves in a Tokamak Plasma by Phase Contrast Imaging," *Physical Review Letters*, vol. 90, no. 15, p. 4, 2003.

[90] Y. Lin, S. J. Wukitch, P. T. Bonoli, E. Marmar, D. Mossessian, E. Nelson-Melby, P. Phillips, M. Porkolab, G. Schilling, S. Wolfe, and J. Wright, "Ion cyclotron range of frequencies mode conversion electron heating in deuterium-hydrogen plasmas in the alcator C-Mod tokamak," *Plasma Physics and Controlled Fusion*, vol. 45, no. 6, p. 1013, 2003.

Disclaimer

This report was prepared as an account of work sponsored by an agency of the United States Government. Neither the United States Government nor any agency thereof, nor any of their employees, makes any warranty, express or implied, or assumes any legal liability or responsibility for the accuracy, completeness, or usefulness of any information, apparatus, product, or process disclosed, or represents that its use would not infringe privately owned rights. Reference herein to any specific commercial product, process, or service by trade name, trademark, manufacturer, or otherwise, does not necessarily constitute or imply its endorsement, recommendation, or favouring by the United States Government or any agency thereof. The views and opinions of authors expressed herein do not necessarily state or reflect those of the United States Government or any agency thereof.